ZIRCONIA-BASED ACID CATALYSTS FOR BIOMASS CONVERSION

By

Wenwen Zhang

A THESIS SUBMITTED TO MACQUARIE UNIVERSITY

FOR THE DEGREE OF

DOCTOR OF PHILOSOPHY

SCHOOL OF ENGINEERING

January 2021

I certify that the work in this thesis has not previously been submitted for a degree nor has it been submitted as part of requirements for a degree to any other university or institution other than Macquarie University.

Wenwen Zhang 31-January-2021

Acknowledgements

Time flies, I have been studied at Macquarie University (MQ) for more than 3 years. A lot of things happened during this time, with happiness and also unhappiness. It is a very precious experience for me and is definitely a very important memory in my life. In my PhD, I've got lots of great help which has supported me in getting through these years, and I appreciate it very much. First and foremost, I sincerely express my deepest gratitude to my principal supervisor, Associate Professor Yijiao Jiang, for supervising me as her PhD student at MQ. I appreciate it very much for her supervision, encouragement, support, and advice for my PhD project. At the same time, I also show many thanks to my co-supervisor, Professor Jun Huang from the University of Sydney, who has also supported me a lot for all my projects.

I would like to acknowledge the research teams I was lucky enough to work with. Dr. Zichun Wang has provided me with great support during my research. Thanks also go to Yuxiang Zhu, Aleksei Marianov, Haimei Xu, Xiaoxia Yang, Shengsheng Gu, Amanj Kheradmand, Alena Kochubei, and Yutong Zhao for being good team colleagues and providing me help during my PhD life. At the same time, I would show my deepest thanks to people who support and help me during my PhD experience: Dr. Susan Law, Ms. Wendy Tao, Dr. Aaron Colusso, Dr. Marion Gaborieau, Dr. Patrice Castignolles, Prof. Alfsons Baiker, Dr. Alf Garcia-Bennett, Mr. Thomas Lawson, Dr. Chao Shen, Mr. Russell Field, Mr. Tony Wang, Dr. Remi Rouquette, Dr. Nicole Cordina, Dr. Liting Deng, Dr. Dominik Kopp, Dr. Kerstin Petroll, Dr. Shufang Zhao, Dr. Jia Ding, Mr. Lizhuo Wang, Mr. Wenjie Yang, Mr. Keith Imrie, and Mr. Walther Adendorff. Thanks for all the support they give me which help accomplish my PhD.

Besides, I would also greatly acknowledge the financial support from the Australian Research Council (ARC) Discovery Projects and the ARC Industrial Transform Research Hub. Meantime, I greatly appreciate the HDR funding support from the School of Engineering at MQ throughout my PhD program. I want to express my great gratitude to the International Research Training Program Scholarship as well.

I would like to present my great thanks to my family. Thanks a lot for their endless love and encouragement which support me a lot in my PhD life.

Last but not least, I sincerely express my deepest gratitude to the examiners for reviewing my thesis and for their valuable comments.

List of publications

Journal publications included in the thesis

[1] **Wenwen Zhang**, Yuxiang Zhu, Haimei Xu, Marianne Gaborieau, Jun Huang, and Yijiao Jiang. Glucose conversion to 5-hydroxymethylfurfural on zirconia: Tuning surface sites by calcination temperatures. Catalysis Today. 2020, 351: 133-140. (Chapter 3) "Reprinted with permission from Zhang, W., Zhu, Y., Xu, H., Gaborieau, M., Huang, J., & Jiang, Y. (2020). Glucose conversion to 5-hydroxymethylfurfural on zirconia: tuning surface sites by calcination temperatures. *Catalysis Today*, 351, 133-140. https://doi.org/10.1016/j.cattod.2018.10.002."

[2] **Wenwen Zhang**, Zichun Wang, Aleksei Marianov, Yuxiang Zhu, Shufang Zhao, Patrice Castignolles, Marianne Gaborieau, Alfons Baiker, Jun Huang, and Yijiao Jiang. Boosting the formation of Brønsted acid sites on flame-made WO_x/ZrO_2 for glucose conversion. ACS Catalysis. Submitted. (Chapter 4)

[3] **Wenwen Zhang**, Zichun Wang, Jun Huang, Yijiao Jiang. Zirconia-based solid acid catalysts for biomass conversion. Energy & Fuels. accepted. "Reprinted with permission from Zhang, W., Wnag, Z., Huang, J., & Jiang, Y. (2021) Zirconia-Based Solid Acid Catalysts for Biomass Conversion, *Energy Fuels*, 35(11), 9209-9227. Copyright 2021 American Chemical Society. DOI:10.1021/acs.energyfuels.1c00709."

Other publications

[1] Amanj Kheradmand, Yuxiang Zhu, **Wenwen Zhang**, Aleksei Marianov, and Yijiao Jiang. Cobalt oxide on mesoporous carbon nitride for improved photocatalytic hydrogen production under visible light irradiation. International Journal of Hydrogen Energy. 2019, 44: 17930-17942.

[2] Zichun Wang, Luke A. O'Dell, Xin Zeng, Can Liu, Shufang Zhao, Wenwen Zhang, Marianne Gaborieau, Yijiao Jiang, and Jun Huang. Insight into three-coordinate aluminum species on ethanol-to-olefin conversion over ZSM-5 zeolites. Angewandte Chemie International Edition. 2019, 58: 2-10.

[3] Yuxiang Zhu, Xianlin Zheng, **Wenwen Zhang**, Amanj Kheradmand, Shengshen Gu, Marcin Kobieblusz, Wojciech Macyk, Haitao Li, Jun Huang, Yijiao Jiang. Near-infrared-triggered nitrogen fixation over upconversion nanoparticles assembled carbon nitride nanotubes with nitrogen vacancies, ACS Applied Materials & Interfaces, accepted.

Conference presentations

[1] **Wenwen Zhang** and Yijiao Jiang. Glucose conversion to a valuable platform chemical on zirconium oxide. School of Engineering HDR Conference in 2018, Macquarie University, Australia, June 7, 2018, **Oral Presentation**.

[2] **Wenwen Zhang** and Yijiao Jiang. Glucose conversion to HMF on zirconium oxide: effect of calcination temperature. 2018 International Symposium on Advancement and Prospect of Catalysis Science & Technology, Sydney, Australia, July 25-27, 2018, **Oral Presentation**.

[3] **Wenwen Zhang** and Yijiao Jiang. Efficient acid-catalyzed conversion of glucose to 5-hydroxymethlfurfural on zirconium tungstate. School of Engineering HDR Conference in 2019, Macquarie University, Australia, June 20, 2018, **Poster Presentation**.

[4] **Wenwen Zhang** and Yijiao Jiang. Efficient acid-catalyzed conversion of glucose to 5-hydroxymethlfurfural on zirconium tungstate. International Symposium on Energy Conversion and Storage Materials 2019. Brisbane, Australia, July 30-August 2. **Oral Presentation**.

Abstract

Zirconia-based acid catalysts have received vastly attention as both catalyst itself and catalyst support owing to its favorable physicochemical properties, and they have been widely applied in catalytic industry. Biomass conversion, such as glucose to 5-hydroxymethylfurfural (HMF) transformation, is of high value in the sustainable manufacturing of green chemicals and it is well known as a viable way to deal with the shortage of fossil fuels and control the CO_2 emission by its consumption. The production of ethyl mandelate (EM) from phenylglyoxal (PG) is also attractive since it is a stereochemical mandelic derivate that has been widely applied in pharmaceutical and chemical industries. This thesis presents the studies of zirconia-based acid catalysts and their application in glucose to HMF and PG to EM conversions.

First, ZrO_2 with different crystalline structures and various surface catalytic properties was fabricated via tuning the thermal treatment. ZrO_2 calcined at 300 °C which is in an amorphous state possesses more Lewis (LAS) and Brønsted acid sites (BAS) than ZrO_2 samples calcined at other temperatures, thus presenting a better catalytic performance in glucose conversion. Second, WO_x/ZrO_2 with high accumulated BAS was synthesized through a single-step flame spray pyrolysis (FSP) method. FSP-made WO_x/ZrO_2 possesses ~80 % of BAS and a BAS to LAS ratio (B/L) of ~4, while the corresponding material prepared by conventional impregnation method exhibits ~50 % of BAS and a B/L ratio of ~1. FSP-made WO_x/ZrO_2 presents outstanding performance in glucose conversion expressed as its prominent HMF selectivity. Third, layered mesoporous ZrO_2/SiO_2 nanospheres (ZrO_2/SiO_2 MNS) with tunable surface acid sites are designed. Z/SZ, with ZrO_2 in the outer layer to produce LAS that triggers the glucose isomerization to fructose, and ZrO_2/SiO_2 in the inner layer to generate BAS that promotes the fructose conversion to HMF, is considered as the ideal structure. Z/SZ can dramatically shorten the induction period

within 15 min which is distinctly shorter than that of the other structured ZrO_2/SiO_2 MNS catalysts (more than 45 min), with over two times higher TOF.

Fourth, hierarchical pore structured ZrO_2/SiO_2 core-shell mesoporous nanospheres (ZrO_2/SiO_2 CS-MNS) with different pore size distributions are designed for PG to EM conversion. Though hierarchical structures of CS-MNS-2-10Zr (larger shell than the core) and CS-MNS-3-10Zr (larger core than the shell) possess lower LAS and BAS than CS-MNS-1-10Zr (well-defined pore with uniform pore size), they can achieve a better catalytic performance in PG conversion, with over two times higher TOF.

In summary, this work provides different modification methods such as tuning thermal treatment, loading metals on zirconia, developing different layer constructions and different hierarchical structures to synthesize a variety of catalytically active complex based on zirconia. It achieves many purposes including modifying the crystalline structures, adjusting the acidity features, and tuning pore size distributions in zirconia-based catalysts. As a result, it can provide different views to comprehensively understand the catalytic performance of catalysts in glucose to HMF and PG to EM conversions, offering key knowledge for enhancing the efficiency of the catalysts in biomass conversion in the future.

Table of Contents

Chapter 1 Introduction

1.1 Background

Energy drives our life, and the consumption of energy correlates strongly with our living standards [1]. No doubt that our demand for energy is continuously rising over the past to the future. In the International Energy Outlook (IEO2016), the overall world energy consumption in 2012 was 549 quadrillion Btu and it is expected to go up to 815 quadrillion Btu in 2040, that is almost a 48 % of increase [2]. Besides the clean energy resources such as wind, water, and solar, *etc*., crude petroleum, gas, and coal are still the predominant resources for world energy supply at the moment [2, 3]. It is estimated that the proportion of fossil fuels will still be stabled at ~78 % of energy use in 2040 [2, 3]. However, according to the investigation from Shahria S. and Erkan T., the calculation of the depletion time of fossil fuel is around 35, 107, and 37 years for oil, coal, and gas, respectively [3].

On the other hand, the consumption of fossil fuels has caused a huge emission of carbon dioxide (CO_2), and the main contributors to the CO_2 emission are coal, natural gas, and liquid fuels. In 2012, the world CO_2 emission related to energy was 32.2 billion metric tons, and the projection is supposed to be 43.2 billion metric tons in 2040 with an increase of 34 % according to IEO2016 [2]. This result has a huge impact on the global warming, which has started at about the time of the onset of the Industrial Revolution when the consumption of fossil fuel experienced sudden acceleration and simultaneously caused a distinct rise of CO_2 emission [1]. What's worse, it is reported that the temperature has risen 0.6 ^{o}C per decade during the last 30 years in high-latitude regions of the Earth, which is twice as fast as the average global warming [4]. Since there are large quantities of organic carbon stored in the permafrost of the Arctic and sub-Arctic regions, the

microbial breakdown of organic carbon and the release of greenhouse gases, CO_2 and methane (CH_4), in this area will be accelerated due to a warming climate with induced environmental changes [4]. This unfavorable phenomenon thus causes a vicious circle and aggravates global warming.

Because of the severe global warming, there is some foreseeable influence on life on the Earth. For example, as the average temperature continues to rise, the growing seasons of plants may be extended, especially in northern latitudes. At the same time, warmer temperatures may also do a favor to the multiplication and spread of pests and this is no doubt a disaster for the agriculture industry. In some areas known for their hot climate and desert topography, climate change may cause its longer dry seasons and more frequent droughts. On the other hand, some animal habitats may become endangered because of the warmer temperature, especially in colder climate. There are several strong impacts that may lead to a tremendous change in life on the Earth, and these influences have attracted great attention from many countries. For instance, due to the thermal expansion of the ocean surface, the receding glaciers, and the melting of the polar ice caps thermal expansion of the ocean surface caused by the global warming, it is estimated that there will be a 30-50 cm rise in the sea level by the end of this century. This has a devastating influence on coastal areas, especially agricultural land in the Southern US, Bangladesh, India, and Egypt [1]. Meanwhile, CO_2 absorption in the ocean will lower its pH level, which highly threatens the life of coral reef, calcareous plankton, and other sea organisms. The increase in violent weather phenomena in recent decades also arise a lot of problems for human lives and properties [1].

Therefore, all the information clearly reveals the crucial and urgent problems we face nowadays. To make it brief, a sustainable future is imperative, and we need to deal with the shortage of fossil fuels and control the CO_2 emission stemming from consuming it. Consequently, political,

economic, and environmental concerns have promoted the research on more sustainable and environmentally friendly energy technologies, such as utilizing biomass as a raw material for the production of chemicals and other fuel substitutes (biorefinery) [5-9]. Biomass, all plants and plant-derived materials, is supposed to have great potential to provide renewable energy for the future, and it is the only available renewable resource for liquid transportation fuel currently [5, 10, 11]. Biorefinery development enables to reduce fossil fuel consumption and CO_2 emission, and it can also establish a robust bio-based industry at the same time [7]. Between 1945 and 1950, 66 % of n-butanol and 10 % of acetone in the United States were produced by fermentation of molasses and starch [6]. From the economic view, biorefinery can in turn provide the financial incentive to stimulate the expansion of the biorefining industry. Therefore, biomass conversion will definitely play a vital role in our future life, especially in the energy and environment areas. Nevertheless, the catalyst is the key to the door of biomass conversion.

Heterogeneous catalysts, especially solid acid catalysts, have a wide application in the chemical industry. As heterogeneous catalysts, solid acid catalysts have outstanding features in product separation and catalyst recycling [12]. On the other hand, most of the biomass conversions in the petrochemical industry are governed by carbocation chemistry, which requires acidic active sites from solid acid catalysts [13, 14]. Thus, solid acid catalysts that contain numerous acidic sites highly meets this purpose. Therefore, they are considered as one of the most popular heterogeneous catalysts and are widely applied in biomass conversion [15-18]. Up to date, different synthesis techniques have been applied for the production of solid acid catalysts, such as wet-impregnation method, chemical liquid deposition method, hydrothermal method, atomic layer deposition, flame spray pyrolysis method, *etc*.

Among different kinds of solid acid catalysts, zirconia-based acid catalysts have received vast attention as both catalyst itself and catalyst support owing to its favorable physicochemical properties [19-21]. Doping with other oxoanions to zirconia can create additional electron-deficiencies which may generate new acid sites or increase the strength of Brønsted acidity, thus can enhance its catalytic performance in reactions such as dehydration, hydrogenation, and hydrogen exchange, *etc*. [20, 22]. Besides, some novel zirconia-based metal-organic frameworks (MOFs) are also proposed as one of the most promising MOF materials for catalytic applications due to the outstanding stability, rich structure types, intriguing properties and functions [23-27]. Therefore, there is no doubt to evidence that zirconia-based acid catalysts will make a big difference in biomass conversion.

1.2 Scope and objectives

This thesis presents the fabrication of zirconia-based acid catalyst and its applications which focus on two reactions: a) glucose conversion to 5-hydroxymethylfurfural (HMF); b) phenylglyoxal (PG) conversion to ethyl mandelate (EM) (Figure 1.1). Of special interest is on glucose conversion to HMF. The major research is to study how different factors, including calcination temperature, metal loading, layer structure, and pore distribution, affect the physicochemical properties of zirconia-based acid catalyst and further influence the catalytic performance in the reactions.

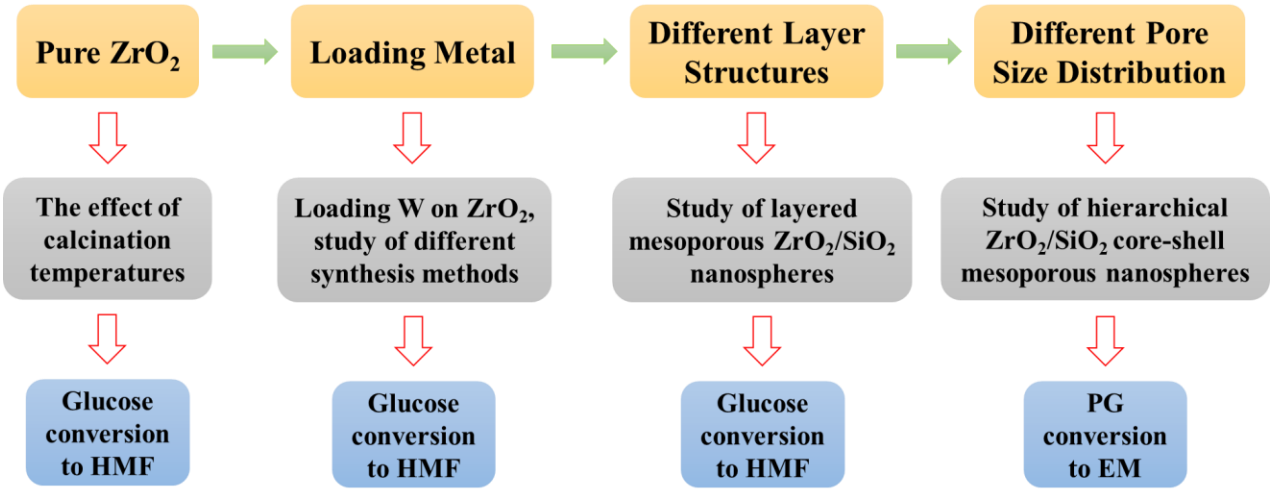

Figure 1.1 A typical work flow of this thesis

The specific objectives of this thesis are:

1) To fabricate different forms of pure zirconia (ZrO_2) by tuning its calcination temperature, and study its performance in glucose conversion to HMF. Through this research, it provides an acid regulation strategy via tuning calcination temperature to adjust the acidic properties for solid acid catalysts.

2) To modify ZrO_2 by doping tungsten to synthesize tungstate zirconia (WO_x/ZrO_2) and to compare the conventional impregnation and flame spray pyrolysis on the catalytic performance in glucose conversion to HMF. Through this research, it provides an acid regulation strategy via loading metals on ZrO_2 to adjust the acidic properties for solid acid catalysts. At the same time, the influence of different synthesis methods on the distribution of acid sites was also studied as another acid regulation strategy.

3) To fabricate layered mesoporous ZrO_2/SiO_2 nanosphere and study how the layer structure affects the catalytic performance in glucose conversion to HMF. The influence of Zr on mesoporous pore structure was also investigated. Through this research, it provides an acid

regulation strategy via tuning the layer structures to adjust the acidic properties for solid acid catalysts.

4) To fabricate hierarchical pore structured ZrO_2/SiO_2 core-shell mesoporous nanospheres and applied the catalysts for phenylglyoxal conversion. The influence of the hierarchical pores on the diffusion of the reactants and products, and further on the catalytic performance is studied.

This thesis consists of the following chapters: Chapter 1 gives the background information and scope of this thesis. Chapter 2 is a literature review about the zirconia-based catalysts and their applications. Chapter 3 presents the study of different forms of pure zirconia by adjusting the calcination temperature, and its catalytic performance in glucose conversion. Particularly, the influence of calcination temperature on its surface acid sites is discussed in detail. Chapter 4 shows the boosting of the Brønsted acidity on flame-made WO_x/ZrO_2 for glucose conversion. Chapter 5 introduces a new model of the layered structured mesoporous ZrO_2/SiO_2 nanosphere. The influence of zirconia on mesoporous pore structure and its catalytic performance in glucose conversion was investigated. Chapter 6 focuses on the fabrication of hierarchical pore structured ZrO_2/SiO_2 core-shell mesoporous nanospheres with different pore size distributions. The catalytic conversions of PG to EM were applied with this catalyst, revealing the crucial function of pore size distribution. Chapter 7 summarizes the key research outcomes of this thesis and features a discussion on the prospects and the challenges on zirconia-based acid catalysts.

References

[1] Ghoniem, A. F., *Prog. Energy Combust. Sci.* **2011**, *37*, 15-51.

[2] International Energy Outlook 2016, in: U.S.E.I. Administration (Ed.), **2016**.

[3] Shafiee, S.; Topal, E. *Energy Policy* **2009**, *37*, 181-189.

[4] Schuur, E. A.; Mcguire, A. D.; Schadel, C.; Grosse, G.; Harden, J. W.; D. Hayes, J.; Hugelius, G.; Koven, C. D.; Kuhry, P.; Lawrence, D. M.; Natali, S. M.; Olefeldt, D.; Romanovsky, V. E.; Schaefer, K.; Turetsky, M. R.; Treat, C. C. Vonk, J. E. *Nature* **2015**, *520*, 171-179.

[5] Perlack, R. D.; Wright, L. L.; Turhollow, A. F; . Graham, R. L; Stokes, B. J.; Erbach, D. C.; Department of Enery, and Oak Ridge National Laboratory (Ed.) **2005**.

[6] Dodds, D. R.; Gross, R. A. *Science* **2019**, *318*, 1250-1251.

[7] Bozell, J. J.; Petersen, G. R. *Green Chem.* **2010**, *12*, 539-554.

[8] Christensen, C. H.; Rass-Hansen, J. C.; Marsden, C.; Taarning, E.; Egeblad, K. *ChemSusChem* **2008**, *1*, 283-289.

[9] Corma, A.; Iborra, S.; Velty, A. *Chem. Rev.* **2007**, *107*, 2411-2502.

[10] Liu, W. J.; Li, W. W.; Jiang, H.; Yu, H. Q. *Chem. Rev.* **2017**, *117*, 6367-6398.

[11] Daoutidis, P.; Rangarajan, S.; Torres, A. I. *AIChE J.* **2013**, *59*, 3-18.

[12] Hattori, H.; Ono, Y. **2015**.

[13] Rinaldi, R.; Schuth, F. *Energy. Environ. Sci.* **2009**, *2*, 610-626.

[14] Busca, G. *Chem. Rev.* **2007**, *107*, 5366-5410.

[15] Hara, M. *Energy Environ. Sci,* **2010**, *3*, 601-607.

[16] Zabeti, M.; Aroua, M. K. *Fuel Process. Technol.* **2009**, *90*, 770-777.

[17] Tanabea, K.; Holderich, W. F. *Appl. Catal. A: Gen.* **1999**, *181*, 399-434.

[18] Huber, G. W.; Barrett, C. J.; Dumesic, J. A. *Science* **2005**, *308*, 1446-1450.

[19] Ho, S. M. *Mater. Sci. Eng.* **1982**, *54*, 23-29.

[20] Nakano, Y.; Iizuka, T.; Hattori, H.; Tanabe, K. *J. Catal.* **1979**, *57*, 1-10.

[21] Parvulescu, V. I.; Bonnemann, H.; Parvulescu, V.; Endruschat, U.; Rufinska, A.; Lehmann, C. W.; Tesche, B.; Poncelet, G. *Appl. Catal. A: Gen.* **2001**, *214*, 273-287.

[22] Cortés-Jácome, M. A.; Angeles-Chavez, C. López-Salinas, E.; Navarrete, J.; Toribio, P.; Toledo, J. A. *Appl. Catal. A: Gen.* **2007**, *318*, 178-189.

[23] Bai, Y.; Xie, L. H.; Rutledge, W.; Li, J. R.; Zhou, H. C. *Chem. Soc. Rev.* **2016**, *45*, 2327-2367.

[24] Chen, J.; Chen, L.; Liu, R.; Huang, X.; Ye, D. *Green Chem.* **2014**, *16*, 2490-2499.

[25] Furukawa, H.; O'Keeffe, M.; Yaghi, O. M. *Science* **2013**, *341*, 974-986.

[26] Feng, D.; Li, J. R.; Jiang, H. L.; Wei, Z.; Zhou, H. C. *Angew. Chem. Int. Ed* **2012**, *51*, 10307-10310.

[27] Guillerm, F. R. V.; Dan-Hardi, M.; Devic, T.; Vishnuvarthan, M.; Campo, B.; Vimont, A.; Clet, G.; Yang, Q.; Maurin, G.; Frey, G.; Vittadini, A.; Gross, S.; Christian, S. *Angew. Chem. Int. Ed.* **2012**, *51*, 9267-9271.

Chapter 2 Literature review

2.1 Solid acid catalysts

Catalysts are essential to modern society in many fields such as energy conversion, chemical manufacture, and environmental technology, *etc*., with a world catalyst market of billions of US dollars per year [1-5]. It is estimated that ~85 % of industrial chemical processes rely on catalysts [1]. For instance, in the decomposition of large molecules, in the polymerization of small molecules, and in the isomerization of rearrangement of molecules [6]. Compared to homogeneous catalysts, the heterogeneous catalysts are environmentally friendly and sustainable due to the simplicity and versatility of process engineering, easy recovery and reuse, less reactor and plant corrosion problems, and environmentally safe disposal [7]. Indeed, 80 % of industrial catalytic processes involve the use of heterogeneous catalysts while homogeneous catalysts and biocatalysts occupy only 17 % and 3 %, respectively [1]. Particularly, nearly all transportation fuel productions are associated with one or more solid acid catalysts [1]. Examples of solid acid catalysts are detailed in Table 2.1.

Table 2.1 Solid acid catalysts [8]

Class	Example
Zeolite	X-, Y-zeolites, Ferrierite, Chabasite, Mordenite, Beta-zeolite, Erionite, ZSM-5, MCM-22, *etc*.
Zeolite-like	Metalloaluminophosphate (*eg*. SAPO), Beryllosilicate, Gallosilicate, Titanosilicate, stanosilicate montmorillonite, *etc*.
Clay	Saponite, Montmorillonite
Metal oxide	SiO_2, Al_2O_3, WO_3, Nb_2O_5, TiO_2, *etc*.
Mixed metal oxide	SiO_2-MgO, SiO_2-Al_2O_3, WO_3-ZrO_2, WO_3-Al_2O_3, WO_3-SnO_2, TiO_2-SiO_2, SiO_2-ZrO_2, *etc*.

Table 2.1 (continued)

Class	Example
Supported acid	H_3PO_4/SiO_2 (SPA), $AlCl_3/SiO_2$, H_3PO_4/SiO_2, heteropolyacids/SiO_2, SO_3H/SiO_2, SO_3H/C, $HClO_4/SiO_2$, BF_3/SiO_2, *etc*.
Sulfated oxide	SO_4/TiO_2, SO_4/ZrO_2, SO_4/SnO_2, *etc*.
Layered transition metal oxide	$HNbWO_6$, $HTaWO_6$, $HNbMoO_6$, *etc*.
Metal salt	$FePO_4$, $Nb_3(PO_4)_5$, $AlPO_4$, $NiSO_4$, *etc*.
Heteropoly compound	$H_3PMo_{12}O_{40}$, $H_4SiW_{12}O_{40}$, $H_3PW_{12}O_{40}$, $H_4SiMo_{12}O_{40}$, *etc*.
Cation exchange resin	Amberlyst-15, Nafion, Nafion-silica composite

There are ~180 different solid acid catalysts categorized as metal oxides, phosphates, resins, and zeolites, *etc.* applied in ~130 different industrial processes such as isomerization, alkylation, dehydration, and condensation, *etc.* [9]. Extensive efforts and investments are dedicated to the heterogeneous catalyst industry, in promoting the development of solid acids (Table 2.2). The fast development of the solid acid catalyst industry also produces significant economic benefit per year in return.

Table 2.2 Representative catalysts applied in the common industrial processes [9]

Process	Catalyst	Company
Isomerization	Zeolites, H-ZSM-5, H-Mordenite, Fe/Mn/sulfated ZrO_2, Ferrierite, B_2O_3/Al_2O_3, H^+ ion-exchange resin, *etc*.	UOP, UCC, Exxon, SNAM, Shell, Mobil Oil, Sun Refining, *etc*.
Alkylation	Zeolites, ZSM-5, Mordenite, MgO, Fe-V-O/SiO_2, Al_2O_3, Sulfated ZrO_2, *etc*.	Mobile-Badger, UOP, Raytheon, Enichem, Chiyoda, BASF, *etc*.

Table 2.2 (continued)

Process	Catalyst	Company
Dehydration and condensation	Al_2O_3, Sulfonic acid resin, $Nb_2O_5 \cdot nH_2O$, Ion-exchange resin, ZrO_2, *etc*.	Petrobrass, UOP, Sumitomo, Bayer, Chisso, *etc*.
Amination	Modified ion-exchange Mordenite, zeolite, Cu, Ni/SiO_2-Al_2O_3, MgO, B_2O_3, TiO_2/SiO_2, *etc*.	Nitto, Du Pont, Kao, USS, Nobel, *etc*.
Cracking	SiO_2-Al_2O_3, zeolite, Calcined kaolin, H-ZSM-5, *etc*.	Mobil, China Petro, Ashland, Davison, Nippon Oil, *etc*.
Etherification	Ion-exchange resin, Al_2O_3, Al-B-P-O, Pillared clay, smectic, *etc*.	IFP, ARCO, SNAM, Ube, BP, Mobil, Exxon, *etc*.
Hydration	Solid phosphoric acid, Ion-exchange resin, Sulfonic acid resin, H-ZSM-5, MgO, MnO_2, *etc*.	Shell, BP, Mitsui Petrochem, Mobil, Reynolds Tobacco, *etc*.
Esterification	Ion-exchange resin, Mercapto-functionalized sulfonated polysiloxane, ZSM-5, SAPO-34 in FCC-catalyst matrix, *etc*.	Davy-McKee, Degussa AG, Mobil, UOP, Tonen, China Petro, *etc*.
Disproportionation	Zeolite, ZSM-5, ZrO_2-Cr_2O_3, $Al_2(SO_4)_3/SiO_2$, SiO_2-Al_2O_3, *etc*.	UOP, Mobil, Mitsubishi Chem., Sumitomo, SNAM, *etc*.

2.2 Fundamentals of solid acid catalysts

2.2.1 Lewis acid theory

The definition of Lewis acid was first proposed by G.N. Lewis in 1923 by generalizing the traditional categories of acid and base [10]. It is generally recognized that Lewis acid-base

electronic theory is an extensive development of the proton and solvent system definitions and it practically covers all acid-base categories [10, 11]. In light of electronic theory, the substance containing a long pair of electrons that could be applied to complete the stable group of another atom is defined as the basic, while the substance that can attract a long pair of electrons from another molecule is classified as the acid [10]. In another word, the basic substance (B) provides a pair of electrons while the acidic substance (A) accepts such a pair of electrons (Equation 2.1) [8, 10].

$$A + :B \rightarrow A : B \qquad (2.1)$$

The acid and base in accordance with this definition are called Lewis acid and Lewis base, respectively. Take an example as shown in Equation 2.2, BF_3 is a Lewis acid and NH_3 corresponds to a Lewis base.

$$BF_3 + : NH_3 \rightarrow F_3B : NH_3 \qquad (2.2)$$

Later, a concept of hard and soft acids and bases (HSAB) was introduced, trying to illustrate the affinities between acid and base which don't lie with the electronegativity or other relevant macroscopic properties [12, 13]. In this definition, small-sized, highly positively charged, and hardly polarized electron accepters are classified as hard acids, while the large-sized with the low positive charge and have easily removed valence electrons are assigned as soft acids [11, 12, 14]. For example, H^+, Na^+, Mg^{2+}, Ti^{4+}, and $AlCl_3$ are commonly recognized as hard acids, while Ag^+, Pd^{2+}, and $GaCl_3$ are soft acids [8]. Normally, hard acids are likely to react with hard bases while soft acids are likely associated with soft bases [8, 11]. This HSAB is a qualitative theory to define hard-soft acid.

2.2.2 Brønsted acid theory

Besides Lewis electronic theory, another approach originated independently in 1923 by J.N Brønsted and T.M Lowry is also considered as a widely spread and practical acid-base theory, which is not limited to aqueous solutions but is also applicable to all proton (H^+)-containing systems [8, 15]. In this definition, an acid (AH) is a proton donor, and a base (B^-) is a proton acceptor (Equation 2.3).

$$AH + B^- \rightarrow A^- + BH \qquad (2.3)$$

The species of AH and A^- are referred to a pair of conjugate acid and base. In the same way, BH and B^- are also conjugate pairs. The acid and base related to this definition are called Brønsted acid and Brønsted base, respectively. Based on this theory, an acid may be positive ions (cations, *eg*. H_3O^+, NH_4^+), neutral molecules (*eg*. $HClO_4$, H_2SO_4), or anions (*eg*. HSO_4^-, OH^-), while base could be negative ions (anions, *eg*. ClO_4^-, SO_4^{2-}) and neutral molecules (*eg*. H_2O) [15]. Take an example as shown in Equation 2.4, NH_4^+ is a Brønsted acid while OH^- is a Brønsted base.

$$NH_4^+ + OH^- \rightarrow NH_3 + H_2O \qquad (2.4)$$

In Brønsted-Lowry theory, the tendency to donate or accept protons, normally significantly influence the strength of acid or base, respectively. It is also generally accepted that stronger acids react to form weaker acids, and vice versa, stronger bases react to form weaker bases [15].

2.2.3 Surface acidity

When the definitions of Lewis and Brønsted acid are applied into solid acids, it mainly means the surface acidity of the catalysts. The solid acid with Lewis acidity usually represents the catalyst with which the surface site can present the property of accepting electron pair, the site is called Lewis acid site (LAS) [8]. Similarly, the solid acid with Brønsted acidity has the surface site which

presents a property of proton donation, and the site is called Brønsted acid site (BAS) [8]. The solid catalyst which contains the LAS or BAS is called the solid acid catalyst. Obviously, a solid catalyst can have either LAS, or BAS, or presents both acidities at the same time.

Normally, unsaturated metal cations can produce surface LAS. When the catalysts undergo high-temperature calcination or heating under vacuum, the surface hydroxyl groups or adsorbed carbon dioxide will be eliminated, then the metal ions such as Al, Sn, Ti, *etc*. will be exposed and serve as LAS [8]. For example, metal cations (*e.g*. Sn^{4+}, Nb^{5+}, and Ta^{5+}) incorporated into the structure of beta zeolites or mesoporous silica-based materials [16, 17]. On the other hand, the LAS can also be introduced by supporting metal compounds on the surface. For instance, metal alkoxides (Al, Zr) or chlorides (Al, Sn) with -OH groups of mesoporous silica can show strongly Lewis acidity [11, 18]. Besides, the possibility to generate the metal component from the metal-organic frameworks (MOF) with a diversity of transition metals could also be largely exploited as Lewis acids [19].

The simplest type of Brønsted acid is the acid in the solid form. A typical one is heteropolyacids such as $H_3PW_{12}O_{40}$. Meanwhile, perchloric acid, sulfuric acids, or benzenesulfonic acids supported on silica gel or mesoporous silica, or solid phosphoric acid entrapped in silica can all be applied as solid Brønsted acids [8]. On the other hand, amorphous carbon materials bearing groups of -OH, $-SO_3H$, and -COOH can also work as efficient Brønsted acid catalysts [20]. The residual acidic hydroxyl groups normally exist on the surface of metal oxides such as Nb_2O_5, Al_2O_3, or WO_3, *etc*. after dehydration, which can donate protons and serve as BAS [8, 21]. Also, a common kind of aluminosilicates, zeolites, is another type of Brønsted acid catalyst [22, 23].

Actually, a lot of solid acid catalysts such as metal oxides, zeolites, or resins possess both LAS and BAS [7, 23]. In the catalysis industry, some complicated reactions require both LAS and BAS

to trigger the reaction and achieve the expected product yield and selectivity. For example, glucose to 5-hydroxymethylfurfural (HMF) transformation is considered a chain reaction which needs LAS to isomerize glucose to fructose, and BAS to dehydrate fructose to HMF [24]. Therefore, the catalyst which can perform both Lewis and Brønsted acidity is supposed to be a prior choice [25].

2.3 Bare zirconia and its application

Among different kinds of solid acid catalysts, zirconia (ZrO_2) and zirconia-based solid acid catalysts are attractive catalysts or catalyst supports owing to their favorable physicochemical properties, including high oxygen storage capacity, strong acidity, remarkable stability, and notable activity, *etc*. [26-30].

Bare ZrO_2 is a polymorphic white crystalline ceramic material that possesses superior hardness, tensile strength, and corrosion resistance. It is well known that ZrO_2, which can be derived from heating amorphous zirconium hydroxide ($Zr(OH)_4$), which may have two co-existing structurally phases, a metastable tetragonal phase and stable monoclinic phase. Their distributions highly rely on the calcination temperature [31-33]. The coordination environments of zirconium and oxygen in ZrO_2 are different in various crystal polymorphs. The Zr^{4+} cation is octacoordinated and the O^{2-} anion is tetracoordinated in a tetragonal polymorph, whereas the Zr^{4+} cation is heptaccorrdinated and the O^{2-} anion is either tri- or tetracoordinated in monoclinic polymorph [28, 34]. The acidity feature of ZrO_2 was studied by Chen *et al*., showing that there were two types of LAS, presenting in different strengths, concentrations, and stabilities [31].

S. Joshi *et al*. studied the catalytic activity of ZrO_2 in cellulose conversion to levulinic acid, and found that the formation of partial oxo complex by ZrO_2 in hydroxide form can facilitate cellulose hydrolysis followed by glucose dehydration, which was similar to $CrCl_3$ [35, 36]. In this reaction

(Figure 2.1), hydrous ZrO_2 forms an oxo complex with the glycosidic oxygen of cellulose to lower the activation energy, then the LAS from Zr^{4+} break down the glycosidic linkage [35]. Through hydrogen bonding, the oxo complex further accelerates the mutarotation of glucose from α-anomer to β-one, which undergoes further isomerization to fructose and dehydration to HMF, and subsequently rehydration to levulinic acid and formic acid [35]. In this research, it achieves a remarkable levulinic acid yield of 53.9 mol% at 180 ^oC, with remarkable stability and cellulose conversion [35].

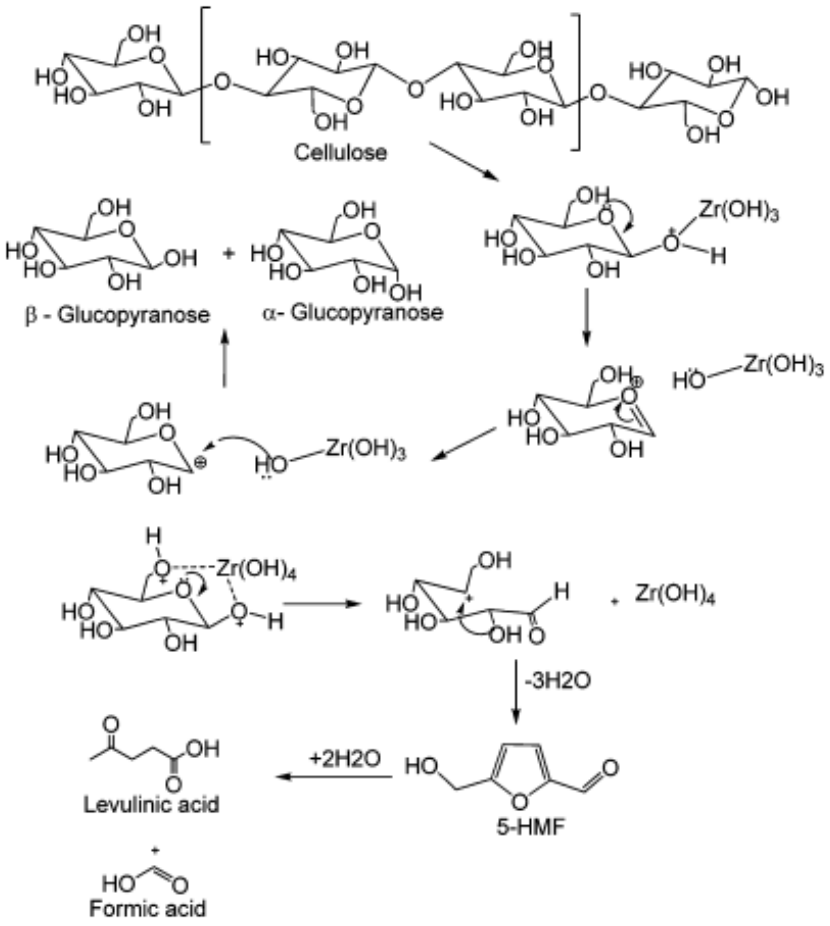

Figure 2.1 Proposed mechanism for cellulose conversion catalyzed by ZrO_2 in hydroxide form under hydrothermal conditions [35]

Due to the specific physicochemical properties, bare ZrO_2 is widely applied as a catalyst or catalyst support, especially in the high-temperature field [27, 28]. According to the research by K. Tomishige *et al*, dimethyl carbonate (DMC) could be selectively synthesized from methanol and CO_2 catalyzed by the pure ZrO_2 prepared via the calcination of $Zr(OH)_4$ at 400 ^oC, with a high DMC formation rate [37]. On the other hand, ZrO_2 was also reported to be highly effective for the isomerization of 1-butene [38]. I.J. Kuo *et al*. did research on cellulose conversion by crystalline mesoporous ZrO_2 nanocatalysts in ionic liquid systems, and they got a maximum of 5.8 % of glucose yield and 29.2 % of HMF yield at 120 ^oC in 3 h reaction [39]. Since ZrO_2 could show prior physiochemical properties in supercritical water, it displays outstanding performance for catalytic aquathermolysis of heavy oil [26]. The overall applications of pure ZrO_2 are summarized in Table 2.3.

2.4 Zirconia as a catalyst support

2.4.1 Sulfated zirconia

In addition to active metals, SO_4^{2-} anions are usually immobilized into ZrO_2 structures to generate exceptionally strong acid sites. The first sulfated zirconia (SZ) was explored as a hydrocarbon isomerization catalyst in 1962 [40]. Since SZ can attribute super-acidity even stronger than the concentrated sulfuric acid, it became popular since it is able to transform butane into isobutane even at room temperature [41, 42]. Similar to the influence of other loading metals, increasing sulfate concentration will retard the crystallization of ZrO_2. In addition, the formation of BAS has been shown to be favored at higher sulfate loading [43]. Moreover, W.H. Chen *et al*. pointed out that though elaborated sulfation treatment of ZrO_2 can lead to the formation and coexistence of strong BAS and LAS, the acid strengths of the existing acid sites is independent of the sulfur contents [31].

Extensive research focus on studying the structure of SZ in order to illustrate the nature of active acid sites [44]. It is generally considered that the structure of SZ is a chelating bidentate complex, in which the sulfated specie chelates to a single zirconium atom (Figure 2.3a) [44, 45]. Upon thermal treatment at high temperature, the BAS can be formed since the SO_4^{2-} ions attached on zirconium atoms can enhance the ability of the adjacent zirconium atoms to donate protons due to the electron inductive effect of two S=O bonds in the sulfate groups [43, 44]. In contrast, less coordinated zirconium atoms have a tendency to withdraw electrons, acting as LAS [43]. The structures of BAS and LAS is shown in Figure 2.2b. It is also reported that further incorporation of metal promoters such as Ga, Al, and Fe, *etc*. into SZ can create additional BAS and LAS [31].

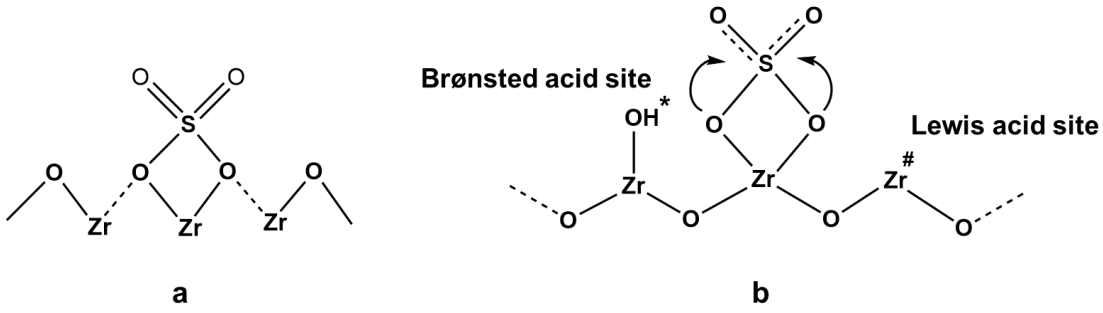

Figure 2.2 The structure (a) and mechanism of BAS and LAS (b) of sulfated zirconia [44]

Li *et al*. discussed the mechanism of n-butane isomerization at low temperature catalyzed by SZ [46]. As shown in Figure 2.3, skeletal isomerization of n-butane on SZ is initiated by dehydrogenation of the alkane, and the formed butene is then protonated by BAS of SZ. The next skeletal isomerization of the formed sec-butyl alkoxy group/carbenium ion consists of the formation of a methyl cyclopropyl carbonium ions, its opening to a primary isobutyl carbenium ion, followed by the final rearrangement to a tertiary tert-butyl carbenium. Afterwards, it desorbs via hydride transfer from n-butane, resulting in a new sec-butyl carbenium ion and isobutane. The overall reaction speed relies on the rate constant of the monomolecular isomerization of the

carbenium ion, the concentration of the olefins in the catalyst zone, and the concentration of the BAS on the SZ [46].

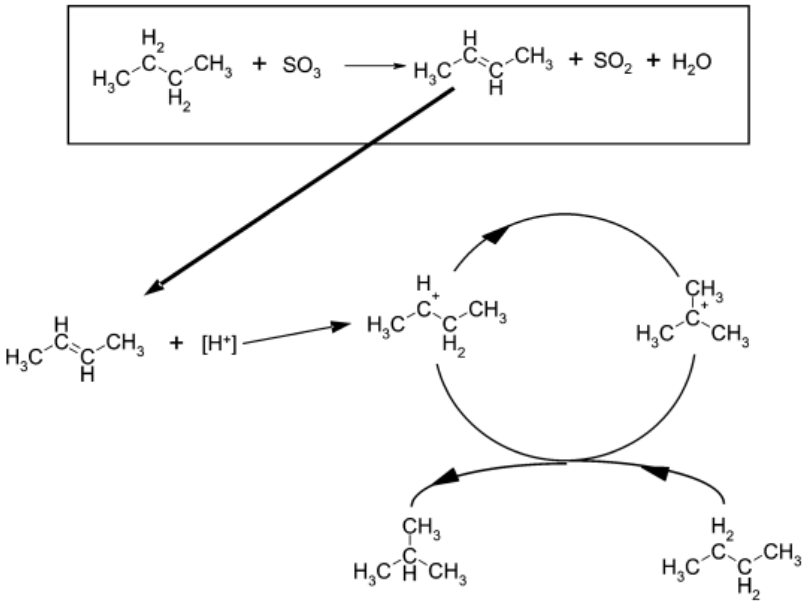

Figure 2.3 Proposed mechanism for the isomerization of n-butane on SZ at low temperature [46]

Strong acidic SZ is widely applied in many catalytic reactions such as Biginelli reaction, Knoevenagel condensation, acylation of aromatic compounds, regioselective ring-opening reaction, alkylation, and transesterification, *etc*. [44]. Specifically, SZ shows advantages in catalyzing these reactions at relative low temperatures. For example, Deshmane successfully synthesized mesoporous nanocrystalline SZ, and it shows good activity for the esterification of free fatty acid in soybean oil with a conversion of 85 % for just 80 min at a low reaction temperature of 60 ^{o}C [47]. Saravanan *et al*. reported a kind of mesoporous SZ which shows an outstanding activity in the esterification of palmitic acid with 88-90 % yield of methyl palmitate at 60 ^{o}C, a much better performance compared to homogenous H_2SO_4 and *p*-toluenesulfonic acid [48]. On the other hand, M.T. Tran *et al*. studied the influence of calcination temperature on the

application of SZ in n-butane and propane transformation, and it was found that the best performance was obtained over the SZ which was calcined at 600 ^{o}C [49].

Engineering molecular structures or doping other metals are useful methods to promote SZ for wide applications. Joo *et al*. synthesized SZ with hollow nanostructures through a robust sol-gel process, which showed superior performance in fructose dehydration to HMF, with an HMF yield of ~65 mol% [50]. The resulting hollow SZ turned out to possess outstanding properties, such as well-maintained structural integrity, prominent mesoporosity, excellent SO_4^{2-} dispersion and a strong acidic surface, which makes it prominent for liquid-phase catalytic process [50]. Alhassan *et al*. prepared ferric-manganese doped SZ and utilized it to synthesize waste cooking oil-based biodiesel, which achieved a yield of ~96.5 % at 180 ^{o}C [51]. When the ferric-manganese doped SZ was applied in n-butane isomerization, its structure was studied by Yamamoto *et al*., and it was shown that ferric oxide and zirconia form interstitial-type solid solutions and the trivalent ferric atoms exist inside the bulk phase of zirconia, locating at the center of distorted oxygen octahedra, while the manganese species mainly present as $MnSO_4$ on the surface of SZ [33]. The overall applications of SZ-based catalysts are summarized in Table 2.3.

2.4.2 Tungstate zirconia

Since the linkage between SO_4^{2-} and zirconia is not strong enough, SZ can be deactivated rapidly during the reactions, and tends to discharge H_2S or SO_x during air treatment, or H_2SO_4 in the presence of water. These issues can cause irreversible loss of catalyst activity and the downstream contamination and corrosion by using SZ. Tungstate zirconia (TZ) is stable at high temperature, and in the presence of H_2, O_2, or in H_2O, making it possess wider applications than SZ [52]. The first TZ, which showed acid strength of $H_0 \leq$ -14.52, was discovered by Hino and Arata in 1987, via impregnating $Zr(OH)_4$ or amorphous zirconia with aqueous ammonium metatungstate

followed by calcination at 800-850 ºC [53]. The resulting materials showed good activity for butane isomerization to isobutane at 50 ºC, and pentane to isopentane at 30 ºC [53]. Since then, more and more studies focus on understanding and controlling the physicochemical properties of TZ, tuning its LAS and BAS, and studying its applications in different catalytic reactions [54-57].

Similar to the influence of other doping metals, the interaction between tungsten oxide and zirconia hinders the crystallization of zirconia from the amorphous status and further transition from tetragonal to monoclinic phase [58-60]. The dispersion of tungsten on the zirconia surface can affect its acidity and activity dramatically, thus a lot of research has focused on the structure of WO_x domains in TZ [58, 61-63]. Iglesia *et al*. proposed a three-stage growth of the WO_x domain with the increase of tungsten concentration as shown in Figure 2.4 [52, 64]. In detail, when the WO_x surface density is lower than 4 W/nm^2, most of the tungsten on the zirconia surface stays as isolated monotungstate, stabilizing through W-O-Zr bonds [64]. Apparently, in isolated monotungstate, WO_x groups don't interact with each other until the surface W density is higher than 4 W/nm^2, so the WO_x species are electronically isolated from each other [64]. As tungsten surface density increases up to ~10 W/nm^2, isolated monotungstate starts to condense into two-dimensional polytungstate domains [52]. At this stage, the electrons become delocalized in the larger domain through bridging W-O-W bonds, forming two-dimensional polytungstate structures and small $(WO_x)_n$ clusters with a diameter of ~0.8-1.0 nm, and this stage will also lead to a monotonic growth in WO_x domain size until a steady domain size is reached corresponding to a polytungstate monolayer at around 8 W/nm^2 [64, 65]. After the surface density increases higher than monolayer WO_x values, bulk WO_x crystals start to show up, which can also be identified by the apparent yellow color of the materials [52]. The technique of atomic-resolution high-angle annular dark-field (HAADF) imaging is applied to distinguish the complicated surface tungsten

dispersion as shown in Figure 2.5 [66]. Based on a lot of research, it is generally considered that the two-dimensional polytungstate and Zr-WO_x clusters with a diameter at ~0.8-1.0 nm possess high catalytic activity, while monotungstate and bulk WO_x crystals are supposed to be less active [64-67].

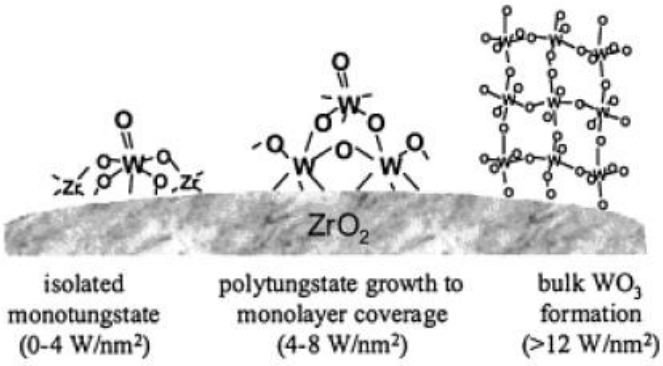

Figure 2.4 Growth of WO_x domain with the increase of WO_x surface density [52]

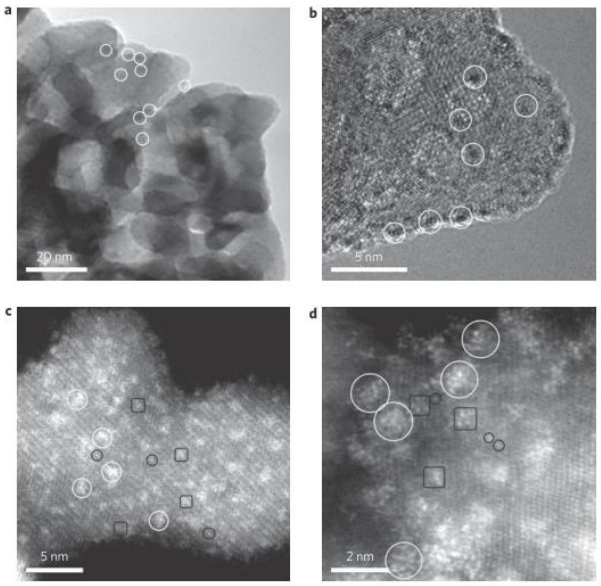

Figure 2.5 Electron microscopy characterization of tungstate zirconia. Bright-field (a), HRTEM micrograph (b) and HAADF (c, d) images. Black circles represent the single W atoms corresponding to surface mono-tungstate species. Black squares point out the surface poly-

tungstate species with several W atoms in W-O-W bridging bonds. White circles illustrate the WO_x clusters at the diameters of ~0.8-1.0 nm [66].

The acidity property of TZ plays a crucial role in its catalytic reaction. The tungsten precursor, preparation method, calcination temperature, and surface tungsten density are the main factors that affect the acidity of TZ, originating from different Zr-W molecular structures [54, 56, 68]. At a higher surface as surface tungsten concentration, the total acid sites will firstly increase to a peak point, and then start to decrease [69, 70]. Specifically, LAS decrease with increasing the tungsten concentration, while BAS shows a trend similar to the total acid sites [70, 71]. This phenomenon is in line with the difference of Zr-W structures at different surface tungsten densities.

Generally, the Lewis acidity of TZ comes from zirconia, which is in accordance with the phenomenon that the introduction of tungsten leads to the decrease of LAS since more zirconium atoms are coordinated with tungsten via Zr-O-W bonds, resulting in less unsaturated Zr^{4+} exposed. The presence of WO_x on the surface of zirconia can significantly increase the BAS of the materials [52, 70]. Galano *et al*. discussed the BAS in dimeric TZ to mimic the polymeric WO_x domain (Figure 2.6), which suggested the fact that not all the H atoms in WO_x domain are equally acidic, but the H (A) atoms at the edge of WO_x domains are the most acidic types, followed by less acidic types of H (B) and H (C) [70]. The decrease of BAS happens when the tungsten content increases to the level higher than monolayer WO_x values, which is explained as the result of the increase of the condensation towards the formation of bulk WO_x crystals [71]. The condensation process will lead to the decrease of the most active acid H, which not only lower in the number of BAS, but also a decrease in the acidity strength per H site [70]. Therefore, it is highly believed that the local coordination and the polymerization extent of the WO_x domain, that cooperatively produce

remarkable variations on the surface chemical properties, differentiate the acidity property of TZ [65, 70].

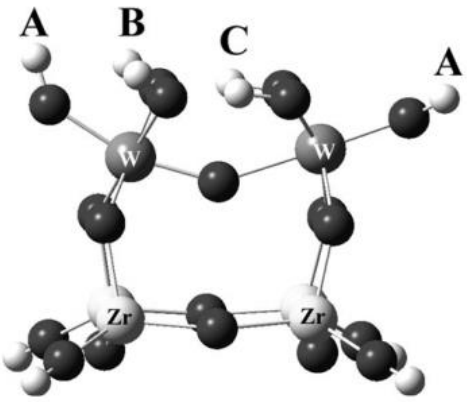

Figure 2.6 Different H sites in dimer tungstate zirconia [70]

When TZ is applied for the hydrogenolysis of cellulose to ethylene glycol, it normally contains three steps: i) hydrolysis of cellulose to glucose, ii) transformation of glucose to glycolaldehyde, and iii) hydrogenation of glycolaldehyde to ethylene glycol [72]. Chai *et al*. further discussed the mechanism of the second step, indicating that the W^{5+}-OH group played an important role in selectively cleaving the glucose C_2-C_3 bond to form glycolaldehyde, through complexation to α- and β-OH groups of glucose (Figure 2.7) [72]. The hydrogen of the α-OH group tends to be positively charged that can easily attack the W^{5+}-OH group of TZ, due to the electron-withdrawing effect. At the same time, the oxygen of the β-OH group coordinates to tungsten and forms a six-membered heterocycle, which subsequently eliminates an H_2O molecule and one H^+ owing to its instability. The circular flow of the electrons of the resulting five-membered heterocycle then breaks the C-C bond and forms glycolaldehyde and erythrose via a redox process. Erythrose could be further decomposed in two glycolaldehyde molecules in a similar way. Glycolaldehyde can be further hydrogenated to ethylene glycol.

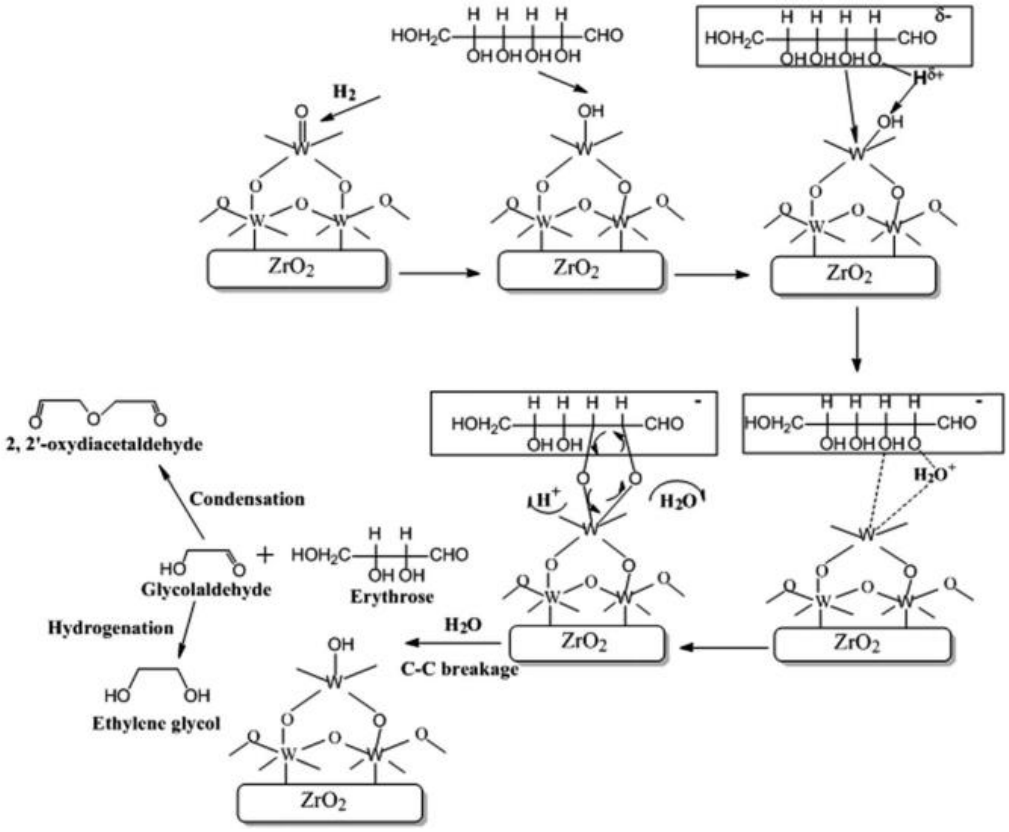

Figure 2.7 Proposed mechanism for selectively breaking the glucose C-C bond [72]

To date, TZ has been one of the most widely-studied solid acid catalyst systems, and it continues to attract more attention in both academia and industry fields as the next generation of the solid acid catalyst [65]. It was reported that TZ can be applied for esterification of used vegetable oil and waste acid oil for the production of biodiesel, and it was showed that the highest acid strength locates at the material with 20 wt% tungsten concentration which also correlated to the highest catalytic activity with a conversion of vegetable oil over 93 %, and waste acid oil over 96 % [73, 74]. Wang *et al*. used TZ as a catalyst to reduce the viscosity of heavy crude oil without the addition of water, and it was reported that the hydrothermal synthesis method can get a better-dispersed tungsten oxide and thus exhibit a higher viscosity reduction activity compared to impregnation method [75]. Gonel *et al*. used one-step microwave-assisted method to synthesize nano-crystalline

TZ which shows a good performance in aldoxime dehydration and alkynes hydration [76]. Another work reported that acetyl salicylic acid can be produced from salicylic acid and acetic anhydride catalyzed by TZ, which can achieve a yield up to ~91 % [77].

Other components such as Pt, Pb, CuO_x, *etc*. were also used to serve as the additional function co-catalyst to enrich the catalytic features of TZ. These multicomponent catalysts have been applied in many reactions such as hydrogenolysis of glycerol, reduction of NO by NH_3, conversion of lignocellulosic-biomass or biomass-derived carbohydrates to water-soluble C_5-C_{15} compounds, *etc*. [78-80]. More specifically, introducing Al in TZ can improve its catalytic performance in dehydration of D-xylose into 2-furfurladehyde, giving a conversion of 98 % and a yield of 51 % [81]. Pt can provide the necessary dissociated hydrogen to generate the active site and to favor the desorption of ionic intermediates, thus doping with 0.05 % Pt can suffice to significantly increase the catalytic activity and stability for n-hexane isomerization [82]. On the other hand, with the addition of SiO_2, TZ can maintain a high surface area (over 500 m^2/g) and high density of Zr-WO_x clusters at the same time, thus produce a large amount of strong BAS which is beneficial for esterification of 1-butanol and acetic acid [83]. The overall applications of TZ-based catalysts are summarized in Table 2.3.

2.4.3 Zirconium phosphate

Zirconium phosphate (ZP) has been well known for several decades, and it was firstly reported in 1956 for its ion-exchange capability which triggered lots of interesting studies in phosphoric acid salt of zirconium [84]. The evolution of the research about ZP starts from understanding its synthesis methods and structures to the designing and fabrication of novel structures and the exploration of its functional applications in recent years [85]. Due to the high acidity, ease of fabrication, modification, functionalization, high water tolerance, high thermal stability, and easy

recovery, ZP has been extensively studied for a variety of reactions driving by acids, such as hydrodeoxygenation, isomerization, dehydration, and ester hydrolysis reactions, *etc.* [85-87]. Moreover, because of the high proton mobility on the surface, ZP also gives rise to a high proton conductivity which makes it a hot candidate for proton-conducting materials [88, 89]. To date, ZP has been recognized as one of the most popular and well-studied materials in the family of transition metal phosphates [90].

Similar to sulfate and tungstate, phosphate shows a strong stabilizing effect on the specific surface area and tetragonal phase of zirconia, which retards the crystallization of zirconia from an amorphous status and further transitions from tetragonal to monoclinic phase [91]. Compared to the amorphous state, crystalline ZP, including α-, γ-, and θ-phase, have attracted substantial attention due to its easily controlled structure and excellent exfoliation [85]. The most vastly investigated phase of ZP is α-zirconium monohydrogen phosphate ($Zr(HPO_4)_2 \cdot H_2O$, α-ZP), a layered compound with an interlayer distance of 7.6 Å and a layer thickness of 6.6 Å (Figure 2.8A) [92]. In this structure, the zirconium atoms in each layer are almost planarly aligned with bridging phosphate groups which locate alternately above and below the zirconium atom plane [93]. Three O atoms of each phosphate group are bonded to three different zirconium atoms arranged at the apexes of a nearly equilateral triangle, while the fourth one points to away from the layer, bonding to a hydrogen atom [92]. As a result, adjacent layers are staggered in a pseudo-hexahedron shape so as to form six-sided cavities between the interlayer regions [92]. In the center of each cavity, there sits a crystallization H_2O molecule, forming a hydrogen bond with the P-OH group [93, 94].

In ZP, the bridging phosphate groups offer ion exchange sites where the protons can be exchanged with cations or other species, which can functionalize the materials with more specific features [95]. Small cations are easy to intercalate with the protons, but the cations which have a large ionic

radius, such as Cs^{+}, Ag^{+}, Cr^{3+}, Ba^{2+}, hydrated Mg^{2+}, *etc*., are not or can only be slowly exchanged by α-ZP due to its small interlayer spacing [96]. Thus, lots of research have been focused on enlarging the interlayer space in order to facilitate the intercalation of bulk molecules in the structure [95-97]. As a consequence, a derivate form of microcrystalline α-ZP, namely θ-ZP framework ($Zr(HPO_4)_2 \cdot 6H_2O$), came out [98]. This form was firstly observed by Clearfield *et al*., and Kijima developed an approach to directly synthesize θ-ZP from solution by a precipitation method [95, 96]. In θ-ZP, it remains the α-ZP-type of the layered structure, but has a larger interlayer distance of 10.4 Å and can fill each cavity with six water molecules (Figure 2.8B) [94, 98].

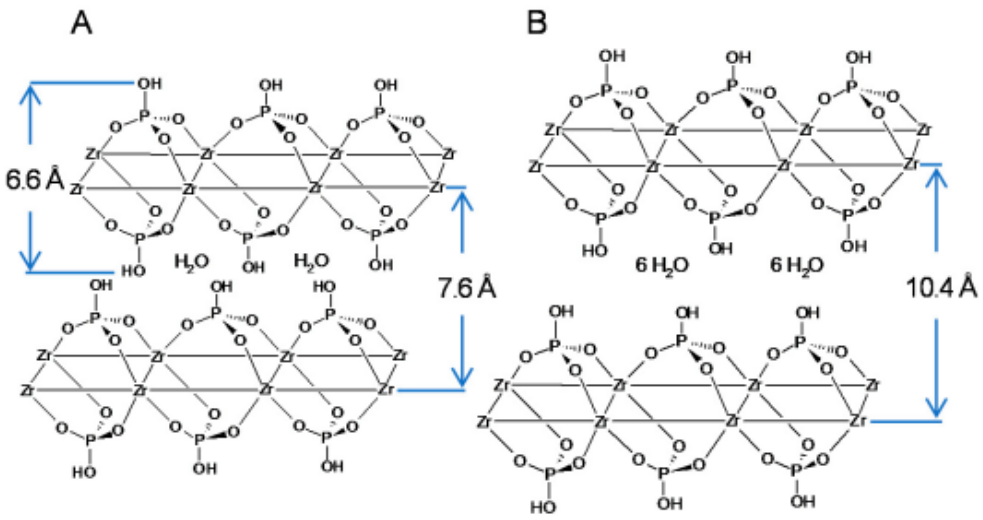

Figure 2.8 (A) The structure of α-ZP; (B) the structure of θ-ZP [94]

The sophisticated structure gives ZP suitable acidity features, in strength and distribution, triggering lots of acid-catalyzed reactions. It is generally postulated that the presence of medium to strong BAS of ZP is mainly ascribed to the surface P-OH and $[P(OH)_2]$ groups, while the LAS may probably arise from Zr^{4+} [91, 93, 99]. Determined by the ammonia temperature-programmed desorption (NH_3-TPD) technique, it was found that ZP showed a higher concentration of total acid

sites and BAS than tin phosphide [99]. The concentration of phosphate and the calcination temperature are found to influence the acidity of ZP. Sinhamahapatra *et al*. mentioned that the total acidity of mesoporous ZP decreases with increasing calcination temperature, probably due to the decrease in surface area and the formation of polyphosphate [100].

Since the synthetic α-ZP can be easily intercalated by amines and undergo exfoliation, Zhu *et al*. synthesized a layered structure of α-ZP exfoliated by n-hexylamine and doped niobium on it via ion exchange, and the resulting material was applied in catalyzing hydrodeoxygenation of HMF to 2,5-dimethylfuran (DMF) [101, 102]. The mechanism of this reaction through the intermediate product, 5-methylfurfural (MF), is depicted (Figure 2.9). As described by the report, H_2 is firstly activated by Ni, and the active H atom will then attack the O atom of the -CH_2OH group which is activated by the LAS of Zr^{4+} at the same time. This hydrodeoxygenation process will produce a primary intermediate of MF. With the help of active H atom and Zr^{4+} species, the carbonyl group of MF will undergo hydrogenation and hydrogenolysis processes to form 5-methylfurfuryl alcohol (MFA). Then, another hydrodeoxygenation process will happen and convert MFA into DMF. The processes of the over-hydrogenation of MFA and furan ring hydrogenation are responsible for the byproducts of tetrahydro-5-methyl-2-furanmethanol (MTHFA) and 2,5-hexanedione (HD). As a result, the Ni-PO_x-ZrO_2 catalyst achieved a 100 % conversion of HMF and a 68.1 % of DMF yield under the reaction condition of 240 ^oC and 5 MPa H_2 in 20 h [102].

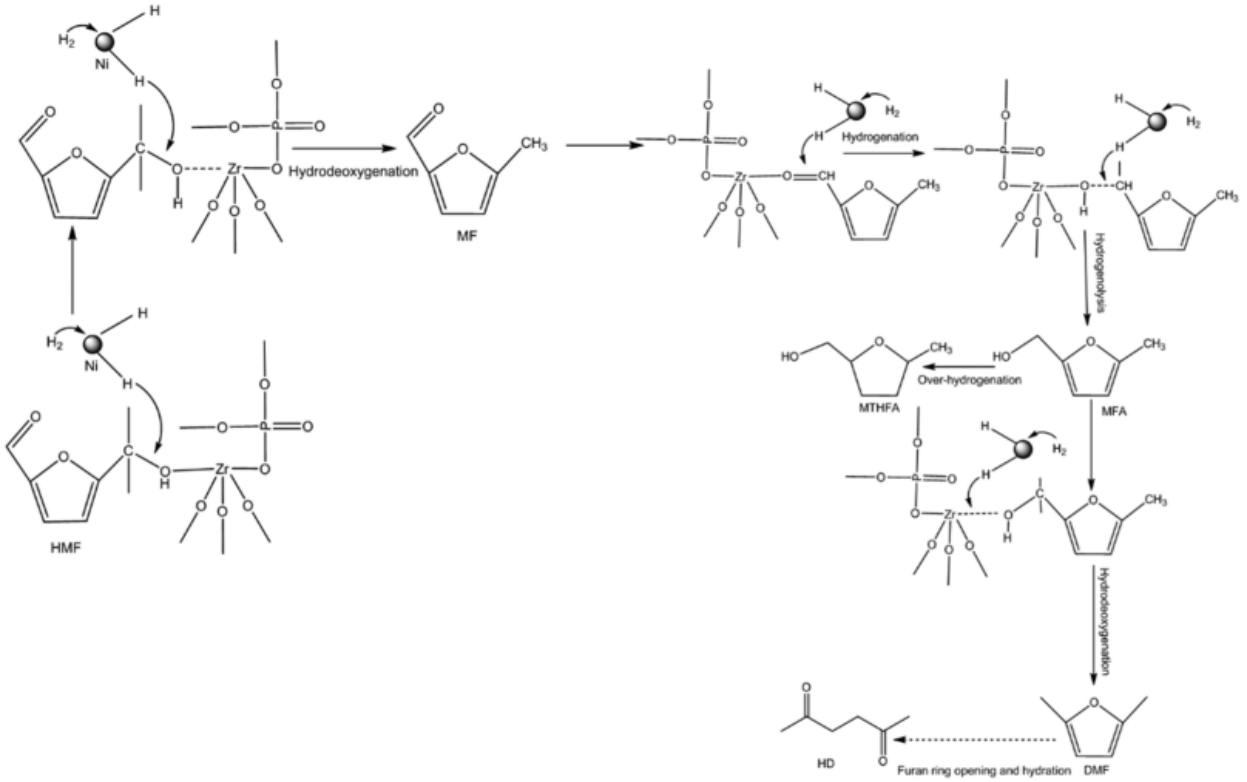

Figure 2.9 Proposed mechanism for the hydrodeoxygenation of HMF to DMF via MF [102]

After several decades of effort in understanding the structures and properties, ZP has shown the magic functionality in many reactions. Antonetti *et al*. used microwave heating to transform fructose and inulin into HMF over ZP, and achieved an HMF yield of ~40 mol % at 190 ^{o}C in 8 min [103]. Salak *et al*. studied the dehydration of fructose to HMF in sub-critical water in the presence of ZP at 240 ^{o}C, and it was found that 80 % of fructose can be decomposed in sub-critical water in 120 s with a selectivity of 61 % [104]. Weingarten *et al*. studied the transformation of glucose to levulinic acid catalyzed by solid metal-phosphate, and it was concluded that ZP is favorable for levulinic acid production, owing to its inherently high surface area and enhanced Brønsted acidity [99]. Jain *et al*. synthesized mesoporous ZP through the hydrothermal method and it showed good catalytic performance in fructose, glucose, and sucrose conversion to HMF [105]. Mesoporous ZP is also reported to show excellent catalytic activity for the synthesis of

substituted coumarins through Pechmann condensation, and it gives a high catalytic activity for the condensation of phenols and ethyl acetoacetate in both conventional heating and microwave-assisted method [106].

The advantage of ZP over other solid catalysts is that the H^+ of the P-OH group can be exchanged by divalent or trivalent cations that can introduce new catalytic sites, or improve and tune its acid features, thus making it a favorite choice for many reactions [107]. Liu *et al*. synthesized a heterogeneous chromium-exchanged ZP catalyst for the catalytic conversion of carbohydrates into HMF, and it achieved HMF yields of 94.5 % and 43.2 % from fructose and glucose, respectively [107]. Miao *et al*. found that mesoporous ZP with abundant ordered meso-structures can improve the dispersion of WO_x species and increase its catalytic performance in liquid phase benzylation of anisole [108]. Zhou *et al*. successfully synthesized single-layer sulfonic ZP nanosheets by anchoring thiol groups on layered ZP nanosheets followed by an oxidation process [109]. The resulting material can be well-dispersed in polar solvents which makes the substrate accessible to the acid functional groups, thus it can be served as an effective catalyst for Bayer-Villiger oxidation of cyclohexanone to ε-caprolactone in the absence of organic solvents [109]. The overall applications of ZP-based catalysts are summarized in Table 2.3.

2.4.4 Other elements doping on zirconia

Besides the most widely used doping components of sulfate, tungstate, and phosphate, there are also some other elements applied in functioning zirconia. For example, mesoporous zirconia was found to be an efficient support for gold-based catalysts for the water-gas shift reaction, which showed higher catalytic activity than the reference catalysts of Au/TiO_2 [110]. Yttria-stabilized zirconia can be applied for the adsorption and reaction of formic acid, and it was reported that the formic acid adsorbed at a temperature below 200 K and dissociated upon heating to room

temperature to produce adsorbed formate and hydroxyl groups [111]. Similar yttria-stabilized zirconia was also synthesized by atomic layer deposition or flame spray pyrolysis techniques for other applications [112, 113]. On the other hand, palladium supported mesoporous zirconia was reported to show effective catalytic activity for the methanol decomposition to hydrogen and carbon monoxide at 160-220 ^{o}C [114].

In order to endow more functions, some complex zirconia-based catalysts containing two metals or more have also been extensively studied. For instance, in the catalyst of gold-vanadia supported on nanostructured mesoporous zirconia, it was found that the presence of gold can enhance the V^{5+} to V^{3+} reduction and the vanadia can stabilize the structure of mesoporous zirconia [115]. Hotz *et al*. found that Rh/$Ce_{0.5}Zr_{0.5}O_2$ nanoparticles offered an outstanding performance for butane-to-syngas conversion, with 100 % of butane conversion and 77 % of hydrogen yield [116]. Kim and Laine successfully synthesized ternary $(Ce_{0.7}Zr_{0.3}O_2)_x(Al_2O_3)_{1-x}$ nanoparticles by flame spray pyrolysis and it offered significant catalytic activities for both NO_x reduction and propane/propene oxidation [117, 118]. In Ru-doped cobalt-zirconia nanocomposites, it was found that cobalt was well-dispersed in the zirconia matrix, and the addition of a Ru promoter in small concentrations was enough to drastically enhance cobalt reducibility and give higher dispersion, which results in a better catalytic performance in Fischer-Tropsch synthesis [119]. Cai *et al*. reported that the co-actions of $Ce_{0.5}Zr_{0.5}O_2$ and CrO_x showed better catalytic performance than the individual effort of $Ce_{0.5}Zr_{0.5}O_2$ and CrO_x for selective catalytic oxidation of NO, proving the phenomenon of synergistic effect for complex zirconia-based catalysts [120]. To make the catalyst more complicated, a quinary catalyst of Ru/Co/ZP/SiO_2, which contains five different active elements, achieved a high catalytic activity and stability during Fischer-Tropsch synthesis [121]. The overall applications of zirconia doped by other elements are summarized in Table 2.3.

2.5 Zirconia supported on mesoporous materials

Besides bare zirconia and catalysts which utilize zirconia as the support, zirconia supported on other mesoporous materials is also very popular. The mesoporous structure is beneficial for the dispersion of active species and the accessibility of the active sites by the bulky reactant [122]. Generally, other co-catalysts with zirconia can be doped in this complex, giving multifunctional active sites compared to individual counterparts, which makes them more efficient in catalytic reactions. In this system, MCM-41 and SBA-15 are common mesoporous materials used as supporting matrix.

2.5.1 Zirconia supported on MCM-41

Mesoporous silica sieves are among the most widely investigated nanomaterials owing to the high surface areas, large pore volumes, well-defined pore structures, and easy preparation methods [123]. Particularly, MCM-41, a structure with a hexagonal arrangement of uniform mesopores whose dimensions could be engineered in the range of 16-100 Å, has attracted increasing attention since it is cheap and possesses the characters of narrow pore size distribution, high surface area, excellent thermal stability, outstanding synthetic versatility, and easy reusability [123-125]. The surface of MCM-41 can be easily tuned, allowing the introduction of a variety of functional groups such as metal nanoparticles, metallic complexes, amines, or thiols, *etc*. onto the silica matrix, which makes it predominant as a support for lots of materials [123, 126]. Therefore, MCM-41 has been widely used in many areas, especially in the catalysis industry. The synthetic methodology of MCM-41 mainly depends on the silica precursors condensation, e.g. sodium silicate or tetraethyl orthosilicate, under basic conditions in the presence of cationic surfactants [123]. The hexagonal arrays of the cylindrical micelles form with the polar groups of the surfactants on the outside, and the silicate species occupy the space between the cylinders, and then the final calcination burns off

the organic materials, forming hollow cylinders [127]. The hydrothermal method is a common technique to incorporate zirconia into the MCM-41 matrix (Figure 2.10) [128].

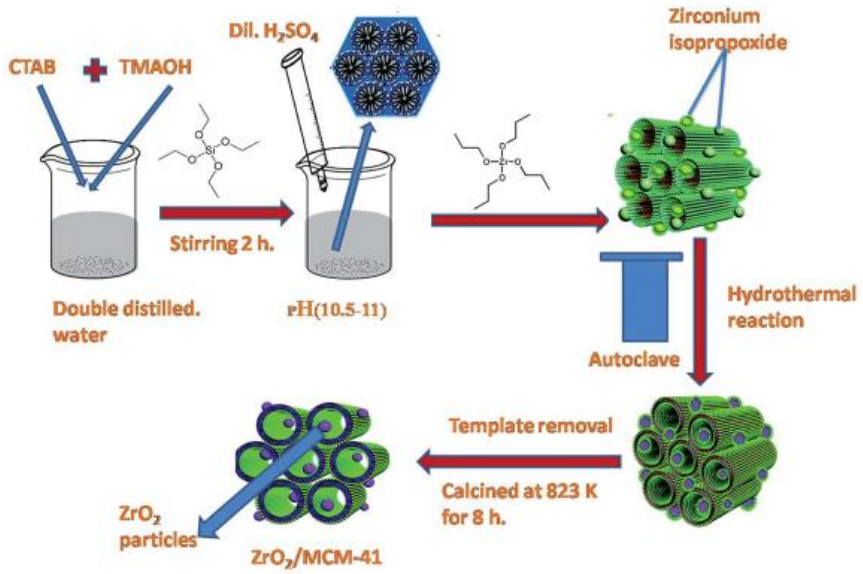

Figure 2.10 Schematic representation of the synthesis of Zr-MCM-41 via hydrothermal method [128]

Peng *et al*. presented a noble-metal-free and highly effective catalytic hydrogenation and acid-catalyzed conversion of furfural to biofuel alkyl levulinate without external H_2, by using isopropanol as the hydrogen donor, and Zr-MCM-41 and amberlyst-15 as the combined catalysts [129]. This report also proposed a plausible mechanism illustrated in Figure 2.11. At the beginning, the unsaturated Zr^{4+} of Zr-MCM-41 binds to isopropanol to form Zr-bound isopropoxide (species **a)** which will then coordinate with the carbonyl oxygen of furfural to yield a six-membered ring transition state (species **b)**. The hydride in species **b** subsequently transfer from alkoxide to the carbonyl group and form intermediate species **c**. Another isopropanol will coordinate with species **c** to form species **d** and then dissociate to release furfuryl alcohol, which will then undergo etherification with isopropanol to form the main intermediate 2-isopropoxymethylfuran (IPMF).

After getting through the processes of protonation, elimination, and isomerization catalyzed by amberlyst-15, the IPMF will be converted to isopropyl levulinate (IPL). With this catalytic strategy, an optimized alkyl levulinate yield of 85.3 % was achieved in a one-pot model at 130 ^{o}C in 24 h [129].

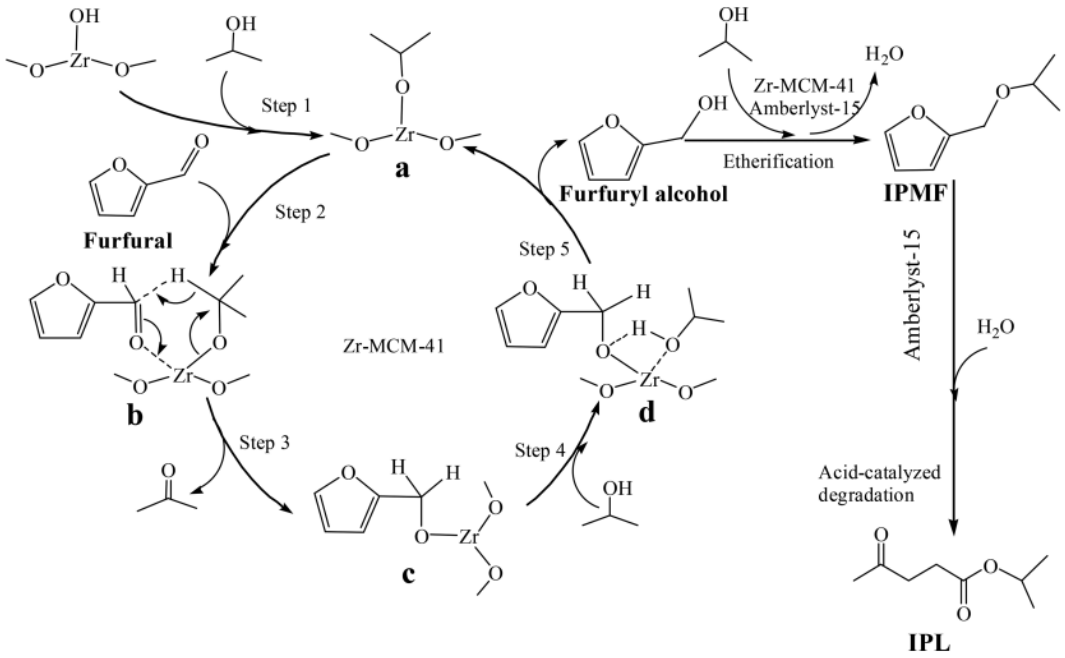

Figure 2.11 Proposed mechanism for isopropyl levulinate synthesis from furfural using isopropanol as the hydrogen donor by combing Zr-MCM-41 and Amberlyst-15 [129]

When zirconia is doped in MCM-41, the solids not only possess all the features of MCM-41 such as good crystallinity, high surface area, and uniform pore size distribution but also improve both of the LAS and BAS, thus can largely widen its applications [130]. For instance, highly dispersed zirconia doped MCM-41 was recently studied for the selective glucose to HMF transformation, that achieved 82 % of glucose conversion with a selectivity of fructose of 13.2 % and HMF of 23 % at 175 ^{o}C [131]. Sawant *et al*. found that the MCM-41 support plays a crucial role in stabilizing catalytically active tungstophosphoric acid along with the tetragonal zirconia phase, and it can

improve the activity for veratrole acetylation at least four times more than the neat material without MCM-41 [132]. Tungsten oxide supported on zirconia doped MCM-41 was also studied by López *et al*., and it was found that after activation at 700 ^{o}C, the catalysts are effective for the transesterification of sunflower oil with methanol at 200 ^{o}C, with a maximum fatty acid methyl ester yield of ~82 % [133]. The uniformly doping Ru clusters in nanosized zirconia-doped MCM-41 can remarkably increase its activity for the hydrogenation of furan derivatives in aqueous solution at room temperature [134].

SZ supported on MCM-41 has been also widely studied. The nanochannels of MCM-41 can provide a large surface area for the dispersion of SZ and a steric restriction on the formation of SZ nanoparticles [135, 136]. Wang *et al*. used grafting technique to produce SZ supported on MCM-41 with a monolayer coverage, and it exhibited improved thermal stability than that of bulk SZ, but with weaker acidity, likely due to the strong interaction between silica and SZ [137]. To deal with this phenomenon, it also indicated that the iteration of this grafting technique can lead to higher coverage of SZ and thus enhance its acidity [137]. Chen *et al*. reported that the catalytic activity of SZ doped MCM-41 for n-butane isomerization can be dramatically improved through the addition of a proper amount of promoter metals, such as Al or Ga [136, 138]. This effect is not monotonic but with an optimum level, and the main reason is based on three factors including increased sulfur loading, balanced LAS and BAS distributions, and higher zirconia dispersion [135]. The overall applications of zirconia-based catalysts supported on MCM-41 are summarized in Table 2.3.

2.5.2 Zirconia supported on SBA-15

Highly ordered large pore mesoporous silica SBA-15 was synthesized in the presence of amphiphilic triblock copolymers in acid media by Zhao *et al*. in 1998 [139]. It is a well-ordered

two-dimensional hexagonal array of mesoporous silica with BET surface areas of 690-1040 m^2/g, uniform pore sizes up to ~300 Å, and pore volume as large as 2.5 cm^3/g [140, 141]. SBA-15 can be synthesized with a wide range of uniform pore sizes and pore wall thicknesses over different methods, varying from plenty of poly (alkylene oxide) triblock copolymers, or the presence of cosolvent organic molecules, or the different synthetic routines [139, 142]. Since the silica wall of SBA-15 can maintain up to 64 Å that is thicker than MCM-41 of ~10 Å, it is supposed to be a better support material with higher thermal stability compared to MCM-41 [140, 141, 143]. Therefore, it has attracted great attention as a potential support in many catalytic reactions [144-148].

Zirconia is mainly located outside the mesoporous channels of SBA-15 as small nanoparticles when it is at low zirconium loading (*e.g.* ~10 %), but predominantly sits inside the mesoporous channels when it is at higher zirconium loading (*e.g.* ~30 %) [149]. Further increasing the zirconia loading (*e.g.* ~50 %) will result in narrowing the mesopores and eventually block the pores [150]. This could affect the dispersion of the active sites and the catalytic acidity, thus potentially impede the activity. To deal with this problem, Krishnan *et al*. reported an efficient NH_3/water vapor-induced internal hydrolysis approach for the post-synthesis coating of zirconia on the mesopore walls of SBA-15, which can alleviate the pore blocking issue [151]. In this method, the hydrolysis of the pre-dispersed precursor inside the pores of SBA-15 in the presence of NH_3/water vapor under autogenously generated pressure tends to disperse the precursor inside the pores evenly, thus obtain a structure with a uniform coating of zirconia on the pore walls after calcination, which even shows an enhanced acidity (Figure 2.12) [151].

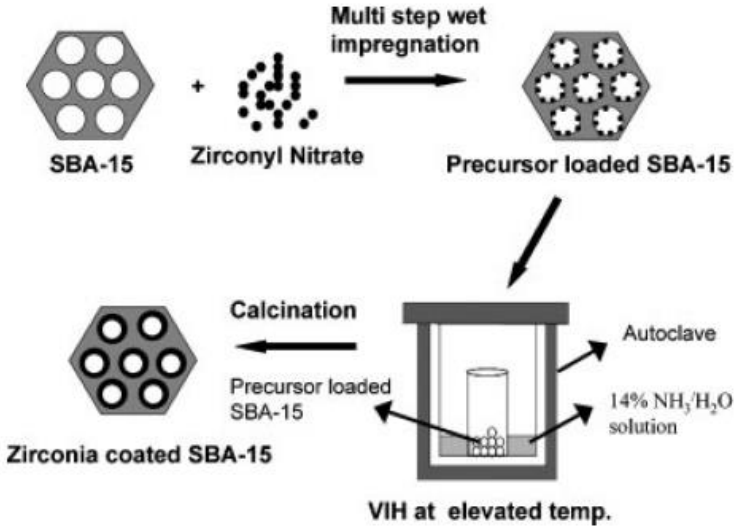

Figure 2.12 Schematic representation of zirconia coating by NH_3/water vapor-induced hydrolysis method [151]

Chen *et al*. applied highly ordered porous Zr-SBA-15 for the pinacol-type rearrangement, and it was found that the zirconia was incorporated into the SBA-15 framework as isolated zirconia species or superficial zirconia clusters with two or more zirconium centers on the pore walls [152]. The plausible mechanism of pinacol rearrangement of 2,3-dimethyl-2,3-butanediol is proposed in Figure 2.13. When the reactants attach to the active sites of the catalysts, the -OH groups of pinacol are coordinated on the adjacent superficial Zr^{4+} species via its O atoms, while the H atoms of the -OH groups are stabilized by a hydrogen bond with lattice oxygens of the zirconia clusters to form acidic protons. In Path 1, the acidic proton of the -OH group will transfer to the other -OH group of the pinacol to form an intermediate III, which subsequently dehydrates into intermediate IV, a lattice oxygen-stabilized carbocation. Afterwards, the electron of the O atom is back donated to the carbon of the C-O bond, and the pinacolone will be formed via alkyl migration. On the other hand, Path 2 also happens as the reaction is prolonged. In this pathway, dehydration firstly happens between the surface-stabilized -OH group and the H atom of the adjacent methyl group, resulting

in a C=C bond. By removing two H_2O molecules, 2,3-dimethyl-2,3-butadiene (DMBD) is formed. Showed in this report, pinacol was completely converted into 81 % of pinacolone and 19 % of DMBD at 110 ^oC in 2 h [152].

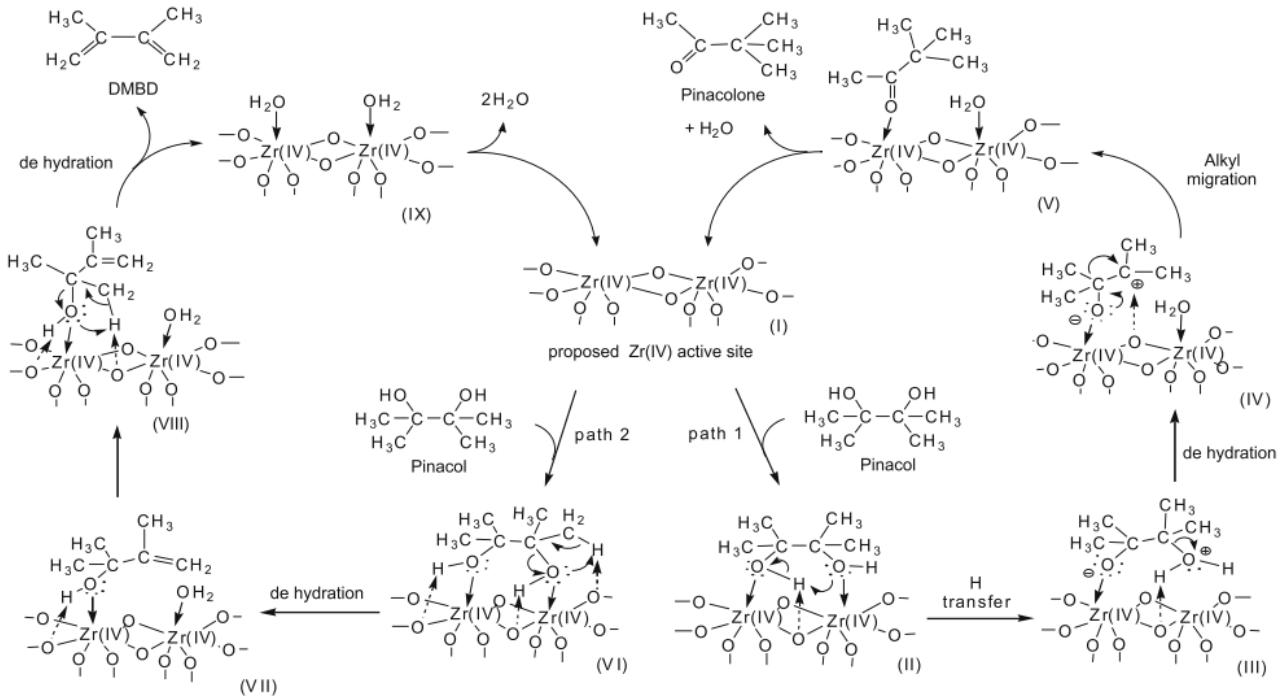

Figure 2.13 Proposed mechanism for pinacol rearrangement over Zr-SBA-15 [152]

Due to the ordered mesoporous structure, hydrothermal stability, and acidity, zirconia coated SBA-15 and its derivatives show a wide range of application. Normally, the acidity of Zr-SBA-15 increases with increasing zirconia loading, and it was found that Zr-SBA-15 with superficial zirconia clusters were the most efficient catalyst [152]. When sulfate is doped on Zr-SBA-15, the total acidity especially BAS can be largely increased, thus can widen its applications [149]. Li *et al*. reported that sulfated Zr-SBA-15 showed an excellent performance in n-pentane isomerization at 35 ^oC, with a conversion of ~93.9 % in 3 h [153]. The sulfated Zr-SBA-15 also exhibited a good activity for cumene cracking, which showed a reaction rate of 6.4 times higher than bulk SZ [154]. Osatiashtiani *et al*. synthesized a novel SBA-15 composite with a conformal monolayer of SZ and

applied it in the aqueous conversion of glucose to HMF, which exhibited a 3-fold enhancement in HMF yield over nonporous SZ [155]. The BAS/LAS ratio can also be tuned through this grafting technique by varying the film thickness and sulfated concentration [155].

On the other hand, zirconia-based catalysts containing tungsten elements have also attracted increasing interests. Due to the strong ZrO_2-WO_x reaction, a moderate amount of zirconia can stabilize the tungstate species in the form of polytungstate species, which leads to a higher Brønsted acidity [122]. Cecilia *et al*. found that the best catalytic performance of tungstate Zr-SBA-15 for glycerol dehydration occurred at the tungsten concentration of 20 wt%, with a conversion of 97 % and acrolein yield of 41 % [156]. Besides, silicotungstic acid coated Zr-SBA-15 was reported to be a good catalyst for esterification of benzyl alcohol and isoamyl alcohol [157, 158]. As for the other co-catalysts coating on Zr-SBA-15, Ru, Ni, Mo, *etc*. are supposed to be the potential candidates in functioning Zr-SBA-15 as well [150, 159]. The overall applications of zirconia-based catalysts supported on SBA-15 are summarized in Table 2.3.

Table 2.3 Summary of applications of zirconia and zirconia-based catalysts

Entry	Catalyst	Applications
1	ZrO_2	Conversion of cellulose to levulinic acid [35], conversion of cellulose to HMF [39], conversion of glucose and fructose to HMF [30], isomerization of n-butane [49]
2	Sulfated-ZrO_2	Dehydration of fructose to HMF [50], n-butane isomerization of n-butane [46], esterification of palmitic acid to methyl palmitate [48], esterification of free fatty oil to biodiesel [47]
3	Fe-Sulfated-ZrO_2	Isomerization of n-butane [33]
4	Mn-Sulfated-ZrO_2	Isomerization of n-butane [33]

Table 2.3 (continued)

Entry	Catalyst	Applications
5	Ru-Sulfated-ZrO_2	Conversion of phenethoxybenzene to aromatic hydrocarbons [160]
6	WO_x-ZrO_2	Hydrogenolysis of cellulose to ethylene glycol [72], conversion of benzaldoxime to acetophenone [76], dehydration of glycerol to acrolein [161], dehydration of fructose to HMF [162], dehydration of 2-butanol to n-butene [71], isomerization of n-pentane [163], isomerization of n-butane [164], hydrolysis of cellobiose to glucose [165], esterification of vegetable oils to biodiesel [73], esterification of waste acid oil to biodiesel [74]
7	PO_x-WO_x-ZrO_2	Dehydration of glycerol to acrolein [166], esterification of palmitic acid to methyl palmitate [167]
8	NbO_x-WO_x-ZrO_2	Dehydration of glycerol to acrolein [168]
9	Pd-WO_x-ZrO_2	Hydrolysis/dehydration/aldol-condensation/hydrogenation of lignocellulosic biomass and biomass-derived carbohydrates [78]
10	Pt-WO_x-ZrO_2	Hydrogenolysis of glycerol to 1,3-propanediol [80], isomerization of n-hexane [82]
11	CuO_x-WO_x-ZrO_2	Reduction of NO [79]
12	PO_x-ZrO_2	Dehydration of fructose to HMF [169], dehydration of inulin to HMF [103], conversion of glucose to levulinic acid [99], synthesis of coumarin derivatives through Pechmann condensation [106], benzylation of benzene [100]
13	Ni-PO_x-ZrO_2	Hydrodeoxygenation of HMF to 2,5-dimethylfuran [102]
14	Cr-PO_x-ZrO_2	Conversion of carbohydrates to HMF [107]
15	SO_3H-PO_x-ZrO_2	Oxidation of cyclohexanone to ε-caprolactone [109]

Table 2.3 (continued)

Entry	Catalyst	Applications
16	Au-VO_x-ZrO_2	Benzene oxidation [115]
17	Y-ZrO_2	Decomposition of formic acid [111]
18	Cr-Ce-ZrO_2	Oxidation of NO [120]
19	Ru/Co/ZrP/SiO_2	Fischer-Tropsch synthesis [121]
20	Zr-MCM-41	Dehydration of glucose to HMF [131]
21	Sulfated/Zr-MCM-41	Isomerization of n-butane [136], ethanolysis of sunflower oil to biodiesel [170]
22	Al-Sulfated/Zr-MCM-41	Isomerization of n-butane [136]
23	Ga-Sulfated/Zr-MCM-41	Isomerization of n-butane [138]
24	TPA/Zr-MCM-41	Acetylation of veratrole [132]
25	WO_x/Zr-MCM-41	Esterification of oleic acid to biodiesel [125], transesterification of sunflower oil to biodiesel [133],
26	Ru/Zr-MCM-41	Hydrogenation of furan derivatives [134]
27	Ru-La/Zr-MCM-41	Hydrogenation of benzene to cyclohexene [171]
28	Zr-SBA-15	Rearrangement of pinacol to pinacolone and 2,3-dimethyl-2,3-butadiene [152]
29	Sulfated/Zr-SBA-15	Bromination of methane [172], cumene cracking and esterification [154], hydrolysis of cellobiose to glucose [173], etherification of HMF to biodiesel [149], isomerization of n-pentane [153], dehydration of glucose to HMF [155]
30	STA/Zr-SBA-15	Esterification of benzyl alcohol to benzyl acetate [158], esterification of isoamyl alcohol [157]
31	Ru/Zr-SBA-15	Conversion of cellobiose to hexitols [150]
32	Ni-Mo/Zr-SBA-15	Hydrodesulfurization of 4,6-dimethyldibenzothiophene [159]

Table 2.3 (continued)

Entry	Catalyst	Applications
33	TPA/Zr-SBA-15	Benzylation of phenol [143]
34	WO_x/Zr-SBA-15	Hydrolysis of cellobiose to monosaccharide [122], dehydration of glycerol to acrolein [156]

2.6 Challenges and perspectives

The catalyst system of zirconia-based acid catalysts is with no-doubt one of the most widely applied catalyst systems in catalysis industry owing to its favorable physicochemical properties that endow the catalyst various advantages such as strong acidity, remarkable stability, and versatility of modification, *etc*., compared to other solid acid catalysts. However, some limitations and challenges are still highlighted for further improvement. The potential aspects which can be improved are present below:

As for the catalytic reactions, the catalytic performance of a catalyst depends on the properties of surface active sites. Thus, manipulating the active sites and their local environment is key to excellent performance of the heterogeneous catalysts. At present, the introduction of other metals or active elements is of the most widely used method to generate multiple active sites or simply tune the acidity properties of the zirconia-based solid acid catalysts. The types and amount of metal doped, preparation methods, or even precursor types usually influence the properties of the materials and result in catalysts with various active characteristics. However, although these methods can enhance the activity of the catalysts, they still have limitations such as the stability and precisely control of the active sites (e.g. the density, strength, accessibility and ratio of BAS and LAS). Based on this point, the exploration of strategy to stabilize and precisely manipulate the active sites on zirconia-based acid catalysts is of great importance.

Besides, the comprehensively study on the interaction between each component is key access to the high performance of zirconia-based solid acid catalysts. This can provide the basic knowledge for rational design of the specific catalyst with desired active sites that may achieve a super high efficiency. On the other hand, exploring the mechanisms of the reactions catalyzed by these catalysts is also important to maximize the reaction efficiency. Actually, density functional theory is very helpful to provide important information to predict the direction of the research. A combination of theoretical calculation and experimental research is a good option.

From the manufacture aspects, the stability of catalysts is always one of the key factors that influences the industrial applicability of the catalysts. As introduced above, either zirconia as a catalyst support or zirconia supported on other mesoporous materials presents the catalysts with more than one major component besides effective element of zirconium. Some of the zirconia-based acid catalysts contains even more than three components. Normally, besides the main character of active sites, the stability of the binary or polynary components will be a main challenge. The loss of the active sites after several runs and regeneration decreases the performance of the catalysts and cause catalyst deactivation. Impregnation, co-precipitation, hydrothermal, chemical liquid deposition, atomic layer deposition *etc*. are the common methods used in the synthesis. In this view, developing a novel synthesis method or improving the existing methods to produce zirconia-based acid catalysts of high stability is promising for the future manufacturing industries. Meanwhile, understanding the catalyst deactivation mechanism to maintain the high activity of these catalysts is highly desirable.

At the same time, the economic manufacture is another important aspect for an industry application of zirconia-based acid catalysts. At present, some of the novel zirconia-based acid catalysts are trapped in the lab and not in the industry. Even though it has excellent efficiency and stability for

some valuable biomass conversions, the obstacle from lab to industry still needs lots of efforts to minimize the cost of the catalyst production and to enhance their feasibility in a large scale. Besides, techniques relating to the complicated zirconia-based catalysts production process should also be carefully considered.

2.7 Catalytic reactions studied in this thesis

2.7.1 Catalytic production of 5-hydrxymethylfurfural from glucose

In recent years, biomass conversion has gained more and more attention since it has the potential to overcome the over-reliance of the fossil fuels. A kind of furan derivatives obtained from biomass, 5-hydroxylmethylfurfural (HMF), is assigned as one of the hottest bio-based chemicals produced from biorefinery carbohydrates since it could be a potential substitute for petroleum-derived intermediate products during the manufacture of polymers and fuels [24, 174, 175]. During the last few years, there has been lots of research about HMF chemistry. As a chemical platform, a variety of valuable compounds can be synthesized based on HMF, such as 2,5-furandicarboxylic acid, 2,5-dimethylfuran, 2,5-bishydroxymethylfuran, 5-hydroxymethylfuroic acid, alkoxymethylfurfurals, 1,6-hexanediol, levulinic acid, formic acid, and adipic acid, *etc.* (Figure 2.14) [176-178]. The potentials of HMF and its derivatives to replace enormously consumed petroleum-based building blocks make it a key role to solve the issues of the shortage of non-renewable energy resources (from fossil fuels) and the environmental pollution stemming from consuming it, thus provide a viable way to achieve a sustainable future [178-181].

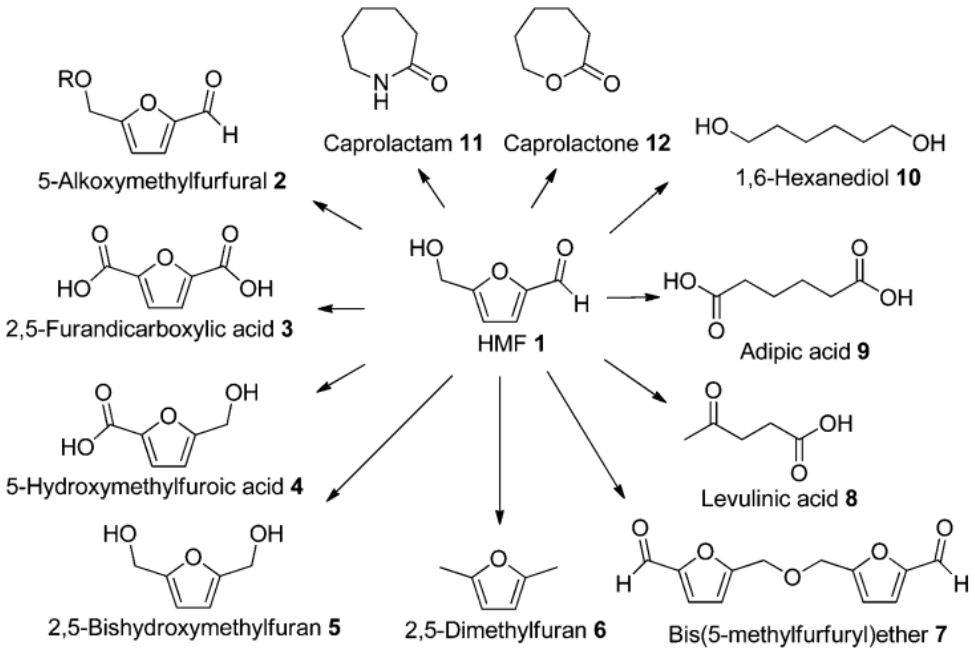

Figure 2.14 HMF as a platform chemical [176]

Up to date, numbers of carbohydrates have been applied to obtain HMF, including cellulose, glucose, and fructose, *etc*. [155, 176, 182]. Among these feedstocks, fructose is supposed to be the most accessible precursor for HMF production since there is only one dehydration step required for the fructose to HMF transformation [183]. However, though high HMF yield from fructose has been largely reported, it is not an ideal feedstock for the production of HMF due to its relatively high cost [105, 184]. Compared with fructose, glucose has the advantages of greater availability and lower cost, making it a preferred feedstock for the production of HMF [182]. According to the previous studies, it is generally considered that both LAS and BAS play important roles for glucose transformation to HMF, with an LAS required for glucose isomerization to fructose, followed by a BAS catalyzed fructose dehydration to HMF (Figure 2.15) [24, 182]. So far, a lot of studies have been focused on the glucose conversion to HMF, from mechanistic to industry aspect [178, 184-186].

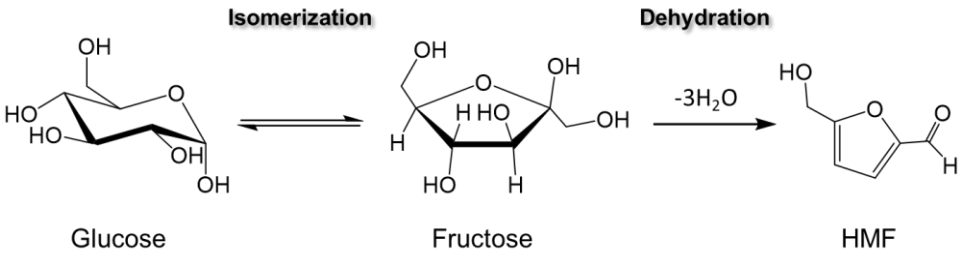

Figure 2.15 Conversion of glucose to HMF

2.7.2 Catalytic production of ethyl mandelate from phenylglyoxal

Mandelic acid and its derivatives are well known as valuable intermediates in pharmaceutical and fine chemical industries due to its specific chiral center [187-189]. In recent years, the efficient preparation of ethyl mandelate (EM) has become a worldwide research priority since it is a very typical mandelic derivate and has been widely applied in stereochemistry [190, 191]. The production of EM can be fulfilled in a single step from phenylglyoxal (PG) via intramolecular Cannizzaro reaction [192, 193]. The Cannizzaro reaction is one of the oldest processes in synthetic organic chemistry with a process of the redox disproportionative conversion of aldehydes into the corresponding alcohols and carboxylic acids (Figure 2.16) [194]. Generally, the Cannizzaro reaction occurs in the presence of concentrated alkali metal hydroxides or other strong bases at high temperature, but later, this reaction was reported to be successfully conducted under milder conditions catalyzed by Lewis acids [195-197]. Moreover, it was reported that a much higher EM yield could be achieved by increasing the Brønsted acidity of the catalysts [198, 199]. Thus, solid acid catalysts turn out to be hot candidates for the production of EM from PG.

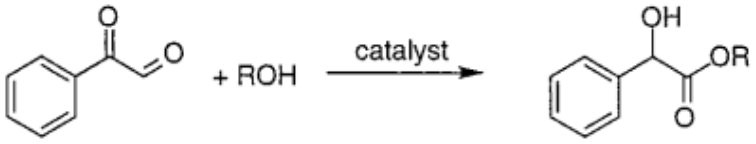

Figure 2.16 Cannizzaro reaction on phenylglyoxal

The two reactions studied in this thesis, glucose to HMF and PG to EM conversions, both need acidity property (LAS or/and BAS) from solid acid catalysts to drive the reactions to the product direction. Meanwhile, the acidity property also has vital influence on the products yield and selectivity that are the direct indexes to evaluate the performance of the catalysts. Thus, the evaluation of acidity property of the catalysts is crucial for estimating the performance of the catalysts in the reactions. At present, titration methods, temperature-programmed desorption (TPD), fourier transform infrared spectroscopy (FTIR), and solid-state nuclear magnetic resonance (NMR) spectroscopy are the common techniques for evaluating the acidity property of the catalysts [21]. Among which, solid-state NMR spectroscopy turns out to be a powerful technique that can not only differentiate the acid types, concentrations, and strength, but also reveal the local structure of the surface acid sites. Hence, this technique is applied all over this thesis projects.

2.8 Summary

In this literature review, the background of the solid acid catalyst, the theory of acid site, and the main types of zirconia and zirconia-based acid catalysts have been presented. It covers bare zirconia, zirconia-based acid catalysts using zirconia as a support, and zirconia-based acid catalysts using zirconia supported on other mesoporous materials. It describes the different aspects of zirconia-based acid catalysts including the structures, acidities, synthesis methods, mechanisms, and applications. In addition, the two acid-catalytic reactions studied in this thesis are also introduced.

To conclude, zirconia and zirconia-based acid catalysts are with no-doubt among the categories of the most practical and functional solid acid catalysts. The advantages include the synthetic versatility, simplicity of process engineering, easy recovery and reusability, mild reaction conditions, and environmentally safe disposal. Not only pure zirconia itself but also functionalized

zirconia including doping other co-catalysts on zirconia particles or zirconia in the mesoporous state, anchoring itself or/and co-catalysts on other mesoporous supports enable the decoration of zirconia-system with a wide variety of functionalities. The obtained multifunctional catalysts normally exhibit excellent catalytic performance in many acid-catalyzed reactions. The foreseeable economic and environmental benefit gives rise to the booming development of a novel family of the catalytic systems, that essentially motivate the research described in this thesis.

References

[1] Jong, K. P. **2009**.

[2] Chapuis, C.; Jacoby, D. *Appl. Catal. A: Gen.* **2001**, *221*, 93-117.

[3] Armor, J. N. *Appl. Catal. B: Environ.* **1992**, *1*, 221-253.

[4] Hu, L.; Hao, W.; Tang, X.; Sun, Y.; Lin, L.; Liu, S. *RSC Adv.* **2012**, *2*, 11184-11206.

[5] Borges, M. E.; Díaz, L. *Renew. Sust. Energ. Rev.* **2012**, *16*, 2839-2849.

[6] Bhaduri, S.; Mukesh, D. **2000**.

[7] Corma, A. *Curr. Opin. Solid St. M.* **1997**, *2*, 63-75.

[8] Hattori, H.; Ono, Y. **2015**.

[9] Tanabea, K.; Holderich, W. F. *Appl. Catal. A: Gen.* **1999**, *181*, 399-434.

[10] Jensen, W. B. *Chem. Rev.* **1978**, *78*, 1-22.

[11] Corma, A.; García, H. *Chem. Rev.* **2003**, *103*, 4307-4365.

[12] Pearson, R. G. *J. Am. Chem. Soc.* **1963**, *85*, 3533-3539.

[13] Parr, R. G.; Chattaraj, P. K. *J. Am. Chem. Soc.* **1991**, *113*, 1854-1855.

[14] Pearson, R. G.; Songstad, J. *J. Am. Chem. Soc.* **1967**, *89*, 1827-1836.

[15] Kauffman, G. B. *J. Chem. Educ.* **1988**, *65*, 28-31.

[16] Corma, A.; Xamena, F. X. L.; Prestipino, C.; Renz, M.; Valencia, S. *J. Phys. Chem. C* **2009**, *113*, 11306-11315.

[17] Corma, A.; Renz, M. S. *Chem. Commun.* **2004**, 550-551.

[18] Prinson, S. S.; Samuel, P.; Singh, A. P. *J. Mol. Catal. A: Chem.* **2007**, *266*, 11-20.

[19] Corma, A., Xamena, F. X. L. *Chem. Rev.* **2010**, *110*, 4606-4655.

[20] Suganuma, S.; Kitano, M.; Yamaguchi, D.; Kato, H.; Hayashi, S.; Hara, M. *J. Am. Chem. Soc.* **2008**, *130*, 12787-12793.

[21] Zichun, W.; Huang, J. **2017**.

[22] Yi, X.; Chen, W.; Li, J.; Xu, S.; Li, C.; Xiao, Y.; Liu, H.; Guo, X.; Liu, S. B.; Zheng, A. *J. Am. Chem. Soc.* **2018**, *140*, 10764-10774.

[23] Okuhara, T. *Chem. Rev.* **2002**, *102*, 3641-3665.

[24] Choudhary, V.; Mushrif, S. H.; Ho, C.; Anderko, A.; Nikolakis, V.; Marinkovic, N. S.; Frenkel, A. I.; Sandler, S. I.; Vlachos, D. G. *J. Am. Chem. Soc.* **2013**, *135*, 3997-4006.

[25] Zhang, Z.; Huber, G. W. *Chem. Soc. Rev.* **2018**, *47*, 1351-1390.

[26] Masudi, A. Muraza, O. *Energy Fuel.* **2018**, *32*, 2840-2854.

[27] Ho, S. M. *Mater. Sci. Eng.* **1982**, *54*, 23-29.

[28] Zhao, Y.; Zhang, M.; Tao, K. *Catal. Commun.* **2002**, *3*, 239-245.

[29] Tsuchiya, H.; Sieber, I.; Schmuki, P. *Small* **2005**, *1*, 722-725.

[30] Watanabe, M.; Iida, T.; Nishimura, R.; Inomata, H. *Appl. Cataly. A: Gen.* **2005**, *295*, 150-156.

[31] Chen, W. H.; Ko, H. H.; Sakthivel, A.; Huang, S. J.; Liu, S. H.; Lo, A. Y.; Tsai, T. C.; Liu, S. B. *Catal. Today* **2006**, *116*, 111-120.

[32] Keramidas, V. G.; White, W. B. *J. Am. Ceram. Soc.* **1974**, *57*, 22-24.

[33] Yamamoto, T.; Takenaka, S.; Yoshida, S.; Onari, T.; Takahashi, Y.; Kosaka, T.; Hasegawa, S.; Kudo, M. *J. Phys. Chem. B* **1999**, *103*, 2385-2393.

[34] Jacob, K. H.; Knözinger, E.; Benier, S. *J. Mater. Chem.* **1993**, *3*, 651-657.

[35] Joshi, S. S.; Pandare, K. V.; Kulkarni, B. D. *Ind. Eng. Chem. Res.* **2014**, *53*, 18796-18805.

[36] Peng, L.; Zhang, J.; Zhuang, J.; Zhang, B.; Gong, Y. *Molecules* **2010**, *15*, 5258-5272.

[37] Tomishige, K.; Ikeda, Y.; Fujimoto, K. *Catal. Lett.* **1999**, *58*, 225-229.

[38] Nakano, Y.; Iizuka, T.; Hattori, H.; Tanabe, K. *J. Catal.* **1979**, *57*, 1-10.

[39] Kuo, I. J.; Suzuki, N.; Yamauchi, Y.; Wu, K. C. W. *RSC Adv.* **2013**, *3*, 2028-2034.

[40] Holm, V. C. F.; Balley, G. C.; Oka, B. **1962**.

[41] Hino, M.; Arata, K. *J. Am. Chem. Soc.* **1979**, *101*, 6439-6441.

[42] Barthos, F. L. R.; Onyestyak, G.; Valyon, J. *J. Phys. Chem. B* **2000**, *104*, 7311-7319.

[43] Ward, D. A.; Ko, E. I. *J. Catal.* **1994**, *150*, 18-33.

[44] Reddy, B. M.; Patil, M. K. *Chem. Rev.* **2009**, *109*, 2185-2208.

[45] Miranda, C. D.; Jurado, S. G.; Vera, C. R. *J. Mol. Catal. A: Chem.* **2015**, 398, 325-335.

[46] Li, X.; Simon, L. J.; Olindo, R.; Lercher, J. A. *J. Catal.* **2005**, *232*, 456-466.

[47] Deshmane, V. G.; Adewuyi, Y. G. *Appl. Cataly. A: Gen.* **2013**, 462-463, 196-206.

[48] Saravanan, B. T. K.; Shukla, R. S.; Bajaj, H. C. *Appl. Catal. B: Environ.* **2015**, *172-173*, 108-115.

[49] Tran, M. T.; Gnep, N. S.; Guisnet, M. *Appl. Catal. A: Gen.* **1998**, *171*, 207-217.

[50] Joo, J. B.; Zhang, Q.; Dahl, M.; Gu, M.; Zaera, F.; Yin, Y. *ChemSusChem* **2013**, *6*, 2001-2008.

[51] Alhassan, F. H.; Taufiq-Yap, Y. H. *Fuel* **2015**, *142*, 38-45.

[52] Baertsch, C. D.; Soled, S. L.; Iglesia, E. *J. Phys. Chem. B* **2001**, 105, 1320-1330.

[53] Hino, M.; Arata, K. *J. Chem. Soc. Chem. Comm.* **1988**, 1259-1260.

[54] Santiesteban, J. G.; Han, S.; Bastian, R. D.; Chang, C. D. *J. Catal.* **1997**, *168*, 431-441.

[55] . Franklin, D. H.; Wachs, I. E. *J. Raman Spectros.* **1995**, *26*, 397-405.

[56] Boyse, R. A.; Ko, E. I. *J. Catal.* **1997**, *171*, 191-207.

[57] Barton, D. G.; Soled, S. L.; Iglesia, E. *Top Catal.* **1998**, *6*, 87-99.

[58] Sohn, J. R.; Park, Y. *Langmuir* **1998**, *15*, 8336-8336.

[59] Cortés-Jácome, M. A.; Angeles-Chavez, C.; López-Salinas, E.; Navarrete, J.; Toribio, P.; Toledo, J. A. *Appl. Catal. A: Gen.* **2007**, *318*, 178-189.

[60] Ross-Medgaarden, E. I.; Knowles, W. V.; Kim, T.; Wong, M. S.; Zhou, W.; Kiely, C. J.; Wachs, I. E. *J. Catal.* **2008**, *256*, 108-125.

[61] Barton, D. G.; Meitzner, G. D.; Fuentes, G. A.; Iglesia, E. *J. Catal.* **1998**, *181*, 57-72.

[62] Scheithauer, M.; Grasselli, R. K.; Knozinger, H. *Langmuir* **1998**, *14*, 3019-3029.

[63] Vaidyanathan, N.; Houalla, M.; Hercules, D. M. *Surf. Interface Anal.* **1998**, *26*, 415-419.

[64] Barton, D. G.; Wilson, R. D.; Soled, S. L.; Iglesia, E. *J. Phys. Chem. B* **1999**, *103*, 630-640.

[65] Zhou, W.; Soultanidis, N.; Xu, H.; Wong, M. S.; Neurock, M.; Kiely, C. J.; Wachs, I. E. *ACS Catal.* **2017**, *7*, 2181-2198.

[66] Zhou, W.; Ross-Medgaarden, E. I.; Knowles, W. V.; Wong, M. S.; Wach, I. E.; Kiely, C. J. *Nat. Chem.* **2009**, *1*, 722-728.

[67] Soultanidis, N.; Zhou, W.; Psarras, A. C.; Gonzalez, A. J.; Iliopoulou, E. F.; Kiely, C. J.; Wachs, I. E.; Wong, M. S. *J. Am. Chem. Soc.* **2010**, *132*, 13462-13471.

[68] Vaudagna, S. R.; Ffgoli, N. S. *Appl. Cataly. A: Gen.* **1997**, *164*, 265-280.

[69] Naito, N.; Niwa, M. *J. Phys. Chem. B* **1999**, *103*, 7206-7213.

[70] Galano, A.; Rodriguez-Gattorno, G.; Torres-García, E. *Phys. Chem. Chem. Phys.* **2008**, *10*, 4181-4188.

[71] Macht, J.; May-Lozano, M.; Soled, S. L.; Wang, Y.; Iglesia, E. *J. Catal.* **2004**, *227*, 479-491.

[72] Chai, J.; Cen, Y.; Guo, J.; Wanga, J.; Fan, W. *RSC Adv.* **2017**, *7*, 8567-8574.

[73] Park, Y. M.; Chung, S. H.; Park, I. S.; Lee, S. Y.; Kim, D. K.; Lee, J. S.; Lee, K. Y. *Bioresour. Technol.* **2010**, *1*, S59-S61.

[74] Park, Y. M.; Eom, H. J.; Lee, J. S.; Lee, K. Y. *Bioresour. Technol.* **2010**, *101*, 6589-6593.

[75] Wang, H.; He, L.; Liu, Z. *Energy Fuel.* **2012**, 6518-6527.

[76] Gonell, F.; Portehault, D.; Julián-López, B.; Vallé, K.; Sanchez, C.; Corma, A. *Catal. Sci. Technol.* **2016**, *6*, 8257-8267.

[77] Zhang, C.; Liu, T.; Wang, H. J.; Wang, F.; Pan, X. Y. *Chem. Eng. J.* **2011**, *174*, 236-241.

[78] Dedsuksophon, K. F. W.; Champreda, V.; Laosiripojana, N. *Bioresour.Technol.* **2011**, *102*, 2040-2046.

[79] Si, Z.; Weng, D.; Wu, X.; Li, J.; Li, G. *J. Catal.* **2010**, *271*, 43-51.

[80] Kurosaka, T.; Naribayashi, I.; Sasaki, Y. *Catal. Commun.* **2008**, *9*, 1360-1363.

[81] Antunesa, M. M.; Fernandesb, A. Candeiasa, J.; Pillingera, M.; Rochac, S. M.; Ribeirob, M. F.; Valente, A. A. *Catal. Today* **2012**, *195*, 127-135.

[82] Falco, M. G.; Comelli, R. A.; Figoli, N. S. *Appl. Cataly. A: Gen.* **2000**, *201*, 37-43.

[83] Kim, T. Y.; Choi, Y.; Baek, J.; Park, J. R.; Yi, J. *J. Mater. Chem.* **2012**, *22*, 10021-11002.

[84] Kraus, K. A. *J. Am. Chem. Soc.* **1956**, *78*, 694-694.

[85] Xiao, H.; Liu, S. *Mater. Des.* **2018**, *155*, 19-35.

[86] Clearfiel, A.; Thakur, D. S. *Appl. Catal.* **1986**, *26*, 1-26.

[87] Ballesteros-Plata, D.; Rodríguez-Aguado, E.; Braos-García, P.; Jiménez-Jiménez, J.; Rodríguez-Castellón, E. *Catalysts* **2017**, *7*, 176-192.

[88] Hogarth, W. H. J.; Drennanb, J.; Lu, G. Q. *J. Mater. Chem.* **2005**, *15*, 754-758.

[89] Vaivars, G.; Mokrani, T.; Petrik, L.; Klavins, J.; Gericke, G.; Linkov, V. *Mater. Sci.* **2004**, *10*, 162-165.

[90] Lin, R.; Ding, Y. *Materials* **2013**, *6*, 217-243.

[91] Spielbauer, D.; Riemer, T.; Zaki, M. I.; Kno1zinger, H. *J. Phys. Chem. B* **1997**, *101*, 4681-4688.

[92] Troup, J. M.; Clearfield, A. *Inorg. Chem.* **1977**, *16*, 3311-3314.

[93] Pica, M. *Catalysts* **2017**, *7*, 190-208.

[94] Sanchez, J.; Narkeviciute, I.; Colón, J. L.; Jaramillo, T. F. *Catalysts* **2017**, *7*, 132-146.

[95] Clearfield, A.; Medina, A. S.; Smith, G. D.; Thomas, J. R. *J. Phys. Chem.* **1969**, *73*, 3424-3430.

[96] Tsuyoshi, K. *Bull. Chem. Soc. Jpn.* **1982**, *55*, 3031-3032.

[97] Marti, A. A.; Colon, J. *Inorg. Chem.* **2003**, *42*, 2830-2832.

[98] Alberti, G.; Gill, J. S. *J. Inorg. Nuc. Chem.* **1976**, *38*, 1733-1738.

[99] Weingarten, R.; Tompsett, G. A.; Fernández, A.; Han, K. S.; Hagaman, E. W.; Conner, W. C.; Dumesic, J. A.; Huber, G. W. *J. Catal.* **2013**, *304*, 123-134.

[100] Sinhamahapatra, A.; Roy, B.; Tarafdar, A.; Bajaj, H. C.; Panda, A. B. *Appl. Cataly. A: Gen.* **2010**, *385*, 22-30.

[101] Sun, L.; Sue, H. J.; Clearfield, A. *New J. Chem.* **2007**, *31*, 39-43.

[102] Zhu, C.; Li, D.; Wang, H.; Zhang, C.; Cui, C.; Chen, L.; Cai, C.; Ma, L. *ACS Omega* **2018**, *3*, 7407-7417.

[103] Antonetti, C.; Licursi, D.; Fulignati, S.; Ribechini, E.; Rivas, S.; Parajó, J. C.; Cavani, F.; Galletti, A. M. R. *Appl. Catal. B: Environ.* **2017**, *206*, 364-377.

[104] Asghari, F. S.; Yoshida, H. *Carbohydr. Res.* **2006**, *341*, 2379-2387.

[105] Jain, A.; Shore, A. M.; Jonnalagadda, S. C.; Ramanujachary, K. V.; Mugweru, A. *Appl. Catal. A: Gen.* **2015**, *489*, 72-76.

[106] Sinhamahapatra, A.; Pahari, S.; Bajaj, H. C.; Panda, A. B. *Appl. Cataly. A: Gen.* **2011**, *394*, 93-100.

[107] Liu, B.; Jin, M.; Zhang, Z. *Ind. Crop. Pro.* **2015**, *76*, 781-786.

[108] Miao, Z.; Song, H.; Chou, L. *RSC Adv.* **2014**, *4*, 22509-22519.

[109] Zhou, Y.; Ding, F.; Brittain, A. D.; Liu, J.; Zhang, M.; Xiao, M.; Meng, Y.; Sun, L. *ACS Appl. Mater. Interfaces* **2014**, *6*, 7417-7425.

[110] Idakiev, V.; Tabakova, T.; Naydenov, A.; Yuan, Z. Y.; Su, B. L. *Appl. Catal. B: Environ.* **2006**, *63*, 178-186.

[111] Dilara, P. A.; Vohs, J. M. *J. Phys. Chem.* **1993**, *97*, 12919-12923.

[112] Shim, J. H.; Huang, H.; Prinz, F. B. *Chem. Mater.* **2007**, *19*, 3580-3854.

[113] Jossen, R.; Pratsinis, S. E.; Watson, M.; Akhtar, M. K. *Nanotechnology* **2005**, *16*, S609-S617.

[114] Kapoor, M. P.; Shen, W. J.; Matsumura, Y. *Catal. Lett.* **2001**, *76*, 139-142.

[115] Idakiev, V.; Andreeva, D.; Blin, J. L.; Gigot, L.; Su, B. L. *Appl. Cataly. A: Gen.* **2003**, *243*, 25-39.

[116] Hotz, N.; Stutz, M.; Loher, S.; Stark, W. J.; Poulikakos, D. *Appl. Catal. B: Environ.* **2007**, *73*, 336-344.

[117] Kim, M.; Laine, R. M. *J. Am. Chem. Soc.* **2009**, *131*, 9220-9229.

[118] Weidenhof, M. R. B.; Stowe, K.; Maier, W. F.; Kim, M.; Azurdia, J.; Gulari, E.; Seker, E.; Barks, A.; Laine, R. M. *J. Am. Chem. Soc.* **2009**, *131*, 9207-9219.

[119] Teoh, W. Y.; Mädler, L.; Grunwaldt, J. D.; Amal, R.; Pratsinis, S. E. *Chem. Mater.* **2008**, *20*, 4069-4079.

[120] Cai, W.; Zhong, Q.; Zhang, S.; Zhang, J. *RSC Adv.* **2013**, *3*, 7009.

[121] Bae, J. W.; Woo, M. H.; Cheon, J. Y.; Ha, K. S.; Jun, K. W.; Lee, D. H.; Jung, H. M. *ChemCatChem* **2011**, *3*, 1342-1347.

[122] Wang, H.; Chang, C.; Zhu, X.; Liu, X.; Han, J.; Ge, Q. *Appl. Cataly. A: Gen.* **2016**, *523*, 182-192.

[123] Martínez-Edo, G.; Pontón, I.; Rio, A. M.; Sánchez-García, D. *Catalysts* **2018**, *8*, 617-679.

[124] Beck, J. S.; Roth, W. J.; Schmitt, K. D.; Chu, C. T. W.; Olson, D. H.; Sheppard, E. W.; McCullen, S. B.; Higgins, J. B.; Schlenker, J. L. *J. Am. Chem. Soc.* **1992**, *114*, 10834-10843.

[125] Jiménez-Morales, I.; Maireles-Torres, P.; Jiménez-López, A. *Appl. Cataly. A: Gen.* **2010**, *379*, 61-68.

[126] Oliveira, R. S.; Bizeto, M. A. *J. Solid State Chem.* **2016**, *235*, 125-131.

[127] Kresge, C. T.; Roth, W. J.; Vartuli, J. C.; Beck, J. S. *Nature* **1992**, *359*, 710-712.

[128] Sahoo, D. P.; Nanda, B.; Parida, K. M. *RSC Adv.* **2015**, *5*, 83707-83724.

[129] Peng, L.; Yu, X.; Li, H.; Zhang, J.; He, L. *Energy Fuel*. **2018**, *33*, 330-339.

[130] Wang, X.; Patarin, J.; Basset, J. M. *Micropor. Mesopor. Mat.* **2001**, *42*, 269-276.

[131] Jiménez-Morales, I.; Santamaría-González, J.; Jiménez-López, A.; Maireles-Torres, P. *Fuel* **2014**, *118*, 265-271.

[132] Sawant, D. P.; Lefebvre, F.; Halligudi, S. B. *J. Mol. Catal. A: Chem.* **2007**, *262*, 98-108.

[133] Jiménez-López, A.; Jiménez-Morales, I.; Santamaría-González, J.; Maireles-Torres, P. *J. Mol. Catal. A: Chem.* **2011**, *335*, 205-209.

[134] Chen, J.; Zhang, J.; Xu, J. *ChemCatChem* **2013**, *5*, 2822-2826.

[135] Wang, J. H.; Mou, C. Y. *Micropor. Mesopor. Mat.* **2008**, *110*, 260-270.

[136] Chen, C. L.; Lin, H. P.; Wong, S. T.; Mou, C. Y. *Appl. Cataly. A: Gen.* **2001**, *215*, 21-30.

[137] Wang, Y.; Choi, S.; Liu, J.; Wang, L. Q.; Peden, C. H. F. *Green Chem.* **2007**, *9*, 540-544.

[138] Wang, W.; Xu, N. P.; Mou, C. Y. *Green Chem.* **2002**, *4*, 257-260.

[139] Zhao, D.; Huo, Q.; Melosh, N.; Fredrickson, G. H.; Chmelka, B. F.; Stucky, G. D. *Science* **1998**, *297*, 548-553.

[140] Zhao, D.; Feng, J.; Chmelka, B. F.; Stucky, G. D. *J. Am. Chem. Soc.* **1998**, *120*, 6024-6036.

[141] Galarneau, A.; Guenneau, F.; Renzo, F. D.; Gedeon, A. *J. Phys. Chem. C* **2007**, *111*, 8268-8277.

[142] Kruk, M.; Ko, C. H.; Ryoo, R. *Chem Mater.* **2000**, *12*, 1961-1968.

[143] Sawant, D. P.; Jacob, N. E.; Lefebvre, F.; Halligudi, S. B. *J. Catal.* **2005**, *235*, 341-352.

[144] Crucianelli, M.; Saladino, R. *Catalysts* **2019**, *9*, 984-1104.

[145] Singh, S.; Setiabudi, H. D.; Nanda, S.; Vo, D. V. N. *Appl. Cataly. A: Gen.* **2018**, *559*, 57-74.

[146] Wang, X.; Chan, J. C. C.; Cheng, S. *J. Phys. Chem. B* **2005**, *109*, 1763-1769.

[147] Zeidan, R. K.; Davis, M. E. *Angew. Chem. Int. Ed.* **2006**, *45*, 6332-6335.

[148] Hartmann, M. *Chem Mater.* **2005**, *17*, 4577-4593.

[149] Barbera, K.; Pistone, A.; Millesi, S.; Malandrino, G.; Gulino, A.; Perathoner, S.; Centi, G. *J. Catal.* **2015**, *323*, 19-32.

[150] Niu, Y.; Zhu, X.; Song, Z.; Xie, X.; Liu, X.; Han, J.; Ge, Q. *Micropor. Mesopor. Mat.* **2014**, *198*, 215-222.

[151] Krishnan, C. K.; Ogura, M. *Adv. Mater.* **2008**, *20*, 2131-2136.

[152] Chen, S. Y. Cheng, S. *J. Catal.* **2010**, *270*, 196-205.

[153] Li, F.; Li, Y.; Li, R.; Xie, K. *Micropor. Mesopor. Mat.* **2007**, *101*, 250-255.

[154] Garg, S.; Kumaran, G. M.; Bal, R.; Gora-Marek, K.; Gupta, J. K.; Sharma, L. D.; Dhar, G. M. *Catal. Today* **2009**, *141*, 125-129.

[155] Osatiashtiani, A.; Lee, A. F.; Granollers, M.; Brown, D. R.; Olivi, L.; Morales, G.; Melero, J. A.; Wilson, K. *ACS Catal.* **2015**, *5*, 4345-4352.

[156] Cecilia, J. A.; García-Sancho, C.; Mérida-Robles, J. M.; Santamaría González, J.; Moreno-Tost, R.; Maireles-Torres, P. *Appl. Cataly. A: Gen.* **2016**, *516*, 30-40.

[157] Sawant, D. P.; Mirajkar, S. P.; Lefebvre, F.; Ariga, K.; Anandanb, S.; Mori, T.; Nishimura, C.; Halligudi, S. B. *J. Mol. Catal. A: Chem.* **2007**, *271*, 46-56.

[158] Sawant, D. P.; Justus, J.; Srinivasu, P.; Halligudi, S. B. *J. Mol. Catal. A: Chem.* **2007**, *276*, 150-157.

[159] Gutiérrez, O. Y.; Fuentes, G. A.; Klimova, T. *J. Catal.* **2007**, *249*, 140-153.

[160] Luo, Z.; He, M.; Zhao, C. *Green Chem.* **2016**, *18*, 433-441.

[161] Ginjupalli, S. R.; Mugawar, S.; Rajan, N. P.; Balla, P. K.; Komandur, V. R. C. *Appl. Surf. Sci.* **2014**, *309*, 153-159.

[162] Kourieh, R.; Rakic, V.; Bennici, S.; Auroux, A. *Catal. Commun.* **2013**, *30*, 5-13.

[163] Kunshan, S.; Zhang, H.; Zhang, Y.; Yi, T.; Tang, K. *J. Catal.* **2013**, *299*, 119-128.

[164] Yori, J. C.; Vera, C. R.; Parera, J. M. *Appl. Cataly. A: Gen.* **1997**, *163*, 165-175.

[165] Kourieh, R.; Marzo, M.; Gervasini, A.; Auroux, A. *Catal. Commun.* **2012**, *19*, 119-126.

[166] Rao, G. S.; Sekhar, M. H.; Ammaji, S.; Chary, K. V. R. *J. Mol. Catal. A: Chem.* **2014**, *395*, 486-493.

[167] Rao, K. N.; Ammaji, S.; Lee, A. F.; Tavener, S. J.; Young, N. A.; Wilson, K. *Green Chem.* **2006**, *8*, 790-797.

[168] Massa, M.; Andersson, A.; Finocchio, E.; Busca, G.; Lenrick, F.; Wallenberg, L. R. *J. Catal.* **2013**, *297*, 93-109.

[169] Chao, M.; Xu, H.; Zhao, H.; Yang, J.; Zhao, J.; Song, H.; Liang, N.; Chou, L. *Fuel* **2015**, *145*, 234-240.

[170] Jiménez-Morales, I.; Maireles-Torres, P.; Jiménez-López, A. *Appl. Catal. B: Environ.* **2011**, *103*, 91-98.

[171] Liao, H.; Zhang, J.; Xiao, Y.; Liu, P.; Hao, F.; You, K.; Luo, H. *Chem. Eng. J.* **2014**, *243*, 207-216.

[172] Degirmenci,V.; Uner, D. *Catal. Today* **2009**, *142*, 30-33.

[173] Degirmenci, V.; Hensen, E. J. M.; Uner, D.; Cinlar, B.; Yilmaz, A.; Santen, R. A. *Catal. Lett.* **2010**, *141*, 33-42.

[174] Choudhary, V.; Pinar, A. B.; Lobo, R. F.; Vlachos, D. G.; Sandler, S. I. *ChemSusChem* **2013**, *6*, 2369-2376.

[175] Bozell, J. J.; Petersen, G. R. *Green Chem.* **2010**, *12*, 539-554.

[176] Putten, R.; Waal, J. C.; Jong, E.; Rasrendra, C. B.; Heeres, H. J.; Vries, J. G. *Chem. Rev.* **2013**, *113*, 1499-1597.

[177] Zhang, J.; Weitz, E. *ACS Catal.* **2012**, *2*, 1211-1218.

[178] Pagán-Torres, Y. J.; Wang, T.; Gallo, J. M. R.; Shanks, B. H.; Dumesic, J. A. *ACS Catal.* **2012**, *2*, 930-934.

[179] Gallo, J. M. R.; Mellmer, M. A.; Dumesic, J. A. *Green Chem.* **2013**, *15*, 85-90.

[180] Binder, J. B.; Raines, R. T. *J. Am. Chem. Soc.* **2009**, *131*, 1979-1985.

[181] Chheda, J. N.; Roman-Leshkov, Y.; Dumesic, J. A. *Green Chem.* **2007**, *9*, 342-350.

182] Wang, T.; Nolte, M. W.; Shanks, B. H. *Green Chem.* **2014**, *16*, 548-572.

[183] Qi, X.; Watanabe, M.; Aida, T. M.; Smith, J. R. L. *Green Chem.* **2008**, 10, 799-805.

[184] Qi, X.; Watanabe, M.; Aida, T. M.; Smith, J. R. L. *Catal. Commun.* **2008**, *9*, 2244-2249.

[185] Huang, R.; Su, R.; He, Z. *Chem. Commun.* **2010**, *46*, 1115-1117.

[186] Román-Leshkov, Y.; Labinger, J. A.; Davis, M. E. *Angew. Chem. Int. Ed.* **2010**, *49*, 8954-8957.

[187] Liu, Z. Q.; Zhang, X. H.; Xue, Y. P.; Xu, M.; Zheng, Y. G. *J. Agric. Food Chem.* **2014**, *62*, 4685-4694.

[188] Poterała, M.; Dranka, M.; Borowiecki, P. *Eur. J. Org. Chem.* **2017**, 2290-2304.

[189] Martinkova, L.; Kren, V. *Appl. Microbiol. Biotechnol.* **2018**, *102*, 3893-3900.

[190] Kasprzak, J.; Rauter, M.; Denter, S.; Becker, K.; Baronian, K.; Bode, R.; Schauer, F.; Piontek, M.; Vorbrodt, H. M.; Kunze, G. *J. Mol. Catal. B: Enzym.* **2016**, *133*, 176-186.

[191] Liu, X. H.; Du, X.; Feng, J.; Wu, M. B.; Lin, J.; Guan, J.; Wang, T.; Zhang, Z. *Catal. Lett.* **2019**, *149*, 1710-1720.

[192] Wang, Z.; Jiang, Y.; Hunger, M.; Baiker, A.; Huang, J. *ChemCatChem* **2014**, *6*, 2970-2975.

[193] Wang, Z.; Jiang, Y.; Baiker, A.; Huang, J. *ACS Catal.* **2013**, *3*, 1573-1577.

[194] Abaee, M. S.; Sharifi, R.; Mojtahedi, M. M. *Org. Let.* **2005**, *7*, 5893-5895.

[195] Kishida, H.; Jin, F.; Yan, X.; Moriya, T.; Enomoto, H. *Carbohydr. Res.* **2006**, *341*, 2619-2623.

[196] Wang, P.; Tao, W. J.; Sun, X. L.; Liao, S.; Tang, Y. *J. Am. Chem. Soc.* **2013**, *135*, 16849-16852.

[197] Russell, A. E.; Miller, S. P.; Morken, J. P. *J. Org. Chem.* **2000**, *65*, 8381-8383.

[198] Wang, Z.; Jiang, Y.; Rachwalik, R.; Liu, Z.; Shi, J.; Hunger, M.; Huang, J. *ChemCatChem* **2013**, *5*, 3889-3896.

[199] Wang, Z.; Jiang, Y.; Jin, F.; Stampfl, C.; Hunger, M.; Baiker, A.; Huang, J. *J. Catal.* **2019**, *372*, 1-7.

Chapter 3 The influence of calcination temperature on the performance of zirconia-based catalyst in glucose conversion

3.1 Introduction

The decreasing petroleum reserves and growing environmental concerns about greenhouse gas emissions have promoted research on biomass as a raw material for the production of chemicals and other fuel substitutes for gas or oil [1-3]. Developing economic, efficient, and environmentally friendly technologies is a promising but at the same time challenging strategy for biomass transformation. 5-Hydroxylmethylfurfural (HMF), a kind of furan derivatives obtained from biomass, has gained much attention recently since it could be a potential substitute for petroleum-derived intermediate products during the manufacture of polymers and fuels [4]. As a chemical platform, a number of important C-6 compounds can be synthesized by HMF, such as alkoxymethylfurfurals, 2,5-furandicarboxylic acid, 5-hydroxymethylfuroic acid, 2,5-dimethylfuran [5]. Some important non-furanic compounds, namely levulinic acid, formic acid, adipic acid, 1,6-hexanediol, *etc.* can also be produced from HMF [1, 5-7].

Dehydration of hexose sugars such as glucose and fructose is considered to be a promising way to produce HMF [5, 8]. Though high HMF yields from fructose have been reported by many researchers, it is not an ideal feedstock for HMF production because of the high cost [9, 10]. Glucose is supposed to be a preferred feedstock for HMF production due to its greater availability and lower cost [2]. Glucose dehydration to HMF is generally initiated by acid catalysts, such as zeolites, amorphous silica-alumina, oxides, and others. Among them, zirconia (ZrO_2) has received considerable attention as both a catalyst and a catalyst support due to its favorable physicochemical properties [11-13]. Doping with other oxoanions to ZrO_2 can create additional electron-deficient

regions and may generate new acid sites and increase the strength of Brønsted acidity, thus can enhance catalytic behavior such as dehydration, hydrogenation and hydrogen exchange [12, 14].

Jiménez-Morales *et al*. studied the dehydration of glucose to HMF in a biphasic system based on mesoporous MCM-41 containing ZrO_2 and achieved an HMF yield of 23 % [15]. Massa *et al*. studied the dehydration of glycerol to acrolein over monoclinic-ZrO_2 doped with tungsten and niobium oxide and attained a 75 % acrolein yield with almost complete transformation of glycerol [16]. Kuo *et al*. did research on the conversion of cellulose to HMF with a catalyst of mesoporous ZrO_2 nanocatalysts in ionic liquid systems, which showed that the crystallinities may affect the acidities of catalysts [17]. It also showed that crystalline mesoporous ZrO_2 nanoparticles, in either the tetragonal or the monoclinic phase, exhibited higher HMF yields than amorphous mesoporous ZrO_2 nanoparticles because of the existence of a relatively strong acidity [17]. López *et al*. found that the increase in the catalytic activity of esterification and transesterification coincided with the formation of polymeric tungsten species in the presence of the tetragonal phase of the ZrO_2 support [18]. Ginjupalli *et al*. found that pure ZrO_2 polymorphs showed mainly weak and moderate acid strength, and the acidity of monoclinic-ZrO_2 was higher than that of tetragonal-ZrO_2, slightly differently from other authors [17, 19].

Different calcination temperatures during the catalyst preparation may cause different physicochemical properties of catalysts, such as crystalline structure, molecular structure of the metal-oxide overlayer, acid density and strength, which in turn results in different catalytic activities [18, 20-23]. Nakano *et al*. reported that different pretreatment temperatures may cause different surface properties of ZrO_2 and cause different catalytic activities in the isomerization of 1-butene. The acidic, basic, oxidizing, and reducing properties of ZrO_2 were independent of each other over different calcination temperatures [12]. Cortés-Jácome *et al*. also found that different

calcination temperatures may lead to different structures and electric valence of the W atoms of tungstate ZrO_2, thus caused different catalytic activities in n-hexane isomerization [14]. The structural chemistry of ZrO_2 has been studied by Ho, and Livage *et al*. [11, 24]. However, the relationship between the calcination temperature and the catalytic performance of ZrO_2 based on structural transformation is yet to be understood.

In the present work, ZrO_2 was prepared at different calcination temperatures. The formation of ZrO_2 by dehydration of $Zr(OH)_4$ was studied by thermogravimetric analysis (TGA) and differential scanning calorimetry (DSC). ZrO_2 calcined at various temperatures was characterized by N_2 adsorption, X-ray diffraction (XRD) and Raman spectroscopy. The acidity of ZrO_2 was studied by temperature-programmed desorption of ammonia (NH_3-TPD) and solid-state nuclear magnetic resonance (NMR) spectroscopy. Their catalytic performance has been tested in the dehydration of glucose.

3.2 Experimental

3.2.1 Catalyst preparation

1.2 g of $Zr(OH)_4$ was added to 20 mL of deionized water. The mixture was then put into an ultrasonic bath for 4 h and stirred for 15 h. The resulting materials were dried at 80 °C for 6 h and calcined for 4 h at 300, 400, 700 or 900 °C.

3.2.2 Catalyst characterization

Thermogravimetric analysis (TGA) and differential scanning calorimetry (DSC) of $Zr(OH)_4$ was obtained on a TGA/DSC STAR^e system (Thermo Fisher Scientific) in a nitrogen atmosphere. The sample was heated from 35 to 1000 °C at a ramp rate of 5 °C/min. Powder X-ray diffraction (XRD) patterns were obtained on a PANalytical X'Pert PRO diffractometer using Cu$K\alpha$ radiation

(λ=0.15406 Å) at 45 kV and 40 mA. Diffraction patterns were collected in a continuous scan mode using a 0.03 step size from 10º to 80º (2θ). The surface area, total pore volume and pore size were determined by nitrogen physisorption at -196 ºC in a TriStar II 3020 analyzer (Micromeritics). The sample was pre-treated under vacuum for 8 h at a temperature of 100 °C. The Raman spectra were recorded at room temperature using an IM-52 Portable Raman microspectrometer (Ω Metrohm Raman), equipped with a confocal microscope with a laser 785 nm emission line at a power of 15 mW. The morphology of ZrO_2 calcined at different temperatures was imaged by scanning electron microscopy (JEOL-7100 FESEM) at 15 kV.

The total number of acid sites were determined by NH_3-TPD on a conventional flow apparatus equipped with a thermal-conductivity detector (TCD). In a typical procedure, ZrO_2 was initially degassed at 300 °C for 1 h under a constant helium flow of 50 mL/min. Afterwards, the sample was cooled down to 80 °C and then absorbed NH_3 (10 vol. % in He, 40 mL/min) for 30 min. After saturation, the ammonia supply line was shut off, and helium was purged at 50 mL/min for 30 min to remove the physically absorbed NH_3. Desorption of NH_3 was monitored in the range of 100-1000 °C with a heating rate of 10 °C/min under a constant helium flow of 50 mL/min.

Trimethylphosphine oxide (TMPO) was used as a probe molecule for ^{31}P solid-state NMR spectroscopy. Prior to the NMR investigations, each sample was subjected to a dehydration treatment at 300 °C for 24 h under vacuum (10^{-5} Torr). Loading of the dehydrated catalyst with TMPO was performed inside a glovebox purged with argon by mixing 110 mg of dehydrated catalyst with 10 mg of TMPO in a rotor with 4 mm external diameter, sealed with a KelF cap afterwards. The TMPO loaded sample inside the sealed rotor was then heated for 2 h at 160 °C. Solid-state ^{31}P NMR experiments were carried out on a Bruker DRX 300 spectrometer, at a Larmor frequency of 121.5 MHz and a spinning rate of 10 kHz MAS (magic-angle spinning). The spectra

were recorded with 3 μs irradiation, 10 s relaxation delay and 64 to 256 scans. The ^{31}P chemical shift scale was externally referenced to trimethylphosphate in $CDCl_3$ at 3.0 ppm [25].

3.2.3 Catalytic reaction

The catalytic tests for glucose dehydration were carried out in 25 mL thick-walled glass reactors heated in an oil bath at 170 °C. In a typical experiment, 2 mL of DMSO/H_2O biphasic solution with 3 wt % of glucose and 1 wt % of catalyst were poured into the reactor. At a specific time, the reactors were removed from the oil bath and quenched by submerging the reactors into an ice-water bath. The solution was centrifuged and then diluted using specific mobile phases. Afterwards, the resulting solution was filtered and analyzed by high-performance liquid chromatography (HPLC).

Glucose, levulinic acid and formic acid were quantified by a Biorad HPX87H (300×7.8) column connected to an Agilent 1290 system equipped with a refractive index detector. The mobile phase was 5 mM sulfuric acid and the flow rate was 0.6 mL/min, with a column temperature of 65 °C. HMF was detected by a reversed-phase C18 column connected to an Agilent 1260 system equipped with a UV detector, and the detection wavelength was set as 284 nm. The mobile phase was 20 % (v/v) methanol aqueous solution and the flow rate was 0.6 mL/min, at a column temperature of 30 °C. The conversion of glucose (Equation 3.1), the yield of HMF, levulinic acid and formic acid (Equation 3.2), and the selectivity (Equation 3.3) were calculated as follows:

$$\%\ \text{conversion of reactant} = \frac{C_{reactant,t=o} - C_{reactant}}{C_{reactant,t=0}} \times 100 \qquad (3.1)$$

$$\%\ \text{yield of product } x = \frac{C_x}{C_{reactant,t=0}} \times 100 \qquad (3.2)$$

$$\%\ \text{selectivity of product } x = \frac{C_x}{C_{reactant,t=0} - C_{reactant}} \times 100 \qquad (3.3)$$

Where, C_x is the molar concentration (mol/L) of species *x*.

3.3 Results and discussion

3.3.1 Physicochemical characteristics of ZrO_2

In this research, ZrO_2 remains XRD amorphous when the calcination temperature is 300 °C (Figure 3.1 and Figure A1, Appendix). It was reported that the structure of amorphous ZrO_2 is a two-dimensional model with a thin plate consisting of a layer of zirconium atoms between two oxygen layers [24]. Since amorphous metal oxides are thermodynamically metastable at elevated temperature, crystallization is unavoidable during thermal treatment [26]. In this research, it presents a tetragonal-ZrO_2 (t-ZrO_2) polymorph (JCPDS card no. 79-1763) at the calcination temperature of 400 °C and rapidly transforms into the monoclinic-ZrO_2 (m-ZrO_2) polymorph (JCPDS card no. 83-0942) at higher temperatures. This phenomenon can be clearly observed as the XRD peak assigning to tetragonal-ZrO_2 polymorph at 30^o is decreasing while the peaks corresponding to monoclinic-ZrO_2 at 28^o and 31^o are increasing as calcination temperature increases. The volume fraction of different ZrO_2 polymorphs and the crystallite size of ZrO_2 were investigated according to Scherrer relationship and other literature based on the peaks at the small range of $26\text{-}33^o$ [27].

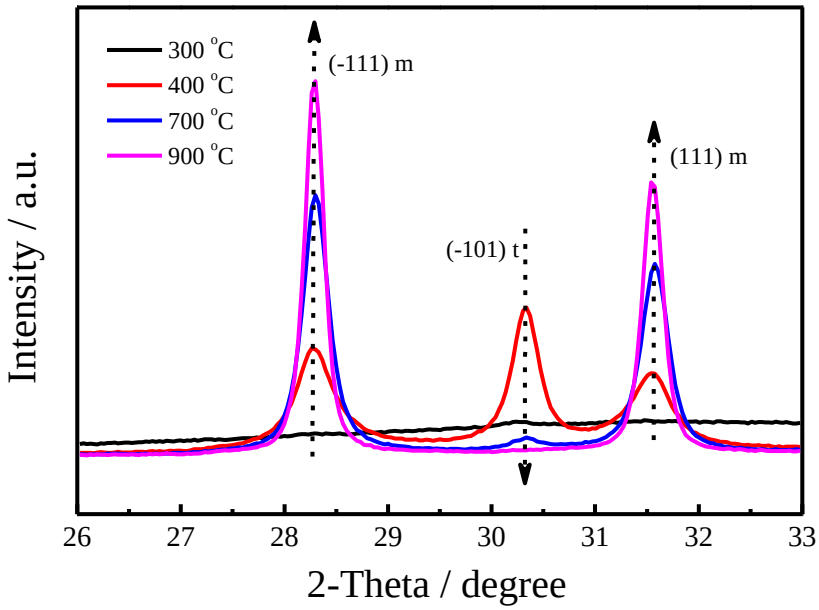

Figure 3.1 XRD patterns of ZrO_2 in the range of 26-33° (m: m-ZrO_2 and t: t-ZrO_2)

As shown in Table 3.1, the volume fraction of t-ZrO_2 in ZrO_2 crystallite is 37.9 % when the calcination temperature is 400 °C, which is much higher than in ZrO_2 calcined at higher temperatures. The phase of t-ZrO_2 is rarely detected at the calcination temperature of 900 °C. It is worth noting that the volume fraction of t-ZrO_2 is decreasing while the crystallite size of t-ZrO_2 is increasing. This is probably because small crystallites of t-ZrO_2 are not as stable as large ones, and they transformed into the m-ZrO_2 first, and only the larger crystallites of t-ZrO_2 are left. The XRD data of ZrO_2 calcined at different temperatures in this research demonstrates a result of sintering, crystallizing, and pore collapsing of ZrO_2 which is in accordance with research from previous literature and also with the TGA and DSC results (Figure A2a and A2b, Appendix) [27].

Table 3.1 BET surface areas and quantitative analysis of the crystallite sizes and volume fractions of different crystalline phases of ZrO_2

Temperature (°C)	BET surface area (m^2/g)	Volume fraction (%)		Crystallite size (nm)	
		t-ZrO_2	m-ZrO_2	t-ZrO_2	m-ZrO_2
300	88.2	-	-	-	-
400	24.2	37.9	62.1	8.2	17.3
700	6.6	3.1	96.9	29.8	27.1
900	1.8	-	100	-	38.3

Figure 3.2 shows the N_2 adsorption-desorption isotherms of ZrO_2 calcined at different temperatures, and the BET surface areas of ZrO_2 are presented in Table 3.1. ZrO_2 calcined at 300 °C presents an isotherm curve of type II, corresponding to nonporous materials [28]. The decrease of BET surface area, and the deformation of isotherm curves and the appearance of hysteresis loops at higher temperatures corroborate the phenomenon of crystallization and particle growth of ZrO_2. The isotherms of ZrO_2 calcined at 700 and 900 °C are of type III with smaller surface areas [29].

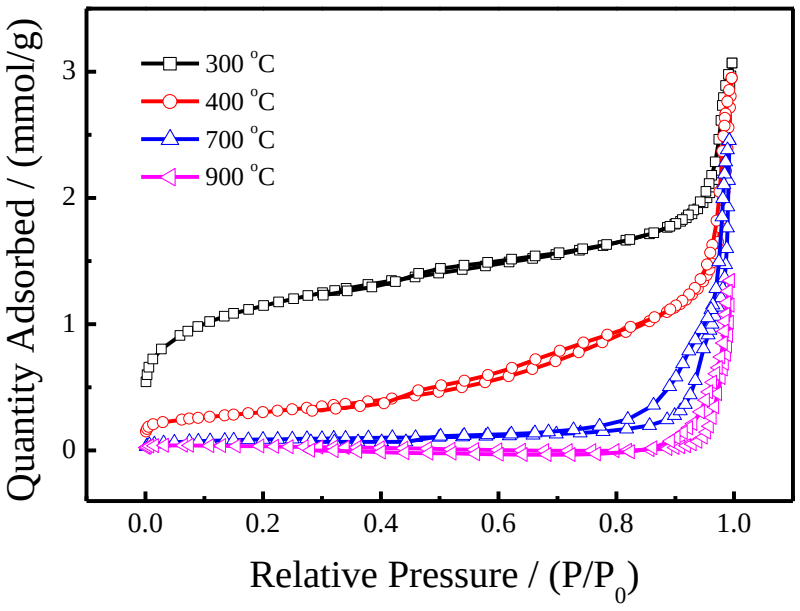

Figure 3.2 N_2 adsorption-desorption isotherms of ZrO_2

Figure 3.3 displays the Raman spectra of ZrO_2 calcined at different temperatures. The Raman bands of ZrO_2 calcined at 300 and 400 °C are very broad at 379(w), 476-520(w), 702(w) and 945(w) cm^{-1}, which are in accordance with mostly amorphous ZrO_2 [27]. As the calcination temperature increases to 700 and 900 °C, the Raman bands of ZrO_2 exhibit totally different patterns at 221(w), 304(w), 333(m), 346(m), 381(m), 474(s), 501(w), 534(w), 557(w), 614(m), 636(m), 755(w), 1372(w), 1430(w), 1529(m), 1585(w) and 1686(w) cm^{-1}, in agreement with the m-ZrO_2 [16]. In view of the Raman results in this research, increasing the calcination temperature accelerates the crystallization of ZrO_2 and tends to give rise to much sharper Raman bands. The disappearance of broad bands and the growth of new bands also reflect the process of the crystallization of ZrO_2. It also shows that part of ZrO_2 calcined at 400 °C may be still in amorphous state due to its similar Raman bands with ZrO_2 calcined at 300 °C.

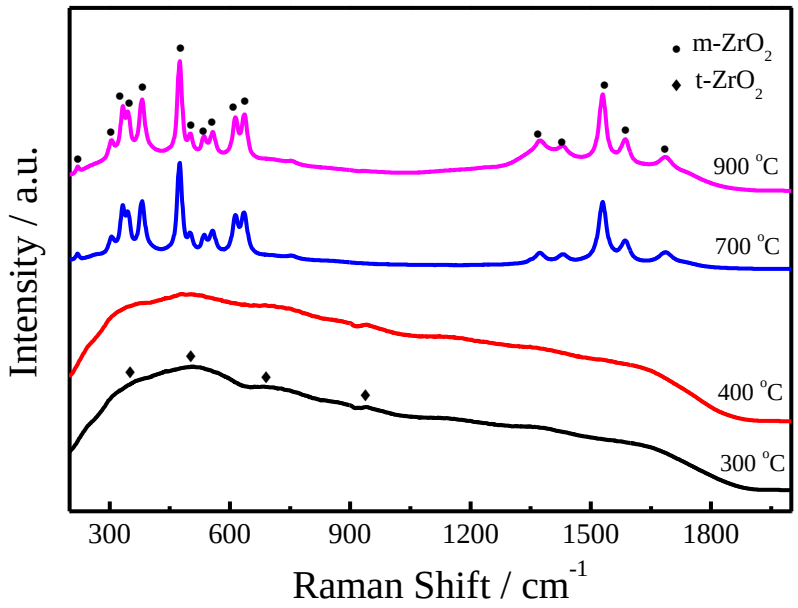

Figure 3.3 Raman spectra (785 nm) of ZrO_2

The morphology of ZrO_2 calcined at different temperatures is displayed in Figure 3.4. Generally, crystallization is divided into three different stages: nucleation, growth and coarsening [26]. The

appearance of small particles shown in ZrO_2 at 400 ^oC demonstrates the occurrence of nucleation process. However, except for the small particles, the morphology of ZrO_2 calcined at 400 ^oC also shows some similarity to the ZrO_2 calcined at 300 ^oC, indicating that there may be still some amorphous ZrO_2 in the sample calcined at 400 ^oC. As the calcination temperature increases, a large number of small crystallites grow into larger ones during the coarsening process, leading to a larger particle size. Grain boundaries are clearly observed in SEM micrographs of ZrO_2 calcined at 700 and 900 ^oC. Due to the fact that all nanocrystals are randomly oriented in space, the coarsening of ZrO_2 is random and disordered, resulting in irregular boundaries [26]. Since further thermal treatment at higher temperature will intensify the coarsening process, the crystallite size of ZrO_2 calcined at 900 ^oC is much larger than the ZrO_2 calcined at 700 ^oC. Different morphologies and crystallization of ZrO_2 may contribute different fluxionality around the catalyst and affect the contact between the catalyst and the reactant, thus affect the catalytic performance in the reaction. It may also cause different acid strengths and distributions, thus have a strong influence on the catalytic performance in the reaction.

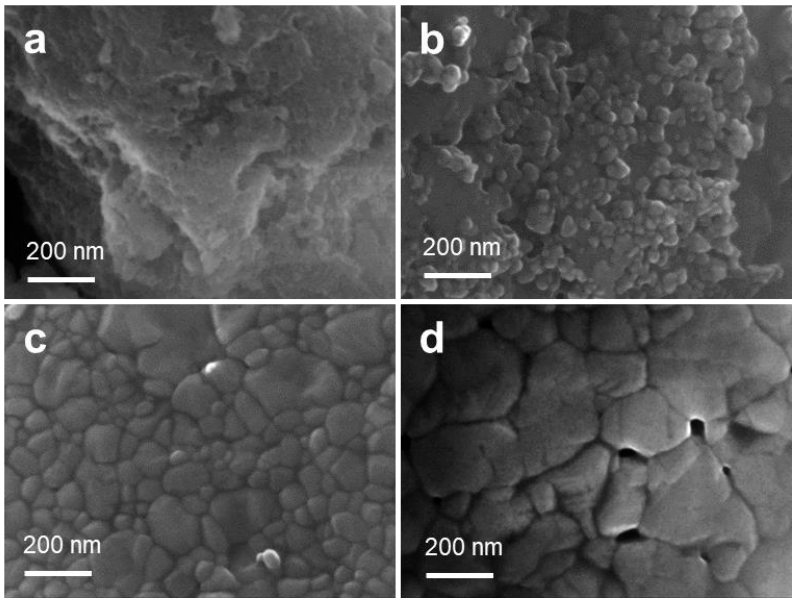

Figure 3.4 SEM micrographs of ZrO_2: (a) 300 °C; (b) 400 °C; (c) 700 °C; (d) 900 °C

3.3.2 Acidity characterization of ZrO_2

NH_3-TPD can provide qualitative information to the overall concentration and strength of acid sites in catalysts, as shown in Figure 3.5. In general, low-temperature desorption peaks (<150 °C) reflect the evolution of physical absorption and hydrogen-bonded ammonia or of weakly held protonated ammonia, and higher-temperature desorption peaks (≥150 °C) correspond to desorption of ammonia coordinated to Lewis acid sites (LAS) and of strongly held ammonia protonated on Brønsted acid (BAS) sites [30]. The TPD profiles of ZrO_2 calcined at 300 °C reveals the coexistence of a broad distribution of acid strengths since the desorption of ammonia at different temperatures is detected. It is conceivable that the peaks at low desorption temperatures are mainly due to desorption of ammonia from BAS while the peaks at higher desorption temperatures are ascribed to desorption of ammonia from LAS.

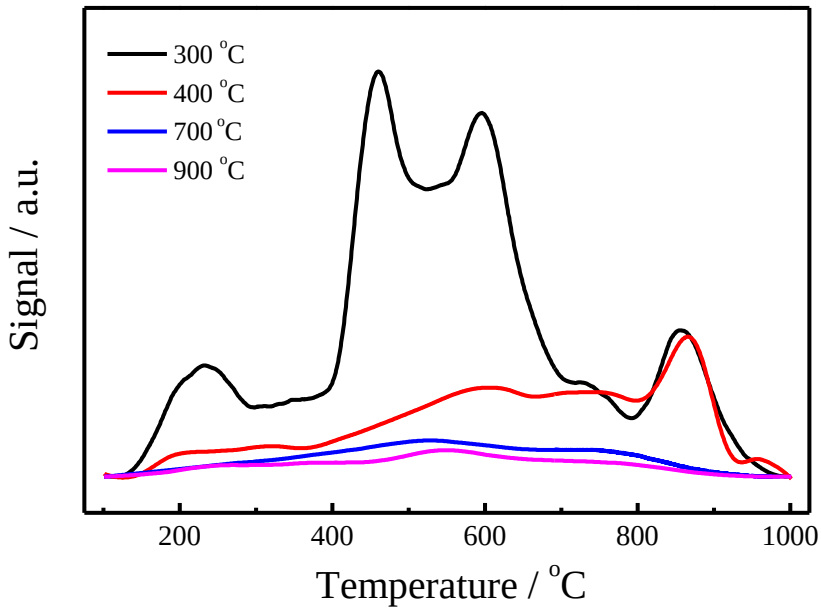

Figure 3.5 NH_3-TPD profiles of ZrO_2

Increasing the calcination temperature of ZrO_2 leads to a distinct decrease in acid concentration and shows a low signal of ammonia desorption. Other studies previously also found that the total acid site concentration decreased with increasing calcination temperature of tungsten ZrO_2, and it appeared to correlate with the loss of surface area [18]. Since the profiles are likely to be overlapped, it is not easy to qualitatively analyze the distribution of the acidity of ZrO_2. Therefore, the surface acidity was calculated as total acidity and expressed in mmol of NH_3 desorbed per gram of catalyst as shown in Table 3.2.

Table 3.2 Quantitative analysis of acid sites in ZrO_2 according to NH_3-TPD profiles and ^{31}P MAS NMR spectra, and turnover frequencies (TOFs) of the glucose conversion on ZrO_2

Temperature	Chemical shift (ppm)[a]				Acid amount (mmol/g cat.)[b]				TOFs
(°C)	39.4	42.4	44.0	60.0	BAS	LAS	Total	B/L	(h^{-1})[c]
300	29.1%	45.3%	-	25.6%	0.200	0.580	0.780	0.345	5.2
400	-	95.7%	-	4.3%	0.013	0.288	0.301	0.045	2.9
700	-	93.3%	6.7%	-	-	0.102	0.102	-	10.2
900	-	89.2%	10.8%	-	-	0.069	0.069	-	8.7

[a.] For comparison, Gaussian-Lorentz simulation results obtained for the samples representing TMPO adsorbed on Brønsted and/or Lewis acid sites (denoted by chemical-shift values) with practically the same chemical shift are aligned in the same column.

[b.] The total acidity was estimated from the NH_3-TPD results, and the BAS and LAS were calculated based on the ^{31}P MAS NMR results, depending on total acidity.

[c.] TOFs were calculated from the total acidity and initial glucose conversion (~10%).

^{31}P MAS NMR of adsorbed TMPO is a useful way to reveal the distributions and strengths of different acid sites. After the TMPO is adsorbed onto an acid catalyst, the base probe molecule tends to form hydrogen bonds with the acid sites [31, 32]. As a result, the density of the electrons surrounding the ^{31}P nucleus neighboring to the oxygen atom of the phosphine oxides decreases with increasing strength of the acid sites, which in turn causes the ^{31}P resonance to shift downfield

[33]. From another aspect, having a downfield shift of ^{31}P MAS NMR could reflect sites that possess a higher acidic strength. According to ^{31}P chemical shift, BAS and LAS are easy to differentiate, and variations in acid strength of both sites can be displayed (Scheme 3.1). The ^{31}P MAS NMR spectra of ZrO_2 are shown in Figure 3.6, and the chemical shifts, distributions and concentrations of acid sites are reported in Table 3.2.

In this research, ZrO_2 calcined at 300 °C displays signals in the spectrum at δ_{31P}=42.4 and 39.4 ppm which can be assigned to different LAS [31, 34]. Simultaneously, another broad peak at δ_{31P}=60.0 ppm is detected and this could be identified as resonance with H^+ attached to the TMPO species due to the presence of BAS, forming $TMPOH^+$ attached to a bridging oxygen atom [31]. Increasing the calcination temperature of ZrO_2 leads to a distinct decrease in BAS, and this type of acid sites can be hardly observed in the sample of ZrO_2 calcined at 700 °C. On the other hand, there is also a diminishing trend of the total number of acid sites as the calcination temperature increases. It is interesting to find that the signal at δ_{31P}=39.4 ppm for ZrO_2 calcined at 300 °C disappears when the calcination temperature goes up to 400 °C and a new peak of LAS appears with a downfield shift at δ_{31P}=44.0 ppm for the ZrO_2 catalyst calcined at 700 °C. It is speculated that one kind of LAS of ZrO_2 shifts downfield as the calcination temperature increases because of the partial redistribution of ZrO_2 in the crystallites, while the main LAS of ZrO_2 remain unchanged. This hypothesis is further confirmed when we note that the proportion of the signal at δ_{31P}=44.0 ppm increases when the calcination temperature reaches 900 °C. The result in this research is somewhat different from those of previous work and this may be due to different precursors and synthesis methods [17, 19]. A similar result is also found in another report, which showed that progressively higher temperatures for the catalyst of sulfated zirconia resulted in the development of at least three types of LAS, along with a decrease in the concentration of BAS [35].

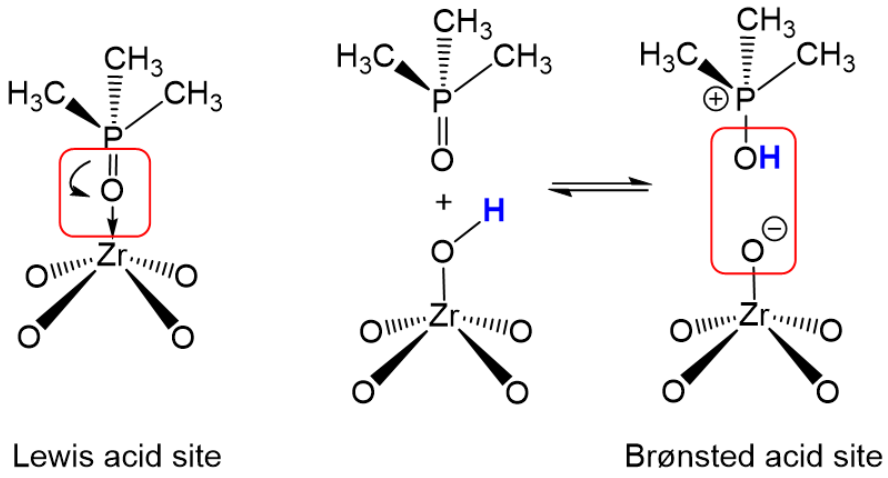

Scheme 3.1 Lewis and Brønsted acid sites in ZrO_2

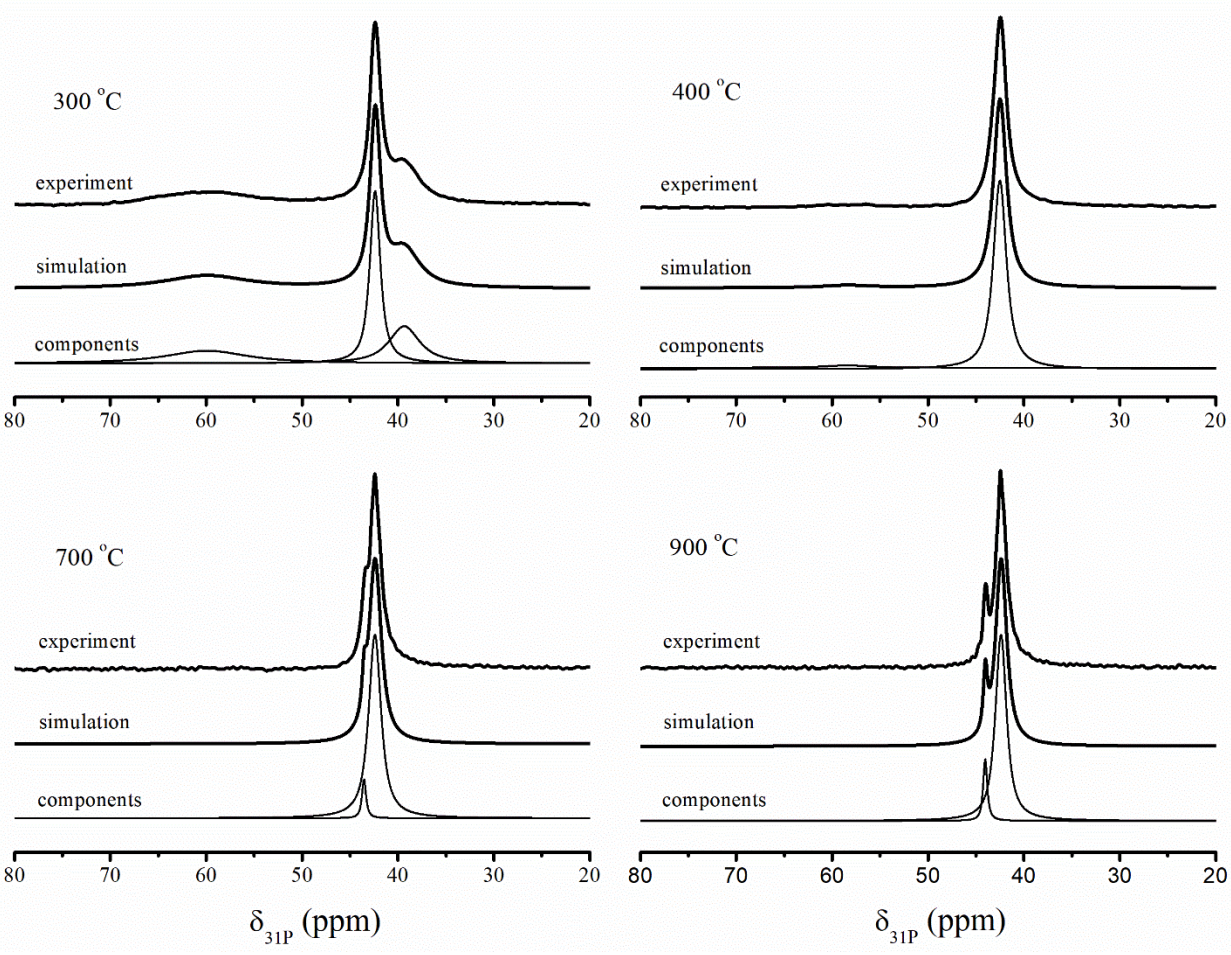

Figure 3.6 ^{31}P MAS NMR spectra of ZrO_2

3.3.3 Catalytic activity of ZrO_2

Figure 3.7 shows the glucose conversion at 170 °C over ZrO_2 calcined at different temperatures. The HMF yield and selectivity are presented in Figure 3.8a and 3.8b. The turnover frequencies (TOFs) were also calculated based on initial glucose conversion as shown in Table 3.2. It is widely known that the acidity of the catalyst plays a crucial role in the acid-catalyzed reaction because it is essential to lower the activation energy barrier by proceeding via protonated intermediates [2]. In this research, different forms of ZrO_2 can achieve an HMF yield of about 35 % with an HMF selectivity of about 40 % (Figure 3.8a and 3.8b), showing similar performance to using a catalyst of the hydrotalcite/Amberlyst system and a little bit lower than using the SO_4^{2-}/ZrO_2-Al_2O_3 system [36, 37]. After 9 h of reaction, the glucose is nearly fully converted. Note that all the HMF yields catalyzed by different forms of ZrO_2 decrease soon after reaching a peak point, due to the further rehydration of HMF to levulinic acid (LA) and formic acid (FA). On the other hand, it seems that the rehydration of HMF to LA and FA happens simultaneously as HMF is generated since the LA yield increases steadily as the HMF yield increases and it still keeps a rising trend when the HMF yield starts to decrease (Figure 3.8, and Figure A3, Appendix). FA is detected mainly in the late reaction process and the yield is very low compared with LA yield. This is probably ascribed to the further reaction of FA with other chemicals in the reaction system (Figure A4, Appendix).

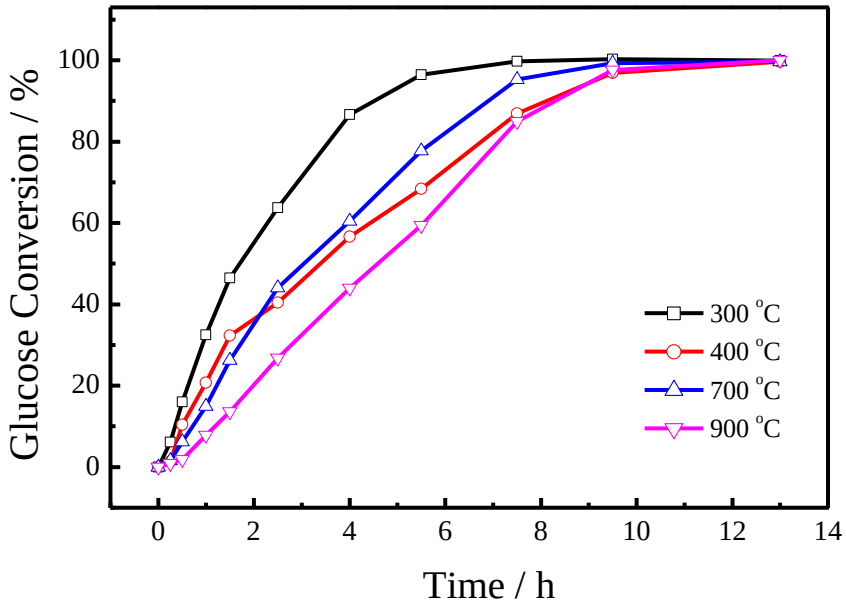

Figure 3.7 Glucose conversion over ZrO_2 at 170 °C

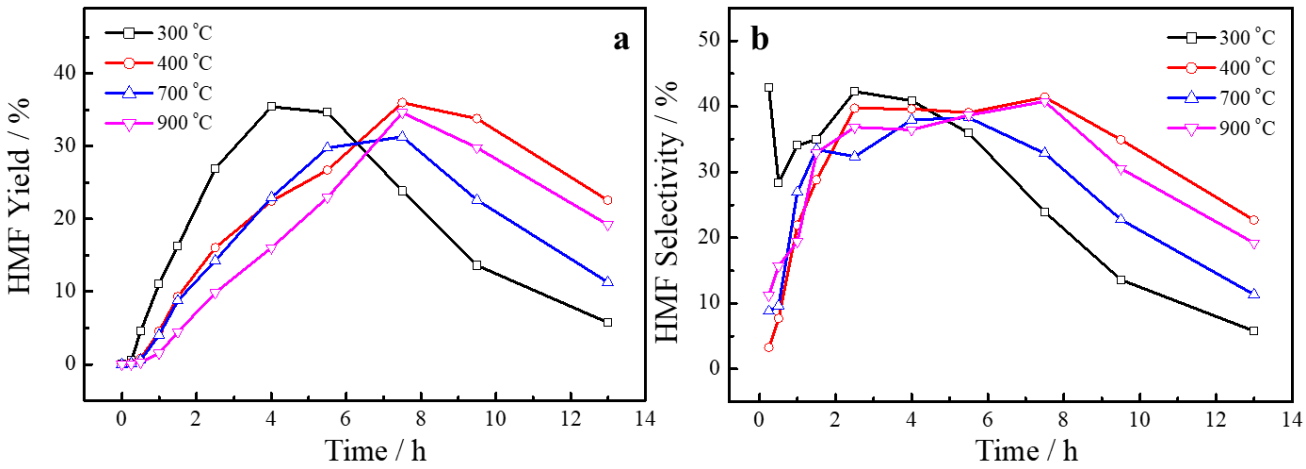

Figure 3.8 HMF yield (a), and HMF selectivity (b)

A proposed reaction pathway of glucose conversion is depicted in Scheme 3.2. Earlier studies reported that both LAS and BAS of the catalyst are active in the reaction, and a LAS is generally required for glucose isomerization to fructose, followed by a BAS catalyzed dehydration of fructose to HMF and further rehydration to LA and FA [1, 2]. Since the ZrO_2 calcined at 300 °C possesses more acid sites than other ZrO_2, it displays a better performance during the reaction. The

presence of BAS may also play a significant role in the reaction as BAS is primarily responsible for the fructose dehydration to HMF [1, 2]. It is noteworthy that different forms of ZrO_2 resulted in different reaction rates but didn't change the maximal HMF yield and selectivity, suggesting that different forms of ZrO_2 can alter the reaction time to reach the maximum yield, but may have a limited function on selectivity. Such results are similar to other published studies [38].

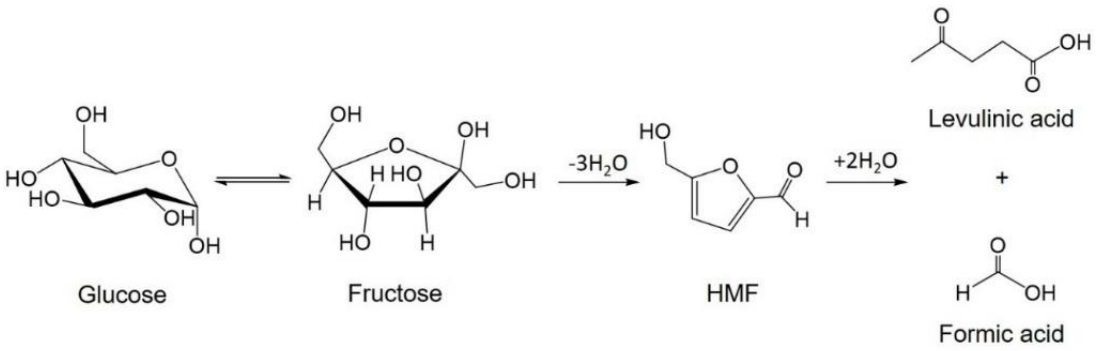

Scheme 3.2 Proposed reaction pathway for HMF formation from glucose

It is likely that the main obstacle for using heterogeneous catalysts in a reaction is the limited accessibility of the reactive sites. Another influence factor for the reaction is that the resulting products must diffuse away from the catalyst active site to be replaced by the next reactant during the reaction, thus fluxionality around the catalysts is also very important [17]. As typical in this reaction, significant carbon-based unknown products are noticed based on the color change of the reaction liquid and generation of dark-colored tarry solids. As reported before, most of the carbon loss during the reaction is attributed to the formation of soluble polymers, insoluble humins, and dark-colored tarry solids [1, 5]. The increase of humins and dark-colored tarry solids produced in the reaction system may block and hinder the reactants from coming to the surface of the catalysts, thus retarding the reaction process. The TOFs of ZrO_2 calcined at 700 and 900 °C turn out to be higher than the TOFs of ZrO_2 calcined at 300 and 400 °C. The overall HMF yield in this research

is low compared with many homogenous catalysts such as $CrCl_2$, $SnCl_2$, and $AlCl_3$, which can achieve a higher HMF yield [5]. However, a heterogeneous catalyst possesses many advantages over a homogenous catalyst because of its simplicity and versatility of process engineering, and being easier to recover and reuse, fewer reactor and plant corrosion problems, and environmentally safe disposal [39]. Taking this into account, ZrO_2 could be regarded as a promising catalyst for glucose conversion.

3.4 Conclusion

ZrO_2 was synthesized at different calcination temperatures. ZrO_2 is in an amorphous state when the calcination temperature is 300 °C, and it starts to crystallize with increasing calcination temperature, which causes a decreasing BET surface area and an increasing crystallite size. It is mainly present in the metastable t-ZrO_2 at 400 °C and rapidly transforms into the thermodynamically stable m-ZrO_2 when the calcination temperature is higher than 700 °C. The t-ZrO_2 phase is rarely detected at the calcination temperature of 900 °C. Quantitative evaluation of acidity by NH_3-TPD and solid-state NMR spectroscopy shows that ZrO_2 possesses both BAS and LAS when the calcination temperature is 300 or 400 °C. Increasing the calcination temperature of ZrO_2 leads to a distinct decrease in BAS, along with a decrease in the total number of acid sites. At the same time, a new type of LAS appears with a downfield shift. For dehydration of glucose catalyzed by different forms of ZrO_2, it is suggested that the strong acidity of the catalyst plays an important role during the reaction and the BAS may be another influence factor. On the other hand, HMF undergoes further rehydration into LA and FA as the reaction proceeds. In this research, ZrO_2 calcined at 300 °C, which possesses more BAS and LAS than other ZrO_2, shows a better catalytic performance in glucose conversion. Different forms of ZrO_2 resulted in different reaction

rates but didn't change the maximum HMF yield and selectivity. ZrO_2 can convert nearly 100 % of the glucose with an HMF selectivity of about 40 %.

References

[1] Choudhary, V.; Mushrif, S. H.; Ho, C.; Anderko, A.; Nikolakis, V.; Marinkovic, N. S.; Frenkel, A. I.; Sandler, S. I.; Vlachos, D. G. *J. Am. Chem. Soc.* **2013**, *135*, 3997-4006.

[2] Wang, T.; Nolte, M. W.; Shanks, B. H. *Green Chem.* **2014**, *16*, 548-572.

[3] Climent, M. J.; Corma, A.; Iborra, S. *Green Chem.* **2011**, *13*, 520-540.

[4] Choudhary, V.; Pinar, A. B.; Lobo, R. F.; Vlachos, D. G.; Sandler, S. I. *ChemSusChem* **2013**, *6*, 2369-2376.

[5] Putten, R.; Waal, J. C.; Jong, E.; Rasrendra, C. B.; Heeres, H. J.; Vries, J. G. *Chem. Rev.* **2013**, *113*, 1499-1597.

[6] Zhang, J.; Weitz, E. *ACS Catal.* **2012**, *2*, 1211-1218.

[7] Pagán-Torres, Y. J.; Wang, T.; Gallo, J. M. R.; Shanks, B. H.; Dumesic, J. A. *ACS Catal.* **2012**, *2*, 930-934.

[8] Osatiashtiani, A.; Lee, A. F.; Granollers, M.; Brown, D. R.; Olivi, L.; Morales, G.; Melero, J. A.; Wilson, K. *ACS Catal.* **2015**, *5*, 4345-4352.

[9] Qi, X.; Watanabe, M.; Aida, T. M.; Smith, J. R. L. *Green Chem.* **2008**, *10*, 799-805.

[10] Jain, A.; Shore, A. M.; Jonnalagadda, S. C.; Ramanujachary, K. V.; Mugweru, A. *Appl. Catal. A: Gen.* **2015**, *489*, 72-76.

[11] Ho, S. M. *Mater. Sci. Eng.* **1982**, *54*, 23-29.

[12] Nakano, Y.; Iizuka, T.; Hattori, H.; Tanabe, K. *J. Catal.* **1979**, *57*, 1-10.

[13] Parvulescu, V. I.; Bonnemann, H.; Parvulescu, V.; Endruschat, U.; Rufinska, A.; Lehmann, C. W.; Tesche, B.; Poncelet, G. *Appl. Catal. A: Gen.* **2001**, *214*, 273-287.

[14] Cortés-Jácome, M. A.; Angeles-Chavez, C.; López-Salinas, E.; Navarrete, J.; Toribio, P.; Toledo, J. A. *Appl. Catal. A: Gen.* **2007**, *318*, 178-189.

[15] Jiménez-Morales, I.; Santamaría-González, J.; Jiménez-López, A.; Maireles-Torres, P. *Fuel* **2014**, *118*, 265-271.

[16] Massa, M.; Andersson, A.; Finocchio, E.; Busca, G.; Lenrick, F.; Wallenberg, L. R. *J. Catal.* **2013**, *297*, 93-109.

[17] Kuo, I. J.; Suzuki, N.; Yamauchi, Y.; Wu, K. C. W. *RSC Adv.* **2013**, *3*, 2028-2034.

[18] Lopez, D. E.; Suwannakarn, K.; Bruce, D. A.; Goodwin-Jr, J. G. *J. Catal.* **2007**, *247*, 43-50.

[19] Ginjupalli, S. R.; Mugawar, S.; Rajan, P.; Balla, P. K.; Komandur, V. R. C. *Appl. Surf. Sci.* **2014**, *309*, 153-159.

[20] Chen, Y. F.; Lee, C. Y.; Yeng, M. Y.; Chiu, H. T. *J. Cryst. Growth* **2003**, *247*, 363-370.

[21] Tran, M. T.; Gnep, N. S.; Guisnet, M. *Appl. Catal. A: Gen.* **1998**, *171*, 207-217.

[22] Chan, S. S.; Wachs, I. E.; Murrell, L. L.; Dspenziere-Jr, N. C. *J. Catal.* **1985**, *92*, 1-10.

[23] Yu, J.; Wang, B. *Appl. Catal. B: Environ.* **2010**, *94*, 295-302.

[24] Livage, J.; Doi, K.; Mazieres, C. *J. Am. Ceram. Soc.* **1968**, *51*, 349-353.

[25] Streck, R.; Barnes, A. J. *Spectrochim. Acta, Part A* **1999**, *55*, 1049-1057.

[26] Li, D.; Zhou, H.; Honma, I. *Nat. Mater.* **2004**, *3*, 65-72.

[27] Ross-Medgaarden, E. I.; Knowles, W. V.; Kim, T.; Wong, M. S.; Zhou, W.; Kiely, C. J.; Wachs, I. E., *J. Catal.* **2008**, *256*, 108-125.

[28] Sing, K. S. W.; Everett, D. H.; Haul, R. A. W.; Moscou, L.; Pierotti, R. A.; Rouquerol, J.; Siemieniewska, T. *Pure Appl. Chem.* **1984**, *57*, 603-619.

[29] Cai, W.; Zhong, Q.; Zhang, S.; Zhang, J. *RSC Adv.* **2013**, *3*, 7009.

[30] Baertsch, C. D.; Soled, S. L.; Iglesia, E. *J. Phys. Chem. B* **2001**, *105*, 1320-1330.

[31] Rakiewicz, E. F.; Peters, A. W.; Wormsbecher, R. F.; Sutovich, K. J.; Muller, K. T. *J. Phys. Chem. B* **1998**, *102*, 2890-2896.

[32] Zhao, Q.; Chen, W. H.; Huang, S. J.; Wu, Y. C.; Lee, H. K.; Liu, S. B. *J. Phys. Chem. B* **2002**, *106*, 4462-4469.

[33] Chen, W. H.; Ko, H. H.; Sakthivel, A.; Huang, S. J.; Liu, S. H.; Lo, A. Y.; Tsai, T. C.; Liu, S. B. *Catal. Today* **2006**, *116*, 111-120.

[34] Sutovich, K. J.; Peters, A. W.; Rakiewicz, E. F.; Wormsbecher, R. F.; Mattingly, S. M.; Mueller, K. T. *J. Catal.* **1999**, *183*, 155-158.

[35] Lunsford, J. H.; Sang, H.; Campbell, S. M.; Liang, C. H.; Anthony, R. G. *Catal. Lett.* **1994**, *27*, 305-314.

[36] Ohara, M.; Takagaki, A.; Nishimura, S.; Ebitani, K. *Appl. Catal. A: Gen.* **2010**, *383*, 149-155.

[37] Yan, H.; Yang, Y.; Tong, D.; Xiang, X.; Hu, C. *Catal. Commun.* **2009**, *10*, 1558-1563.

[38] Xiong, X.; Yu, I. K. M.; Chen, S. S.; Tsang, D. C. W.; Cao, L.; Song, H.; Kwon, E. E.; Ok, Y. S.; Zhang, S.; Poon, C. S. *Catal. Today* **2018**, *314*, 52-61.

[39] Corma, A. *Curr. Opin. Solid St. M.* **1997**, *2*, 63-75.

Chapter 4 Boosting the formation of Brønsted acid sites on flame-made WO_x/ZrO_2 for glucose conversion

4.1 Introduction

Rapid rising of the global population has led to tremendous challenges for mankind caused by the limited sources of raw materials such as fossil fuels, producing environmental pollution and global warming by its consumption [1, 2]. Hence, a sustainable future is imperative and it has to be implemented based on renewable feedstocks rather than fossil fuels [3-6]. With the advances in biomass utilization technologies, biomass resources have become a prospective alternative feedstock for the production of fuels and useful chemicals [7, 8]. In this regard, glucose, one of the most common carbohydrates, has gained much attention as a promising biomass feedstock due to its low cost and great abundance [9]. Substantial efforts have been mostly focused on its dehydration to 5-hydroxylmethylfurfural (HMF), a versatile and multifunctional compound, which can be converted into a variety of fine chemicals and liquid biofuels [10-13]. The potential of HMF to replace petroleum-based building blocks makes it a key compound that could contribute to solving some important current issues [1, 2, 6]. Up to date, one of the biggest challenges of glucose to HMF conversion is its selectivity, especially in the case of heterogeneous catalysis.

According to the widely accepted mechanism, both Lewis (LAS) and Brønsted acid sites (BAS) in the catalyst are active in the reaction, with LAS generally responsible for the glucose isomerization to fructose, followed by BAS catalyzed dehydration of fructose to HMF, and further rehydration to levulinic acid and formic acid [8, 9, 14]. Regarding the catalyst design, the total acidity is considered as a primary factor, but the specific concentration of LAS and BAS, respectively, may also affect the reaction significantly. Though LAS are very important for the

start of this cascade process, the reversible isomerization of glucose to fructose renders the prediction of the distribution of the final products difficult. It has been reported that BAS play a crucial role in this reaction by driving the reaction to HMF direction [8].

Unlike other techniques such as wet-chemical synthesis, chemical liquid deposition, and atomic layer deposition, flame spray pyrolysis (FSP) is a single-step method combining synthesis and calcination that facilitates the production of thermally stable nanoparticles in milliseconds [15-17]. With great control over particle size, morphology, composition, and other physicochemical properties, FSP has been demonstrated to be a versatile technique favorable for catalyst development and production [16, 18-20]. Especially, due to the use of high temperature (up to 2000 K) and rapid quenching, FSP facilitates the synthesis of materials dominated by metastable phases and polymorphs [18, 21, 22]. It has been reported that FSP enables the synthesis of catalysts with higher density of BAS compared to other synthesis techniques [21, 23, 24]. Furthermore, this technique has been used at a production level of millions of tons per year in various industries valued at $15 billion each year, making it scalable and profitable [22, 25]. It is believed that with the fast evolution of this technique, FSP would play a crucial role in the future catalyst industry.

To date, tungstate-zirconium oxides (WO_x/ZrO_2) have received considerable attention as solid acid catalysts due to the strong acidity and remarkable stability [26-28]. They show excellent activity in various important reactions, such as aldoxime dehydration, glycerol dehydration, alkynes hydration, n-pentane isomerization, and n-hexane isomerization [29-32]. There are some studies about multifunctional FSP-made materials based on zirconia or tungsten oxide [33-35]. Mueller *et al*. reported a high production rate of FSP-made zirconia nanoparticles up to 600 g/h, with good control of particle size and crystal structure [36]. Pokhrel *et al*. successfully synthesized ultrafine single crystalline, single-phase tungsten oxide nanomaterials using the FSP technique [37].

Boningari *et al*. investigated the low-temperature selective catalytic reduction of NO with ammonia in the presence of excess oxygen by FSP-made V/ZrO_2 and showed that doping with tungsten strongly enhances the reactive lattice oxygen content, thus improving the material's activity resulting in ~98 % conversion in the temperature range of 180-240 ^oC [38]. Though WO_x/ZrO_2 has been widely known for its great catalytic performance, the acidity of the FSP-WO_x/ZrO_2 and its application in glucose conversion are yet to be understood.

With this in mind, we synthesized novel WO_x/ZrO_2 catalysts by single-step FSP. Using this high-throughput technique, we aimed to prepare WO_x/ZrO_2 mixed oxides with high BAS population density and uniform distribution of both metals within the material structure. As a reference, samples with the same composition were prepared by conventional impregnation (IM) for comparison. The materials were characterized by N_2 adsorption, X-ray diffraction (XRD), Raman spectroscopy, transmission electron microscopy (TEM), and X-ray photoelectron spectroscopy (XPS). The acidity of these catalysts was quantitatively investigated by temperature-programmed desorption of ammonia (NH_3-TPD) and solid-state nuclear magnetic resonance (NMR) spectroscopy, and their catalytic performance was tested in the dehydration of glucose to HMF.

4.2 Experimental

4.2.1 Catalyst preparation

WO_x/ZrO_2 by flame spray pyrolysis method (FSP-WO_x/ZrO_2): Rapid and scalable single-nozzle FSP was used for the catalyst synthesis [17]. The precursor solutions for the preparation of FSP-WO_x/ZrO_2 were obtained via dissolving appropriate amount of zirconium propoxide and tungsten ethoxide in toluene (0.5 M concentration by metal), followed by a filtration step using a glass filter. Then, the precursor solutions were pumped through a capillary at a rate of 5 mL/min, and nebulized at 5 L/min O_2. Afterwards, the resulting spray was ignited via an annular supporting

methane/oxygen flame (1.5/0.9 L/min). Particles were collected on a cooled Whatman GF6 filter (257 mm diameter), and a Busch SV 1040C vacuum pump aiding for the recovery of the particles. The resulting powders are named as W/Zr 1/10-FSP and W/Zr 1/4-FSP, representing the W/Zr atom ratio of 1/10 and 1/4, respectively.

WO_x/ZrO_2 by impregnation method (IM-WO_x/ZrO_2): similar to the research from Kourieh *et al*. [39]. $Zr(OH)_4$ was impregnated with 0.01 g/mL $(NH_4)_6H_2W_{12}O_{40}\cdot 4H_2O$. The mixture was immersed in an ultrasonic bath for 4 h and then stirred overnight. The resulting material was dried at 80 °C for 6 h and then calcined at 700 °C for 4 h. The final products were designated W/Zr 1/10-IM and W/Zr 1/4-IM, corresponding to the W/Zr atom ratio of 1/10 and 1/4, respectively. The Zr contents are constant for all the four samples, and the W concentration was varied according to the atomic ratio.

4.2.2 Catalyst characterization

Powder X-ray diffraction (XRD) patterns were carried out on a PANalytical X'Pert PRO diffractometer using Cu$K\alpha$ radiation (λ=0.15406 Å) at 45 kV and 40 mA. A continuous scan mode (0.03 step size from the 2θ of 10^o to 80^o) was applied for collecting the diffraction patterns. N_2-physisorption isotherms were tested at the temperature of 77 K (by liquid nitrogen) on a TriStar II 3020 analyzer (Micromeritics). The surface areas were calculated using the BET method, and the pore sizes and pore volumes were determined by Barret-Joyner-Halenda theory. Before measurements, the samples were pre-treated under vacuum for 8 h at 100 °C. The Raman spectra were obtained by an IM-52 Portable Raman microspectrometer (Ω Metrohm Raman) equipped with a confocal microscope with a laser 785 nm emission line at 15 mW. The morphology and element distribution of WO_x/ZrO_2 were examined using a JEOL 2100F transmission electron microscopy (TEM) operating at 200kV. The surface chemical composition of WO_x/ZrO_2 was

determined by X-ray photoelectron spectroscopy (XPS) on an ESCALAB250Xi spectrometer (Thermo Scientific, USA) equipped with an Al Kα X-ray radiation source (E=1486.68 EV). Binding energies were calibrated to the C 1s peak at 284.8 eV. Proper Gaussian-Lorentzian distributions were employed for the fitting of each peak in the XPS spectra.

The total numbers of acid sites were determined by NH_3-TPD on a conventional flow apparatus equipped with a thermal conductivity detector (TCD). The testing materials were initially degassed at 500 °C for 1 h under helium atmosphere at a flow rate of 50 mL/min. Then, the samples were cooled down to 100 °C and exposed to NH_3 (10 vol. % in He, 40 mL/min) for 45 min. When it reached to the saturation state, the NH_3 supply line was shut off and helium was again purged for 1h to remove the physically adsorbed NH_3. Afterwards, the desorption of NH_3 was monitored from 150 to 700 °C at a heating rate of 5 °C/min under helium atmosphere at a flow rate of 50 mL/min.

^{31}P solid-state NMR spectroscopy was used to further differentiate the LAS and BAS, and the acid strength of each acid. The probe molecule for the test in this research is trimethylphosphine oxide (TMPO). For the pre-treatment of the materials, each sample was dehydrated at 300 °C for 24 h under vacuum. Loading TMPO on the dehydrated catalyst was performed inside a glovebox purged with argon by mixing 10 % (wt/wt) of TMPO in a 4-mm rotor, sealed with a KelF cap afterwards. The sealed sample loaded with TMPO was then heated at 160 °C for 2 h under argon flow. Solid-state ^{31}P NMR experiments were carried out on a Bruker DRX 300 spectrometer, at a Larmor frequency of 121.5 MHz, and a spinning rate of 10 kHz MAS (magic-angle spinning). The spectra were recorded with 1.95 μs 90^o pulse, 10 s relaxation delay, and 64 to 256 scans. The ^{31}P chemical shifts were externally referenced to K_2HPO_4 at 3.0 ppm [25].

4.2.3 Catalytic reaction

The reaction of glucose conversion was carried out in 25 mL thick-walled glass reactors at 170 °C in an oil bath. In a typical procedure, 2 mL of DMSO/H_2O solution with 3 wt % of glucose and 1 wt % of catalyst was poured into the glass reactor. During the reaction, the reactors were removed from the oil bath and quenched by submerging the reactors in an ice-water bath at a specific time. The solution was then centrifuged, and the supernatant liquid was taken and diluted with specific mobile phases. Afterward, the resulting solution was filtered and analyzed by high-performance liquid chromatography (HPLC).

Glucose, formic acid, and levulinic acid were quantified via HPLC. The column used was Biorad HPX87H (300×7.8) and the system was Agilent 1290 equipped with a refractive index detector. The testing condition was 65 °C as the column temperature and 5 mM sulfuric acid as the mobile phase, with a flow rate of 0.6 mL/min. On the other hand, HMF was determined by a reversed-phase C18 column connected to an Agilent 1260 system equipped with a UV detector, and the detection wavelength was set as 284 nm. In this test, 20 % (v/v) methanol aqueous solution was applied as the mobile phase and the flow rate was set at 0.6 mL/min. The column temperature was 30 °C. The glucose conversion (Equation 4.1), the product yields (Equation 4.2) and its selectivity (Equation 4.3) were calculated as follows:

$$\%\ \text{conversion of reactant} = \frac{C_{reactant,t=o} - C_{reactant}}{C_{reactant,t=0}} \times 100 \qquad (4.1)$$

$$\%\ \text{yield of product } x = \frac{C_x}{C_{reactant,t=0}} \times 100 \qquad (4.2)$$

$$\%\ \text{selectivity of product } x = \frac{C_x}{C_{reactant,t=0} - C_{reactant}} \times 100 \qquad (4.3)$$

Where, C_x is the molar concentration (mol/L) of the species *x*.

4.3 Results and discussion

4.3.1 Physicochemical characteristics of WO_x/ZrO_2

All WOx/ZrO_2 catalysts showed Type ΙΙΙ isotherms, implying a weak adsorbent-adsorbate interaction, characteristic for materials, which are nonporous or have very low porosity (Figure A5, Appendix). BET surface areas of the impregnated samples (IM) were within 21.5±1 m^2/g, while those of the FSP-made catalysts were significantly dependent of the composition ranging from 10.8 m^2/g for W/Zr 1/10-FSP to 24.6 m^2/g for W/Zr 1/4-FSP. Higher W loading normally results in a larger surface area, which is in accordance with the FSP-WO_x/ZrO_2 samples but not observed with IM-WO_x/ZrO_2 in the present work (Table A1, Appendix) [26]. Pore volumes of the catalysts prepared by impregnation were ≃ 0.05 cm^3/g, while those of the FSP-made catalysts were ≤ 0.036. Generally, the W surface density of WO_x/ZrO_2 is supposed to correlate with the activity of the catalyst by influencing its surface active sites, and quantitative analysis of W surface density in this research was calculated according to previous literature based on its surface area and W content (Table A1, Appendix) [29]. It revealed that the average surface density of W on the materials synthesized in the present work is higher than that in previous research, mainly due to lower surface area [27, 29, 40].

Powder XRD was employed to study the crystalline phases of the materials as shown in Figure 4.1. As emerges from Figure 4.1a, the majority of XRD peaks of WO_x/ZrO_2 correspond to tetragonal-ZrO_2 (t-ZrO_2) and monoclinic-ZrO_2 (m-ZrO_2) phases, irrespective of the preparation method. Specifically, higher W content favors the generation of t-ZrO_2, and in FSP-WO_x/ZrO_2 larger crystallites are formed than in IM-WO_x/ZrO_2 (Table A1, Appendix). Note that reflections corresponding to monoclinic WO_3 (m-WO_3) can be detected in the IM-WO_x/ZrO_2, and the intensity of this reflection becomes stronger as the W content is increased, suggesting the existence

of crystalline WO_3 in the IM-WO_x/ZrO_2 catalyst (Figure 4.1b) [26, 29]. In contrast, the FSP-WO_x/ZrO_2 samples show XRD patterns lacking any notable reflections in this area. Based on these results, we infer that IM probably yields a material containing WO_x and ZrO_2 crystallites mainly existing as separate phases, while the synthesis with FSP results in materials with uniform distribution of W and Zr within the bulk material.

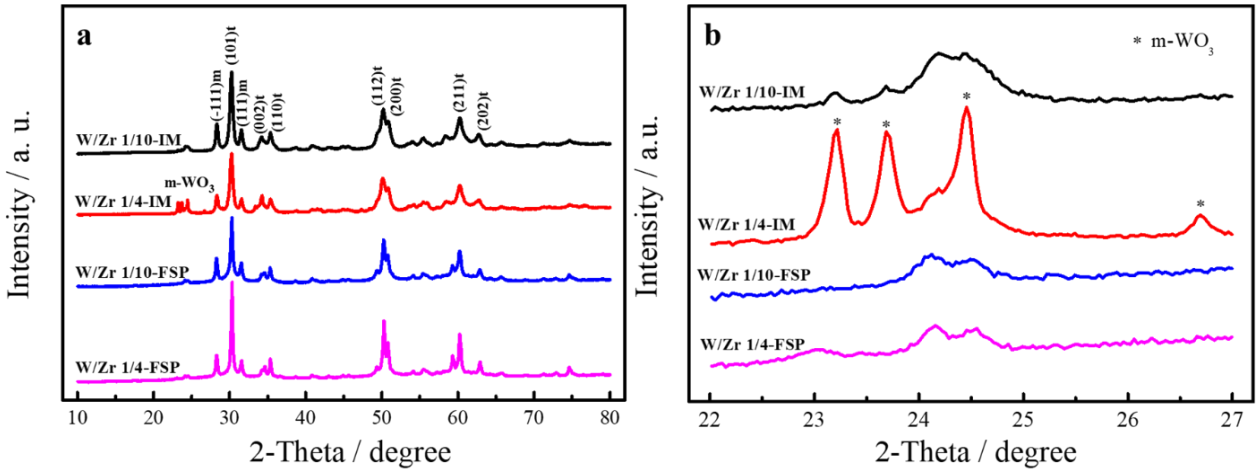

Figure 4.1 XRD patterns of WO_x/ZrO_2 (a), and in a small range of 22-26° corresponding to W-containing phases (b)

Raman spectroscopy was employed to further clarify the identity of phases present in the catalysts. As shown in Figure 4.2, both IM-WO_x/ZrO_2 catalysts show Raman bands at ~271(m), ~331(m), ~344(w), ~380(m), ~474(m), ~500(w), ~536(w), ~557(w), ~614(w), ~636(w), ~713(m), ~804(s), and ~1020 cm^{-1}, corresponding to crystalline ZrO_2 and WO_x [40, 41]. In stark contrast to the IM-WO_x/ZrO_2 samples, both corresponding FSP-WO_x/ZrO_2 samples exhibit a very broad low-intensity signal spanning from 200 to 1800 cm^{-1}. However, such a dramatic change is not surprising considering the nature of these samples. Indeed, the material in question must be able to absorb photons of the incident laser to show inelastic light scattering. Hence, a sample that has no significant absorption band at 785 nm will afford a blank spectrum. While a separate WO_x phase

has yellow color and the tail of the absorption band matches the laser wavelength, the off-white material prepared via FSP lacks any significant absorption in the visible range and thus shows no distinct Raman signals. In this case, the FSP-WO_x/ZrO_2 turns out to possess a uniform distribution of W within the material. The observations described above are in full agreement with the results from XRD.

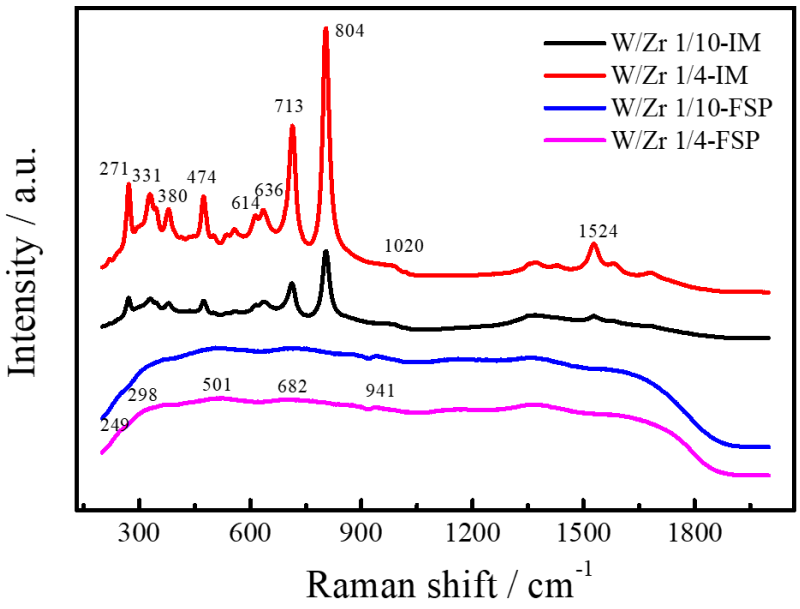

Figure 4.2 Raman spectra of WO_x/ZrO_2

The morphology of the WO_x/ZrO_2 catalysts synthesized via the two different methods was investigated by HRTEM (Figure A6, Appendix). Samples prepared by impregnation (IM) were made up of aggregates of bulk crystals caused by the strong interaction of WO_x with the ZrO_2 support during crystallization. In contrast, FSP generated much smaller and more homogeneously distributed particles, as corroborated by XRD and Raman results [40]. EDS elemental mapping revealed the presence of well-distributed W over Zr in all the WO_x/ZrO_2 samples (Figure A7, Appendix).

Previous research showed that monotungstate (i.e., isolated W atoms) and polytungstate (i.e., interconnected two-dimensional WO_x species with W atoms linked by oxygen bridging bonds) begin to emerge when the WO_x coverage is lower than 2.5 $W \cdot nm^{-2}$ [29]. In Figure 4.3, lattice defects (areas encircled by yellow dash lines) can be observed in all WO_x/ZrO_2 particles, which may be ascribed to the existence of mono- or polytungstate. As shown in Figure 4.3a, W/Zr 1/10-IM displays fine crystallites with almost clear lattice fringes extending directly to the grain surface, and some polytungstate at the boundaries of the ZrO_2 particles, appearing as tiny dark plaques marked by white arrows. With increasing W content, sub-nanometer dark flecks are discernible in W/Zr 1/4-IM and W/Zr 1/4-FSP, marked by white circles. As a consequence of the strong interaction between WO_x species and surface defect sites on the ZrO_2 support, surface W atoms were found to sit preferentially above Zr columns [29, 42]. Therefore, it is speculated that these sub-nanometer dark flecks are three-dimensional Zr-WO_x clusters. Indeed, these clusters can also be found at lower W concentration, but not that prominent. Additionally, the rough border of the crystallites in W/Zr 1/4-IM and W/Zr 1/4-FSP decorated with small nanoclusters marked by black arrows can also be assigned to WO_x clusters. Similar structures are also observed with W/Zr 1/10-FSP (Figure 4.3c), but not as obvious as those at higher W concentrations. Note that the rough border of FSP-WO_x/ZrO_2 is more glaring than that of IM-WO_x/ZrO_2 at the same W concentration. This further proves that FSP can efficiently hinder the sintering of W atoms on the ZrO_2. Consequently, the highly dispersed W is likely to settle in particle boundaries since the edges of surface ZrO_2 pits provide a large number of step edge sites for trapping WO_x. Zhou *et al*. explained that these clusters were most likely caused by the intermixing of a small amount of ZrO_x species within these WO_x clusters to form Zr-WO_x clusters which are responsible for the catalytic activity [42]. Further insight into the morphology was gained from the lattice spacing of the crystallites.

The *d*-spacing of 0.2837 in W/Zr 1/10-IM matches (111) planes of m-ZrO_2. It seems that there is a thick atom layer of W covering all the ZrO_2 lattice in W/Zr 1/4-IM since it mainly shows a *d*-spacing of 0.3213 nm and 0.2478 nm, corresponding to (120) and (221) planes of m-WO_3, respectively. It is noteworthy that there are small particles (marked by red circles) in W/Zr 1/10-FSP, showing a *d*-spacing of 0.2837, 0.2554, and 0.2478, which could be ascribed to (111) planes of m-ZrO_2, (110) planes of t-ZrO_2, and (221) planes of m-WO_3, respectively. There may also exist a ZrO_2 phase in small particles of W/Zr 1/4-FSP though Figure 4.3d only shows particles with a *d*-spacing of 0.2478. It could be speculated that these tiny particles are separate three-dimensional Zr-WO_x clusters. The *d*-spacing of 0.2554 and 0.2837 in bulk FSP-WO_x/ZrO_2 crystallites are in agreement with planes from t-ZrO_2 and m-ZrO_2.

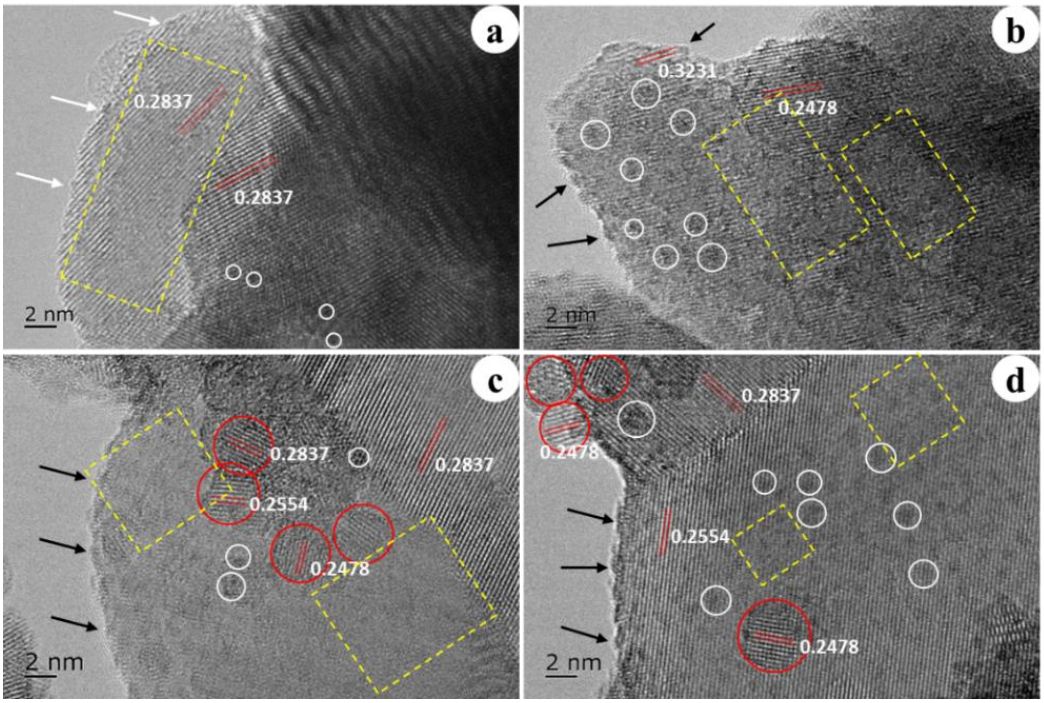

Figure 4.3 HRTEM images of WO_x/ZrO_2: (a): W/Zr 1/10-IM; (b): W/Zr 1/4-IM; (c): W/Zr 1/10-FSP; and (d): W/Zr 1/4-FSP

Further, XPS was used to investigate the surface electronic properties of the catalysts. As shown in Figure 4.4a, the XPS spectra of Zr 3d are well described by a doublet peak corresponding to the spin-orbit of Zr $3d_{5/2}$-Zr $3d_{3/2}$. The integral intensities of its components relate as 3:2 and the spin-orbit splitting (the difference between Zr $3d_{5/2}$ and Zr $3d_{3/2}$) is 2.40 eV. The Zr $3d_{5/2}$ spectra in W/Zr 1/10-IM and W/Zr 1/10-FSP exhibit a peak at 182.3 eV that is attributed to the binding energy of the Zr-O bond. It is proposed that most of Zr atoms are present as Zr^{4+} due to the relatively high binding energy [33]. The peak shifting of Zr $3d_{5/2}$ from 182.3 to 182.4 eV for W/Zr 1/4-IM and 182.5 eV for W/Zr 1/4-FSP is ascribed to the formation of strongly deformed Zr^{4+} cations caused by strong interaction with W atoms, in the formation of Zr-O-W bonds, which is also in agreement with the HRTEM results (Figure 4.3b and 4.3d) [43].

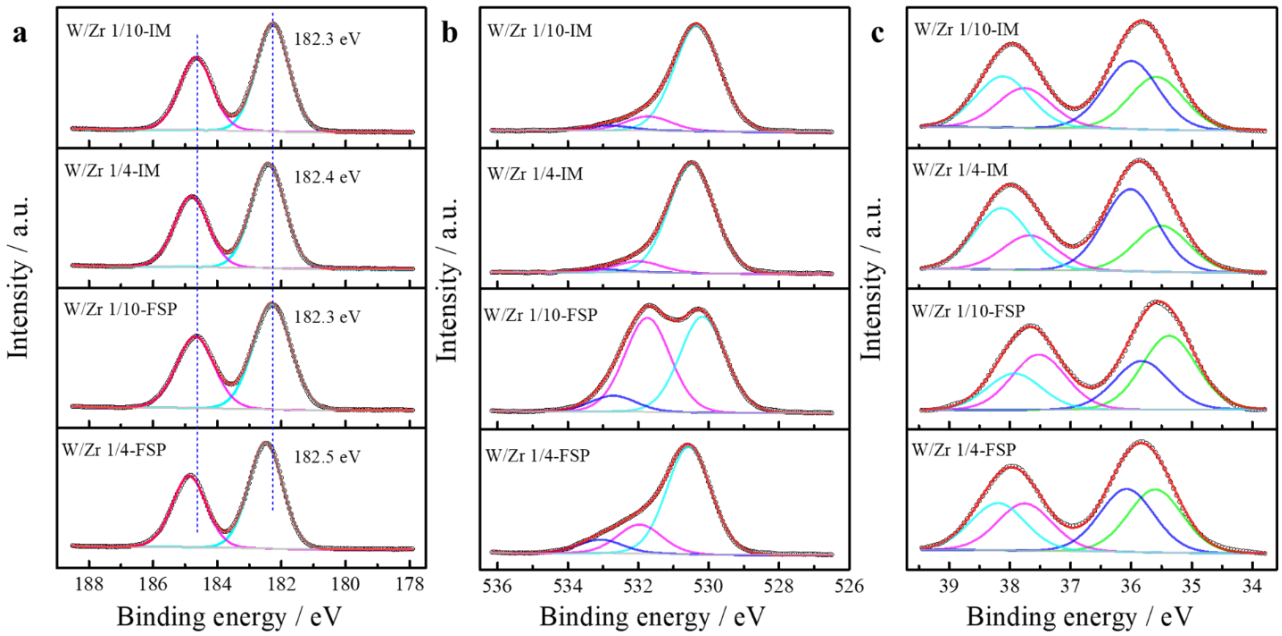

Figure 4.4 XPS of WO_x/ZrO_2: (a) Zr 3d spectra; (b) O 1s spectra; and (c) W 4f spectra

The asymmetric peaks observed in the O 1s spectra presented in Figure 4.4b can be deconvoluted in three individual sub-peaks (O1, O2, and O3) via proper Gaussian-Lorentzian fitting. The low binding energy of O1 centered at 530.4±0.2 originates from the O^{2-} ions forming bonds with metals

(Zr-O-W) [44, 45]. The medium binding energy of O2 centered at 531.8±0.2 is mainly ascribed to the O^{2-} ions near the oxygen deficient region (where presents the oxygen vacancies) within the metal matrix, and the high binding energy of O3 centered at 532.9±0.2 is typically attributed to metal hydroxide [45, 46]. Note that the binding energy of O1s of W/Zr 1/4-IM and W/Zr 1/4-FSP is slightly higher than that of W/Zr 1/10-IM and W/Zr 1/10-FSP, regardless of O1, O2, or O3 sub-peaks. This is probably because the flowing of electron density from ZrO_2 into the WO_x phase through Zr-O-W linkages reduces the electron density around the oxygen atoms, resulting in a minor shift of the O1s binding energy to higher bonding energy, and this phenomenon is more obvious when there are more W atoms [43].

The position and relative integrated peak intensity ratios of O 1s sub-peaks are listed in Table A3 (Appendix). The sub-peak of O1 seems to play a dominant role in O 1s spectra, with the highest intensity ratio, indicating the presence of a large amount of metal-oxygen bonds in the WO_x/ZrO_2 matrix. The more W atoms, the larger is the ratio of O1/Otot, corresponding to the presence of more W-O bonds. It is noteworthy that the intensity ratio of O2/Otot for FSP-WO_x/ZrO_2 is much higher than that of IM-WO_x/ZrO_2. The ability of FSP to inhibit sintering of W atoms on the ZrO_2 lattice weakens the average W-O bond, hence inducing more oxygen vacancies in the metal matrix [45]. The higher concentration of W atoms of W/Zr 1/4-FSP strengthens the W-O bonds, causing less oxygen deficient formation than in W/Zr 1/10-FSP. The ability of FSP to produce oxygen deficiency may result in more metastable W^{5+}. FSP also produces more metal hydroxide than IM. The hydroxyl groups on metals may have different forms, such as Zr-O(H)-Zr or W-O(H)-Zr, which in turn contribute to the formation of BAS [28].

To gain information about the chemical state of W, the XPS study of W in WO_x/ZrO_2 is shown in Figure 4.4c. The binding energies of W $4f_{7/2}$ and W $4f_{5/2}$ were de-convoluted into two pairs of peaks that are representative of W atoms with different oxidation states. Though the binding energy measured is close to the value measured for $Al_2(WO_4)_3$, the occurrence of this species cannot be based unambiguously on binding energy alone. It is suggested that the W 4f binding energy located at 35.9 ± 0.2 eV is ascribed to the characteristic of W^{6+} while the one located at 35.5 ± 0.1 eV corresponds to W^{5+} (Table A4, Appendix) [47, 48]. It clearly shows that higher W content leads to a higher W^{6+}/W^{5+} ratio, indicating that more W species migrated to the surface to form patches of Zr-WO_x clusters and were partially oxidized to W^{6+}, in line with the HRTEM result. In agreement with O 1s spectra, the W^{6+}/W^{5+} ratio of FSP-WO_x/ZrO_2 is much lower than that of IM-WO_x/ZrO_2, suggesting that more W^{5+} exist in the FSP-WO_x/ZrO_2 matrix. Indeed, the coordination of W-OH to the unsaturated Zr^{4+} sites may lead to the formation of W^{5+}, and this behavior can promote the generation of BAS, similar to the behavior of Al^{V} in silica networks [24].

The superficial W/Zr atomic ratios of the catalysts have also been calculated based on Zr 3d and W 4f by the respective sensitivity factors from the XPS measurements (Table A4, Appendix). Plausibly, higher W concentration leads to a higher W/Zr ratio. Nevertheless, the W/Zr ratio of W/Zr 1/10-FSP is much lower than that of any other samples, and it also possesses the lowest W^{6+}/W^{5+} ratio. Though the W/Zr ratio is very high for W/Zr 1/4-FSP, it still has a high W^{5+} concentration. According to the previous results, we hypothesize that W locates on the ZrO_2 matrix in a pile-up form, which results in a high superficial W/Zr atomic ratio in IM-WO_x/ZrO_2, but W and Zr are uniformly mixed in FSP-WO_x/ZrO_2, and this produces lots of three-dimensional Zr-WO_x clusters leading to a low W/Zr atomic ratio. Higher W concentration enriches the three-dimensional Zr-WO_x clusters with W atoms and consequently results in a high W/Zr atomic ratio.

4.3.2 Acidity characterization of WO_x/ZrO_2

The surface acidity is an important property of catalysts for assessing their dehydration functionality. The NH_3-TPD profile of WO_x/ZrO_2 exhibits a broad peak centered at around 300 ^oC, indicating the presence of weak, medium, and strong acidity (Figure A8, Appendix) [49]. As shown in Table 4.1, higher W concentration leads to higher total acidity, irrespective of BAS or LAS [29]. FSP-WO_x/ZrO_2 generates slightly more acid sites than IM-WO_x/ZrO_2. On the other hand, the broad NH_3 desorption peak of FSP-WO_x/ZrO_2 slightly shifts to higher temperature, and it also indicates more desorption at a temperature higher than 500 ^oC, suggesting that there may exist more strong acid sites in FSP-WO_x/ZrO_2.

Generally, the distribution of acidic strengths in a catalyst, which dictates its catalytic performance, is anticipated to be inhomogeneous since it largely depends on local proximity and overall structural properties of the catalyst [50]. The ^{31}P MAS NMR technique is effective for identifying acid types (i.e., BAS and/or LAS), and for determining subtle differences in acid strength and acid site distributions in various solid acids [51]. It was reported that the ^{31}P NMR chemical shift observed for the adsorbed TMPO probe molecules increases linearly with increasing acid strengths of the solid acids [52]. Typically, the experimentally observed ^{31}P MAS NMR shift range of TMPO adsorbed at well accessible BAS is δ_{31P}=55-90 ppm, while the presence of LAS is usually indicated the peak at δ_{31P} < 55 ppm [50, 53-56]. Significant changes in line shape and chemical shift among WO_x/ZrO_2 synthesized by the two methods are observed. As shown in Figure 4.5, the ^{31}P NMR chemical shifts of the peak at 42 ppm in the IM-WO_x/ZrO_2, and 48 ppm in the FSP-WO_x/ZrO_2 are assigned to LAS, while the peaks at 62±1 and 76 ppm belong to the $TMPOH^+$ ions associated with different BAS with varied acid strengths (ranging from weak to strong). The difference of the chemical shifts attributed to LAS in WO_x/ZrO_2 synthesized by the two methods may be ascribed

to the difference in the local chemical environment. As shown in Table 4.1, the IM-WO_x/ZrO_2 catalysts have similar ratios of LAS to BAS. Unlike FSP, IM produces another BAS at a chemical shift of 76 ppm, but with a very low ratio, which is less than 10 %. It is noteworthy that the FSP-WO_x/ZrO_2 catalysts exhibit an outstanding proportion of BAS. The B/L ratios are 4.587 for W/Zr 1/10-FSP and 3.717 for W/Zr 1/4-FSP, which ratios are much higher than those of IM-WO_x/ZrO_2 (B/L ratio of around 1.0), or WO_x/ZrO_2 from other studies [27, 29].

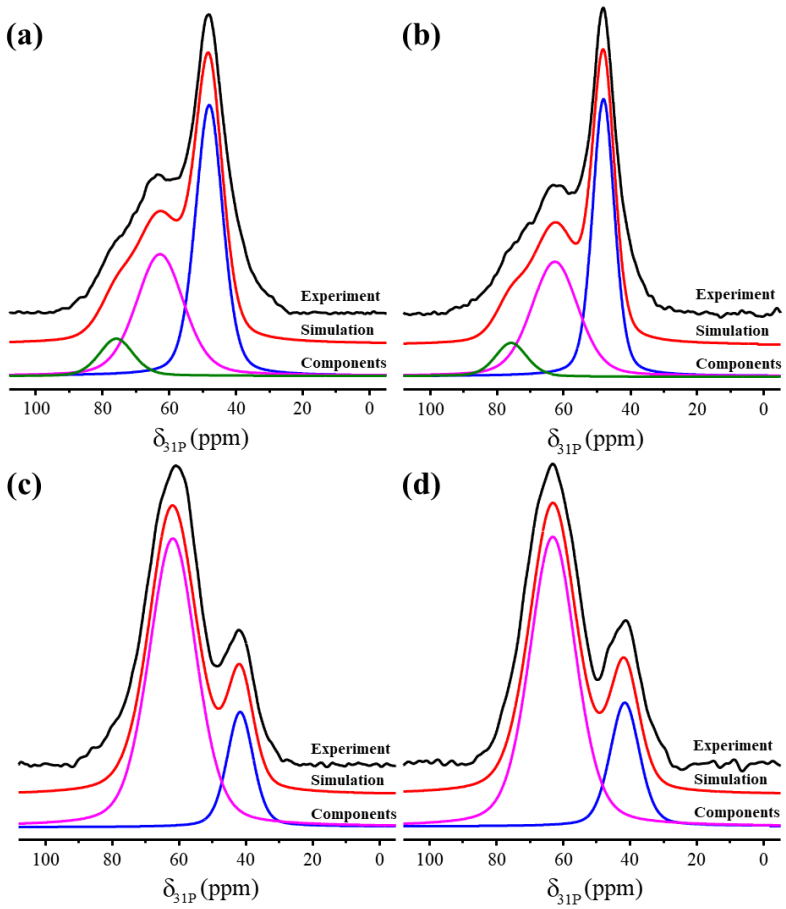

Figure 4.5 ^{31}P MAS NMR spectra of WO_x/ZrO_2: (a) W/Zr 1/10-IM; (b) W/Zr 1/4-IM; (c) W/Zr 1/10-FSP; and (d) W/Zr 1/4-FSP

Table 4.1 Quantitative analysis of acid sites in WO_x/ZrO_2 according to NH_3-TPD profiles and ^{31}P MAS NMR spectra, and turnover frequencies (TOFs) of the glucose conversion on WO_x/ZrO_2

	Chemical shift (ppm)[a]				Acid amount (mmol/g cat.)[b]			
	76	62±1	48	42	BAS	LAS	Total	B/L
W/Zr 1/10-IM	8.8	40.0	51.2	-	0.050	0.052	0.102	0.95
W/Zr 1/4-IM	8.4	42.9	48.7	-	0.077	0.074	0.151	1.053
W/Zr 1/10-FSP	-	82.1	-	17.9	0.101	0.022	0.123	4.587
W/Zr 1/4-FSP	-	78.8	-	21.2	0.138	0.037	0.175	3.717

[a.] For comparison, Gaussian-Lorentz simulation results obtained for the samples representing TMPO adsorbed on Brønsted and/or Lewis acid sites (denoted by chemical-shift values) with practically the same chemical shift are aligned in the same column.

[b.] The total acidity was estimated from the NH_3-TPD results, and the BAS and LAS were calculated based on the ^{31}P MAS NMR results, depending on total acidity.

The proposed schematic representation of WO_x/ZrO_2 synthesized via the two methods is displayed in Figure 4.6. When W is loaded onto the ZrO_2 support, it will interact with the surface Zr-OH groups and then WO_x species tightly anchor on the ZrO_2 surface by eliminating water molecules or coordinating to the unsaturated Zr^{4+} sites through their hydroxyl groups during the sample calcination [57]. As for the product, the surface isolated monotungstate is usually present at low W surface density (<4 W/nm^2). When the surface density of W increases (up to ~10 W/nm^2), isolated monotungstate species condense into oligomeric two-dimensional polytungstate domains, and besides disordered mixed oxide, Zr-WO_x clusters (~0.8-1.0 nm in size), will coexist with the surface mono- and polytungstate species once the surface W density exceeds monolayer coverage [58-60]. A further increase in W loading will result in the formation of bulk WO_x crystals. Among these species, the two-dimensional oligomeric polytungstate and Zr-WO_x clusters are considered as the parts, which possess high activity, while monotungstate and bulk WO_x crystals are supposed to exhibit very low catalytic activity [58]. Normally, nano-grained materials have distinctly

different properties compared to bulk ones since the number of surface atoms or molecules can be comparable to the number inside the materials.

In the present study, it is apparent that IM-WO_x/ZrO_2 contains all these entities since W locates on the ZrO_2 matrix in a pile-up form and both of the samples have a high W surface density. However, in the FSP process, precursor solutions undergo a process of spray evaporation/or decomposition, nucleation, and surface growth/or condensation [22]. The rapid quenching and short residence time of the components in the flame can prevent significant sintering of the W atoms upon deposition on ZrO_2 and therefore maintain a high surface dispersion of W. In other words, uniform distribution of W on ZrO_2 can be achieved in FSP-WO_x/ZrO_2, which promotes the formation of Zr-WO_x clusters. Some of the Zr-WO_x clusters are similar to those reported in the literature with a size of ~0.8-1.0 nm while some others may occupy larger space as three-dimensional clusters (around 1-3 nm shown in HRTEM) [29]. In these clusters, the coordination of W-OH to the unsaturated Zr^{4+} sites results in a remarkable decrease in LAS on the surface of ZrO_2 and promotes the formation of bridging W-O(H)-Zr hydroxyl groups, which act as BAS, as shown in Table 4.1 (62 ± 1 ppm) and similar to other research [57]. This formation of BAS is probably created by electron-deficient regions from the anionic dopants of WO_x^{2-} that attract electrons and increase the polarity of the acidic $O^{-\delta}$-$H^{+\delta}$, similar to the bridging Al-O(H)-Si groups in microporous zeolites [57]. Therefore, the FSP-WO_x/ZrO_2 has a much higher density of BAS (~80 %) and much higher B/L ratios than IM-WO_x/ZrO_2. A small amount of BAS at 76 ppm of the IM-WO_x/ZrO_2 may probably be ascribed to the acidity produced between the two separate phases of WO_x and ZrO_2, which results in different chemical environment compared to samples made by the FSP method.

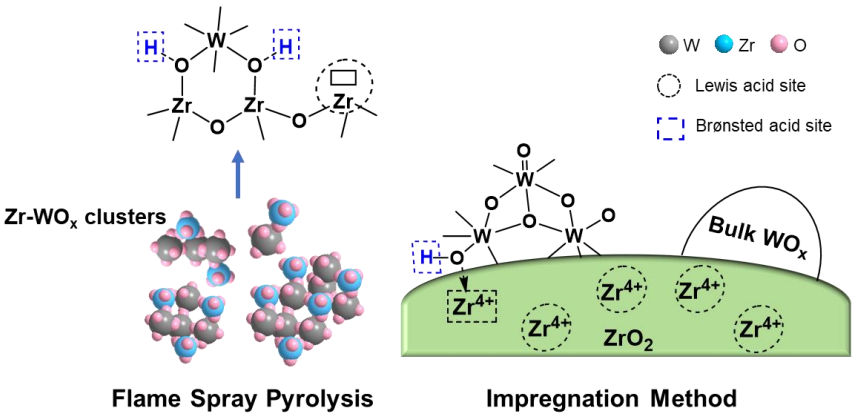

Figure 4.6 Schematic representation of WO_x/ZrO_2

4.3.3 Catalytic activity of WO_x/ZrO_2

The performance of the differently prepared catalysts was evaluated using the glucose to HMF transformation at 170 °C (Figure 4.7 and Figure A9, Appendix). It is proposed that the disappearance of glucose from the reaction mixture takes place due to its fast isomerization into fructose, which subsequently dehydrates to HMF. More than 50 % of glucose was transformed within 1 h with all WO_x/ZrO_2 catalysts. Compared to the previous research of pure ZrO_2, which shows maximum 30 % of glucose conversion in 1 h, the WO_x/ZrO_2 catalysts in this research can achieve a much better performance in the reaction [61]. On the other hand, the variation of the W content had little effect on the glucose conversion within similarly prepared materials. Note that the FSP-WO_x/ZrO_2 (~100 %) shows higher activity than IM-WO_x/ZrO_2 (~90 %) in glucose conversion. FSP-WO_x/ZrO_2 affords higher HMF yield within a significantly shorter time compared to IM-WO_x/ZrO_2, with much higher selectivity. Levulinic acid (LA) and formic acid (FA) were also detected while the reaction proceeded. The decrease of HMF yield and the increase of LA and FA yields after 4 h further evidence that the LA and FA are produced by the rehydration of HMF.

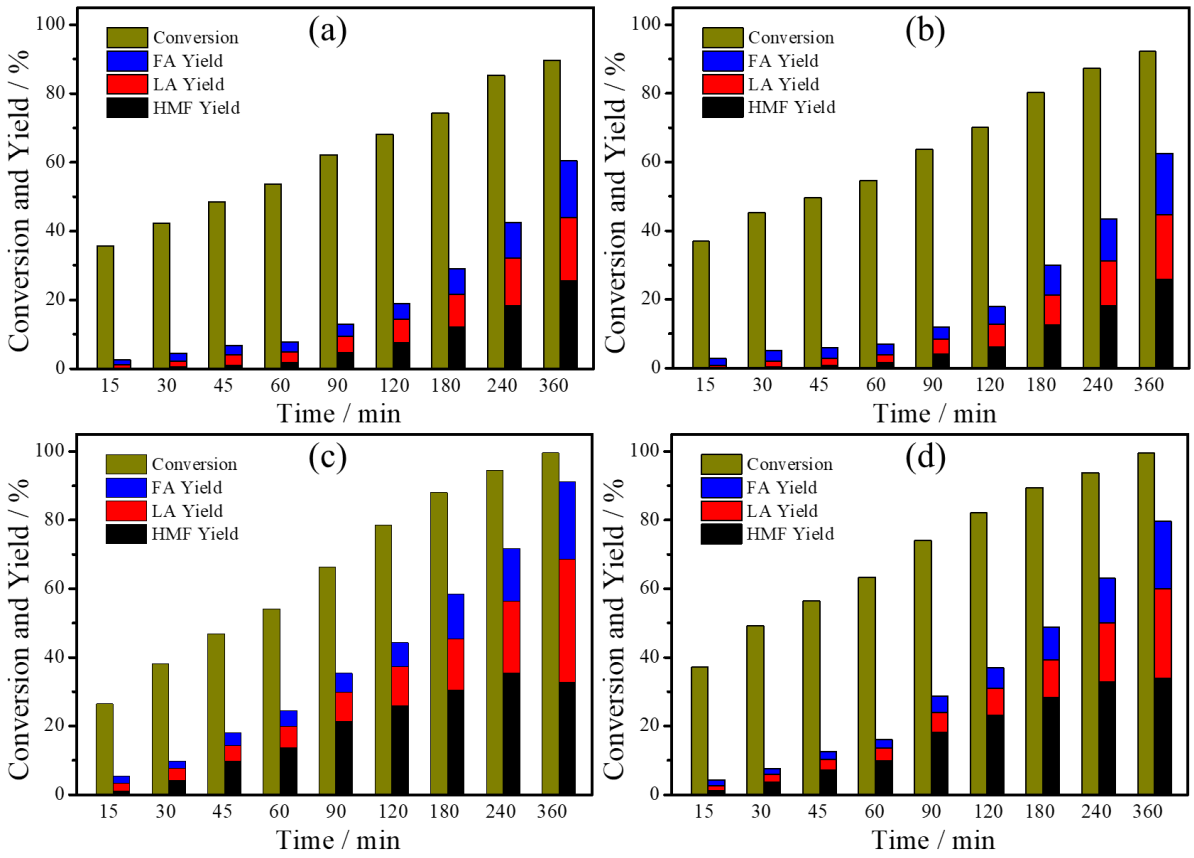

Figure 4.7 Glucose conversion and yields in HMF, LA and FA at 170 °C over (a) W/Zr 1/10-IM, (b) W/Zr 1/4-IM, (c) W/Zr 1/10-FSP, and (d) W/Zr 1/4-FSP

The catalytic data of glucose conversion after 6 h of reaction is compiled in Table 4.2. As concerns the activity, the most active catalyst, W/Zr 1/10-FSP, with the highest B/L ratio of 4.587, was followed by W/Zr 1/4-FSP with B/L of 3.717, showing slightly lower activity. W/Zr 1/10-IM and W/Zr 1/4-IM with similar B/L ratios of 0.953 and 1.053, respectively, exhibit similar performance. Previous studies reported that the isomerization of glucose occurs mainly on LAS, thus TOFs were calculated based on the amount of LAS and glucose conversion as an averaged value after 6 h of reaction [8]. The FSP-WO_x/ZrO_2 catalysts with a higher B/L ratio afford an outstanding performance in glucose conversion compared to IM-WO_x/ZrO_2, showing over two times higher TOFs. Therefore, we infer that the B/L ratio plays a crucial role in glucose conversion, irrespective

of the total acidity. FSP-WO_x/ZrO_2 containing a large amount of BAS and possessing a high B/L ratio achieves a better performance in glucose conversion, probably through driving the reaction to HMF direction that can overcome the equilibrium limitation of the isomerization step [62]. At the same time, it also evidences the cooperative effect between BAS and LAS on glucose conversion and the importance of generating BAS. Considering the secondary products, LA and FA, the best catalyst is W/Zr 1/10-FSP achieving an estimated HMF selectivity at around 55.8-68.8 %, which is comparative to some homogenous catalysts [8, 63]. The reusability of W/Zr 1/10-FSP was also tested under identical conditions, and after five cycles, no significant activity loss was observed (Figure 4.8).

Table 4.2 Catalytic data of glucose conversion after 6 h of reaction

	$C_{glucose}$ / %	Y_{HMF} / %	S_{HMF} / %	Y_{LA} / %	S_{LA} / %	Y_{FA} / %	S_{FA} / %	TOF $(h^{-1})^a$
W/Zr 1/10-IM	89.7	25.5	28.4	18.3	20.4	16.5	18.4	171.7
W/Zr 1/4-IM	92.3	25.8	28.0	18.9	20.5	17.8	19.3	125.3
W/Zr 1/10-FSP	99.6	32.9	33.0	35.7	35.8	22.7	22.8	380.4
W/Zr 1/4-FSP	99.6	33.9	34.1	26.0	26.1	19.6	19.7	273.3

[a] TOFs were calculated from the amount of LAS and glucose conversion as an averaged value after 6 h of reaction.

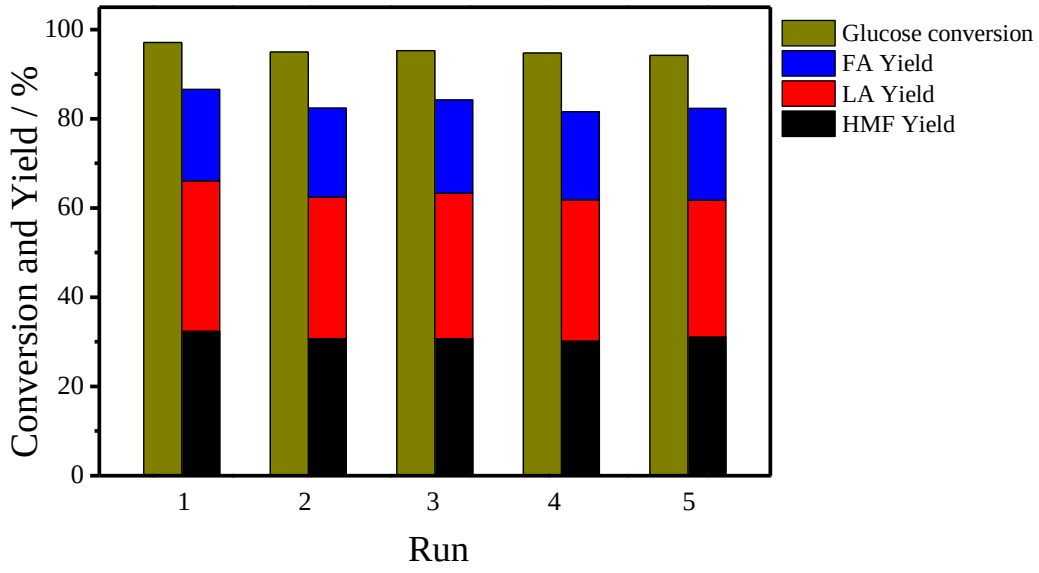

Figure 4.8 Reusability test of W/Zr 1/10-FSP in glucose conversion for 5 cycles

The proposed mechanism of glucose isomerization to fructose and its dehydration to HMF and further rehydration to LA and FA is shown in Figure 4.9. Generally, glucose isomerization to fructose occurs on the LAS provided by Zr atoms followed by fructose dehydration to HMF on BAS from bridging W-O(H)-Zr groups. First, the oxygen atom of the -OH group adjacent to the aldehyde group of the acyclic glucose form is coordinated to a Zr atom with H^+ coordinating to the O atom next to it. Then, the oxygen of the -C=O group coordinates to the same LAS with the formation of a five-membered cyclic intermediate, which undergoes hydride shift leading to switching of -C=O and $-CO^-$ groups positions. Via the reaction with the H^+ adsorbed in the first step on the O atom next to Zr LAS, the restoration of the -OH group then forms fructose. The -OH groups of fructofuranose can be easily protonated with mobile H^+ from BAS. The loss of H_2O molecules induces a rearrangement in the molecule, resulting in the dissociation of H^+ from the -C-H bond and the formation of -C=C and -C=O double bonds. After three consecutive dehydrations with the rearrangements, HMF can be successfully produced. Later on, with the presence of H_2O, the HMF can be further rehydrated into LA and FA. According to this mechanism,

multiple BAS are expected to participate in the process since fructose undergoes the loss of three water molecules. It further evidences the importance of BAS in glucose conversion.

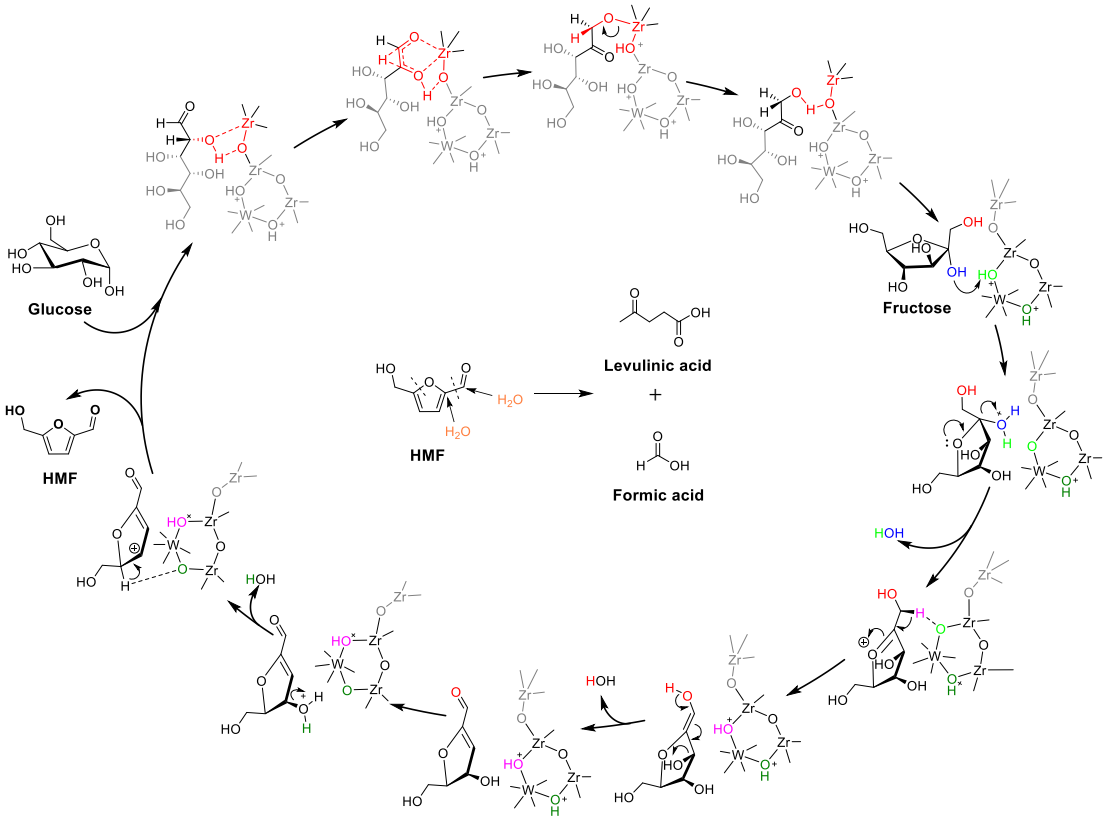

Figure 4.9 Schematic representation of glucose isomerization to fructose and its dehydration to HMF and further rehydration to LA and FA.

4.4 Conclusion

WO_x/ZrO_2 catalysts with uniform distribution of both metals and high density of BAS were successfully synthesized by single-step flame spray pyrolysis (FSP), and their structural and catalytic properties in the dehydration of glucose to 5-hydroxylmethylfurfural (HMF) were compared to those of corresponding WO_x/ZrO_2 catalysts prepared by conventional impregnation (IM). XRD, Raman spectroscopy, morphological studies, and XPS indicated that IM derived WO_x/ZrO_2 is made up of W located on the ZrO_2 support in a pile-up form while corresponding

FSP-made catalysts exhibit a uniform distribution of W on the ZrO_2 with a much higher concentration of three-dimensional Zr-WO_x clusters. The coordination of W-OH to the unsaturated Zr^{4+} sites in these clusters results in a remarkable decrease of the LAS concentration on the ZrO_2 surface and promotes the formation of bridging W-O(H)-Zr hydroxyl groups acting as BAS. FSP-made WO_x/ZrO_2 catalysts have a much higher population densities of BAS (~80%) resulting in higher B/L ratios than the corresponding WO_x/ZrO_2 catalysts prepared by impregnation, as evidenced by NH_3-TPD and ^{31}P solid-state NMR. FSP-WO_x/ZrO_2 catalysts show a better catalytic performance in glucose conversion than the IM-WO_x/ZrO_2 and higher HMF selectivity. The study revealed that the B/L ratio plays a crucial role in glucose conversion, irrespective of different total acidity. The best catalyst in this research of W/Zr 1/10-FSP achieves an estimated HMF selectivity at around 56-69 %, which is comparative to that of some homogenous catalysts. Considering the further rehydration of HMF into levulinic acid and formic acid, the actual HMF selectivity is much higher.

References

[1] Van-Putten, R. J.; Van-der Wall, J. C.; de-Jong, E.; Rasrendra, C. B.; Heeres, H. J.; de-Vries, J. G. *Chem. Rev.* **2013**, *113*, 1499-1597.

[2] Binder, J. B.; Raines, R. T. *J. Am. Chem. Soc.* **2009**, *131*, 1979-1985.

[3] Zhao, H.; Holladay, J. E.; Brown, H.; Zhang, Z. C. *Science* **2007**, *316*, 1597-1600.

[4] Sun, Z. H.; Bottari, G.; Afanasenko, A.; Stuart, M. C. A.; Deuss, P. J.; Fridrich, B.; Barta, K. *Nat. Catal.* **2018**, *1*, 82-92.

[5] Hu, L.; Lin L.; Wu, Z.; Zhou, S.; Liu, S. *Appl. Catal. B: Environ.* **2015**, *174-175*, 225-243.

[6] Zhang, Z.; Huber, G. W. *Chem. Soc. Rev.* **2018**, *47*, 1351-1390.

[7] Weingarten, R.; Tompsett, G. A.; Conner-Jr.,W. C.; Huber, G. W. *J. Catal.* **2011**, *279*, 174-182.

[8] Choudhary, V.; Mushrif, S. H.; Ho, C.; Anderko, A.; Nikolakis, V; Marinkovic, N. S.; Frenkel, A. I.; Sandler, S. I.; Vlacho, D. G. *J. Am. Chem. Soc.* **2013**, *135*, 3997-4006.

[9] Wang, T.; Nolte, M. W.; Shanks, B. H. *Green Chem.* **2014**, *16*, 548-572.

[10] Swift, T. D.; Nguyen, H.; Erdman, Z.; Kruger, J. S.; Nikolakis, V.; Vlachos, D. G. *J.Catal.* **2016**, *333*, 149-161.

[11] Moreno-Recio, M.; Santamaría-González, J.; Maireles-Torres, P. *Chem. Eng. J.* **2016**, *303*, 22-30.

[12] Jiménez-Morales, I.; Moreno-Recio, M.; Santamaría-González, J.; Maireles-Torres, P.; Jiménez-López, A. *Appl. Cata. B: Environ.* **2015**, *164*, 70-76.

[13] Huang, W.; Hu, X.; Zhai, J., Zhu, N.; Guo, K. *Materials Today Sustainability* **2020**, *10*, 1-8.

[14] Román-Leshkov, Y.; Moliner, M.; Labinger, J. A.; Davis, M. E. *Angew. Chem. Int. Ed.* **2010**, *49*, 8954-8957.

[15] Huang, J.; Jiang, Y. J.; Vegten, N. V.; Hunger, M.; Baiker, A. *J. Catal.* **2011**, *281*, 352-360.

[16] Strobel, R.; Baiker, A.; Pratsinis, S. E. *Adv. Powder Technol.* **2006**, *17*, 457-480.

[17] Huang, J.; Vegten, N. V.; Jiang, Y. J.; Hunger, M.; Baiker, A. *Angew. Chem. Int. Ed.* **2010**, *49*, 7776-7781.

[18] Strobel, R.; Pratsinis, S. E. *J. Mater. Chem.* **2007**, *17*, 4743-4756.

[19] Mädler, L.; Kammler, H. K.; Mueller, R.; Pratsinis, S. E. *J. Aerosol Sci.* **2002**, *33*, 369-389.

[20] Koirala, R.; Buechel, R.; Krumeich, F.; Pratsinis, S. E. Baiker, A. *ACS Catal.* **2014**, *5*, 690-702.

[21] Koirala, R.; Pratsinis, S. E.; Baiker, A. *Chem. Soc. Rev.* **2016**, *45*, 3053-3068.

[22] Teoh, W. Y.; Amal, R.; Mädler, L. *Nanoscale* **2010**, *2*, 1324-1347.

[23] Wang, Z.; Jiang Y. J.; Yi, X.; Zhou, C.; Rawal, A.; Hook, J.; Liu, Z.; Deng, F.; Zheng, A.; Hunger, M.; Baiker, A.; Huang, J. *Sci. Bull.* **2019**, *64*, 516-523.

[24] Wang, Z.; Jiang Y. J.; Jin, F.; Stampfl, C.; Hunger, M.; Baiker, A.; Huang, J. *J. Catal.* **2019**, *372*, 1-7.

[25] Gurav, A.; Kodas, T.; Pluym, T.; Xiong, Y. *Aerosol Sci. Technol.* **1993**, *19*, 411-452.

[26] Zhang, C.; Liu, T.; Wang, H. J.; Wang, F.; Pan, X. Y. *Chem. Eng. J.* **2011**, *174*, 236-241.

[27] Kunshan, S.; Zhang, H.; Zhang, Y.; Yi, T.; Tang, K. *J. Catal.* **2013**, *299*, 119-128.

[28] Galano, A.; Rodriguez-Gattornob. G.; Torres-García, E. *Phys. Chem. Chem. Phys.* **2008**, *10*, 4181-4188.

[29] Soultanidis, N.; Zhou, W.; Psarras, A. C.; Gonzalez, A. J.; Iliopoulou, E. F.; Kiely, C. J.; Wachs, I. E.; Wong, M. S. *J. Am. Chem. Soc.* **2010**, *132*, 13462-13471.

[30] Massa, M.; Andersson, A.; Finocchio, E.; Busca, G.; Lenrick, F.; Wallenberg, L. R. *J. Catal.* **2013**, *297*, 93-109.

[31] Cortés-Jácome, M. A.; Angeles-Chavez, C.; López-Salinas, E.; Navarrete, J.; Toribio, P.; Toledo, J. A. *Appl. Catal. A: Gen.* **2007**, *318*, 178-189.

[32] Gonell, F.; Portehault, D.; Julián-López, B.; Vallé, K.; Sanchez, C.; Corma, A. *Cataly. Sci. Technol.* **2016**, *6*, 8257-8267.

[33] Kim, M.; Laine, R. M. *J. Am. Chem. Soc.* **2009,** *131*, 9220-9229.

[34] Hotz, N.; Stutz, M. J.; Loher, S.; Stark, W. J.; Poulikakos, D. *Appl. Catal. B: Environ.* **2007,** *73*, 336-344.

[35] Jossen, R.; Heine, M. C.; Pratsinis, S. E.; Augustine, S. M.; Akhtar, K. M. *Appl. Catal. B: Environ.* **2007,** *69*, 181-188.

[36] Mueller, R.; Jossen, R.; Pratsinis, S. E. *J. Am. Ceram. Soc.* **2004,** *87*, 197-202.

[37] Pokhrel, S.; Birkenstock, J.; Schowalter, M.; Rosenauer, A.; Mädler, L. *Cryst. Growth Des.* **2010,** *10*, 632-639.

[38] Boningari, T.; Koirala, R.; Smirniotis, P. G. *Appl. Catal. B: Environ.* **2012,** *127*, 255-264.

[39] Kourieh, R.; Rakic, V.; Bennici, S.; Auroux, A. *Catal. Commun.* **2013,** *30*, 5-13.

[40] Ross-Medgaarden, E. I.; Knowles, W. V.; Zhou, W.; Kiely, C. J.; Wachs, I. E. *J. Catal.* **2008,** *256*, 108-125.

[41] Ross-Medgaarden, E. I.; Wachs, I. E. *J. Phys. Chem. C.* **2007,** *111*, 15089-15099.

[42] Zhou, W.; Ross-Medgaarden, E. I.; Knowles, W. V.; Wong, M. S.; Wachs, I. E.; Kiely, C. J. *Nat. Chem.* **2009,** *1*, 722-728.

[43] Ginjupalli, S. R.; Mugawar, S.; Rajan-N, P.; Balla, P. K.; Komandur, V. R. C. *Appl. Surf. Sci.* **2014,** *309*, 153-159.

[44] Bang, S.; Lee, S.; Ko, Y.; Park, J.; Shin, S.; Seo, H.; Jeon, H. *Nano. Res. Let.* **2012,** *7*, 1-11.

[45] Lim, J. H.; Lee, S. M.; Kim, H. S.; Kim, H. Y.; Park, J.; Jung, S. B.; Park, G. C.; Kim, J. Joo, J. *Sci. Rep* **2017,** *7*, 1-10.

[46] Yang, B. S.; Park, S.; Oh, S.; Kim, Y. J.; Jeong, J. K.; Hwanga, C. S.; Kim, H. J. *J. Mater. Chem.* **2012,** *22*, 10994-10998.

[47] Si, Z.; Weng, D.; Wu, X.; Li, J.; Li, G. *J. Catal.* **2010,** *271*, 43-51.

[48] Salvatl-Jr, L.; Makovsky, L. E.; Stencel, J. M.; Brown, F. R.; Hercules, D. M. *J. Phys. Chem.* **1981,** *85*, 3700-3707.

[49] Cecilia, J. A.; García-Sancho, C.; Mérida-Robles, J. M.; González, J. S.; Moreno-Tost, R. Maireles-Torres, P. *Appl. Catal. A: Gen.* **2016,** *516*, 30-40.

[50] Zheng A.; Liu, S. B.; Deng, F. *Chem. Rev.* **2017,** *117*, 12475-12531.

[51] Zheng, A.; Huang, S. J.; Liu, S. B.; Deng, F. *Phys. Chem. Chem. Phys.* **2011,** *13*, 14889-14901.

[52] Zheng, A.; Huang, S. J.; Chen, W. H.; Wu, P. H.; Zhang, H.; Lee, H. K.; de-Ménorval, L. C.; Deng, F.; Liu, S. B. *J. Phys. Chem. A* **2008,** *112*, 7349-7356.

[53] Zhao, Q.; Chen, W. H.; Huang, S. J.; Wu, Y. C.; Lee, H. K.; Liu, S. B. *J. Phys. Chem. B.* **2002,** *106*, 4462-4469.

[54] Lang, S.; Benz, M.; Obenaus, U.; Himmelmann, R.; Hunger, M. *ChemCatChem* **2016,** *8*, 2031-2036.

[55] Zhao, R.; Zhao, Z.; Li, S.; Zhang, W. *J. Phys. Chem. Let.* **2017,** *8*, 2323-2327.

[56] Feng, N.; Zheng, A.; Huang, S. J.; Zhang, H.; Yu, N.; Yang, C. Y.; Liu, S. B.; Deng, F. *J. Phys. Chem. C.* **2010,** *114*, 15464-15472.

[57] Xu, J.; Zheng, A.; Yang, J.; Su, Y.; Wang, J.; Zeng, D.; Zhang, M.; Ye, C.; Deng, F. *J. Phys. Chem. B.* **2006,** *110*, 10662-10671.

[58] Zhou, W.; Soultanidis, N.; Xu, H.; Wong, M. S.; Neurock, M.; Kiely, C. J.; Wachs, I. E. *ACS Catal.* **2017,** *7*, 2181-2198.

[59] Baertsch, C. D.; Soled, S. L.; Iglesia, E. *J. Phys. Chem. B.* **2001,** *105*, 1320-1330.

[60] Barton, D. G.; Shtein, M.; Wilson, R. D.; Soled, S. L.; Iglesia, E. *J. Phys. Chem. B.* **1999,** *103*, 630-640.

[61] Zhang, W.; Zhu, Y.; Xu, H.; Gaborieau, M.; Huang, J.; Jiang, Y. *Catal. Today* **2020**, *351*, 133-140.

[62] Caratzoulas, S.; Davis, M. E.; Gorte, R. J.; Gounder, R.; Lobo, R. F.; Nikolakis, V.; Sandler, S. I.; Snyder, M. A.; Tsapatsis, M.; Vlachos, D. G. *J. Phys. Chem. C.* **2014,** *118*, 22815-22833.

[63] Rasrendra, C. B.; Soetedjo, J. N. M.; Makertihartha, I. G. B. N.; Adisasmito, S.; Heeres, H. J. *Top. Catal.* **2012,** *55*, 543-549.

Chapter 5 Tailoring Brønsted acid sites on Lewis acidic mesoporous SiO_2/ZrO_2 nanospheres for glucose conversion

5.1 Introduction

Mesoporous nanosphere (MNS) is an emerging nanoreactor to realize a better catalytic performance based on its unique nanostructure for the reactant transfer and molecular diffusion. Compared to the conventional catalysts, MNS can change the basic chemical nature of molecules and the elements within them, and then alter how they behave in chemical reactions, thus it has several advantages such as the capability of performing parallel chemical reactions, removing undesirable products, and enhancing the catalytic behavior, *etc*. [1, 2]. Besides, multiple reaction sites can also be controllably located on different spatial positions of the MNS such as the exterior and interior surface of the particles, the void of the particles, and anisotropic positions to obtain optimal catalytic behaviors [3]. Based on these outstanding features, MNS nanoreactors can be used not only to speed up reactions but also to gain new fundamental insights of chemical reaction systems [2]. In recent years, different types of MNS based nanoreactors have been widely applied in the catalysis process. [4-8]. In turn, great efforts have also been devoted to the fundamental understanding and rational designing of nanoreactors via tailoring their architecture and catalytic sites.

Among different structures of MNS based nanoreactors, the layered MNS is a promising category for improving the distribution of multi-functional sites with tailored properties, thus it is widely applied in many catalytic reactions such as esterification, glucose conversion, and hydrolysis of saccharides *etc*. [9-11]. Zhou *et al*. successfully synthesized a novel layered sulfonic acid-functionalized zirconium phosphate that presents effective catalytic activity in the oxidation of

cyclohexanone to ε-caprolactone [12]. Monolayered tungstate zirconia was also reported to be effective for skeletal isomerization of butane [13]. The diffusion routes of the reactive molecules in layered MNS nanoreactors could be designed to exactly match along with the sequence of the reaction stages, making the reaction process more precise and efficient. The porosity of the layered MNS nanoreactor also has an impact on the diffusion of the reactants and products via influencing sorption and desorption behaviors, thus affecting its catalytic performance [14].

Compared to liquid acids, solid acid catalysts have powerful bifunctional acidities when well dispersing Lewis (LAS) and Brønsted acid sites (BAS) on the surface [15]. For example, in amorphous silica-alumina, the defects in the alumina phase are related to the formation of LAS while the bridging -OH groups mainly form BAS [16]. In zirconium oxophosphate, the LAS originates from zirconia while the BAS is from bridging or terminal hydroxyl groups of P-OH [17]. So far, bifunctional catalysts such as amorphous silica-alumina, zeolite beta, and ZSM-5 have been reported to present good performance in reactions such as cyclohexanol dehydration, HMF production, and conversion of glyceraldehyde to ethyl lactate, *etc*. [16, 18, 19]. Besides the strong surface acidity, the zirconia-silica (ZrO_2/SiO_2) system has good chemical resistance to alkaline corrosion and low thermal expansions, and it combines the favorable chemical properties of zirconia with high surface area and thermal/mechanical stability arising from silica, thus it could be a good candidate for the design of layered MNS nanoreactors [20].

Glucose has been well-known as an important biomass feedstock in biorefining for the production of fine chemicals such as 5-hydroxymethylfurfural, 2,5-furandicarboxylic acid, 5-hydroxymethylfuroic acid, levulinic acid, formic acid, *etc*. [21-23]. It is generally recognized that both LAS and BAS make contributions to glucose conversion: LAS normally acts on the glucose isomerization to fructose, then followed by BAS catalyzed dehydration of fructose to HMF and its

derivatives [22, 24]. It is reported that Lewis acid such as $CrCl_3$ or $AlCl_3$ is efficient for glucose isomerization, but is not as good as the systems with pure Brønsted acid or the combination of Brønsted and Lewis acids for fructose dehydration to HMF [22, 25]. Jiang *et al*. studied glucose conversion over zirconium doped mesoporous KIT-6 and found that the LAS with an uncoordinated Zr^{4+} defect center occupy a decisive position in glucose isomerization and the BAS from silanol groups mainly works for the dehydration of fructose [26]. In the study of Sn-beta zeolite for aldose-to-ketose isomerization reactions, it reveals that the metal Lewis acid center promotes the C2-C1 hydrogen shift, thus playing a crucial role in the isomerization reactions [27]. When Sn-beta zeolite is combined with Brønsted acid catalysts such as HCl or Amberlyst-15, it can largely accelerate the dehydration step [28]. With this in consideration, layered MNS nanoreactor with specific distribution of LAS and BAS is of great interest for this reaction.

In this research, layered mesoporous ZrO_2/SiO_2 nanospheres (ZrO_2/SiO_2 MNS) were designed as bifunctional acid nanoreactors with ordered distribution of LAS and BAS inside MNS. The structures and texture of the materials were also well characterized. The accessibility of acid sites and their strength/density were investigated by temperature-programmed desorption of ammonia (NH_3-TPD) and ^{31}P solid-state NMR spectroscopy using trimethylphosphine oxide (TMPO) as a probe molecule. Their catalytic performance was tested in glucose conversion.

5.2 Experimental

5.2.1 Catalyst preparation

The synthesis procedure of ZrO_2/SiO_2 MNS was modified based on the literature [29]. A mixture of surfactant solutions containing cetyltrimethylammonium bromide (CTAB), ethylene glycol (EG), NH_3, and H_2O was stirred at 60 ^oC for 30 min. Then a solution of the inner layer was slowly added under stirring at 60 ^oC and kept stirring for another 4 h. Then, an opaque dispersion

nanoparticle was obtained. Then, the outer layer was achieved by a regrowth process via adding another mixture to the dispersion and stirring at 60 °C for another 1 h. The layer solution is composed of a mixture of Zr or Si precursor, zirconium propoxide and tetraethylorthosilicate, and 3-aminopropyltriethoxysilane (APTES). The molar ratio of CTAB, EG, NH_3, H_2O, APTES is 0.53: 52: 12.8: 1075: 0.17. The as-synthesized particles were then dried and calcined at 500 °C for 6 h to remove the surfactant. The resulting samples are named as Z/S-X, SZ/S-X, S/SZ-X, and Z/SZ-X, corresponding to different components in different layers, as shown in Figure 1. X, which is 10, 30, 50, and 70, indicates the amount of Zr [at%] compared to the total molar atoms in the inner layer. The final molar compositions of Zr and Si in different layers are shown in Table A5 (Appendix)**.**

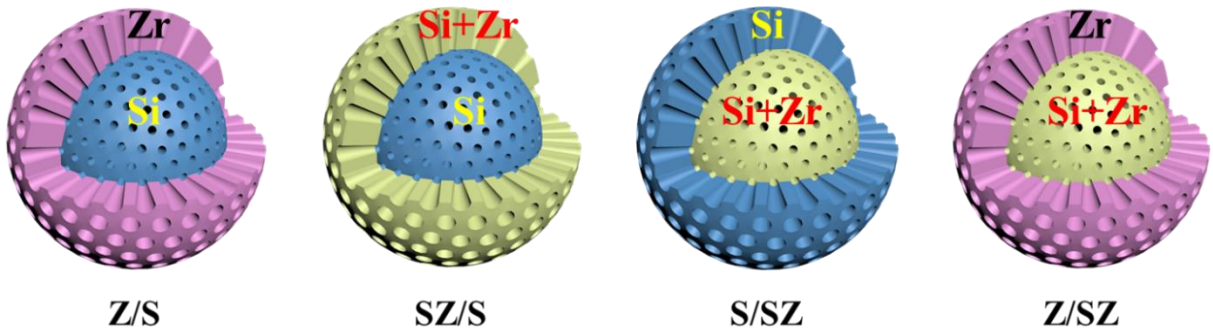

Figure 5.1 The model of the layered ZrO_2/SiO_2 MNSs

5.2.2 Catalyst characterization

Powder X-ray diffraction (XRD) and N_2-physisorption isotherms were carried out according to the experimental parameters from Chapter 3. High-resolution transmission electron microscopy (HRTEM) was carried out by an FEI Titan 80/300 ST unit. The instrument was equipped with a Cs corrector for spherical aberration of the objective lens. For imaging, a high-angle annular dark-field (HAADF) detector, and a GATAN post-column imaging filter were used. In all the experiments, the microscope was operated at an acceleration voltage of 300 kV.

The total numbers of acid sites were calculated through NH_3-TPD on a conventional flow apparatus equipped with a thermal conductivity detector (TCD). The testing materials were initially degassed at 500 °C for 1 h under helium atmosphere at a flow rate of 50 mL/min. Then, the samples were cooled down to 50 °C and exposed to NH_3 atmosphere (10 vol. % in He, 40 mL/min) for 30 min. When it reached to the saturation state, the NH_3 supply line was shut off and the sample was again purged under helium at 50 mL/min for 60 min to remove the physically adsorbed NH_3. Afterwards, the desorption of NH_3 was monitored from 50 to 650 °C at a heating rate of 5 °C/min under helium atmosphere at a flow rate of 50 mL/min.

^{31}P solid-state NMR spectroscopy was used to further differentiate the LAS and BAS, and the acid strength of each acid. The probe molecule for the test in this research is trimethylphosphine oxide (TMPO). For the pre-treatment of the materials, each sample was dehydrated at 300 °C for 24 h under vacuum. Loading TMPO on the dehydrated catalyst was performed inside a glovebox purged with argon by mixing 10 % (wt/wt) of TMPO in a 4-mm rotor, sealed with a KelF cap afterwards. The sealed sample loaded with TMPO was then heated at 160 °C for 2 h under argon flow. ^{31}P magic-angle spinning (MAS) NMR experiments were obtained from a Bruker DRX 300 spectrometer, at a Larmor frequency of 121.5 MHz, and a spinning rate of 10 kHz. The spectra were recorded with 3 μs excitation, 10 s relaxation delay, and 64 to 256 scans. The ^{31}P chemical shifts were externally referenced to K_2HPO_4 at 3.0 ppm [25].

5.2.3 Catalytic reaction

The reaction of glucose conversion was carried out in 25 mL thick-walled glass reactors at 170 °C in an oil bath. In a typical procedure, 2 mL of DMSO/H_2O solution with 3 wt % of glucose and 1 wt % of catalyst was poured into the glass reactor. During the reaction, the reactors were removed from the oil bath and quenched by submerging the reactors in an ice-water bath at a specific time.

The solution was then centrifuged, and the supernatant liquid was taken and diluted with specific mobile phases. Afterward, the resulting solution was filtered and analyzed by high-performance liquid chromatography (HPLC).

Glucose, HMF, formic acid, and levulinic acid were quantified via HPLC. The column used was Biorad HPX87H (300×7.8) and the system was Agilent 1290 equipped with a refractive index detector and a UV detector. The testing condition was 65 °C as the column temperature and 5 mM sulfuric acid as the mobile phase, with a flow rate of 0.6 mL/min. On the other hand, fructose was analyzed by an Agilent Hi-Plex Ca (300×7.7) column connected to an Agilent 1290 system equipped with a refractive index detector. In this test, the mobile phase was ultrapure water and the flow rate was set at 0.6 mL/min, with a column temperature of 85 °C. The glucose conversion (Equation 5.1), the product yields (Equation 5.2) and its selectivity (Equation 5.3) were calculated as follows:

$$\%\ \text{conversion of reactant} = \frac{C_{reactant,t=o} - C_{reactant}}{C_{reactant,t=0}} \times 100 \qquad (5.1)$$

$$\%\ \text{yield of product } x = \frac{C_x}{C_{reactant,t=0}} \times 100 \qquad (5.2)$$

$$\%\ \text{selectivity of product } x = \frac{C_x}{C_{reactant,t=0} - C_{reactant}} \times 100 \qquad (5.3)$$

Where, C_x is the molar concentration (mol/L) of the species *x*.

5.3 Results and discussion

5.3.1 Physicochemical characteristics of the ZrO_2/SiO_2 MNS

The XRD patterns of the ZrO_2/SiO_2 MNS are shown in Figure 5.2, which show two broad bands in 2θ ranges of 15-40^o and 40-70^o, suggesting the amorphous nature [30]. As Zr concentration increases, the peak at lower angle corresponding to Si broadens and slightly shifts to higher angle.

At the same time, the intensity of the peak at higher angle corresponding to Zr starts to increase as well. Other literature mentioned that there is an amorphous phase separation consisting in silica-rich and zirconia-rich interconnected domains before crystallization at calcination temperature over 947 ^{o}C [31, 32]. The calcination temperature of 500 ^{o}C in this research may result in a non-diffractive structure mainly from the amorphous silica at low Zr concentration [32]. As Zr concentration increases, abundant amount of Zr may cause part of Zr incorporated into the Si network, leading to the shift of peak that corresponding to amorphous silica. The incorporation of Zr in Si network may form the structure of Zr-O(H)-Si that acts as BAS. This is further certified by the result from Z/SZ structure that shows peaks different from other structures. As shown in Figure 5.2d, the peak at 30^{o} is different from the other structures at 25^{o} while the peak corresponding to Zr is obtained in all the Zr concentrations. This is probably because that Z/SZ has a relatively higher Zr concentration than other structures, and it may cause plenty of Zr-O(H)-Si formed in the structure. In all cases, there is no obvious diffraction associated with the crystalline phase of zirconia, indicating no bulk crystalline zirconia present in these structures, similar to other mesoporous materials [33].

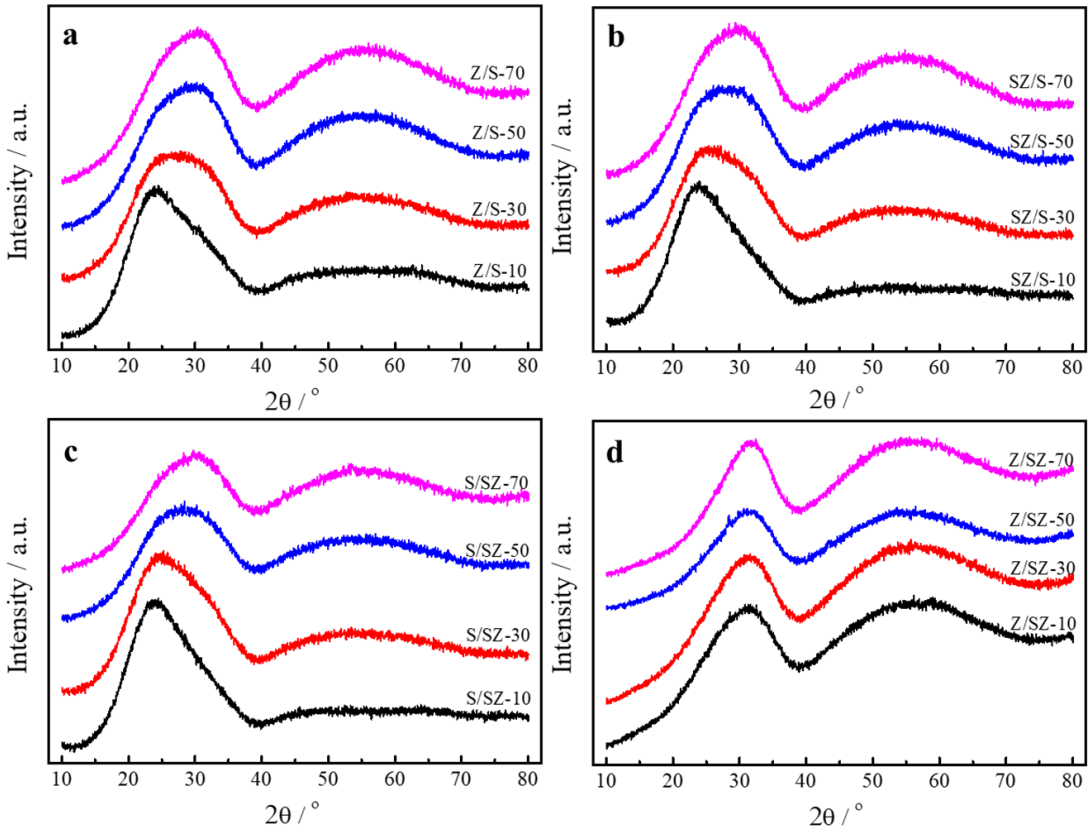

Figure 5.2 XRD patterns of the ZrO_2/SiO_2 MNS: (a) Z/S; (b) SZ/S; (c) S/SZ; and (d) Z/SZ

Nitrogen adsorption-desorption isotherms and pore size distribution profiles for the as-synthesized ZrO_2/SiO_2 MNS are shown in Figure 5.3. The BET surface area, pore size distribution, and pore volume are listed in Table 5.1. Consistently, the BET surface area shows an overall trend of decrease as Zr content increases, similar to pore volume. Except for Z/S, which turns out that Z/S-30 possesses the highest BET surface area and pore volume among that structure with different Zr concentrations. There are remarkable differences among different structures in terms of the BET surface area or the total pore volume. Specifically, Z/S, SZ/S, and S/SZ show relatively higher BET surface areas and pore volumes than Z/SZ.

All the isotherm curves in Figure 5.3 appear to be type IV, corresponding to the typical mesoporous materials, but with various capillary condensation behaviors, presumably as a result of adsorption

and desorption in different kinds of cavities or pores [34]. At the same time, it also displays different hysteretic loops in nitrogen uptake at the pressure range of p/p_0=0.8-1.0 among different structures. Z/S presents an H2 hysteresis loop, indicating the disordered pores, while SZ/S and S/SZ, which are mixtures of Zr and Si in one layer with another layer of pure Si, display typical H1 hysteresis loops, representing the well-defined pores with uniform pore size. However, the hysteresis loops in Z/SZ presents in H4 type, showing the presence of narrow slit-like pores and the pores in the micropore region. The difference of the pore structures may cause a different interaction between Zr and Si, thus result in different acidity that may have an influence on the reactions.

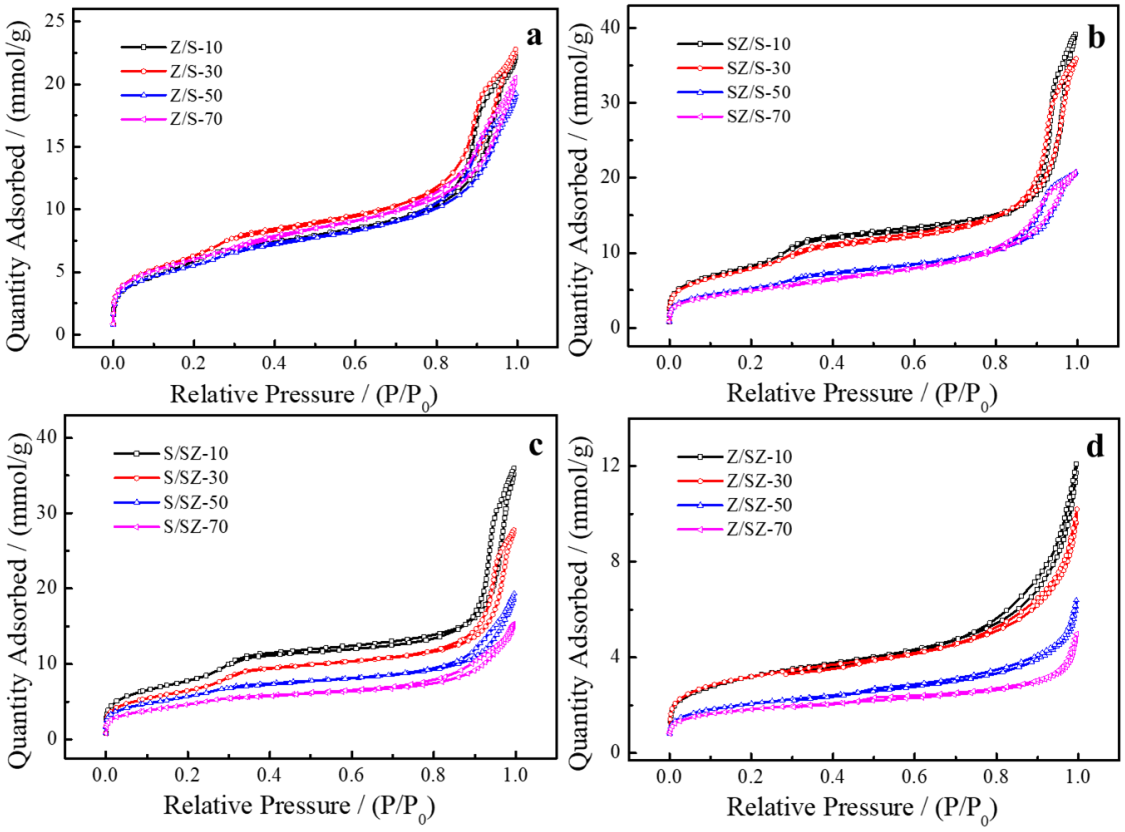

Figure 5.3 N_2 adsorption-desorption isotherms of the ZrO_2/SiO_2 MNS: (a) Z/S; (b) SZ/S; (c) S/SZ; and (d) Z/SZ

Pore-size-distribution curves in Figure 5.4, as derived by the non-linear density function theory (NLDFT), show that there is little difference in cage size between SZ/S and S/SZ at around 3.6 nm, and Z/S at around 3.3 nm. The higher Zr concentration leads to a poor pore size distribution in all the samples. The pore size of Z/SZ is much smaller than all the other structures, in agreement with its low BET surface area and H4 type hysteresis loop. There is also an evidence of micro-porosity from the t-plot curves in Z/SZ, which are not found in other structures. Based on the results above, it suggests that the mixture of Si and Zr either in the inner layer or the outer later can largely sustain the pore structures of the materials, the outer layer with monometal Zr somehow still maintain a good pore structure, while large amount of Zr in both inner and outer layer can affect the pore structure significantly. The variety of pore structures may lead to the different pore sites in the inner and outer layers and thus result in a different distribution of acid sites in the materials.

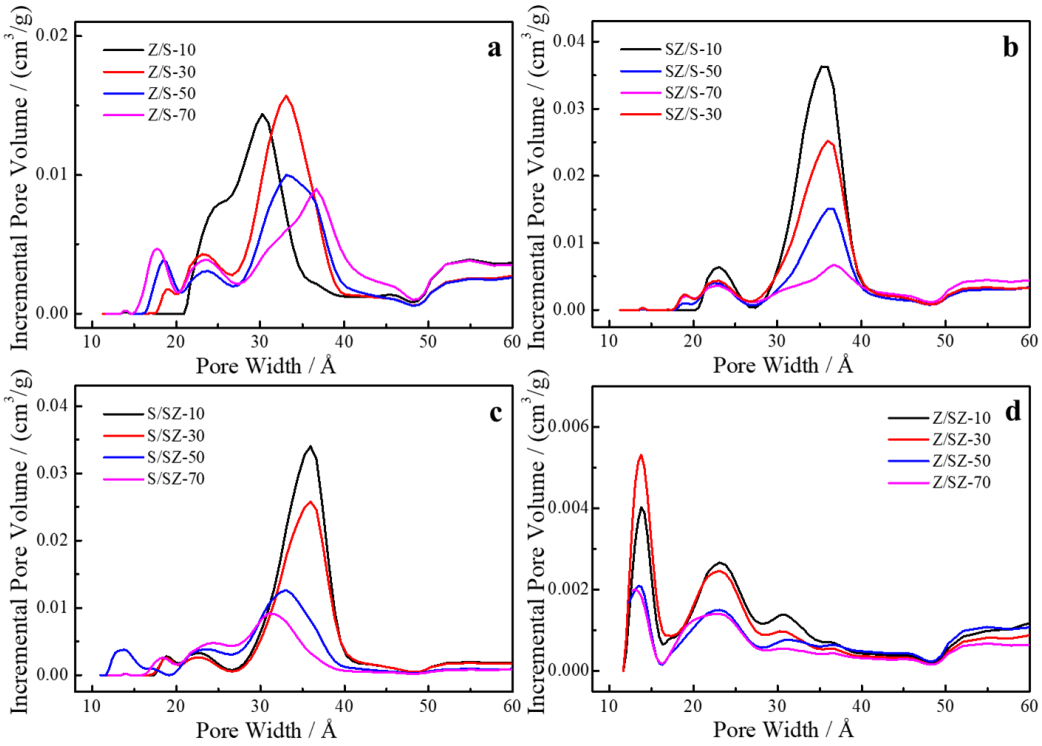

Figure 5.4 Pore-size distribution of the ZrO_2/SiO_2 MNS: (a) Z/S; (b) SZ/S; (c) S/SZ; and (d) Z/SZ

Table 5.1 BET surface area, pore size and pore volume of the ZrO_2/SiO_2 MNS

Sample	BET surface area (m^2/g)	Average pore size (nm)	Pore volume (cm^3/g)
Z/S-10	507.2	3.0	0.517
Z/S-30	545.5	3.3	0.561
Z/S-50	462.1	3.3	0.481
Z/S-70	487.2	3.7	0.507
SZ/S-10	704.2	3.6	0.714
SZ/S-30	654.2	3.6	0.722
SZ/S-50	433.9	3.6	0.501
SZ/S-70	403.7	3.6	0.506
S/SZ-10	684.3	3.6	0.638
S/SZ-30	565.3	3.6	0.536
S/SZ-50	482.2	3.3	0.411
S/SZ-70	390.5	3.1	0.351
Z/SZ-10	248.6	N/A	0.246
Z/SZ-30	243.2	N/A	0.213
Z/SZ-50	158.3	N/A	0.134
Z/SZ-70	137.9	N/A	0.096

HAADF technique was applied to study the morphology of the samples with low Zr concentration. As shown in Figure 5.5, the porous structures of SZ/S-10 and S/SZ-10 can be fully sustained and this is probably because the zirconia penetrates into the silica network uniformly in the mixture layer. It can be seen that the bright dots of Zr and dark dots of Si are distributed evenly which further demonstrates the interaction between zirconia and silica. The size of the particle is ~50 nm for both SZ/S-10 and S/SZ-10. Z/S-10 contains little porous feature and Z/SZ-10 almost has no porous characteristic. As shown in the enlarged figures, there are more bright dots of Zr in Z/S-10 than SZ/S-10 and S/SZ-10 which may further illustrate the settlement of zirconia in the meso-

pores. Z/SZ-10 has an outstanding phenomenon of bright dots corresponding to the huge amount of Zr over all the structures, and this specific feature may provide a strong interaction between zirconia and silica which may contribute to the formation of BAS. It has been mentioned that the addition of zirconia may cause a distortion of the silica network, and high zirconia concentration may result in poor ordering of the mesoporous structure and even collapse of the pores [35-37]. This result is fully in agreement with the BET analysis above, confirming the designed structures.

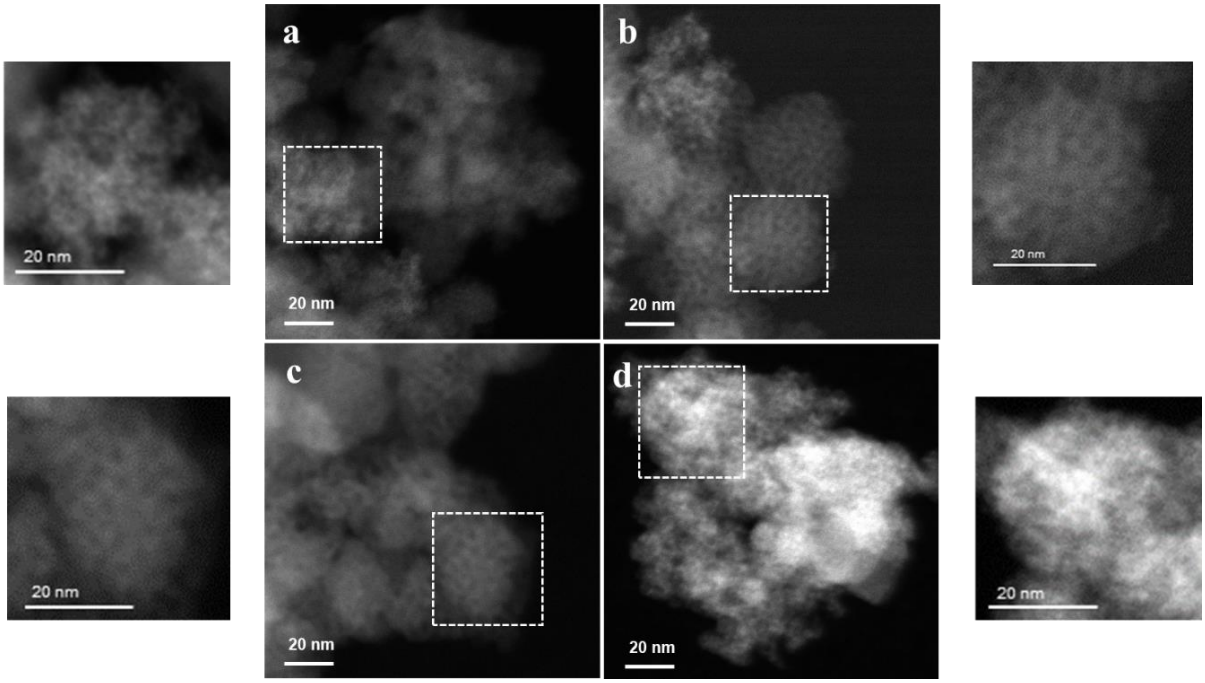

Figure 5.5 HAADF images of the ZrO_2/SiO_2 MNS: (a) Z/S-10; (b) SZ/S-10; (c) S/SZ-10; and (d) Z/SZ-10

The EDX mapping of the ZrO_2/SiO_2 MNS with low Zr concentration is shown in Figure 5.6. It can be observed that when the Zr precursor is mixed with Si precursor, such as SZ/S-10 and S/SZ-10, both of Zr and Si can achieve a better dispersion with each other. It results in less concentrated Zr red dots and Si green dots compared to Z/S-10 and Z/SZ-10. However, these two elements are still overall homogenously dispersed with each other for all the samples. Yasutaka K. *et al*.

mentioned that Zr could be incorporated more uniformly in the mesoporous silica matrix comparing to other metals such as Ce or Ti, without co-crystallization or co-precipitation of other phases, which may in turn contribute to an enhanced performance [36].

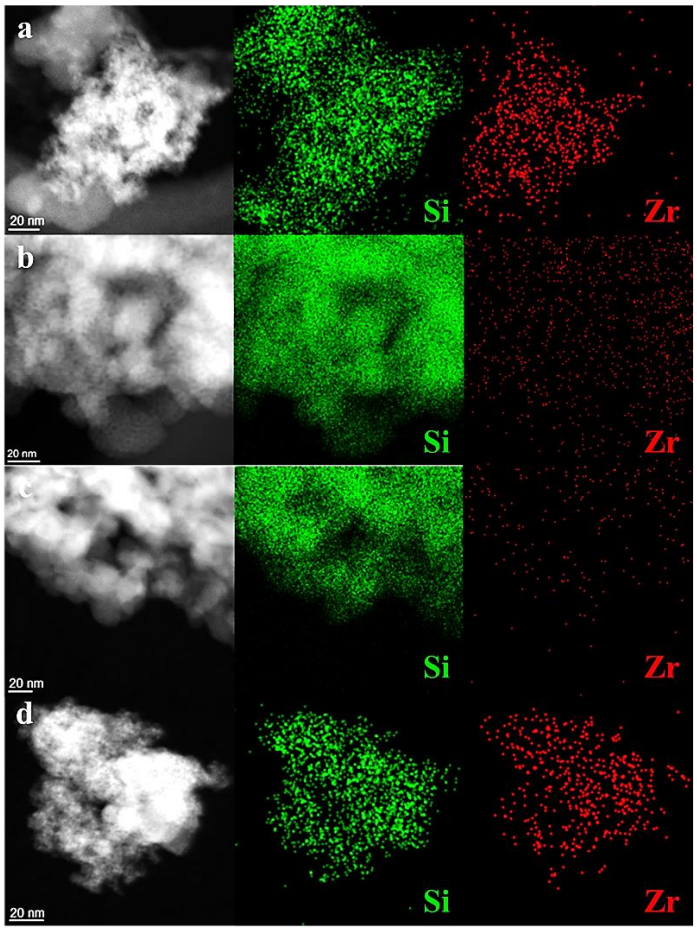

Figure 5.6 EDX mapping of the ZrO_2/SiO_2 MNS: (a) Z/S-10; (b) SZ/S-10; (c) S/SZ-10; and (d) Z/SZ-10

5.3.2 Acidity characterization of the ZrO_2/SiO_2 MNS

The qualitative information to the overall concentration and strength of the acid sites in a catalyst can be determined by NH_3-TPD. The NH_3-TPD profiles of ZrO_2/SiO_2 MNS with low Zr concentration are shown in Figure 5.7. Generally, the low-temperature desorption peaks reflect the evolution of physical adsorbed and hydrogen-bonded ammonia, and the high-temperature

desorption peaks correspond to desorption of ammonia coordinated to LAS and of protonated ammonia on BAS [38]. Different structures of the material usually lead to different acid properties, *i.e.*, quantity or strength [39]. The NH_3-TPD profiles of Z/S-10, SZ/S-10, and S/SZ-10, record a low-temperature desorption peak from 100-400 ^oC assigned to the NH_3 adsorbed on weak acid sites, in agreement with other literatures [40, 41]. Z/SZ-10 shows a much broader NH_3 desorption peak from 150-600 ^oC, which is totally different from the other materials. The temperature of NH_3 desorption peak also shifts to higher value, implying its higher strength of acidity than other materials. Further deconvolution of the broad peak presents three different peaks locating at the temperatures of 235, 335, and 450 ^oC, indicating its weak, medium and strong acidity arising from its complicated structure.

The total acidity of the materials was calculated and expressed in mmol of NH_3 desorbed per gram of catalyst, as shown in Table 5.2. Z/S-10 and SZ/S-10 show similar and the lowest amount of acidity, probably because of the relatively simple and similar structure arrangement. S/SZ-10 presents a higher acidity, which may be ascribed to the fact that the layer of Si+Zr in S/SZ-10 is surrounded by another layer of Si that can further react with the surface Zr of the inner layer and produce more Zr with empty orbital which leads to higher acidity. Z/SZ-10 possesses the highest amount of the acidity over all the structures, and this may be due to the massive amount of Zr in this material that can make sufficient Zr react with Si or Zr itself and then lead to a large increase of acidity.

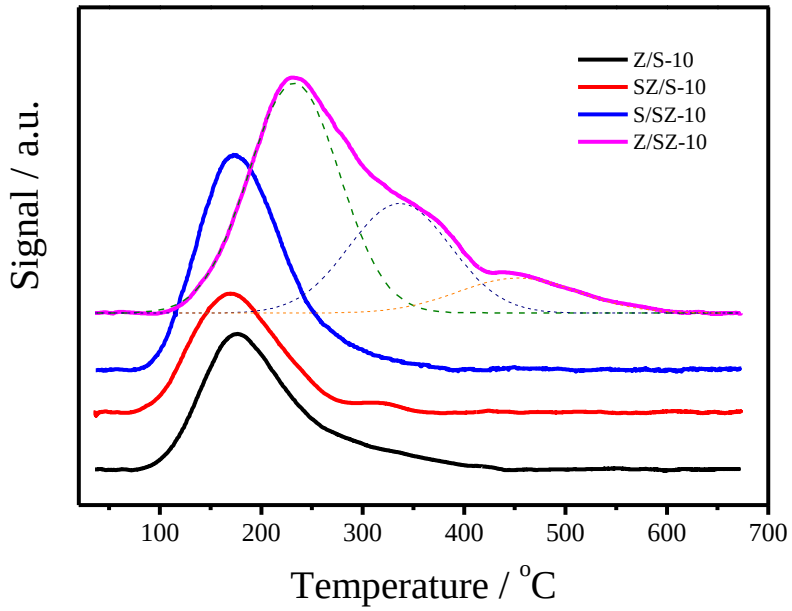

Figure 5.7 NH_3-TPD profiles of the ZrO_2/SiO_2 MNS with low Zr concentration

Generally, the distribution of acidic strengths is a crucial feature for the catalyst that dictates its catalytic performance, and it largely depends on local proximity and the overall structural properties [42]. ^{31}P MAS NMR of adsorbed TMPO is an effective technique for identifying acid types (i.e., BAS and/or LAS), and for determining subtle differences in acid strength and distributions of acid sites [43]. Hydrogen-bonded complexes are usually formed after TMPO is adsorbed onto acid catalyst, thus the density of the electrons surrounding the ^{31}P nucleus should decrease with increasing strength of acidity, which in turn causes the ^{31}P resonance to shift downfield [43-46]. From another aspect, having a downfield shift of ^{31}P MAS NMR could reflect sites that possess a higher acidic strength. Specifically, the ^{31}P NMR chemical shift detected for the adsorbed TMPO probe molecules increases linearly with increasing acidic strengths of the solid acids [47]. BAS and LAS are easy to differentiate, and the variations in acidic strength for both BAS and LAS can also be presented according to the ^{31}P MAS NMR result. The ^{31}P MAS NMR spectra of the ZrO_2/SiO_2 MNS are shown in Figure 5.8 and 5.9 and the chemical shifts,

distributions, and concentrations of acid sites are summarized in Table 5.2 and Table A6 (Appendix).

Generally, BAS locates at chemical shift of δ_{31P}=55-90 ppm, while LAS locates at δ_{31P} < 55 ppm [42, 45, 48-50]. As shown in Figure 5.8, Z/S-10, SZ/S-10 and S/SZ-10 show one peak at ca. 45 ppm, which is assigned to LAS arising from the presence of zirconia. Note that no chemical shift attributed to BAS is observed in these samples, and this is probably because of the low Zr concentration which is not enough for the formation of Si-O(H)-Zr bonds. In Figure 5.8d, Z/SZ-10 presents two peaks at ca. 45 ppm and 60 ppm, respectively, indicating that it possesses the features of both LAS and BAS, with a B/L ratio of 1.244. It is suggested that the zirconia in the outer layer mainly produces LAS while the BAS may come from the interfacial Si-O(H)-Zr bonds between the two layers due to the overwhelming amount of Zr in the outer layer. It turns out that Z/SZ-10 contains LAS similar to Z/S-10 and SZ/S-10, and lower than S/SZ-10. It indicates that Z/SZ, which contains Zr in the outer layer and Si+Zr in the inner layer is more beneficial to the formation of BAS. The proposed formation of LAS and BAS of Z/SZ is depicted in Scheme 5.1.

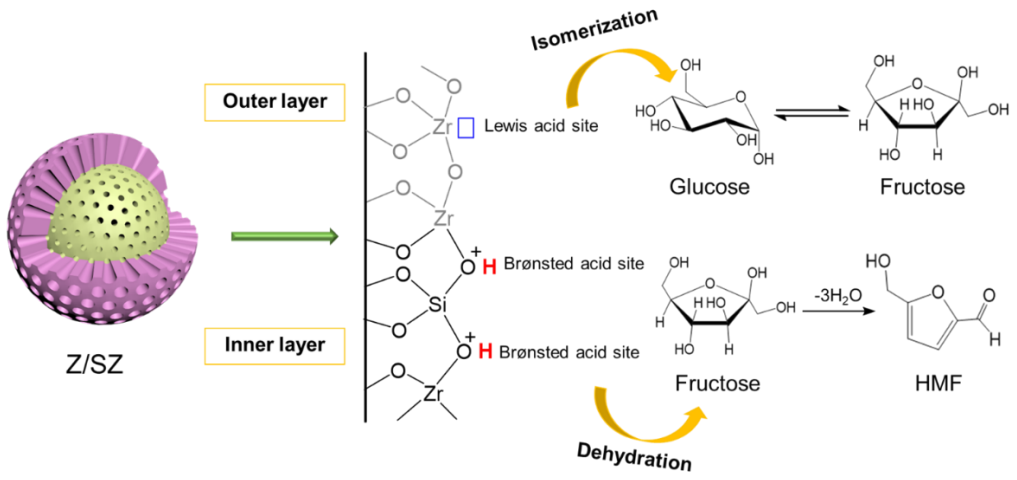

Scheme 5.1 Formation of LAS and BAS on Z/SZ, and the plausible mechanism of glucose conversion in Z/SZ

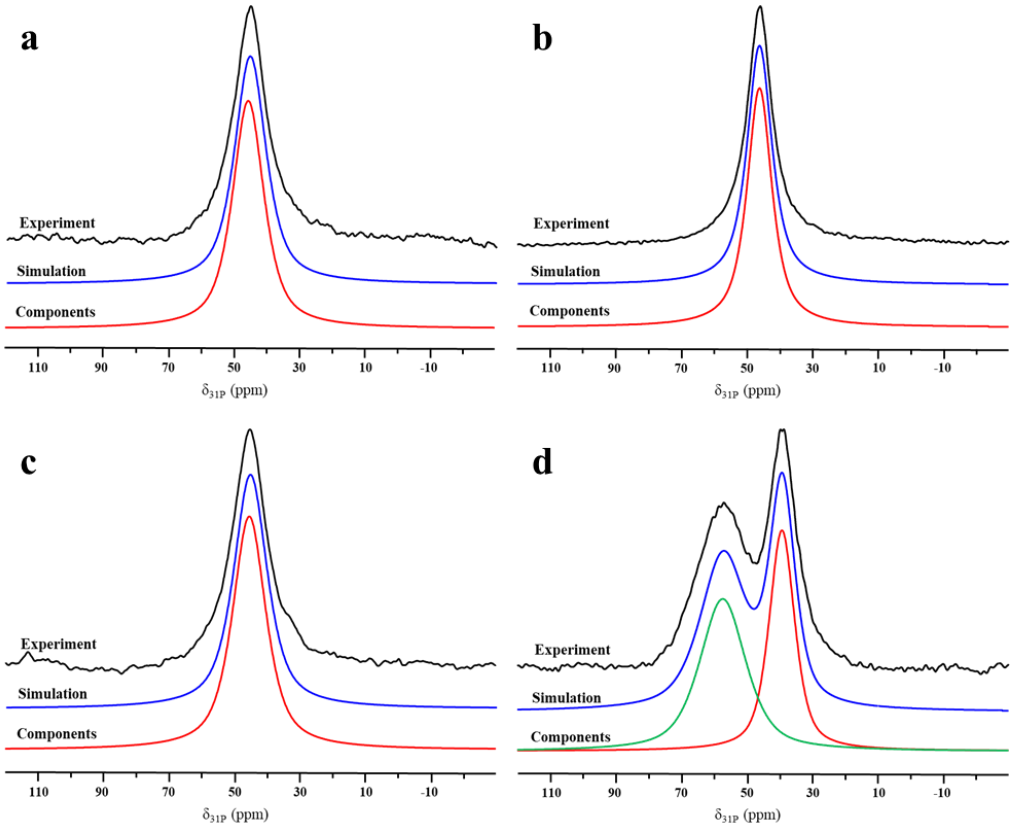

Figure 5.8 ^{31}P MAS NMR spectra of the ZrO_2/SiO_2 MNS: (a) Z/S-10; (b) SZ/S-10; (c) S/SZ-10; and (d) Z/SZ-10

In terms of Z/S-70, SZ/S-70, and S/SZ-70 as shown in Figure 5.9, the materials start to produce BAS when the Zr concentration increases. This is probably because higher Zr concentration can promote the formation of Si-O(H)-Zr bonds which can in turn donate protons, acting as BAS. At the same time, Z/SZ-70 also presents both LAS and BAS, but the LAS locate at the chemical shift of 40 ppm instead of 45 ppm, and the fraction of LAS increases largely (Table A6, Appendix). This may because of the fact that Z/SZ-70 changes dramatically due to the massive introduction of Zr. It seems that the low proportion of Si in this sample is not beneficial for the formation of Si-O(H)-Zr bonds. As a result, this material tends to present the chemical form similar to pure zirconia which normally contains more LAS than BAS [51].

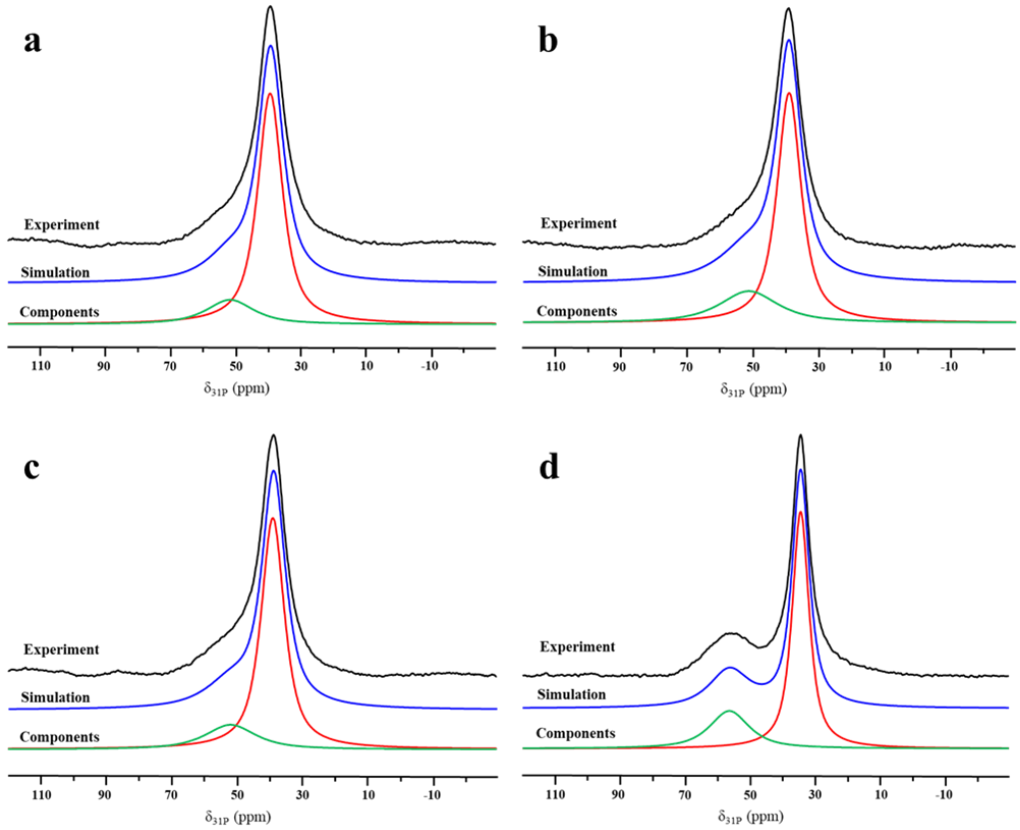

Figure 5.9 ^{31}P MAS NMR spectra of the ZrO_2/SiO_2 MNS: (a) Z/S-70; (b) SZ/S-70; (c) S/SZ-70; and (d) Z/SZ-70

Table 5.2 Quantitative analysis of acid sites in the ZrO_2/SiO_2 MNS according to NH_3-TPD profiles and ^{31}P MAS NMR spectra

	Chemical shift (ppm)[a]		Acid amount (mmol/g cat.)[b]			
	60	45	Brønsted	Lewis	Total	B/L
Z/S-10	-	100	-	0.211	0.211	-
SZ/S-10	-	100	-	0.220	0.220	-
S/SZ-10	-	100	-	0.375	0.375	-
Z/SZ-10	55.5	44.5	0.314	0.252	0.566	1.244

[a.] For comparison, Gaussian-Lorentz simulation results obtained for the samples representing TMPO adsorbed on Brønsted and/or Lewis acid sites (denoted by chemical-shift values) with practically the same chemical shift are aligned in the same column.

[b.] The total acidity was estimated from the NH_3-TPD results, and the BAS and LAS were calculated based on the ^{31}P MAS NMR results, depending on total acidity.

5.3.3 Catalytic activity of the ZrO_2/SiO_2 MNS

Figure 5.10 shows the glucose conversion, fructose yield, and HMF yield over the ZrO_2/SiO_2 MNS with low Zr concentration at 170 °C. It is observed that Z/S-10, SZ/S-10, and S/SZ-10, which only contain LAS, show no glucose conversion at the first 30 min and start to convert glucose when the reaction lasts for 45 min (Figures 5.10a-c). This phenomenon indicates that these samples have caused distinct induction periods in glucose conversion. It also suggests that the acid strength make no significant contribution to glucose conversion since these three structures present similar behaviors at the beginning of reaction though they possess different acid strengths. As a result, the relatively higher acid strength of S/SZ-10 turns out to present the lowest turnover frequency (TOF) compared to the other two structures, shown in Figure 5.11.

On the contrary, Z/SZ-10, which possesses slightly higher LAS than Z/S-10 and SZ/S-10, and lower LAS than S/SZ-10, but contains a large amount of BAS, presents a fast conversion of glucose and rarely shows induction period (Figure 5.10d). Earlier studies pointed out that the glucose isomerization to fructose is reversible, mainly triggered by LAS, and the dehydration of fructose to HMF is irreversible, mostly induced by BAS [22]. Based on the results in this research, it is highly suggested that the presence of BAS can accelerate the conversion of glucose by driving the reaction to HMF direction that can overcome the equilibrium limitation of the isomerization step [24]. In other words, the BAS is vital for glucose conversion. Once there is HMF formed, it can largely contribute to the accumulation of fructose and further transformation of fructose to HMF. Thus, the induction period can be significantly shortened, in agreement with other literature [52]. Z/SZ-10 turns out to exhibit twice higher TOF than all the other samples (Figure 5.11).

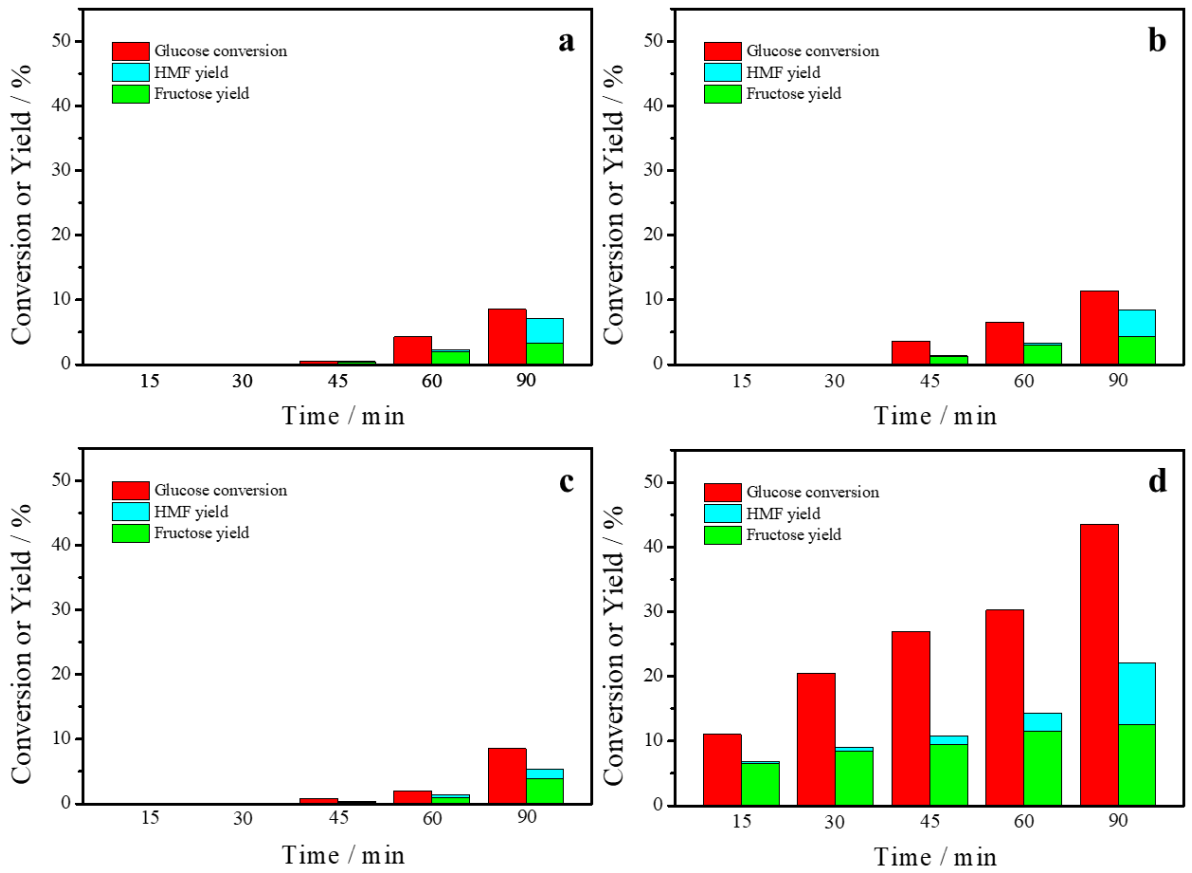

Figure 5.10 Glucose conversion, fructose yield and HMF yield over the ZrO_2/SiO_2 MNS at 170 ^oC: (a) Z/S-10; (b) SZ/S-10; (c) S/SZ-10; and (d) Z/SZ-10

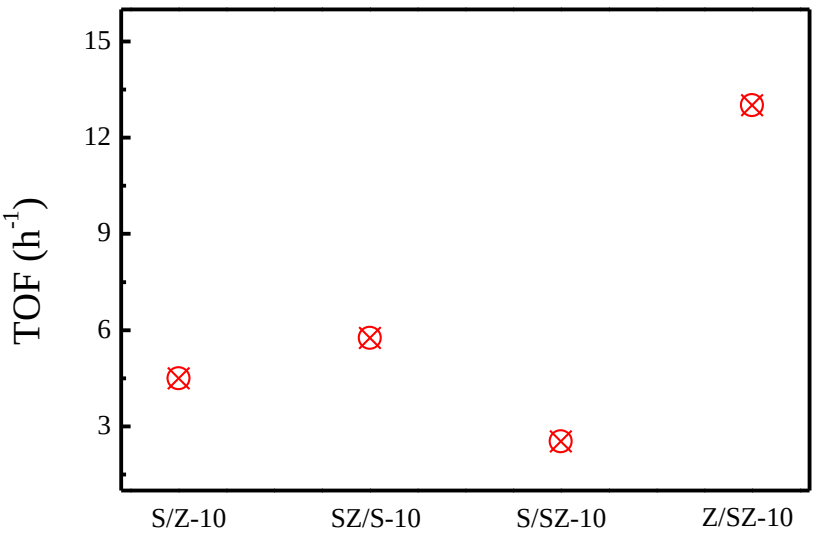

Figure 5.11 Turnover frequencies (TOFs) of the ZrO_2/SiO_2 MNS with low Zr concentrations

When a huge amount of Zr is introduced in the structures, the glucose conversion turns out to be different as shown in Figure 5.12. Since there are BAS formed in Z/S-70, SZ/S-70, and S/SZ-70, the induction periods of these samples are distinctly shortened, which further proves the importance of BAS in glucose conversion (Figures 5.12a-c). The fraction of BAS in Z/SZ-70 is about half of that in Z/SZ-10, but the improvement of the catalytic performance is not as significantly as other structures (Figure 5.12d and Table A6, Appendix). This may be ascribed to the fact that there are BAS existing in Z/SZ-10 throughout all the Zr concentrations, and a specific amount of BAS are sufficient for triggering the reaction to HMF direction. Obviously, the BAS in Z/SZ among all the Zr concentrations are sufficient for glucose conversion.

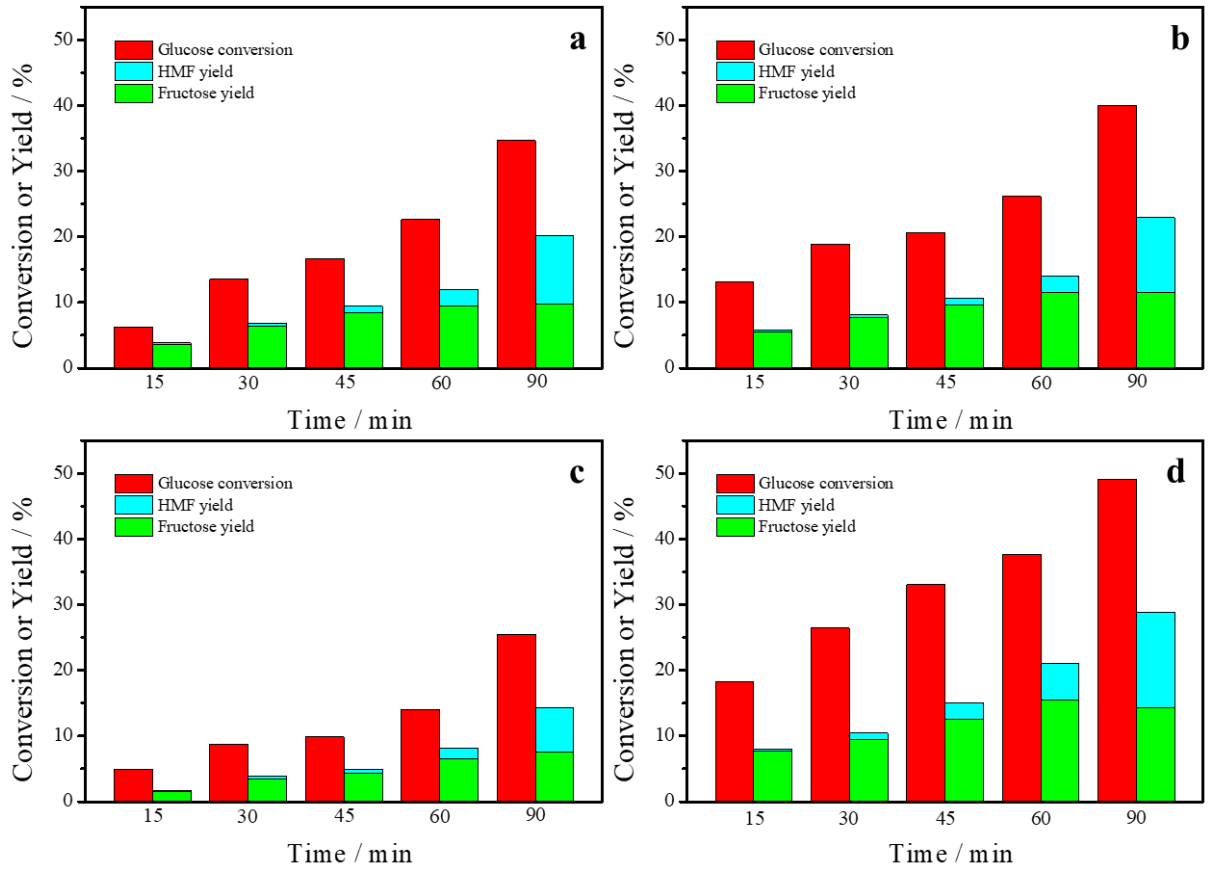

Figure 5.12 Glucose conversion, fructose yield and HMF yield over the ZrO_2/SiO_2 MNS at 170 ^oC: (a) Z/S-70; (b) SZ/S-70; (c) S/SZ-70; and (d) Z/SZ-70

This hypothesis can be further evidenced by the results from Z/SZ-30 and Z/SZ-50 since the improvement of the catalytic performances over both Z/SZ-30 and Z/SZ-50 is also not as prominent as other structures (Figure A10 and Figure A11, Appendix). As for Z/S, SZ/S, and S/SZ, it seems that more Zr concentration leads to a shorter induction period, which may be due to the increase of BAS formed in the materials (Figure A10 and Figure A11, Appendix).

Note that S/SZ shows the lowest activity compared to the other samples regardless of Zr concentration. This is probably attributed to the diffusion effect. The outer layer of S/SZ is silica and the zirconia part which mainly produces acid sites exists in the inner layer of the particles, thus there may be a diffusion barrier that slows down the reaction. Similar phenomenon can be also found in other literature [53, 54]. Overall, Z/SZ is of the prior choice for glucose conversion among all the samples in this research since it mainly produces LAS in the outer layer and BAS in the inner layer along with the interface between the two layers, which may create a tandem structure with different acidic properties in each layer. The plausible mechanism of the reaction in Z/SZ is depicted in Scheme 5.1. The glucose firstly diffuses to the outer layer of Z/SZ and isomerizes to fructose by LAS, then the intermediate product of fructose goes into the inner layer and further dehydrates into HMF. Through tuning the LAS and BAS distribution at different layers in the particles, Z/SZ is of great benefit for glucose isomerization to fructose and further dehydration to HMF. As a result, Z/SZ shows an outstanding catalytic performance over other structures at all the Zr concentrations. It brings about a strategy of tunable way to enhance the catalytic performance of glucose conversion.

The result of glucose conversion over the ZrO_2/SiO_2 MNS at the reaction time of 5 h is presented in Table 5.3. In general, the glucose conversion and HMF yield turn out to be similar among all the different catalysts at the reaction time of 5 h (glucose conversion at 80~95 % and HMF yield

at 31~38 %). To some extent, this result illustrates that the acid strength or distribution doesn't affect much on this reaction when it reaches a certain extent or a dynamic equilibrium state for a long time of reaction in a single batch. This may be also ascribed to the production of humins that affects the reaction process. On the other hand, levulinic acid (LA) and formic acid (FA) are also detected due to the rehydration of HMF [51]. Higher Zr concentration shows slightly higher product yields which may be ascribed to the presence of BAS. Meanwhile, Z/SZ produces more LA and FA than other samples due to its prominent structure and acid distribution. Take this into account, the actual HMF selectivity of the best catalyst in this research is ~50 %, which is comparable to some homogeneous catalysts [55, 56]. Overall, it seems that the Zr concentration and the layer structures of the ZrO_2/SiO_2 MNS can affect the acid strength and distribution of the catalyst which then in turn affect its catalytic performance in glucose conversion.

Table 5.3 Glucose conversion over the ZrO_2/SiO_2 MNS at 170 ^oC at the reaction time of 5 h

Sample	Glucose conversion / %	HMF yield / %	Levulinic acid yield / %	Formic acid yield / %
Z/S-10	80.1	31.2	2.4	1.3
Z/S-30	88.5	31.9	3.1	2.5
Z/S-50	91.8	34.6	5.7	4.0
Z/S-70	92.8	36.6	8.2	5.5
SZ/S-10	89.1	33.1	3.5	1.6
SZ/S-30	89.5	33.3	4.2	3.1
SZ/S-50	92.4	34.8	5.5	4.3
SZ/S-70	94.9	36.9	9.8	7.7
S/SZ-10	76.7	28.4	1.2	0.7
S/SZ-30	84.6	29.5	2.3	1.5
S/SZ-50	84.9	33.6	3.9	2.6
S/SZ-70	87.7	36.2	5.9	3.5
Z/SZ-10	96.3	35.4	12.4	10.9

Z/SZ-30	91.8	34.9	11.5	9.1
Z/SZ-50	91.6	35.5	10.3	8.2
Z/SZ-70	94.7	38.0	12.0	9.4

The stability during the reaction process is one of the most important features of heterogeneous acid catalysts. The reusability of Z/SZ-10 in this research was tested under identical conditions as shown in Figure 5.13. The catalyst still maintains ~93 % of glucose conversion with an HMF yield at ~33 % after five recycles, indicating that there is no significant change of the catalytic behavior.

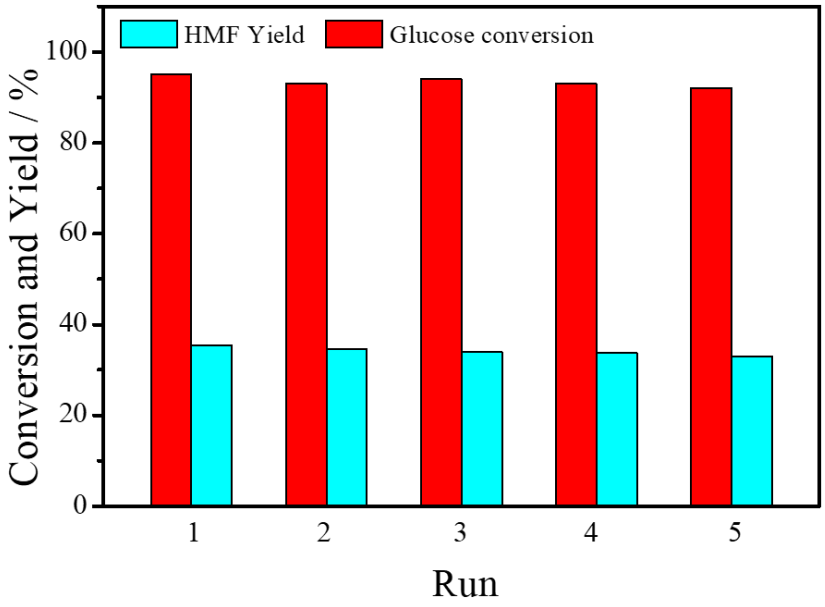

Figure 5.13 The stability test of glucose conversion over Z/SZ-10 catalyst after 5 recycles at 170 ^{o}C

5.4 Conclusion

In conclusion, different layered ZrO_2/SiO_2 MNS with tunable LAS and BAS are successfully designed as the bifunctional nanoreactors. The XRD and BET results show the amorphous nature of all the layered ZrO_2/SiO_2 MNS. The Zr is found to be homogenously dispersed in all the samples according to the HAADF image. The acidity test shows that Z/SZ possesses much higher acidity

than all the other materials when the Zr concentration is low. The Z/SZ-10 is the only one that produces BAS, and it is suggested that the zirconia in the outer layer of Z/SZ-10 mainly produces LAS while the BAS may come from the interfacial Si-O(H)-Zr bonds. The increase of Zr content contributes to the formation of BAS in Z/S, SZ/S, and S/SZ which may be due to the formation of Si-O(H)-Zr bonds. Thanks to the presence of BAS, Z/SZ-10 can dramatically shorten the induction period and exhibit over twice higher TOF compared to other samples. It is found that the BAS can accelerate the conversion of glucose by driving the reaction to HMF direction that can overcome the equilibrium limitation of the isomerization step. Z/SZ, which contains LAS in the outer layer and BAS in the inner layer and layer interface turns out to show the best performance in glucose conversion among all the catalysts. Considering about the rehydration of HMF into LA and FA, the actual HMF selectivity of Z/SZ is ~50 % with a conversion of ~95 %, which is comparable to some homogeneous catalysts. This result is of high importance for the future development of biomass manufacture.

References

[1] Tian, H.; Liu, J. *Adv. Mater.* **2019**, *31*, 1-30.

[2] Kaur, M.; Singh, B. *Chem. Senses.* **2018**, *9*, 1-8.

[3] Zhu, W.; Chen, Z.; Pan, Y.; Dai, R.; Wu, Y.; Zhuang, Z.; Wang, D.; Peng, Q.; Chen, C.; Li, Y. *Adv. Mater.* **2018**, 1-30.

[4] Chen, J.; Zhang, R.; Han, L.; Tu, B.; Zhao, D. *Nano Res.* **2013**, *6*, 871-879.

[5] Liu, B.; Yu, S.; Wang, Q.; Hu, W.; Jing, P.; Liu, Y.; Jia, W.; Liu, Y.; Liu, L.; Zhang, J. *Chem. Commun.* **2013**, *49*, 3757-3759.

[6] Lv, M.; Zhang, Y.; Xin, Q.; Yin, D.; Yu, S.; Liu, S.; Li, L.; Xie, C.; Wu, Q.; Yu, H.; Liu, Y. *Chem. Eng. J.* **2020**, *396*, 1-12.

[7] Jing, L.; Zhang, X.; Guan, R.; Yang, H. *Catal. Sci. Technol.* **2018**, *8*, 2304-2311.

[8] Li, P.; Cao, C. Y.; Liu, H.; Yu, Y.; Song, W. G. *J. Mater. Chem. A* **2013**, *1*, 12804-12810.

[9] Centi, G.; Perathoner, S. *Micropor. Mesopor. Mat.* **2008**, *107*, 3-15.

[10] Zhou, Y.; Noshadi, I.; Ding, H.; Liu, J.; Parnas, R.; Clearfield, A.; Xiao, M.; Meng, Y.; Sun, L. *Catalysts* **2018**, *8*, 1-8.

[11] Takagaki, A.; Tagusagawa, C.; Domen, K. *Chem. Commun.* **2008**, 5363-5365.

[12] Zhou, Y.; Ding, F.; Brittain, A. D.; Liu, J.; Zhang, M.; Xiao, M.; Meng, Y.; Sun, L. *ACS Appl. Mater. Interfaces* **2014**, *6*, 7417-7425.

[13] Naito, N.; Niwa, M. *J. Phys. Chem. B* **1999**, *103*, 7206-7213.

[14] Rinaldi, R.; Schuth, F. *Energy Environ. Sci.* **2009**, *2*, 610-626.

[15] Yang, J.; Zheng, A.; Zhang, M.; Luo, Q.; Yue, Y.; Ye, C.; Lu, X.; Deng, F. *J. Phys. Chem. B* **2005**, *109*, 13124-13131.

[16] Wang, Z.; Jiang, Y.; Stampfl, C.; Baiker, A.; Hunger, M.; Huang, J. *ChemCatChem* **2019**, *12*, 287-293.

[17] Xu, H.; Wang, Z.; Miao, Z.; Zhu, Y.; Marianov, A.; Wang, L.; Castignolles, P.; Gaborieau, M.; Huang, J.; Jiang, Y. *ACS Sustain. Chem. Eng.* **2019**, *7*, 8931-8942.

[18] Moreno-Recio, M.; Santamaría-González, J.; Maireles-Torres, P. *Chem. Eng. J.* **2016**, *303*, 22-30.

[19] Swift, T. D.; Nguyen, H.; Erdman, Z.; Kruger, J. S.; Nikolakis, V.; Vlachos, D. G. *J. Catal.* **2016**, *333*, 149-161.

[20] Gao, X.; Fierro, J. L. G.; Wachs, I. E. *Langmuir* **1999**, *15*, 3169-3178.

[21] Putten, R.; Waal, J. C.; Jong, E.; Rasrendra, C. B.; Heeres, H. J.; Vries, J. G. *Chem. Rev.* **2013**, *113*, 1499-1597.

[22] Choudhary, V.; Mushrif, S. H.; Ho, C.; Anderko, A.; Nikolakis, V.; Marinkovic, N. S.; Frenkel, A. I.; Sandler, S. I.; Vlacho, D. G. *J. Am. Chem. Soc.* **2013**, *135*, 3997-4006.

[23] Zhang, J.; Weitz, E. *ACS Catal.* **2012**, *2*, 1211-1218.

[24] Caratzoulas, S.; Davis, M. E.; Gorte, R. J.; Gounder, R.; Lobo, R. F.; Nikolakis, V.; Sandler, S. I.; Snyder, M. A.; Tsapatsis, M.; Vlachos, D. G. *J. Phys. Chem. C* **2014,** *118*, 22815-22833.

[25] Tang, J.; Guo, X.; Zhu, L.; Hu, C. *ACS Catal.* **2015**, *5*, 5097-5103.

[26] Jiang, C.; Zhu, J.; Wang, B.; Li, L.; Zhong, H. *Chin. J. Chem. Eng.* **2018**, *26*, 1270-1277.

[27] Choudhary, V.; Pinar, A. B.; Lobo, R. F.; Vlachos, D. G.; Sandler, S. I. *ChemSusChem* **2013**, *6*, 2369-2376.

[28] Choudhary, V.; Pinar, A. B.; Sandler, S. I.; Vlachos, D. G.; Lobo, R. F. *ACS Catal.* **2011**, *1*, 1724-1728.

[29] Ishii, H.; Ikuno, T.; Shimojima, A.; Okubo, T. *J. Colloid Interface Sci.* **2015**, *448*, 57-64.

[30] Idakiev, V.; Tabakova, T.; Naydenov, A.; Yuan, Z. Y.; Su, B. L. *Appl. Catal. B: Environ.* **2006**, *63*, 178-186.

[31] Gaudon, A.; Lallet, F.; Boulle, A.; Lecomte, A.; Soulestin, B.; Guinebretière, R.; Dauger, A. *J. Non-Cryst. Solids* **2006**, 352, 2152-2158.

[32] Gaudon, A.; Dauger, A.; Lecomte, A.; Soulestin, B.; Guinebretière, R. *J. Eur. Ceram. Soc.* **2005**, *25*, 283-286.

[33] Ward, A. J.; Pujari, A.; Costanzo, L.; Masters, A. F.; Maschmeyer, T. *Nano. Res. Let.* **2011**, *6*, 1-8.

[34] Sing, K. S. W.; Everett, D. H.; Haul, R. A. W.; Moscou, L.; Pierotti, R. A.; Rouquerol, J.; Siemieniewska, T. *Pure Appl. Chem.* **1984**, *57*, 603-619.

[35] Yang, F. M.; Chen, L.; Au, C. T.; Yin, S. F. *Environ. Prog. Sustain. Energy* **2015**, *34*, 1814-1821.

[36] Kuwahara, Y.; Kang, D. Y.; Copeland, J. R.; Bollini, P.; Sievers, C.; Kamegawa, T.; Yamashita, H.; Jones, C. W. *Chem-Eur. J.* **2012**, *18*, 16649-16664.

[37] Kuwahara, Y.; Kang, D. Y.; Copeland, J. R.; Brunelli, N. A.; Didas, S. A.; Bollini, P.; Sievers, C.; Kamegawa, T.; Yamashita, H.; Jones, C. W. *J. Am. Chem. Soc.* **2012**, *134*, 10757-10760.

[38] Baertsch, C. D.; Soled, S. L.; Iglesia, E. *J. Phys. Chem. B* **2001**, *105*, 1320-1330.

[39] Xu, Y.; Liu, Z.; Han, Z.; Zhang, M. *RSC Adv.* **2017**, *7*, 7140-7149.

[40] Li, G.; Gao, L.; Sheng, Z.; Zhan, Y.; Zhang, C.; Ju, J.; Zhang, Y.; Tang, Y. *Catal. Sci. Technol.* **2019**, *9*, 4055-4065.

[41] Chu, X.; Zhou, D.; Li, D.; Xia, K.; Gan, N.; Lu, X.; Nie, R.; Xia, Q. *Micropor. Mesopor. Mat.* **2016**, *230*, 166-176.

[42] Zheng, A.; Liu, S. B.; Deng, F. *Chem. Rev.* **2017**, *117*, 12475-12531.

[43] Zheng, A.; Huang, S. J.; Liu, S. B.; Deng, F. *Phys. Chem. Chem. Phys.* **2011**, *13*, 14889-14901.

[44] Chen, W. H.; Ko, H. H.; Sakthivel, A.; Huang, S. J.; Liu, S. H.; Lo, A. Y.; Tsai, T. C.; Liu, S. B. *Catal. Today* **2006**, *116*, 111-120.

[45] Zhao, Q.; Chen, W. H.; Huang, S. J.; Wu, Y. C.; Lee, H. K.; Liu, S. B. *J. Phys. Chem. B* **2002**, *106*, 4462-4469.

[46] Rakiewicz, E. F.; Peters, A. W.; Wormsbecher, R. F. *J. Phys. Chem. B* **1998**, *102*, 2890-2896.

[47] Zheng, A.; Huang, S. J.; Chen, W. H.; Wu, P. H.; Zhang, H.; Lee, H. K.; Menorval, L. C.; Deng, F.; Liu, S. B. *J. Phys. Chem. A* **2008**, *112*, 7349-7356.

[48] Lang, S.; Benz, M.; Obenaus, U.; Himmelmann, R.; Hunger, M. *ChemCatChem* **2016**, *8*, 2031-2036.

[49] Zhao, R.; Zhao, Z.; Li, S.; Zhang, W. *J. Phys. Chem. Let.* **2017**, *8*, 2323-2327.

[50] Feng, N.; Zheng, A.; Huang, S. J.; Zhang, H.; Yu, N.; Yang, C. Y.; Liu, S. B.; Deng, F. *J. Phys. Chem. C* **2010**, *114*, 15464-15472.

[51] Zhang, W.; Zhu, Y.; Xu, H.; Gaborieau, M.; Huang, J.; Jiang, Y. *Catal. Today* **2020**, *351*, 133-140.

[52] Bayu, A.; Guan, G.; Karnjanakom, S.; Hao, X.; Kusakabe, K.; Abudula, A. *Chemistry Select* **2016**, *1*, 180-188.

[53] Mamo, W.; Chebude, Y.; Márquez-Álvarez, C.; Díaz, I.; Sastre, E. *Catal. Sci. Technol.* **2016**, *6*, 2766-2774.

[54] Lin, S. Y.; Mckeigue, K.; Maldarelli, C. *Langmuir* **1991,** *7*, 1055-1066.

[55] Pagán-Torres, Y. J.; Wang, T.; Gallo, J. M. R.; Shanks, B. H.; Dumesic, J. A. *ACS Catal.* **2012**, *2*, 930-934.

[56] Wang, T.; Nolte, M. W.; Shanks, B. H. *Green Chem.* **2014**, *16*, 548-572.

Chapter 6 Tailoring the hierarchical pores of ZrO_2/SiO_2 core-shell mesoporous nanospheres for phenylglyoxal conversion

6.1 Introduction

The intramolecular Cannizzaro reaction, which is redox disproportionative conversion of α-keto aldehydes into α-hydroxy carboxylic acid, has been well-known in synthetic organic chemistry since 1897 [1, 2]. The products, mandelic acid and its derivatives, are of great value as intermediates in the synthesis of pharmaceuticals and fine chemicals due to its specific chiral center [3-5]. Therefore, it makes the synthesis of α-hydroxy carboxylic acid and its derivatives from biomass resources promising in green chemistry [6]. In recent years, the efficient preparation of ethyl mandelate (EM) has become a worldwide research priority since it is a stereochemical mandelic derivate that has been widely applied in pharmaceutical and chemical industries [7, 8]. The production of EM can be fulfilled in a single step from biomass materials, phenylglyoxal (PG), via intramolecular Cannizzaro reaction [9, 10].

Solid acid catalyst is a green candidate for catalyzing PG to EM transformation because of its simplicity and versatility of process engineering, and being easier to recover and reuse, fewer reactor and plant corrosion problems, and environmentally safe disposal [11]. Recently, several zeolites and metal doped MCM-41 have been applied for efficient catalytic conversion of C_3 sugars to α-hydroxy carboxylates in alcohols, and the PG conversion to EM has been extensively studied as well [12-14]. Specifically, an outstanding performance was found to be achieved by dealuminated USY zeolite with an EM yield of 95 % and selectivity of 97 % [12]. In the mechanism of PG conversion to EM by Lewis acids dominant reaction, the Lewis acid sites (LAS)

firstly activate the carbonyl function of the aldehyde by attacking the O atom, and then a hemiacetal forms with the help of alcoholic media. Afterwards, an isomerization step happens involving a formal shift of 1,2-hydride between the carbonyl group and the hydrogen donor, with the coordination and activation of the carbonyl group by LAS, and finally forms EM [6, 12]. It was reported that increasing the relative weak BAS of the catalysts can also improve the activity of the catalysts in PG conversion [10, 14, 15].

Besides the influence of acidic strengths and distribution, the pore structures of solid acid catalysts also play a dominant role on the conversion of PG to EM since it can largely affect the diffusion behavior of the big molecules of reactants and products in the catalyst pores, named shape-selectivity. It was reported that [Al]MCM-41, which has much weaker acidic strength than zeolite deAl-HY, presents 8-58 times higher TOFs for PG conversion compared to zeolite. The mesopores of MCM-41 (~4.0 nm) can offer much better reactant and product diffusion than the micropores of dealuminated zeolites Y (~1.1 nm) [15]. Based on this, hierarchical pore structure is more attractive because it can not only raise the effective diffusion coefficient but also reduce the diffusion length [16]. In addition, it can also increase coke tolerance and heighten the effective collisions between substrates and active sites [17-19]. Therefore, hierarchical pore structure can achieve a better shape-selectivity which will result in a higher efficiency in catalytic reactions.

Core-shell mesoporous nanospheres (CS-MNS) have received considerable attention in catalysis industry due to its interesting properties such as stabilizing the shell structure, adding porosity of the catalyst, coordinating between the core and shell function that enabling a higher efficiency, *etc*. [20-22]. Hoon-Joo *et al*. reported a core-shell mesoporous nanosphere consisting of Pt metal core coated with a mesoporous silica shell which can show the similar catalytic activity as bare Pt for ethylene hydrogenation and CO oxidation, but present an outstanding thermally stable property at

a temperature up to 750 ^{o}C that was unlikely for bare Pt nanoparticles because of the aggregation or deformation [23]. Similar catalysts can be also found in other literatures based on the metals of Au, Ce, Zr and Al, *etc*. [24-26]. The application of core-shell mesoporous nanospheres covers a broad range including hydrogenation, oxidation, cross-coupling, and tandem deprotection-Knoevenagel and Henry reactions, *etc*. [22].

With this in mind, hierarchical pores of ZrO_2/SiO_2 core-shell mesoporous nanospheres (ZrO_2/SiO_2 CS-MNS) with different pore size distribution were synthesized. The materials were characterized by Fourier-transform infrared spectroscopy (FT-IR), N_2 adsorption, X-ray diffraction (XRD), transmission electron microscopy (TEM), and energy dispersive spectrometer (EDS). Their acidities were quantitatively investigated by solid-state nuclear magnetic resonance (NMR) spectroscopy. Their catalytic performance was tested in PG conversion to EM.

6.1 Experimental

6.2.1 Catalyst preparation

The synthesis procedure of silica core-shell mesoporous nanospheres (CS-MNS) was modified based on the literature [20]. Different kinds of pore structures were modeled in Figure 6.1.

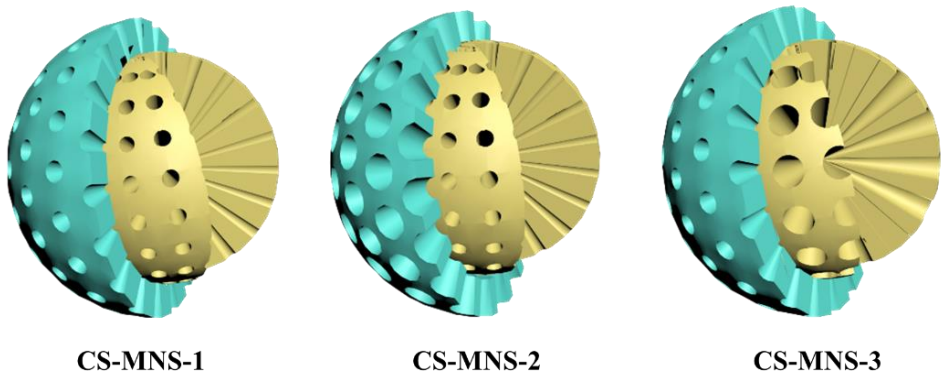

Figure 6.1 The model of the different pore structures in CS-MNS

Preparation of the CS-MNS with the same pores in the shells as the cores: a mixture of surfactant solutions containing cetyltrimethylammonium bromide (CTAB), ethylene glycol (EG), NH_3, and H_2O was stirred at 60 ^oC for 30 min. Then a mixture of 3-aminopropyltriethoxysilane (APTES) and tetraethylorthosilicate (TEOS) was dropwise added into this solution. Afterwards, the mixture was stirred at 60 ^oC for another 4 h to obtain the opaque dispersion nanoparticles. The as-synthesized particles then underwent a regrowth process via adding the same amount of APTES-TEOS mixture to the dispersion and stirring at 60 ^oC for another hour. The molar compositions of the final mixtures are shown in Table 6.1. The surfactant was removed by Lentz method [27, 28]. Basically, the as-synthesized dispersion was dropwise added into a biphasic mixture of hexamethyldisiloxane (HMDS), HCl, 2-propanol and H_2O that was previously stirred at 72 ^oC for 30 min. The mixture was then stirred at 72 ^oC for another 30 min. During this process, trimethylsilylation of the silanol groups on both the internal and external surfaces of the nanospheres happened by the cleavage of HMDS and exchange of the surfactant cations with protons. The trimethylsilylated mesoporous nanospheres were centrifuged from the organic phase and were washed by 2-propanol for three times. The final CS-MNS were dried at 60 ^oC overnight and the sample is denoted as CS-MNS-1.

Preparation of the CS-MNS with larger pores in the shells than the cores: CS-MNS with larger pores in the shells than the cores were synthesized via similar process described above, but a pore expanding agent, 1,3,5-trimethylbenzene (TMB), was added before the regrowth step and stirred for 30 min. The molar ratio of TMB/CTAB was 4, and the molar compositions of the final mixtures are listed in Table 6.1. The surfactant was removed by Lentz method as described above and the sample is denoted as CS-MNS-2.

Preparation of the CS-MNS with larger pores in the cores than the shells: CS-MNS with larger pores in the cores than the shells were synthesized with the help of TMB in the seed production process that can expand the pores in the cores and more CTAB in the regrowth process that can decrease the TMB/CTAB ratio in the liquid phase of the particle dispersion. Basically, a mixture of surfactant solution containing CTAB, EG, NH_3, and H_2O was stirred at 60 ^oC for 30 min, and the TMB was then added into the mixture and vigorously stirred for another 30 min. The APTES-TEOS mixture was then dropwise added into the solution and stirred for 4 h to produce the seed nanospheres with larger pores. Seven times higher than that used for synthesizing the seed nanospheres of CTAB was added into the dispersion after the seed nanospheres were formed, and the mixture was stirred for another 30 min. An APTES-TEOS mixture was then added, and the mixture was stirred for 2 h. The molar compositions of the final mixtures are shown in Table 6.1. The surfactant was removed by Lentz method as described above and the sample is denoted as CS-MNS-3.

Table 6.1 The final molar composition for preparing the CS-MNS

Sample	TEOS	APTES	CTAB	NH_3	EG	H_2O	TMB
CS-MNS-1	2.00	0.34	0.53	12.8	52	1075	0
CS-MNS-2	2.00	0.34	0.53	12.8	52	1075	2.12
CS-MNS-3	2.00	0.34	3.71	12.8	52	1075	2.12

Preparation of the ZrO_2/SiO_2 CS-MNS: Zirconia was loaded on different CS-MNS by wet impregnation method. Basically, 90 mg of CS-MNS was dispersed in 2-propanol and stirred at 30 ^oC for 30 min. A specific amount of zirconium propoxide (ZP) was dissolved in 2-propanol and slowly added into this CS-MNS/2-propanol solution. The resulting mixture was afterwards stirred for another 24 h. The final nanoparticles were dried and calcined at 300 ^oC for 4 h, and the resulting

materials were named as CS-MNS-X-Y (X corresponds to the different types of structure, and Y represents to the ZP amount, 1 %, 5 %, 10 %, and 30 % molar ratio of the CS-MNS).

6.2.2 Catalyst characterization

Fourier transform infrared spectra (FT-IR) were carried out by a Nicolet 6700 FT-IR spectrometer with a 4 cm^{-1} resolution and 32 scans in the range of 4000-600 cm^{-1}. The surface area, pore size, and total pore volume were determined by nitrogen physisorption at -196 ^{o}C in a TriStar II 3020 analyzer (Micromeritics). The samples were pre-treated under vacuum at 100 °C for 8 h. Powder X-ray diffraction (XRD) patterns were obtained on a PANalytical X'Pert PRO diffractometer using Cu$K\alpha$ radiation (λ=0.15406 Å) at 45 kV and 40 mA. The diffraction patterns were obtained under a step size of 0.03 from 10^{o} to 80^{o} (2θ) in a continuous scan mode. High-resolution transmission electron microscopy (HRTEM) on JEM-2100 was employed to investigate the textural properties of the materials. For the preparation of TEM samples, a small amount of the sample powders was dispersed in pure ethanol and immerged in an ultrasonic bath for 10 min. A drop of the colloidal suspension was added on a copper grid coated with carbon film. Afterwards, the samples were air dried at room temperature.

The probe molecule in this research for the test of ^{31}P magic-angle spinning (MAS) NMR spectroscopy is trimethylphosphine oxide (TMPO). Prior to the measurements, each sample was dehydrated at 300 °C for 24 h under vacuum. Loading of the dehydrated samples with TMPO was fulfilled inside a glovebox purged with argon by mixing 10 % (wt/wt) of TMPO in a 4-mm rotor, sealed with a KelF cap afterwards. The TMPO loaded materials inside the sealed rotor were then heated at 160 °C for 2 h under argon flow. The ^{31}P MAS NMR experiments were performed on a Bruker DRX 300 spectrometer, at a Larmor frequency of 121.5 MHz, and a spinning rate of 10

kHz. The spectra were recorded with 3 μs excitation, 10 s relaxation delay, and 64 to 256 scans. The ^{31}P chemical shifts were externally referenced by K_2HPO_4 at 3.0 ppm [25].

6.2.3 Catalytic reaction

The catalytic tests for PG conversion to EM were carried out in the tightly closed 25 mL thick-walled glass reactors at 90 °C in an oil bath. For each procedure, 50 mg of catalyst and 1.25 mL of ethanol (0.4 M) was poured into the reactor. At the specific intervals, the reactors were removed from the oil bath and quenched by submerging the reactors in an ice-water bath. Specific amount of the reaction liquid was taken and centrifuged, and then diluted by ethanol and filtered by 0.22 μm filter. The resulting liquid was analyzed by a gas chromatograph (Shimadzu GC2014) equipped with a capillary column (Rtx-5 column, 30 m×0.25 mm×3 μm) and flame ionization detector (FID). The main products were identified from known standards. The selectivity to specific products I (S_i) was calculated according to Equation (6.1):

$$S_i\ (\%) = 100 \times (i) / [(PG)_0 - (PG)] \qquad (6.1)$$

In which (i) is the molar concentration of the product I, and $(PG)_0$ and (PG) correspond to the molar concentrations of PG before and after the reaction, respectively. Ethanol was used to wash the catalyst after reaction for three times and dried at 60 ^oC before calcination at 300 ^oC for 4 h to remove the organic residues. The reusability of the materials was tested by repeating the reaction under the same reaction conditions for five times.

6.3. Results and discussion

6.3.1 Synthesis of the CS-MNS

The cationic surfactant, CTAB, was used as the mesoporous template for the synthesis of CS-MNS in this research and Lentz method was applied to remove the CTAB in the post synthesis step. FT-

IR analysis was carried out to confirm the complete removal of CTAB. Corresponding to the characterization of CTAB as shown in Figure 6.2a, the CS-MNS with surfactant show strong absorption peaks at 2918 and 2850 cm^{-1} which are assigned as the symmetric and asymmetric stretching vibration of the methylene chains, while the multiple absorption bands at the region of 1400-1500 cm^{-1} mainly arise from the C-H bending vibration [29, 30]. On the other hand, these peaks observed in the CS-MNS with surfactant are absent in the CS-MNS after removing the CTAB via Lentz method, indicating the complete removal of surfactant. In Figure 6.2b, the peaks at 1043 and 942 cm^{-1} are ascribed to the asymmetric stretching vibration Si-O-Si and asymmetric bending of Si-OH, respectively [31]. The stretching vibration of Si-OH and -OH of physical adsorbed water molecules locate at the broad peak at 2700-3700 cm^{-1}. Meanwhile, there is a small peak at 2962 cm^{-1} which denotes to the asymmetric stretching vibration of C-H bond belonging to $-CH_3$ group, due to the trimethylsilylation of the silanol groups on both internal and external surfaces of the CS-MNS particles. The FT-IR result highly proves the successful removal of the surfactant in the materials.

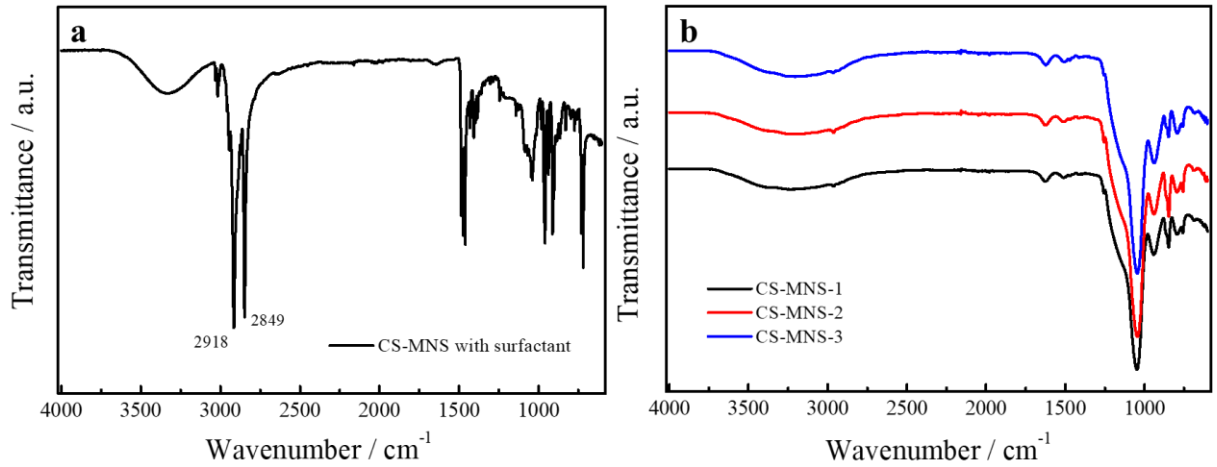

Figure 6.2 FT-IR of CS-MNS with surfactant (a) and after removing surfactant via Lentz method (b)

6.3.2 Physicochemical characteristics of the ZrO_2/SiO_2 CS-MNS

Nitrogen physisorption was used to identify the different pore structures of the materials. Figure 6.3 shows the N_2 adsorption-desorption isotherms and the pore size distributions calculated by the non-linear density function theory (NLDFT) according to previous literature [32]. Table 6.2 presents the BET surface area, pore volume and pore size of the materials. According to Figure 6.3a, all the isotherm curves of CS-MNS are type IV which are typical of mesoporous materials, but characterized by different multilayer adsorption steps and capillary condensation behaviors, indicating different pore structures [32, 33]. The hysteresis loops observed at p/p_0=0.9-1.0 for all the CS-MNS were attributed to interparticle voids. After monolayer adsorption, there is only one stage at p/p_0 = ~0.3 corresponding to multilayer adsorption, and a following H1 hysteresis loop turns out in the isotherm curve of CS-MNS-1, demonstrating a well-defined pore with uniform pore size at 3.7 nm (Figure 6.3a and 6.3b). On the other hand, multi gas uptake stages of multilayer adsorption at p/p_0=0.3-0.5 were detected in the sample of CS-MNS-2, indicating the disordered distribution of pores. The H2 hysteresis loop and wide pore size distribution (3.9 nm and 5.2 nm) in NLDFT results also demonstrate a structure of different pore size distribution. It is suggested that TMB acts as a pore expander during the regrowth procedure accompanied by the rearrangement of the silicate frameworks [20]. As for the structure of CS-MNS-3, the stage of multilayer adsorption at p/p_0=~0.4 and the much sharper H1 pore condensation process at p/p_0=0.9-1.0 indicates the presence of a narrower pore size distribution in the shell. Two peaks were observed at 4.5 nm and 5.2 nm in pore size distribution of CS-MNS-3. It is likely that the addition of CTAB plays an important role for the formation of the smaller pores in the shell by decreasing the micelle size during the regrowth step [20]. The BET surface areas of CS-MNS-1, CS-MNS-2, and CS-MNS-3 are 713.1 m^2/g, 823.8 m^2/g, and 579.0 m^2/g, respectively. There is no

evidence of microporosity for all the samples from their t-plot curves. It is concluded that CS-MNS with different pore sizes distribution in the core and shell were successfully synthesized.

Nitrogen physisorption was also applied for the CS-MNS after loading 10 % of Zr as shown in Figure 6.3c and 6.3d. Basically, all the materials still keep the main characteristic of the N_2 adsorption-desorption behavior, but with lower BET surface areas and pore volumes due to the induction of zirconia. The pore size distribution has shift to smaller value for the small pore size, and the big pore size of 5.2 nm still remains. The overall NLDFT pore size distribution peaks become broader than the CS-MNS without loading zirconia. As shown in Figure A12 and Table A7 (Appendix), the CS-MNS with a higher Zr concentration (30 %) shows similar result as that with 10 % of Zr, but with slightly wider hysteresis loops. Based on these results, it is suggested that the pore structures of the CS-MNS are not changed after loading zirconia, even at high zirconia concentrations.

Table 6.2 BET surface areas, pore sizes and pore volumes of CS-MNS

Sample	BET surface area (m^2/g)	Average pore size (nm)	Pore volume (cm^3/g)
CS-MNS-1	713.1	3.7	0.632
CS-MNS-2	823.8	3.9, 5.2	0.831
CS-MNS-3	579.0	4.5, 5.2	0.646
CS-MNS-1-10Zr	698.8	3.2	0.512
CS-MNS-2-10Zr	677.5	3.3, 5.2	0.617
CS-MNS-3-10Zr	567.0	4.2, 5.2	0.553

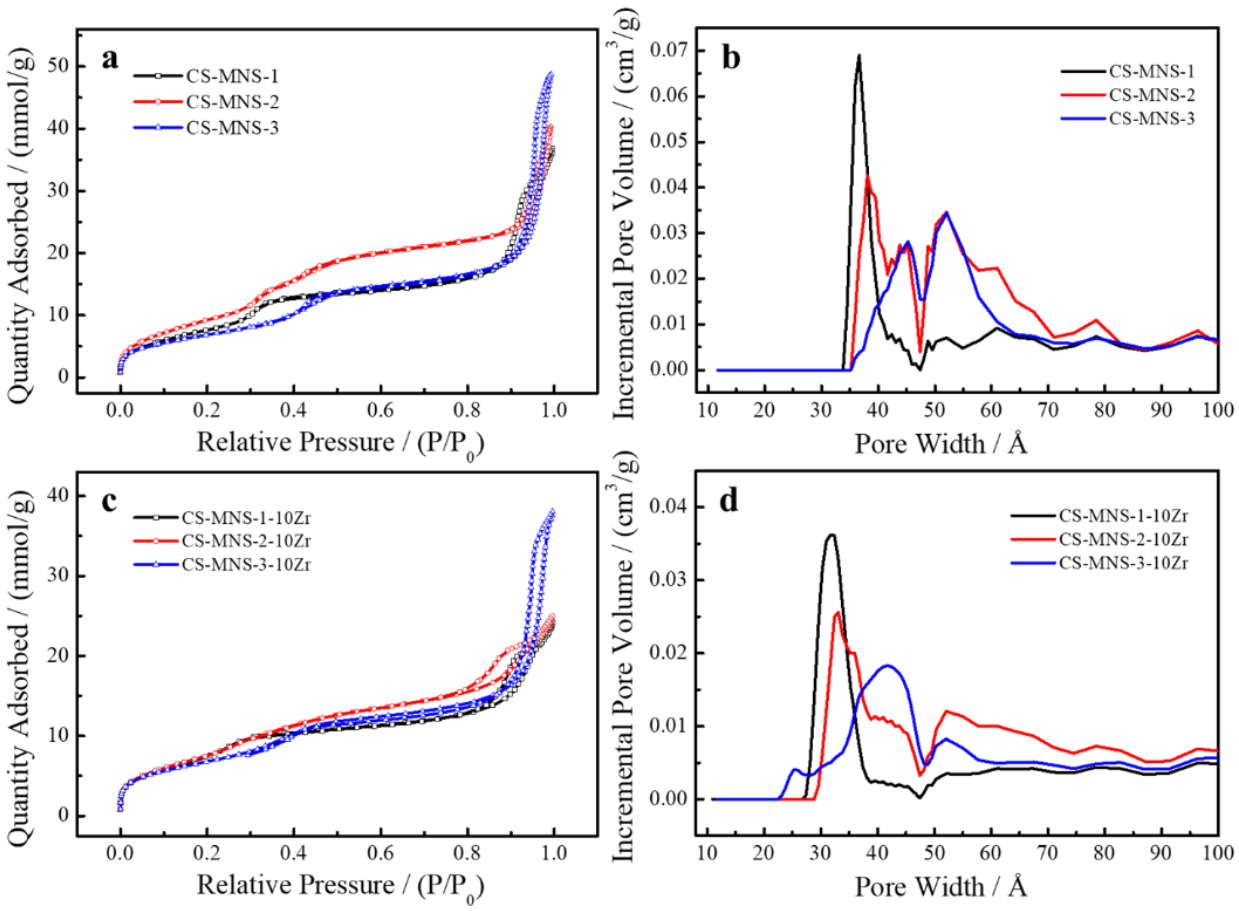

Figure 6.3 N_2 adsorption-desorption isotherms (a, c) and pore size distributions (b, d) of CS-MNS: (a, b) CS-MNS-1, CS-MNS-2, and CS-MNS-3; (c, d): CS-MNS-1-10Zr, CS-MNS-2-10Zr, and CS-MNS-3-10Zr

The XRD patterns of the CS-MNS loading 10 % of Zr are presented in Figure 6.4. All the materials display two broad peaks in 2θ ranges of 15-40^o and 40-70^o, suggesting the amorphous nature [34]. Normally, pure mesoporous silica presents one broad XRD peak at 15-40^o [35]. In this case, the broad peak at 40-70^o is mainly ascribed to the introduction of zirconia which has been incorporated into the silica framework. There is no obvious diffraction associated with the crystalline phase of zirconia, indicating no bulk crystalline zirconia presents in these structures [36].

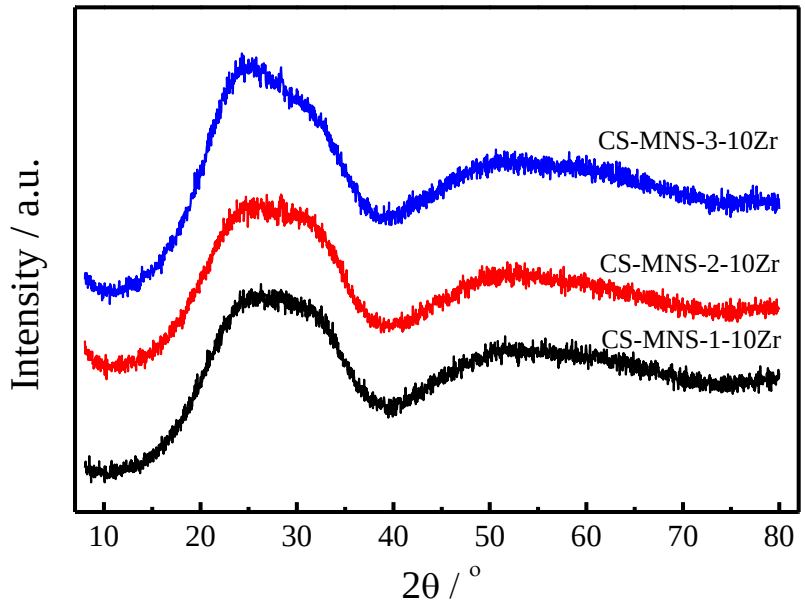

Figure 6.4 XRD patterns of the CS-MNS loading 10 % Zr

Figure 6.5 presents the TEM images of the CS-MNS loading 10 % Zr, which shows spherical particles of all the samples. The average sizes of CS-MNS-1-10Zr, CS-MNS-2-10Zr, and CS-MNS-3-10Zr are ~65.9 nm, ~77.6 nm, and ~63.6 nm in diameter, respectively. Since there is no pore expanding agent or more surfactant added during the synthesis process, the TEM images of CS-MNS-1-10Zr show particles with the uniform light and dark field, indicating its uniform pore size distribution (Figure 6.5a). However, in the sample of CS-MNS-2-10Zr, it presents the particles that have relatively denser/darker inner parts and looser/brighter outer parts, suggesting a core-shell structure, and it also displays distinct larger pores in the shell than the cores (Figure 6.5b). As for the sample of CS-MNS-3-10Zr, though the particles also show darker inner parts and brighter outer parts, the inner parts contain apparently larger pores while the shell parts display smaller pores (Figure 6.5c). The TEM result further evidences that the ZrO_2/SiO_2 CS-MNS with different pore structures were successfully synthesized and it is also in agreement with the BET results and the literature [20].

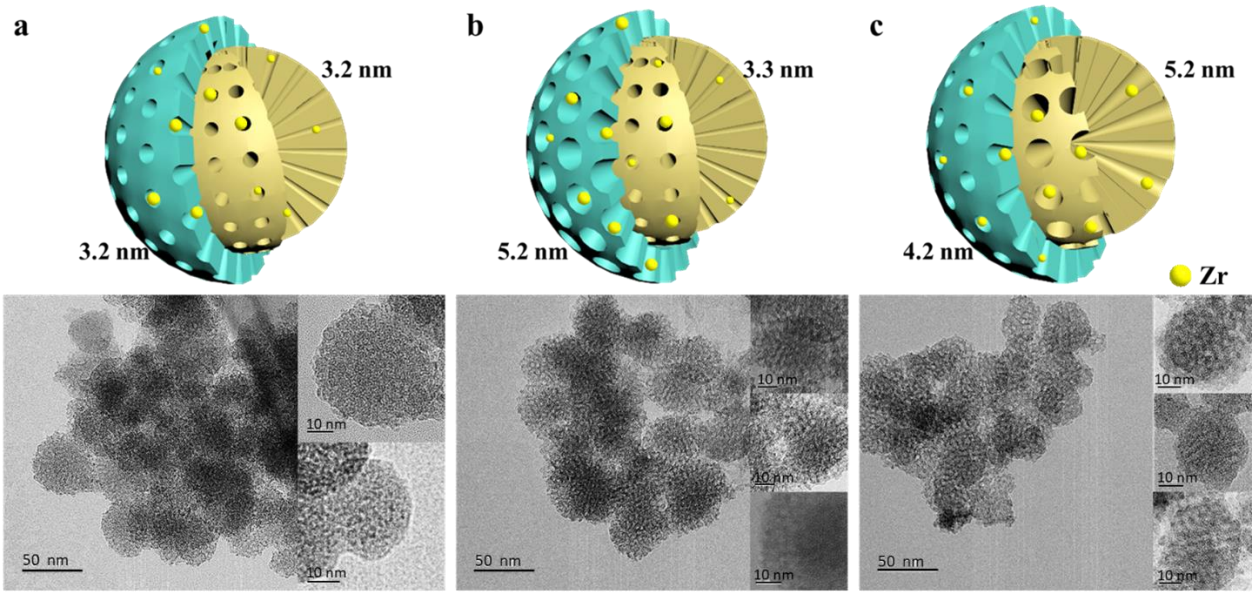

Figure 6.5 TEM images of the CS-MNS loading 10 % Zr, and the shape model of each structure: (a) CS-MNS-1-10Zr; (b) CS-MNS-2-10Zr; and (c) CS-MNS-3-10Zr (Pore size in this figure is from the BET results above, and the insets mainly present the morphology of specific one particle)

The element distribution of the CS-MNS loading 10 % Zr is shown in Figure 6.6. For all the materials, the elements of Si and Zr are overall homogenously dispersed. Yasutaka K. *et al*. reported that Zr could be incorporated more uniformly in the mesoporous silica matrix comparing to other metals such as Ce or Ti, without co-crystallization or co-precipitation of other phases, which may in turn contribute to an enhanced performance [37].

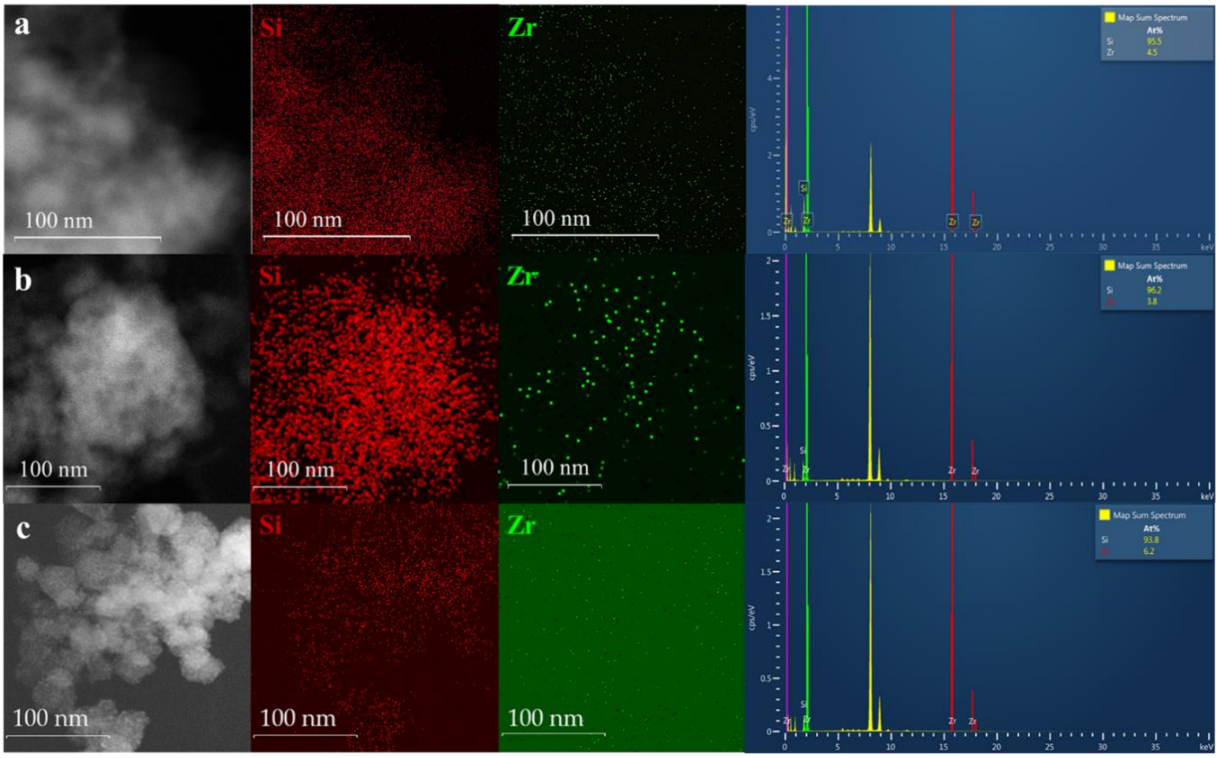

Figure 6.6 EDS mapping of the CS-MNS loading 10 % Zr: (a) CS-MNS-1-10Zr; (b) CS-MNS-2-10Zr; and (c) CS-MNS-3-10Zr

6.3.3 Acidity characterization of the ZrO_2/SiO_2 CS-MNS

Generally, the overall concentration and strength of the acidity along with the distribution of acid sites in the catalyst is an important feature for the catalytic performance in the reactions. ^{31}P MAS NMR is an effective technique for identifying Lewis acid sites (LAS) and Brønsted acid sites (BAS), and the subtle differences in acid strength and distributions for the catalysts [38]. The overall concentration of the acidity can also be determined by the quantitative analysis comparing to the standard. Up to date, trialkylphospine oxides (R_3PO) have been widely studied as the practical probe molecules in ^{31}P MAS NMR. Compared to triethylphosphine oxide (TEPO), tributylphosphine oxide (TBPO), and trioctylphosphine oxide (TOPO), trimethylphosphine oxide (TMPO) is the most popular one since it has the smallest kinetic diameter of ca. 0.55 nm that is

comparable to the aperture of typical ten-membered ring zeolites [39]. Having a downfield shift of ^{31}P MAS NMR adsorbed TMPO could reflect sites that possess a higher acidic strength. The ^{31}P MAS NMR spectra of the CS-MNS loading 10 % Zr are shown in Figure 6.7 and the chemical shifts, distributions, and concentrations of acid sites are reported in Table 6.3.

Normally, the BAS and LAS are experimentally observed of ^{31}P MAS NMR shift at δ_{31P}=55-90 ppm and δ_{31P} < 55 ppm, respectively [39-41]. However, there is an overlap of the isotropic shift ranges for BAS and LAS for NMR acidity probes including TMPO, thus a universal classification of BAS and LAS based on the ^{31}P MAS NMR shift of TMPO is hard to be exactly identified [42]. In Figure 6.7, the ^{31}P signals at 44 ppm and 61 ppm are no doubt assigned to LAS and BAS, respectively. Due to the wet impregnation synthesis method, the Lewis acidity may come from the presence of zirconia while the Brønsted acidity is probably ascribed to the strong interaction between Zr and Si by forming Zr-O(H)-Si bonds. The chemical shift at 52 ppm is defined as weak BAS from weak interaction between Zr and Si.

According to Table 6.3, it shows that the CS-MNS after loading Zr mainly present Lewis acidity which occupies more than half of the total acidity. Due to the different pore structures, zirconia may locate at different parts of the mesopores, which may result in different extents of zirconia aggregation, and also different strength of interactions between Zr and Si, thus it may generate different acidic features. As summarized in Table 6.3, CS-MNS-1-10Zr possesses the highest total acidity than the other two structures, regardless of LAS or BAS. This may be due to the fact that the uniform distribution of the pore size in CS-MNS-1-10Zr enables Zr evenly located in the mesopores of the materials, which in turn largely reduce zirconia aggregation. As a result, more Zr can be exposed and execute its Lewis acidic nature. At the same time, uniform distribution of Zr in the mesopores can also increase the number of Zr interacted with Si, thus promote the

formation of Zr-O(H)-Si bonds, acting as BAS. However, hierarchical structures of CS-MNS-2-10Zr and CS-MNS-3-10Zr may cause slight zirconia aggregation in the pores of the materials. The less Zr exposed and less Zr reacting with Si lead to a lower acidity. Different hierarchical structures contribute to different extents of zirconia aggregation, generating different acidic features. In this research, CS-MNS-3-10Zr produces higher acidity than CS-MNS-2-10Zr, regardless of LAS and BAS. Based on the quantitative result, the CS-MNS loading 10 % Zr turn out to contain slightly higher acidity than the ZrO_2/SiO_2 from the other research [9].

As for the B/L ratio, CS-MNS-1-10Zr displays the highest ratio than CS-MNS-2-10Zr and CS-MNS-3-10Zr, indicating that it contains the lowest fraction of LAS. In another words, though hierarchical structures of CS-MNS-2-10Zr and CS-MNS-3-10Zr have lower acidity than CS-MNS-1-10Zr, the zirconia aggregation will lead to a higher fraction of LAS. The different acidic features along with the different pore structures will probably endow the catalysts special catalytic activity in chemical reactions, thus achieving the different performance in the reaction.

Table 6.3 Quantitative analysis of acid sites in the CS-MNS loading 10 % Zr according to ^{31}P MAS NMR spectra, and turnover frequencies (TOFs) of the PG conversion over the catalysts

	Chemical shift (ppm)[a]			Acid amount (μmol/g cat.)[b]				TOF (h^{-1})[c]
	44	52	61	BAS	LAS	Total	B/L	
CS-MNS-1-10Zr	60.8	35.1	4.1	71.5	110.8	182.3	0.65	14.0
CS-MNS-2-10Zr	64.3	30.6	5.1	36.5	65.8	102.3	0.55	35.1
CS-MNS-3-10Zr	66.8	27.0	6.2	45.8	92.3	138.1	0.50	34.5

[a.] For comparison, Gaussian-Lorentz simulation results obtained for the samples representing TMPO adsorbed on Brønsted and/or Lewis acid sites (denoted by chemical-shift values) with practically the same chemical shift are aligned in the same column.

[b.] The total acidity was calculated based on the standard of K_2HPO_4, and the specific BAS and LAS were calculated according to the simulation results.

[c.] TOF calculated based on initial PG conversion (~ 10%) and the total acidity.

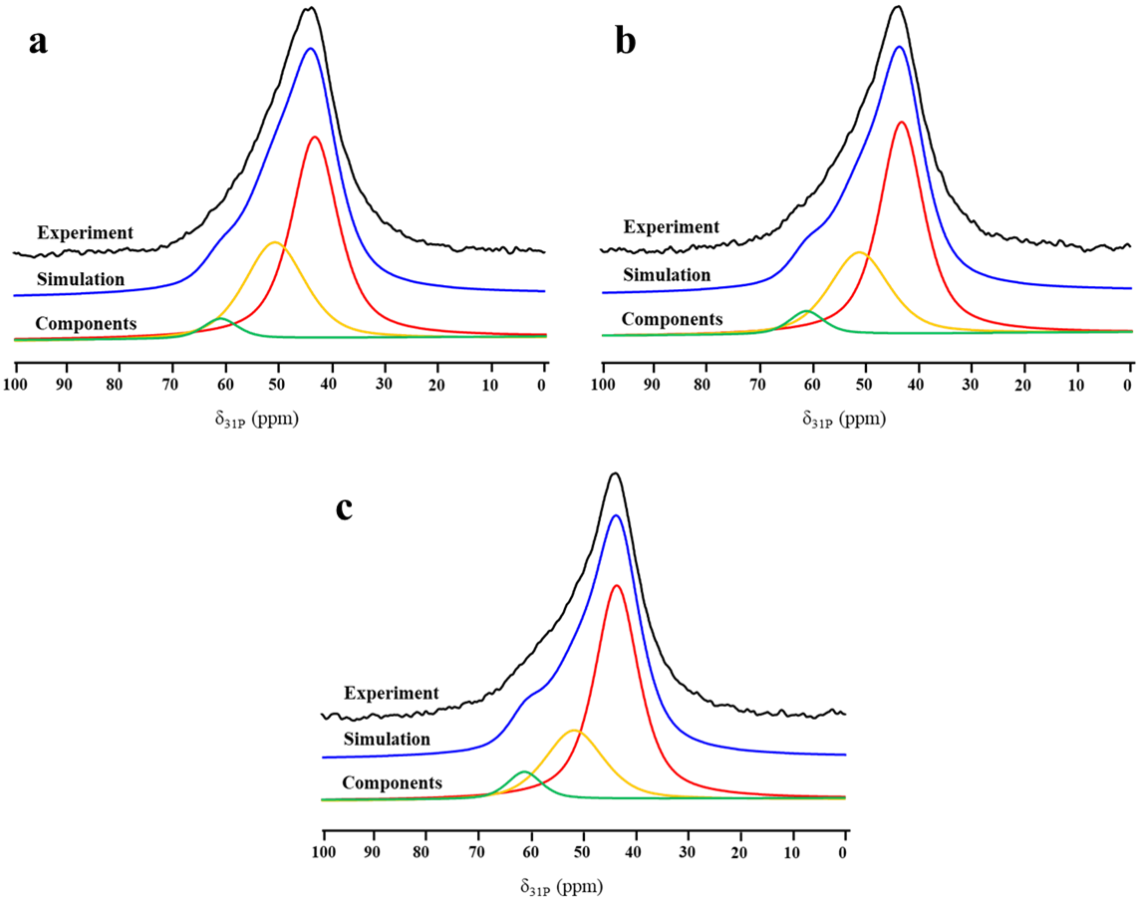

Figure 6.7 ^{31}P MAS NMR spectra of the CS-MNS loading 10 % Zr: (a) CS-MNS-1-10Zr; (b) CS-MNS-2-10Zr; and (c) CS-MNS-3-10Zr

6.3.4 Catalytic activity of the ZrO_2/SiO_2 CS-MNS

The catalytic conversion of PG to EM in ethanol was performed over different ZrO_2/SiO_2 CS-MNS at 90 ^oC. The pure CS-MNS without loading zirconia, which is exclusively characterized by nonacidic surface SiOH groups, is unable to convert PG to EM and shows almost no PG conversion even after 6 h, similar to the literature (Table 6.4) [15]. As shown in Figure 6.8, all the structures display an increasing catalytic activity in PG conversion as zirconia concentration increases. The improvement of the catalytic performance in CS-MNS-2 and CS-MNS-3 are more prominent than

CS-MNS-1, especially at the Zr concentration of 5 % and 10 %. The overall selectivity of EM is stable at 97-99 % at all the reaction stages, similar to other literature [9, 10, 15].

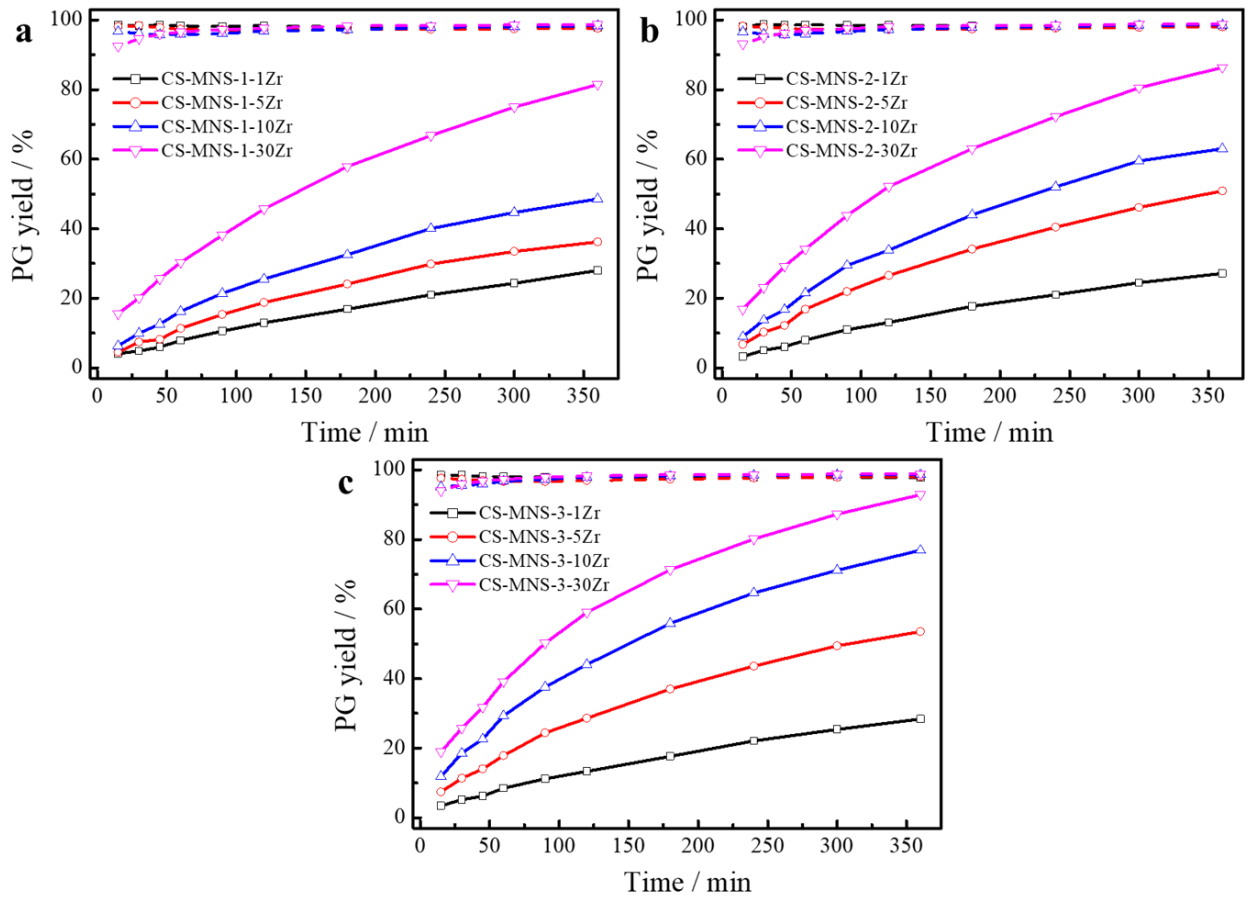

Figure 6.8 Catalytic conversion of PG in ethanol (———) and selectivity of EM (------) over different CS-MNS loading 1 %, 5 %, 10 %, and 30 % of Zr: (a) CS-MNS-1; (b) CS-MNS-2; (c) CS-MNS-3

Detailed reaction results after 6 h are listed in Table 6.4. When 1 % of Zr was loaded on CS-MNS, the pore structure has little effect on the catalytic performance in PG conversion (~28 %), and this is probably ascribed to the very low acidity due to the low Zr loading. As zirconia concentration increases to 5 %, the hierarchical pore structures start to play its role in the reaction. The CS-MNS-2-5Zr (~51 %) and CS-MNS-3-5Zr (~54 %) show prominent performance than the structure of

CS-MNS-1-5Zr (~36 %). Further increase of the zirconia content highlights the advantages of hierarchical pore structures, and it shows the superiority when the Zr concentration is 10 %. Due to the different hierarchical structures, CS-MNS-3-10Zr presents the best catalytic performance at a PG conversion of ~77 %, follows CS-MNS-2-10Zr at ~63 %, and the lowest conversion of 49 % goes into CS-MNS-1-10Zr. Xu *et al*. reported that there is a balance of BAS and LAS for the PG conversion to EM, and a suitable B/L ratio was achieved when the B/L ratio is 0.48 [6]. In this research, the best catalyst CS-MNS-3-10Zr shows a B/L ratio of 0.50, which is in agreement with the previous literature (Table 6.3) [6]. When the Zr concentration increases to 30 %, CS-MNS-1-30Zr, CS-MNS-2-30Zr, and CS-MNS-3-30Zr display PG conversions of ~81 %, ~86 %, and ~93 %, respectively. According to the results of PG conversion, CS-MNS-3 with smaller shell and larger cores displays the best performance among all the structures. Compared to the research from Xu *et al*. and Wang *et al.*, which attained maximum PG conversions of ~73 % and ~68 %, respectively, the catalyst in this research can achieve a better performance with a maximum PG conversion of ~93 % [6, 9].

Table 6.4 Catalytic results of PG conversion after 6 h of reaction

Sample	C_{PG} / %	S_{PG} / %	Sample	C_{PG} / %	S_{PG} / %
CS-MNS-1	3.6	97.6	CS-MNS-3	3.3	97.1
CS-MNS-2	2.8	96.5	-	-	-
CS-MNS-1-1Zr	28.0	97.8	CS-MNS-1-10Zr	48.6	98.3
CS-MNS-2-1Zr	27.1	98.2	CS-MNS-2-10Zr	63.0	98.6
CS-MNS-3-1Zr	28.4	97.7	CS-MNS-3-10Zr	76.9	98. 7
CS-MNS-1-5Zr	36.3	97.6	CS-MNS-1-30Zr	81.4	98.7
CS-MNS-2-5Zr	50.8	98.0	CS-MNS-2-30Zr	86.4	98.9
CS-MNS-3-5Zr	53.5	98.1	CS-MNS-3-30Zr	92.9	98.8

The turnover frequency (TOF) is often used as an indicator to evaluate the performance of active sites during the reaction. The calculated TOFs based on the total acidity of the CS-MNS loading 10 % of Zr are summarized in Table 6.3. The relatively large pore size of 3.2-5.2 nm of the materials is preferable for the diffusion of the reactants, thus it presents much better performance than other non-porous materials [9]. As shown in Table 6.3, CS-MNS-1-10Zr presents a TOF of 14.0 h^{-1}, which is the lowest among all the structures. According to the reaction pathway of PG to EM, the molecular size will undergo a process of expanding due to the interaction with alcoholic oxygen and the introduction of ethoxy group [6, 10]. Based on this point, it suggests that the hierarchical pore structures can promote the PG conversion since they can not only heighten the effective collision between the substrates and active sites but also promote the diffusion of the reactants to the active sites because of its special steric features [19]. As a result, though CS-MNS-2-10Zr and CS-MNS-3-10Zr possess much lower acidity than CS-MNS-1-10Zr, they can achieve a much better catalytic performance, with the TOFs more than twice over CS-MNS-1-10Zr. The resulting TOFs of 35.1 and 34.5 h^{-1} for CS-MNS-2-10Zr and CS-MNS-3-10Zr, respectively, are higher than the TOFs obtained from other silica-zirconia materials from the literature and other solid acid catalyst such as silica-alumina [9, 10].

The reusability of the CS-MNS-3-10Zr was tested under identical conditions as shown in Figure 6.9. The catalyst can still achieve ~70 % of PG conversion, and there is no significant change of the EM selectivity, indicating that the catalyst can maintain stable catalytic behavior after 5 recycle uses. The partial loss of the catalytic activity could be due to the blockage of some active sites by the unknown byproducts. This research further illustrates the important role of hierarchical pore structures in the catalytic reactions which contain the variation of the molecular chain length.

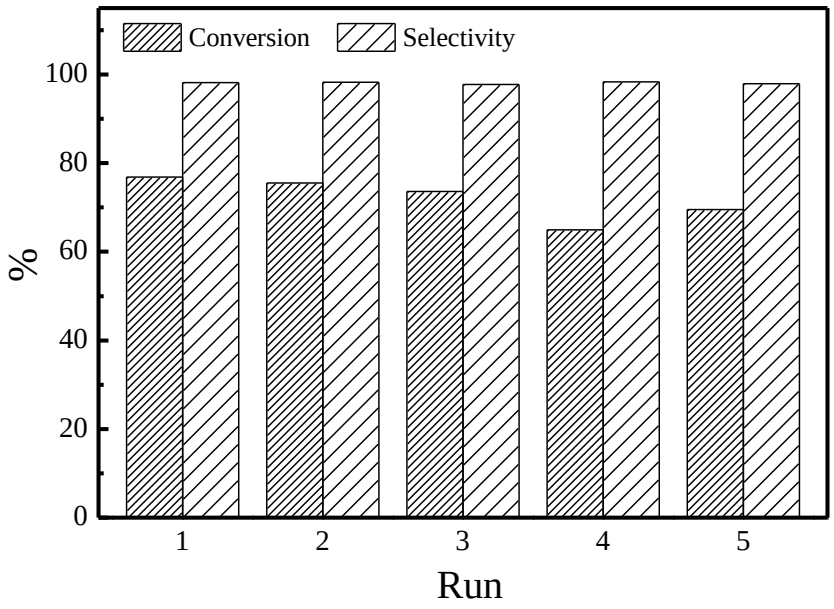

Figure 6.9 Recycling experiments of CS-MNS-3-10Zr for the PG conversion

There are three possible mechanisms of PG conversion to EM on MNSs presented below (Figure 6.10). In Mechanism 1, it involves activation of PG aldehyde oxygen with mobile BAS with following attack of ethanol molecule on adjacent carbon atom. The resulting hemiacetal then adsorbs on LAS where it undergoes intramolecular Cannizzaro reaction (formation of five-membered cyclic intermediate with H shift from -CHO group to -CO group) producing EM. In Mechanism 2, it requires only LAS which both activate the molecule for alcohol adhesion and following Cannizzaro reaction. Mechanism 3 is catalyzed by sufficient BAS, which will produce the undesirable byproducts of phenylglyoxal diethyl acetal. The catalysts in this research are dominant by LAS and weak BAS, it can be presumed that the first two mechanisms may dominate for the reaction process. The high EM selectivity also certifies this proposal. In both Mechanism 1 and 2, there is a process of molecular size expanding due to the introduction of ethoxy group, which further confirms that hierarchical structures are favorable for this reaction since the special steric features may be benefit for molecular extension.

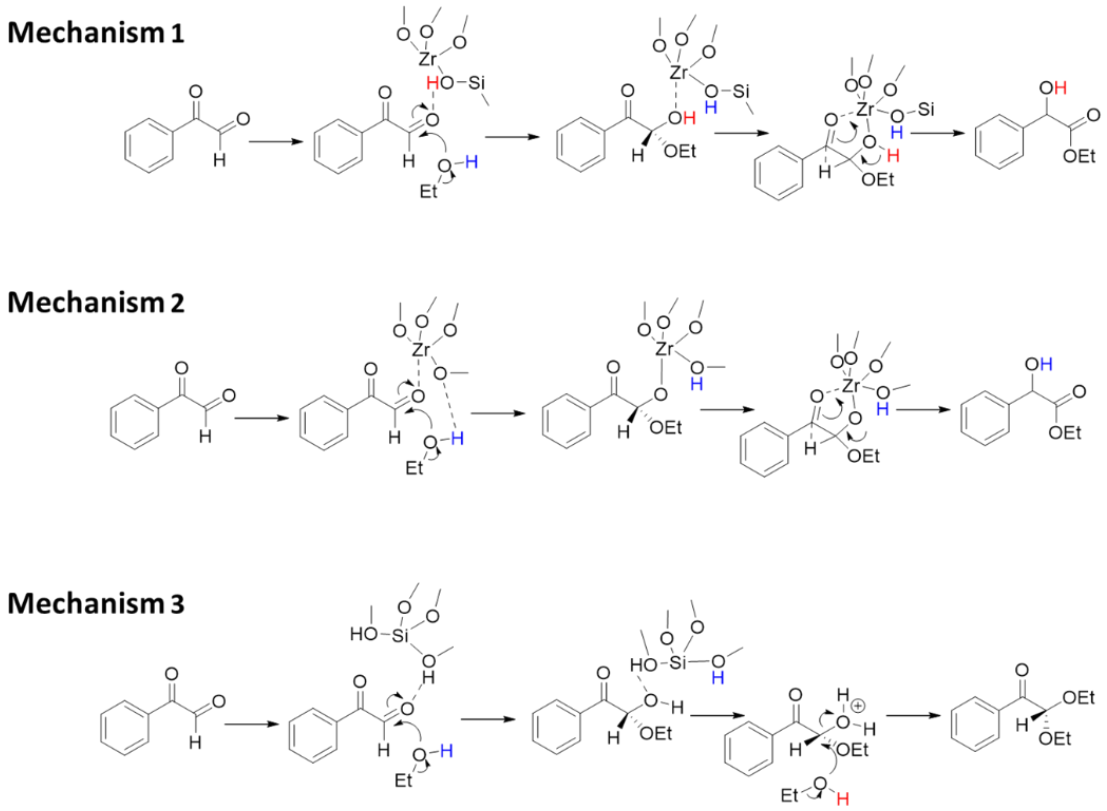

Figure 6.10 Proposed mechanisms of PG conversion to EM over different acid sites of MNSs: mechanism (1) is driven by LAS and BAS; mechanism (2) is driven by LAS; and mechanism (3) is driven by BAS

6.4. Conclusion

Hierarchical pores of ZrO_2/SiO_2 CS-MNS with different pore size distributions were synthesized. The FT-IR results clearly prove the successful removal of the surfactant, and XRD results show the amorphous nature of all the materials. The BET and TEM results further confirm the different pore structures of the CS-MNS. When zirconia was loaded on the CS-MNS, the different pore structures still remain and Zr was homogeneously distributed in the particles. Hierarchical structures may cause slight zirconia aggregation, which results in less Zr exposed and less Zr reacting with Si in the materials. As a result, CS-MNS-2-10Zr and CS-MNS-3-10Zr contain lower

acidity than CS-MNS-1-10Zr, regardless of LAS and BAS. In study of PG to EM conversion, all the materials display an increasing catalytic activity in PG conversion as zirconia concentration increases. When zirconia concentration is 1 %, there is no obvious difference in catalytic activity among different structures. Higher zirconia concentration highlights the advantages of hierarchical pore structures, and the superiority is prominent at the Zr concentration of 10 %. CS-MNS-3-10Zr presents a PG conversion of ~77 %, follows CS-MNS-2-10Zr at ~63 %, and CS-MNS-1-10Zr displays a PG conversion of 49 %. The highest PG conversion goes into CS-MNS-3-30Zr at ~93 % with an EM selectivity of ~99 %. Since hierarchical structure can not only heighten the effective collision between the substrates and the active sites but also promote the diffusion of the reactants to the active sites, it is beneficial for PG conversion. As a result, CS-MNS-2-10Zr (35.1 h^{-1}) and CS-MNS-3-10Zr (34.5 h^{-1}) achieve the TOFs more than twice over CS-MNS-1-10Zr (14.0 h^{-1}). This research is of great interest for the study of the role of hierarchical pore structures in the catalytic reactions which contain the variation of the molecular chain length.

References

[1] Wang, P.; Tao, W. J.; Sun, X. L.; Liao, S.; Tang, Y. *J. Am. Chem. Soc.* **2013**, *135*, 16849-16852.

[2] Abaee, M. S.; Sharifi, R.; Mojtahedi, M. M. *Org. Let.* **2005**, *7*, 5893-5895.

[3] Liu, Z. Q.; Zhang, X. H.; Xue, Y. P.; Xu, M.; Zheng, Y. G. *J. Agric. Food Chem.* **2014**, *62*, 4685-4694.

[4] Poterała, M.; Dranka, M.; Borowiecki, P. *Eur. J. Org. Chem.* **2017**, 2290-2304.

[5] Martinkova, L.; Kren, V. *Appl. Microbiol. Biotechnol.* **2018**, *102*, 3893-3900.

[6] Xu, H.; Wang, Z.; Miao, Z.; Zhu, Y.; Marianov, A.; Wang, L.; Castignolles, P.; Gaborieau, M.; Huang, J.; Jiang, Y. *ACS Sustain. Chem. Eng.* **2019**, *7*, 8931-8942.

[7] Kasprzak, J.; Rauter, M.; Denter, S.; Becker, K.; Baronian, K.; Bode, R.; Schauer, F.; Piontek, M.; Vorbrodt, H. M.; Kunze, G. *J. Mol. Catal. B: Enzym.* **2016**, *133*, 176-186.

[8] Liu, X.; Du, X.; Feng, J.; Wu, M. B.; Lin, J.; Guan, J.; Wang, T.; Zhang, Z. *Catal. Lett.* **2019**, *149*, 1710-1720.

[9] Wang, Z.; Jiang, Y.; Hunger, M.; Baiker, A.; Huang, J. *ChemCatChem* **2014**, *6*, 2970-2975.

[10] Wang, Z.; Jiang, Y.; Baiker, A.; Huang, J. *ACS Catal.* **2013**, *3*, 1573-1577.

[11] Corma, A. *Curr. Opin. Solid St. M.* **1997**, *2*, 63-75.

[12] Pescarmona, P. P.; Janssen, K. P. F.; Delaet, C.; Stroobants, C.; Houthoofd, K.; Philippaerts, A.; Jonghe, C. D.; Paul, J. S.; Jacobs, P. A.; Sels, B. F. *Green Chem.* **2010**, *12*, 1083-1089.

[13] Clippel, F.; Dusselier, M.; Rompaey, R. V.; Vanelderen, P.; Dijkmans, J.; Makshina, E.; Giebeler, L.; Oswald, S.; Baron, G. V.; Denayer, J. F.; Pescarmona, P. P.; Jacobs, P. A.; Sels, B. F. *J. Am. Chem. Soc.* **2012**, *134*, 10089-10101.

[14] Li, L.; Stroobants, C.; Lin, K.; Jacobs, P. A.; Sels, B. F.; Pescarmona, P. P. *Green Chem.* **2011**, *13*, 1175-1181

[15] Wang, Z.; Jiang, Y.; Rachwalik, R.; Liu, Z.; Shi, J.; Hunger, M.; Huang, J. *ChemCatChem* **2013**, *5*, 3889-3896.

[16] Peng, P.; Gao, X. H.; Yan, Z. F.; Mintova, S. *Natl.Sci. Rev.* **2020**, *7*, 1726-1742.

[17] Li, R.; Wang, P.; Ma, S.; Yuan, F.; Li, Z.; Zhu, Y. *Chem. Eng. J.* **2020**, *379*, 1-12.

[18] Shen, X.; Kang, J.; Niu, W.; Wang, M.; Zhang, Q.; Wang, Y. *Catal. Sci. Technol.* **2017**, *7*, 3598-3612.

[19] Du, Y. Y.; Jin, Q.; Feng, J. T.; Zhang, N.; He, Y. F.; Li, D. Q. *Catal. Sci. Technol.* **2015,** *5*, 3216-3225.

[20] Ishii, H.; Ikuno, T.; Shimojima, A.; Okubo, T. *J. Colloid Interface Sci.* **2015**, *448*, 57-64.

[21] Zhang, Q.; Joo, J. B.; Zaera, F.; Yin, Y. *Acc. Chem. Res.* **2013**, *46*, 1816-1824.

[22] Gawande, M. B.; Goswami, A.; Asefa, T.; Guo, H.; Biradar, A. V.; Peng, D. L.; Zboril, R.; Varma, R. S. *Chem. Soc. Rev.* **2015**, *44*, 7540-7590.

[23] Joo, S. H.; Park, J. Y.; Tsung, C. K.; Yamada, Y.; Yang, P.; Somorjai, G. A. *Nat. Mater.* **2009**, *8*, 126-131.

[24] Chen, J.; Zhang, R.; Han, L.; Tu, B.; Zhao, D. *Nano Res.* **2013**, *6*, 871-879.

[25] Kim, M.; Laine, R. M. *J. Am. Chem. Soc.* **2009**, *131*, 9220-9229.

[26] Kim, M.; Hinklin, T. R.; Laine, R. M. *Chem. Mater.* **2008**, *20*, 5154-5162.

[27] Hoshikawa, Y.; Yabe, H.; Nomura, A.; Yamaki, T.; Shimojima, A.; Okubo, T. *Chem. Mater.* **2010**, *22*, 12-14.

[28] Lentz, C. W. *Inorg. Chem.* **1964**, *3*, 574-579.

[29] Su, G.; Yang, C.; Zhu, J. J. *Langmuir* **2015**, *31*, 817-823.

[30] Quan, G.; Pan, X.; Wang, Z.; Wu, Q.; Li, G.; Dian, L.; Chen, B.; Wu, C. *J. Nanobiotechnol.* **2015**, *13*, 7.

[31] Feifel, S. C.; Lisdat, L. *J. Nanobiotechnol.* **2011**, *9*, 1-12.

[32] Garcia-Bennett, A. E.; Lund, K.; Terasaki, O. *Angew. Chem. Int. Ed.* **2006**, *45*, 2434-2438.

[33] Sing, K. S. W.; Everett, D. H.; Haul, R. A. W.; Moscou, L.; Pierotti, R. A.; Rouquerol, J.; Siemieniewska, T. *Pure Appl. Chem.* **1984**, *57*, 603-619.

[34] Idakiev, V.; Tabakova, T.; Naydenov, A.; Yuan, Z. Y.; Su, B. L. *Appl. Catal. B: Environ.* **2006**, *63*, 178-186.

[35] Hu, L. H.; Ji, S. F.; Jiang, Z.; Song, H. L.; Wu, P. Y.; Lint, Q. Q. *J. Phys. Chem. C* **2007**, *111*, 15173-15184.

[36] Ward, A. J.; Costanzo, L.; Masters, A. F.; Maschmeyer, T. *Nano. Res. Let.* **2011**, *6*, 1-8.

[37] Kuwahara, Y.; Kang, D. Y.; Copeland, J. R.; Bollini, P.; Sievers, C.; Kamegawa, T.; Yamashita, H.; Jones, C. W. *Chem-Eur. J.* **2012**, *18*, 16649-16664.

[38] Zheng, A.; Huang, S. J.; Liu, S. B.; Deng, F. *Phys. Chem. Chem. Phys.* **2011**, *13*, 14889-14901.

[39] Zheng, A.; Liu, S. B.; Deng, F. *Chem. Rev.* **2017**, *117*, 12475-12531.

[40] Lang, S.; Benz, M.; Obenaus, U.; Himmelmann, R.; Hunger, M. *ChemCatChem* **2016**, *8*, 2031-2036.

[41] Feng, N.; Zheng, A.; Huang, S. J.; Zhang, H.; Yu, N.; Yang, C. Y.; Liu, S. B.; Deng, F. *J. Phys. Chem. C* **2010**, *114*, 15464-15472.

[42] Haw, J. F.; Shimizu, K.; Venkatraman, T. N.; Luigi, D. P.; Song, W.; Barich, D. H.; Nicholas, J. B. *J. Am. Chem. Soc.* **2000**, *122*, 12561-12570.

Chapter 7 Conclusion and future work

7.1 Conclusion

This thesis covers the study of zirconia-based catalysts and their catalytic performance in glucose to HMF and PG to EM conversions. Through different modification methods, such as tuning thermal treatment, loading tungsten on zirconia, developing different layer constructions and different hierarchical structures, a variety of catalytically active complex based on zirconia were designed and fabricated. It provides valuable strategies for solid acid catalyst design, including manipulating the crystalline structure, acidity strength, acid sites distribution, and pore size distributions *etc*. At the same time, a comprehensive understanding of the mechanisms in these reactions were also studied, which contributed key knowledge for enhancing the efficiency of the catalysts in biomass conversion.

First, the impact of calcination temperature on ZrO_2 and its catalytic activity in glucose conversion was investigated. It shows that ZrO_2 is in an amorphous state when the calcination temperature is 300 °C, and it starts to crystallize with increasing calcination temperature, which causes a decrease of BET surface area and an increase of crystallite size. The ZrO_2 possesses both LAS and BAS when the calcination temperature is 300 or 400 °C. Increasing the calcination temperature leads to a distinct decrease in BAS, along with a decrease in the total number of acid sites. At the same time, a new type of LAS appears with a downfield shift. It is suggested that the strong acidity of the catalyst plays an important role during glucose conversion, and the BAS may be another influencing factor. ZrO_2 calcined at 300 °C, which possesses more BAS and LAS than ZrO_2 calcined at higher temperature, shows a better catalytic performance in glucose conversion.

Further manipulating the acidity features of ZrO_2 is through loading tungsten on it. The single-step FSP and conventional impregnation methods were applied in the synthesis process. All the materials possess low surface areas, resulting in a relatively high W surface density presented in different forms. The WO_x/ZrO_2 synthesized from conventional impregnation method (IM-WO_x/ZrO_2) is made up of W located on the ZrO_2 support in a pile-up form. Unlike IM-WO_x/ZrO_2, the rapid quenching and short residence time of the components in the flame prevent W atoms from significant sintering on ZrO_2 support and therefore maintain high surface dispersion of W. As a result, excellent uniform distribution of W on ZrO_2 support can be achieved in FSP-made WO_x/ZrO_2 (FSP-WO_x/ZrO_2), which in turn produces more three-dimensional Zr-WO_x clusters, either in the small size range of ~0.8-1.0 nm or large size of 1-3 nm. The coordination of W-OH to the unsaturated Zr^{4+} sites in these clusters results in a remarkable decrease of LAS concentration on the surface of ZrO_2 and promotes the formation of bridging W-O(H)-Zr hydroxyl groups which act as BAS. Therefore, FSP-WO_x/ZrO_2 facilitates much higher population densities of BAS (~80 %) and creates significantly higher BAS to LAS ratios (B/L) than IM-WO_x/ZrO_2, as evidenced by NH_3-TPD and ^{31}P MAS NMR. Based on this advantage, FSP-WO_x/ZrO_2 shows a better catalytic performance than IM-WO_x/ZrO_2 in glucose conversion, expressing as its high HMF selectivity. It is concluded that the B/L ratio plays a crucial role in glucose conversion, virtually independent of the total acidity of the catalysts.

In order to adjust the distribution of LAS and BAS, layered mesoporous ZrO_2/SiO_2 nanospheres (ZrO_2/SiO_2 MNS) were designed. It shows that the introduction of Zr can affect the pore structures of ZrO_2/SiO_2 MNS. Non-bulk crystalline zirconia was detected in the materials, and the Zr is found to be homogenously dispersed in all the structured ZrO_2/SiO_2 MNS. The structure of Z/SZ possesses higher acidity with more BAS than all the other structured MNS ZrO_2/SiO_2 catalysts

when the Zr concentration is low. It is suggested that the ZrO_2 in the outer layer of Z/SZ mainly produces LAS while the BAS may come from the interfacial and inner part due to the formation of Si-O(H)-Zr bonds. The increase of Zr content contributes to the formation of BAS in Z/S, SZ/S, and S/SZ which may be due to the formation of Si-O(H)-Zr bonds. In the study of the catalytic performance in glucose conversion over these ZrO_2/SiO_2 MNS, it is found that the BAS can accelerate the conversion of glucose by driving the reaction to HMF direction that can overcome the equilibrium limitation of the isomerization step. Z/SZ, which contains LAS in the outer layer and BAS in the inner layer and layer interface turns out to show the best performance in glucose conversion over all the catalysts. It is suggested that the BAS can accelerate the conversion of glucose by driving the reaction to HMF direction that can overcome the equilibrium limitation of the isomerization step.

Other than the layered structure, the hierarchical pore structured ZrO_2/SiO_2 core-shell mesoporous nanospheres (ZrO_2/SiO_2 CS-MNS) with different pore size distributions were also developed to investigate its effect on the catalytic performance. The loading of zirconia is found to have little influence on the pore structure of the CS-MNS, and it seems that the Zr is homogeneously distributed in the catalysts. However, hierarchical structures may cause slightly zirconia aggregation, which results in less Zr exposed and less Zr reacting with Si in the materials. As a result, hierarchical ZrO_2/SiO_2 CS-MNS present lower acidity than ZrO_2/SiO_2 CS-MNS with uniform pore size distribution. Since hierarchical structure can not only heighten the effective collision between the substrates and the active sites but also promote the diffusion of the reactants to the active sites, it is favorable for some reactions which contain molecular size expanding during the process, such as PG to EM conversion. Therefore, the hierarchical structures with no mater larger shell than the core or smaller shell than the core can both present better catalytic performance

than the structure with uniform pore size distribution in PG to EM conversion, presenting as higher PG conversion and higher TOFs.

7.2 Future work

This thesis presents the exploration of zirconia-based catalysts and their application in biomass conversion. It is demonstrated that the catalytic performance of the zirconia-based catalysts in glucose to HMF and PG to EM conversions can be tuned by modifying its surface acidity properties through varying the crystalline structures, loading metals on zirconia, or supporting zirconia on other mesoporous materials.

This thesis reveals that the presence of BAS in the catalysts is beneficial for the catalytic performance in glucose conversion. The catalysts which contain BAS show much better activity than other catalysts which contain only LAS or a low fraction of BAS. Based on this result, the exploration of the relationship between the B/L ratio and the catalytic performance is very promising. On the other hand, though the BAS of the zirconia-based catalyst can be improved by loading metals on it, the precise control of the B/L ratio in the catalysts still needs to be further explored.

As it is well known that both LAS and BAS of the catalyst are active in glucose conversion, and LAS are generally required for glucose isomerization to fructose, followed by a BAS catalyzed dehydration of fructose to HMF. The detailed mechanism about how LAS or BAS (by only one type of the acid site itself or through the cooperation of the two types of acid sites) work at the molecular level on glucose conversion is still remained to be clearly studied and this part is probably one of the most difficult challenges faced nowadays. Though lots of plausible mechanisms have been proposed by other literature, further evidenced via abundant experimental

or theoretical analysis are desirable to unveil the mechanism mystery. Hence, this will largely help the design of more efficient catalysts for glucose conversion. At the same time, further rehydration of HMF also happens during the reaction, lowering the final presented HMF yield. How to avoid this reaction happening is also significant for HMF production.

Another aspect is about the solvent used in glucose conversion. Adding a co-solvent such as an organic phase in the aqueous media is good for the reaction through converting the produced HMF to a less reactive derivative, or removing the HMF from the aqueous media to extracting organic phase, or introducing adsorbents which can selectively enrich HMF in the reaction system. The organic phase used in this thesis is DMSO that is commonly used in other literature. However, organic solvents are still considered as non-environmental solutions. H_2O is a green solvent and it is abundant compared to other organic solvents, making it the priority choice. In this case, though this reaction in H_2O is of high challenge and low productive at the moment, designing the catalysts which can work well in the pure aqueous phase is very worthwhile and competitive. On the other hand, the reaction temperature in this reaction is 170 ^oC, which needs much energy.

Regarding the layered ZrO_2/SiO_2 MNS, the layer contents are designed on only two components, silica and zirconia. So multiple elements such as other metals included in the layered MNS can also be another highlight to fabricate multifunctional catalysts.

For the hierarchical pore structured ZrO_2/SiO_2 CS-MNS, the difference of the pore size is not big, so it will be much interesting to design core-shell mesoporous materials with larger difference of the pore size, which may enable the catalysts to reach a higher selectivity in some reactions containing long chain molecules.

As for the catalytic reactions studied in this thesis, glucose to HMF and PG to EM conversions, which are important processes in the field of biorefinery. Preparation of more efficient, stable,

recyclable, inexpensive zirconia-based catalysts for these reactions is always of the high interest in catalysis industry. At the same time, developing more applicable biorefinery process is also worth to be comprehensively studied to stimulate the expansion of the biorefining industry.

Appendix

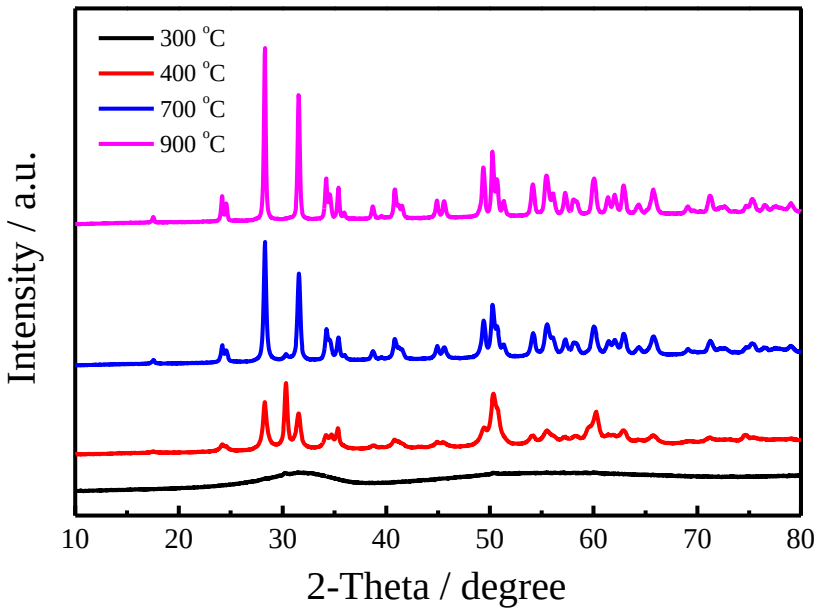

Figure A1 XRD patterns of ZrO_2 calcined at different temperatures

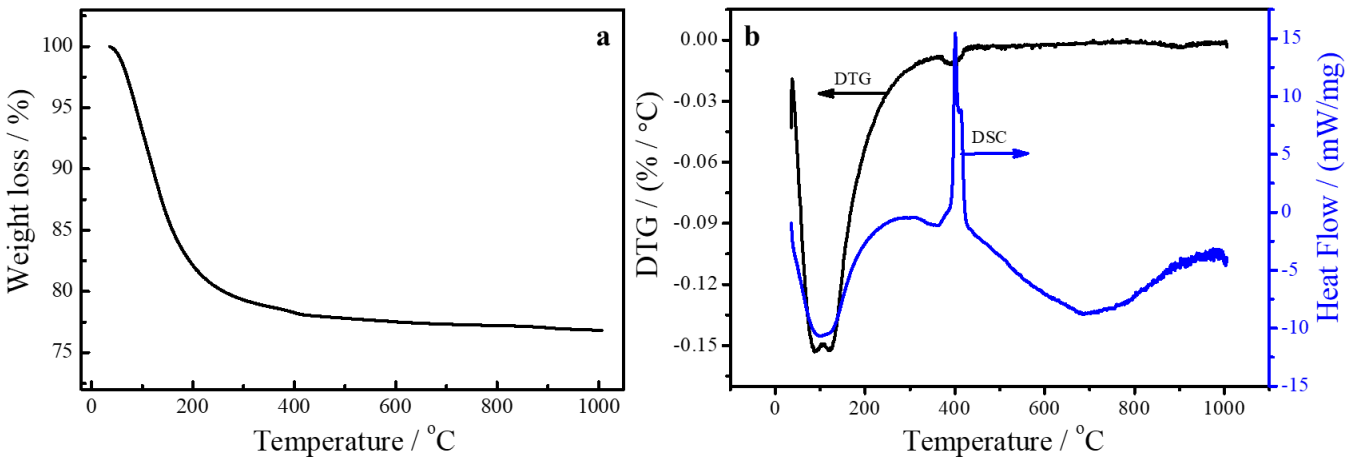

Figure A2 TGA curve (a), DTG and DSC curves of $Zr(OH)_4$ (b)

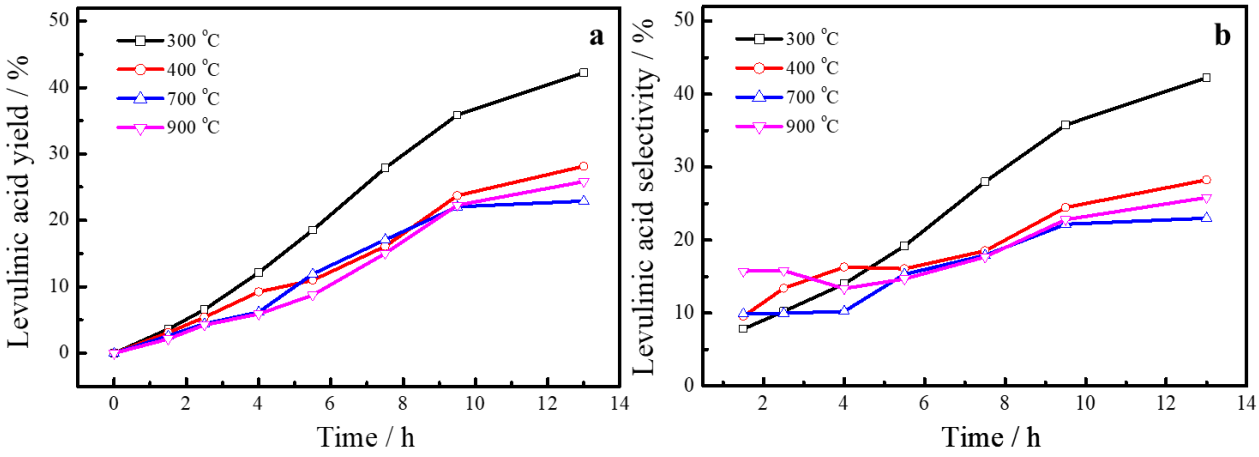

Figure A3 Levulinic acid yield (a) and selectivity (b) with ZrO_2 at 170 °C

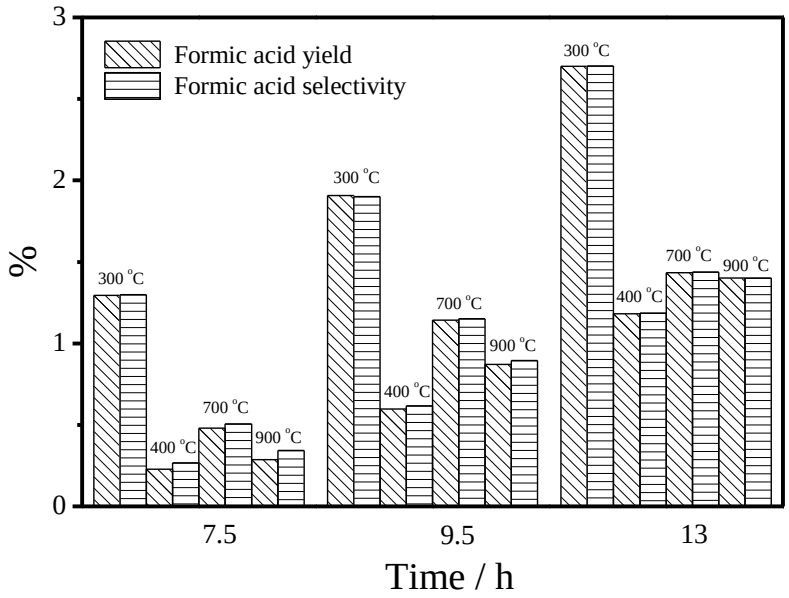

Figure A4 Formic acid yield and selectivity with ZrO_2 at 170 °C

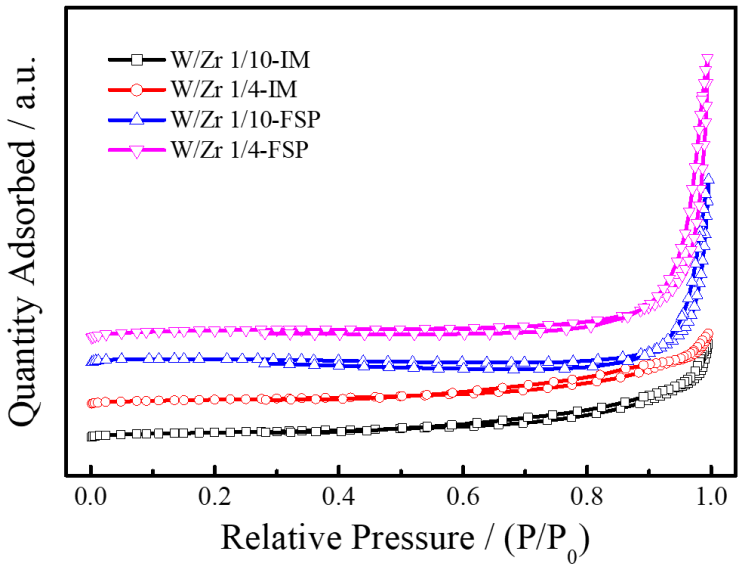

Figure A5 N_2 adsorption-desorption isotherm of WO_x/ZrO_2

Table A1 Surface area, total pore volume, average pore size and calculated tungsten surface density values of WO_x/ZrO_2

	BET surface area (m^2/g)	Pore volume (cm^3/g)	Average pore size (nm)	Surface density (W-atom · nm^{-2})
W/Zr 1/10-IM	22.4	0.050	8.1	18.5
W/Zr 1/4-IM	20.6	0.049	8.1	40.3
W/Zr 1/10-FSP	10.8	0.018	9.1	38.4
W/Zr 1/4-FSP	24.6	0.036	12.8	33.8

Table A2 Quantitative analysis of the crystallite size and volume fraction of different crystalline phases of ZrO_2 in WO_x/ZrO_2

	Volume fraction of (%)		Crystallite size (nm)	
	t-ZrO_2	m-ZrO_2	t-ZrO_2	m-ZrO_2
W/Zr 1/10-IM	68.1	31.9	19.4	24.5
W/Zr 1/4-IM	72.4	27.6	18.9	25.5
W/Zr 1/10-FSP	64.8	35.2	26.9	30.5
W/Zr 1/4-FSP	71.3	28.7	36.6	31.5

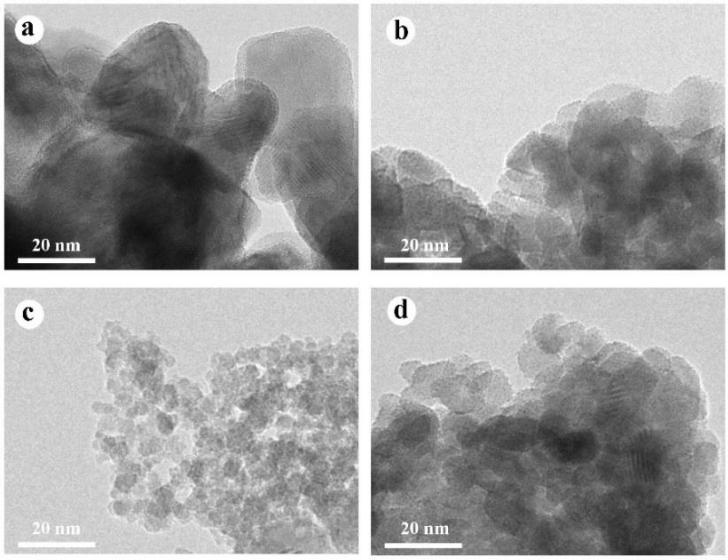

Figure A6 TEM images of WO_x/ZrO_2 (a: W/Zr 1/10 IM; b: W/Zr 1/4 IM; c: W/Zr 1/10 FSP; d: W/Zr 1/4 FSP)

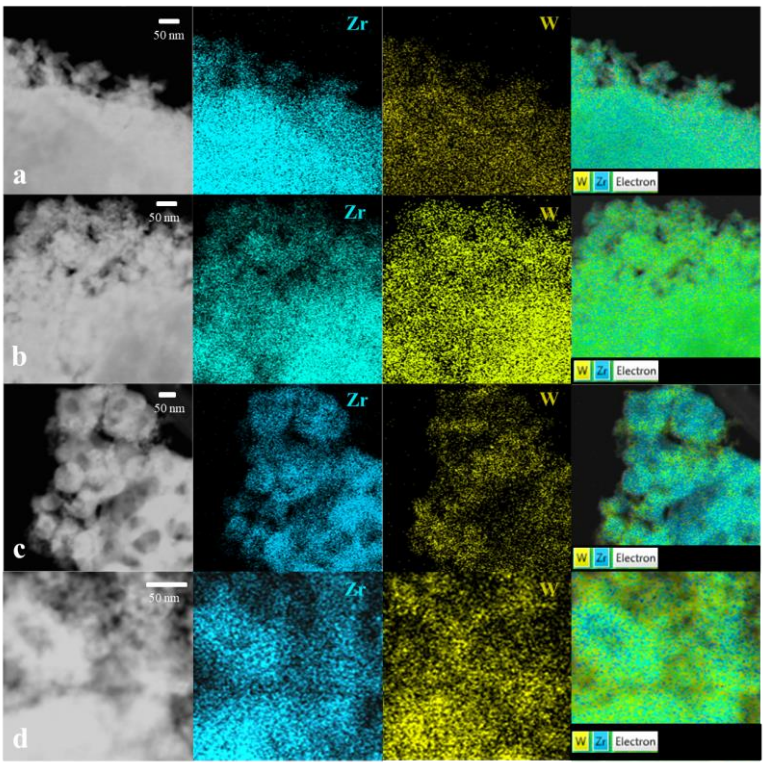

Figure A7 EDS images of WO_x/ZrO_2: (a) W/Zr 1/10-IM; (b) W/Zr 1/4-IM; (c) W/Zr 1/10-FSP; and (d) W/Zr 1/4-FSP

Table A3 XPS peak positions of O1, O2, and O3 sub-peaks de-convoluted from the O 1s peak, and the relative integrated intensity ratios of WO_x/ZrO_2

	O1		O2		O3	
	Position (eV)	Ratio (O1/Otot)	Position (eV)	Ratio (O2/Otot)	Position (eV)	Ratio (O3/Otot)
W/Zr 1/10-IM	530.3	84.8	531.7	11.3	532.8	3.9
W/Zr 1/4-IM	530.5	88.5	532.0	9.0	533.0	2.5
W/Zr 1/10-FSP	530.2	46.6	531.7	45.7	532.7	7.7
W/Zr 1/4-FSP	530.6	71.7	532.0	19.3	533.1	9.0

Table A4 XPS parameters of the W (4f) region in WO_x/ZrO_2

	BE (eV)	Assignment	W (%)	W^{6+}/W^{5+}	W (at%)	Zr (at%)	W/Zr
W/Zr 1/10-IM	36.0	W^{6+}	56.3	1.29	3.71	19.85	0.19
	35.6	W^{5+}	43.7				
W/Zr 1/4-IM	36.0	W^{6+}	64.0	1.78	4.47	19.4	0.24
	35.5	W^{5+}	36.0				
W/Zr 1/10-FSP	35.8	W^{6+}	39.7	0.66	1.12	12.32	0.09
	35.4	W^{5+}	60.3				
W/Zr 1/4-FSP	36.1	W^{6+}	49.9	1.00	4.68	14.29	0.34
	35.6	W^{5+}	50.1				

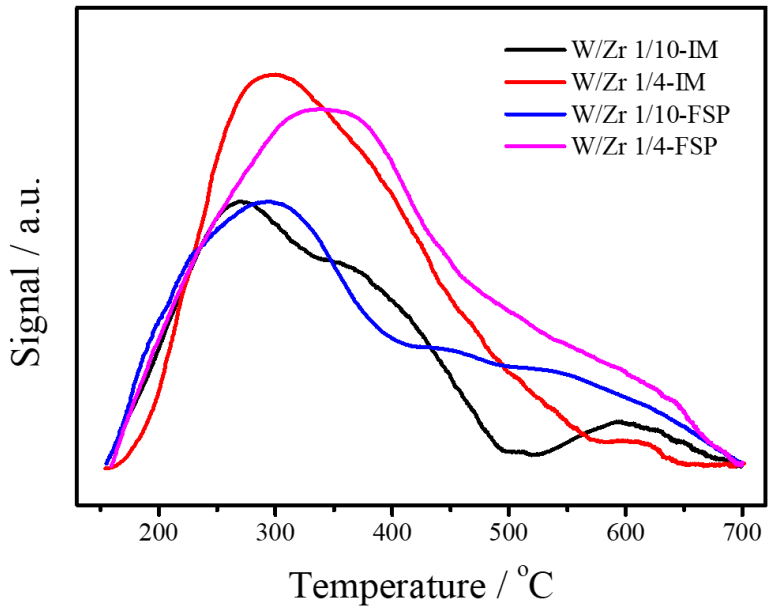

Figure A8 NH_3-TPD profiles of WO_x/ZrO_2

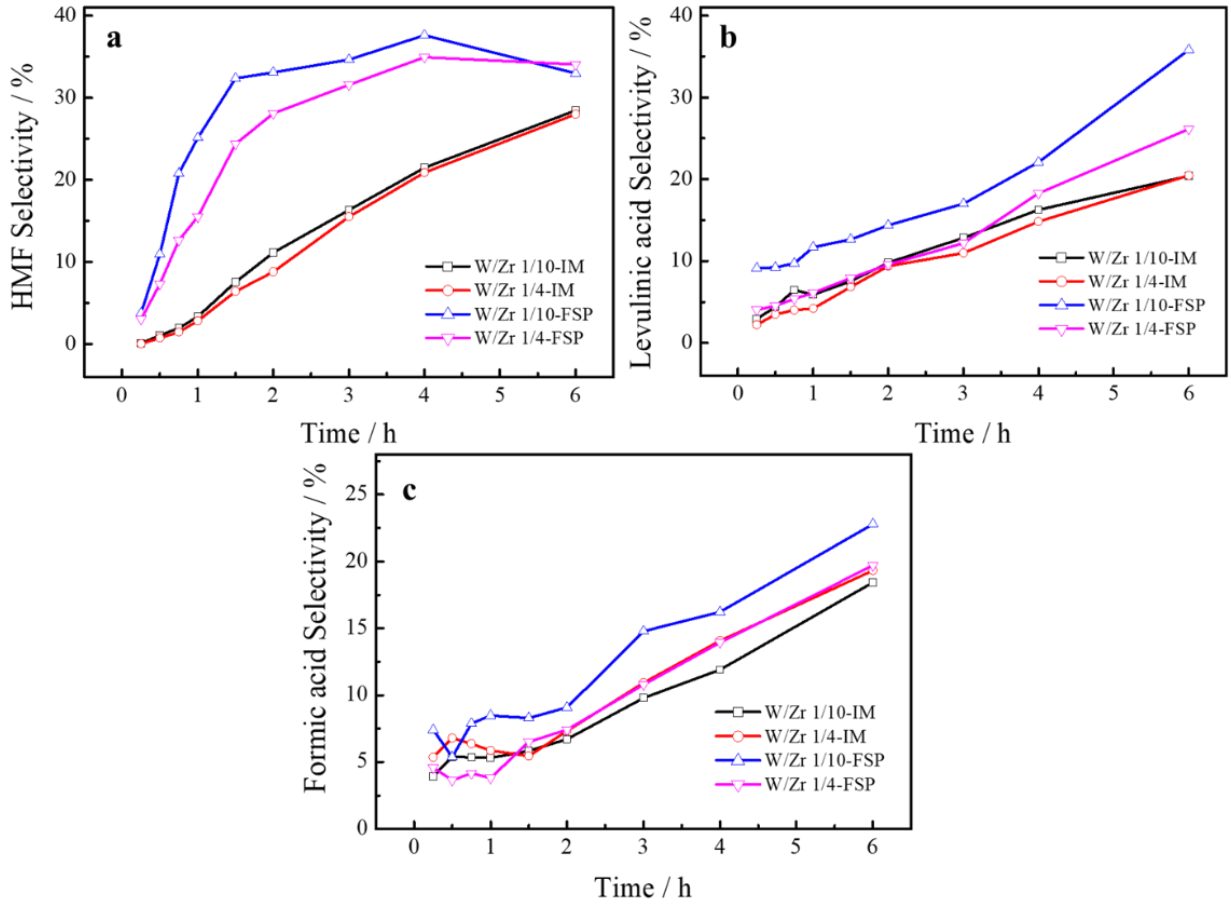

Figure A9 The selectivity of products: (a) HMF; (b) levulinic acid; and (c) formic acid

Table A5 The final molar compositions of Zr and Si for the ZrO_2/SiO_2 MNSs

	Sample	Zr	Si	Sample	Zr	Si
Inner layer	Z/S-10	-	1.0	S/SZ-10	0.1	0.9
Outer layer		0.1	-		-	1.0
Inner layer	Z/S-30	-	1.0	S/SZ-30	0.3	0.7
Outer layer		0.3	-		-	1.0
Inner layer	Z/S-50	-	1.0	S/SZ-50	0.5	0.5
Outer layer		0.5	-		-	1.0
Inner layer	Z/S-70	-	1.0	S/SZ-70	0.7	0.3
Outer layer		0.7	-		-	1.0
Inner layer	SZ/S-10	-	1.0	Z/SZ-10	0.1	0.9
Outer layer		0.1	0.9		1.0	-
Inner layer	SZ/S-30	-	1.0	Z/SZ-30	0.3	0.7
Outer layer		0.3	0.7		1.0	-
Inner layer	SZ/S-50	-	1.0	Z/SZ-50	0.5	0.5
Outer layer		0.5	0.5		1.0	-
Inner layer	SZ/S-70	-	1.0	Z/SZ-70	0.7	0.3
Outer layer		0.7	0.3		1.0	-

Table A6 Quantitative analysis of acid sites in the ZrO_2/SiO_2 MNSs with high Zr concentration according to ^{31}P MAS NMR spectra

	Chemical shift (ppm)[a]				B/L
	60±1	56	45±1	40	
Z/S-70	-	16.7	83.3	-	0.200
SZ/S-70	-	24.8	75.2	-	0.330
S/SZ-70	-	18.6	81.4	-	0.229
Z/SZ-70	26.9	-	-	73.1	0.368

[a.] For comparison, Gaussian-Lorentz simulation results obtained for the samples representing TMPO adsorbed on Brønsted and/or Lewis acid sites (denoted by chemical-shift values) with practically the same chemical shift are aligned in the same column.

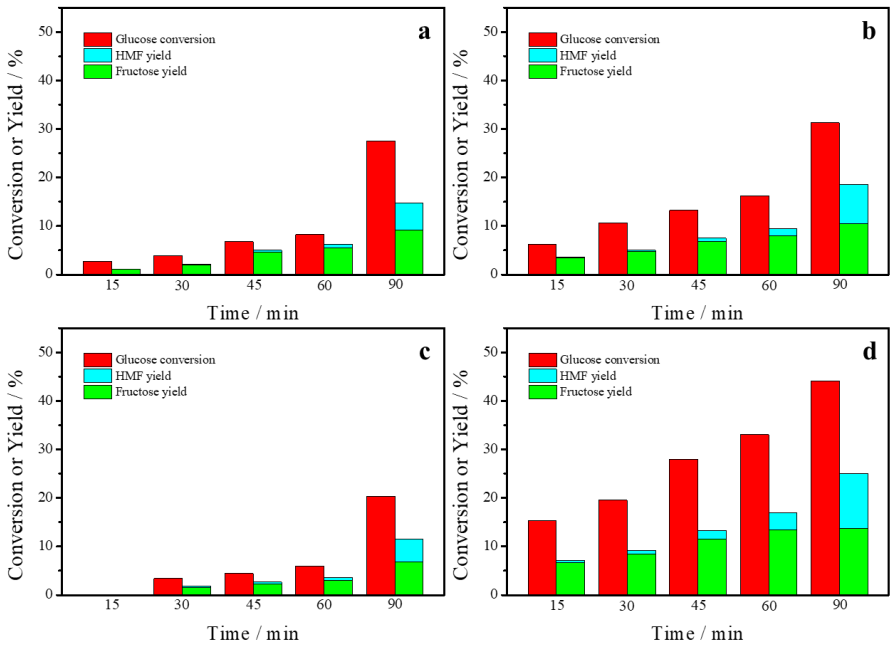

Figure A10 Glucose conversion, fructose yield and HMF yield over the ZrO_2/SiO_2 MNS at 170 ^oC: (a) Z/S-30; (b) SZ/S-30; (c) S/SZ-30; and (d) Z/SZ-30

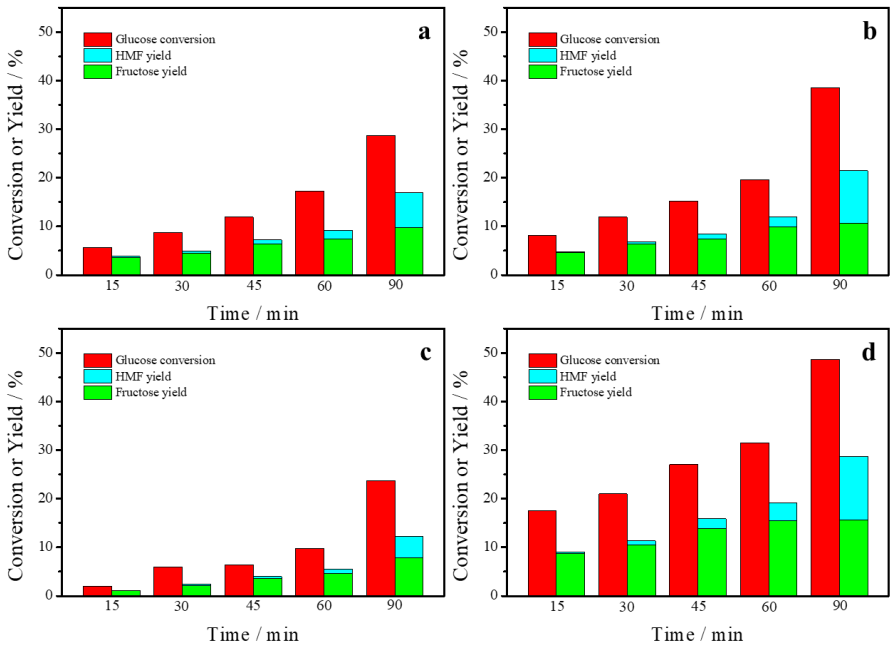

Figure A11 Glucose conversion, fructose yield and HMF yield over the ZrO_2/SiO_2 MNS at 170 ^oC: (a) Z/S-50; (b) SZ/S-50; (c) S/SZ-50; and (d) Z/SZ-50

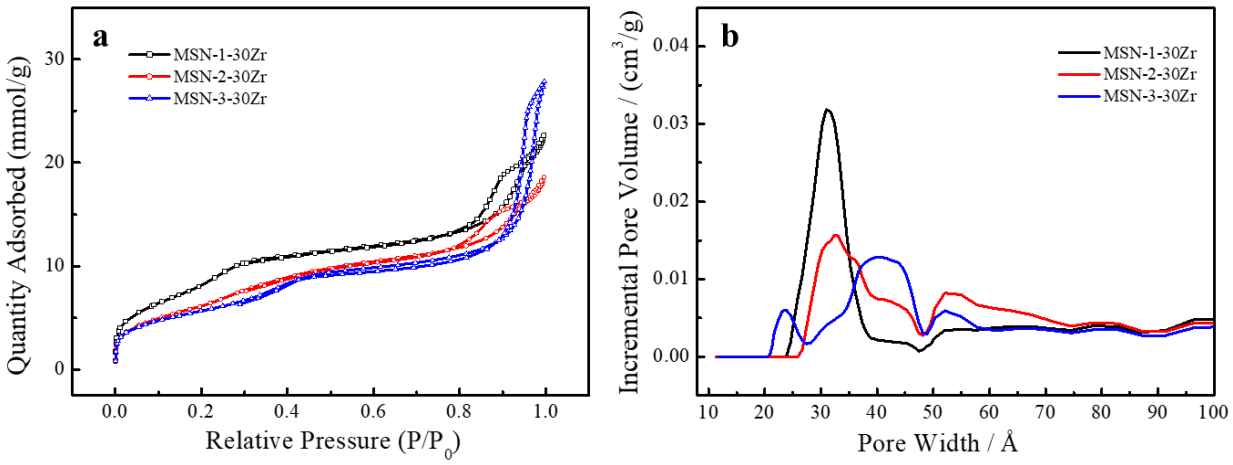

Figure A12 N_2 adsorption-desorption isotherm (a) and pore size (b) of MNSs after loading 30 % of zirconia

Table A7 BET surface area, pore size and pore volume of MNSs after loading 30 % of zirconia

Sample	BET surface area (m^2/g)	Average pore size (nm)	Pore volume (cm^3/g)
MNS-1-30Zr	759.4	3.2	0.526
MNS-2-30Zr	545.8	3.3, 5.2	0.463
MNS-3-30Zr	467.0	4.2, 5.2	0.426